Particle-scale Numerical Study on Screening Processes

S M Arifuzzaman

A thesis in fulfilment of the requirements for the degree of

Doctor of Philosophy

Centre for Infrastructure Engineering (CIE)

School of Engineering, Design and Built Environment (SoEDBE)

Western Sydney University, NSW, 2751, Australia

June 2022

Declaration

I hereby declare that all materials presented in this thesis are of my own work, except for quotations and summaries, which have been duly acknowledged. I also declare that this thesis contains no materials that have been summited previously, either in full or in part, for any degree at Western Sydney University or other institution except for publications.

S M ARIFUZZAMAN

Date: 25.06.22

Dedication

I dedicate this thesis to
my parents
for their constant support and unconditional love.
I love you both dearly.

ABSTRACT

Particle screening is a common and important process in many industries, including mining engineering, agricultural materials processing, recycling, and pharmaceuticals. Many industrial processes involve the classification of particles according to their sizes. Thus, extensive research attention has been paid to the sieving of granular materials, which include various fundamental particle behaviours, such as segregation, stratification, and packing, etc. Screening operation design, control, and optimisation are critical to the overall performance and profitability of the processing plant. Despite that screening is widely used, the understanding of the effects of the control variables relating to screen geometries, operational circumstances, and particle characteristics is still limited. A deeper comprehension of the process can improve screen performance and bring economic benefits.

In screening, there are generally two processes for the sieving particles: stratification/percolation in the particle bed on screen mesh and the passage of through the screen apertures. Spontaneous percolation is a common phenomenon and has been studied extensively. However, percolation under vibration has not been comprehensively studied previously. In this thesis, the effect of vibration on particle percolation is firstly studied as the first research component. The discrete element method (DEM) is used to investigate the percolation of small particles in a vibrated bed of large particles. When the size ratio is greater than 0.154 and spontaneous percolation does not happen vibration can enable percolation. The percolation velocity increases with the increase in vibration amplitude and frequency followed by subsequent decline. Furthermore, a machine learning model is used to predict percolation velocity. The percolation threshold size ratio can be calculated as a function of vibration conditions. Machine learning has also shown to be effective in the modelling of parameters proposed in current particle segregation theories. The combination of DEM, machine learning, and percolation theory can be explored further to model related industrial processes such as sieving and mixing.

In spite of the widespread usage of vibrating screens in the industry, current process models face difficulty while considering the enormous controlling variables and complicated particle-particle interactions. As the second component of the thesis, a new process model for vibrating screens is developed by using a combination of discrete element method simulation and physics-informed machine learning. The relationship between the passing rate and local condition is first established using machine learning on data generated by a series of controlled

DEM simulations while assuming that the particle passing through a section of a screen was dependent on the local screen and flow conditions. In particular, a universal local passing function is developed to predict the passing flow rates of different size particles on a screen segment, according to the segment's vibration conditions, inclination angle, and the inlet flow. Furthermore, the process model can be applied not only to the original simulated incline vibrating screen, but also to modified screens with different inclination angles and vibration conditions in different segments without affecting the local passing function. The model could help in the intelligent design, control of industrial screens and other particle classification processes.

Furthermore, a multi-layer vibrating screen is the primary method for fine materials sizing in the process industry. The third component of the thesis develops a screening process model for the inclined double layer-vibrating screen using a combination of DEM simulation and machine learning, which is extended from the second component. The passing particles from the top layer and the upper stream flow of the bottom layer are considered for the bottom layer inlet. The process model for the entire screen can then be created by connecting different segments using mass continuity. According to local vibration conditions, incline angle and inlet flow, local passing functions are developed for top and bottom layer screens respectively to predict the passing rates of different size particles on a screen segment on the top layer and the bottom layer. This double-layer process model helps predict the passing of particles on a local part-by-part basis, which can be used for the development of smart operations for industrial screens. The work paves the way for the integration of DEM simulation, data modelling and process modelling that can guide the intelligent design and control of industrial screens.

However, none of the previous studies examined screen choking in detail including the threshold of the controlling variable and the feed rate. Therefore, it is necessary to develop a more generalised model to predict the choking of the screen process. Considering the gap, in the fourth component of the thesis, a decision-making logical judgement model of screen process choking is developed by combining DEM simulation and machine learning classification. The particle inlet in a particular section of the screen and the flow controlling variables are regarded as dependent variables while building the database The machine learning database is generated by a series of controlled DEM simulations to create the choking logical model. The proposed logical binary function for screen choking can predict whether or not choking will occur under specific conditions. The safe operational conditions without choking

can be identified under different constraints by using this model. The logical choking model could also predict the complex feed threshold in the screening.

One of the most important factors in screening is the particle's shape. Theoretical developments of particles contact force model and particles shape are receiving increasing attention in recent years for DEM. In the final research component of the thesis, a novel algorithm for simulating superellipse shaped particles and their packing is proposed. The method creates an explicit force models based on Fourier series for identical superellipses, which is the first in the literature. The results demonstrated that the explicit force model established by this method can be effectively used in DEM simulations. The method is applied for a wide range of superellipse shapes. The errors between the approximate Fourier series and the original solutions are analyzed and found to be small. The packing of superellipses is complexly dependent on squareness, aspect ratio and friction. These findings offer a novel approach for developing explicit force models for non-spherical particles while improving the understanding of non-spherical particle packing. It is an attempt to model non-spherical particle packing and could be implemented in the screening process in the future.

In summary, the research in this thesis is useful for the fundamental understanding of the effect of particles' contact force, operational conditions, particle properties, percolation and sieving on the screening process. Moreover, the novel process models based on artificial intelligence modelling, DEM simulation, and physics laws can help the design, control and optimisation of screening processes.

ACKNOWLEDGEMENTS

First of all, I would like to take this opportunity to express my heartfelt appreciation to my principal supervisor Associate Professor Kejun Dong for his continuous support, advice, perseverance, gracious assistance and motivation during this PhD journey, which ensured my completion of this PhD project. Dr Dong has been a great mentor to me. I'd like to express my gratitude to him for supporting my research and helping me to grow as a young researcher. His advice on both science and my professional life has been invaluable. I am the luckiest person on the planet to have a supervisor who is both good and honest. My heartfelt thanks to my co-supervisors, Associate Professor Haiping Zhu and Associate Professor Qinghua Zeng, for their insightful advice, positive encouragement and never-ending inspiration in the writing of this thesis.

I'd like to express my gratitude to the ARC Research Hub for the Computational Particle Technology and Western Sydney University for providing me the prestigious scholarships to pursue this research. For their technical and administrative assistance, I am thankful to the Engineering staff at CIE and resources (WSU) including Felicity Koulouris and others.

The members of Dr Dong's research group have made a significant contribution to my personal and professional development at Western Sydney University. The group has been a strong pillar of friendships, as well as helpfulness and coordination. My heartfelt thanks to Erfan Keshavarzian, Ruizhi Jin and Dr Reza Amirifar for their encouragement and insightful discussions. I am thankful to friends Dr Sheikh Imamul Hossain, M. Zohurul Islam, Dr MB Hosain, Dr M. Saidul Islam and others in Sydney and my other friends in Bangladesh for their support and advice. These people never failed me when I felt lonely.

I am highly grateful to my parents, S. M. Wahiduzzaman and Asma Zaman, my siblings, S. M. Asrafuzzaman, Kanij Fatema, and other members of my family (Maria Mousumi, Abu Said, beloved nephew Azfar, Arfan and Wasif) for their unwavering sacrifice, patience and love. Especially, my father (my best teacher and friend), who gave me encouragement and mental support always. Due to COVID-19, I lost him during this study period. I always remember his inspirational sentence, 'Do something new, which will outlive you on the planet and assists others'.

I don't know how to acknowledge Dr Md. Shakhaoath Khan Vai ('Vai' means elder brother in Bengali), how to thank him. If I try a thousand times, it would not be enough. He has become

an elder brother who has shielded me from frustration, a mentor who has helped me become stronger, a tutor who has taught me how to be a good researcher and, most importantly, a good human. I always like the way you guide me. Your sincerity, wisdom, compassion and regimen boosted my self-assurance. I consider myself lucky, and I am grateful for the chance to collaborate with you.

I am also thankful to all my respected teachers from school (Lions School, Khulna, Bangladesh), college (M.M. City College, Khulna, Bangladesh) and university (Khulna University, Bangladesh) for educating me and taught me to be a good person in life. I am hugely appreciative to Professor Dr Sarder Firoz Ahmmed (Khulna University, Bangladesh) for his motivation, guidance, research concept and for turning me into an early researcher.

Finally, I'd like to express my gratitude to my beloved wife, Kanij Fatama (Kona), for being a lovely life partner and best friend. I have no words to thank you enough for your unwavering love and care for me.

Thank you.

List of publications

The publications generated from the present thesis are as follows. Two papers are in published status and three are under review and submission.

Published:

1. Arifuzzaman, SM, Dong, K, Zhu, H & Zeng, Q 2021, 'DEM study and machine learning model of particle percolation under vibration', *Advanced Powder Technology*, vol. 33, no. 5, 103551. https://doi.org/10.1016/j.apt.2022.103551

2. Arifuzzaman, SM, Dong, K, Hou, Q, Zhu, H & Qinghua, Z 2020, 'Explicit contact force model for superellipses by Fourier transform and application to superellipses packing, *Powder Technology*, vol. 36, no. 1, pp. 112-123. https://doi.org/10.1016/j.powtec.2019.10.018

3. Arifuzzaman, SM, Dong, K & Yu, A 2022, 'Process model of vibrating screen based on DEM and physics-informed machine learning', *Powder Technology*, p. 117869. https://doi.org/10.1016/j.powtec.2022.117869

Under Review/ submission:

4. Arifuzzaman, SM, Dong, K & Yu, A 2022, 'Process model of inclined double layer vibrating screen based on DEM and machine learning', *Powder Technology* (to be submitted soon).

5. Arifuzzaman, SM, Dong, K & Yu, A 2022, 'Judgement model for choking of vibrating screen based on DEM and machine learning', *Minerals Engineering* (to be submitted soon).

The following conference papers are also prepared and presented based on the studies undertaken during this research project.

1. Arifuzzaman, SM, Dong, K & Yu, A 2021, 'Process model of vibrating screen based on DEM and machine learning', *The 3rd international symposium on computational*

particle technology (CPT-2021), November 17-21, 2021. SEU-Monash Joint Research Institute, Suzhou, China.

2. Arifuzzaman, SM, Dong, K & Yu, A 2021, 'DEM study and machine learning model of particles passing along inclined vibrating screen', in *Recent advances in computational methods and applications: proceedings for the fifth Australasian conference on computational mechanics* (ACCM 2021), Western Sydney University, Sydney, Australia, 13-15 December 2021.
https://doi.org/10.26183/t5jn-8y77

Contents

List of figures

List of tables

CHAPTER I: Introduction

1.1 Background to the study

Screening is a technique for classifying materials based on particle size. Screening is essential for sizing separation in a variety of industrial sectors including metallurgy, powder technology, ceramics, agriculture and mining (Dong, K, Wang & Yu 2013; Dong, K, Yu & Brake 2009; Guises et al. 2009; Li, Z & Tong 2017; Qiao et al. 2018; Wang, C, Dong & Yu 2015; Wolff 1954; Xiong et al. 2017; Yu, C et al. 2023; Zhao, L-L et al. 2019; Zhou, Z-Y et al. 2011). The screen consists of a deck surface with numerous apertures (Wolff 1954). Many researchers have investigated the effects of controlling parameters and analysed the characteristics of screening processes (Asbjörnsson et al. 2016; Cleary, Paul W, Sinnott, Matthew D & Morrison, Rob D 2009; Cleary, Paul W., Sinnott, Matthew D. & Morrison, Rob D. 2009; Dong, HL et al. 2012; Dong, K, Yu & Brake 2009; Liu, C et al. 2013; Wolff 1954). Many theoretical, experimental and numerical models were develop and used by industry to reduce production costs and process duration (Cleary, Paul W, Sinnott, Matthew D & Morrison, Rob D 2009; Cleary, Paul W., Sinnott, Matthew D. & Morrison, Rob D. 2009; Cleary, PW, Wilson & Sinnott 2018; Dong, K, Yu & Brake 2009). However, the fundamental understanding of this process is still limited due to the complexity of screen geometry, operating conditions, particle packing and particle properties, which makes the existing screen models not general.

In screening, particles are sieved with two main processes: stratification/percolation and the passage through apertures (Napier-Munn & Wills 2006). Previous research on the stratification process mostly concentrated on spontaneous percolation, which is small particles percolate through a static bed formed by large particles. Numerous parameters have been used to describe the percolation process in addition to percolation velocity. The distribution of percolating particles residence time changes with packing height, restitution coefficient and particle properties with bed geometry (Bridgwater, J, Cooke & Scott 1978; Bridgwater, J. , Sharpe & Stocker 1969; Li, J et al. 2010; Rahman et al. 2008; Williams & Shields 1967; Zhou, H et al. 2016). Percolating particles are found to move in the radial direction while primarily moving downwards, which can be modelled as dispersion (Zhu et al. 2009). Particles with a high coefficient of restitution can move longer distances and with larger radial dispersion (Bridgwater, J & Ingram 1971; Bridgwater, J. , Sharpe & Stocker 1969). The density of materials also influences percolation of particles. The transverse dispersion decreases and longitudinal dispersion increases with the increase in particle density (Lominé & Oger 2009, 2010). Denser particles percolate faster, so the particles made from materials such as steel

(Bridgwater, J, Cooke & Scott 1978) increases percolation velocity. Conversely, an increase in damping coefficient increases the percolation velocity and decrease radial dispersion (Zhu et al. 2009). In the percolation of cohesive fine particles, transverse dispersion is smaller than longitudinal dispersion for higher damping coefficient (Zhou, H et al. 2018). Furthermore, the percolation velocity for spontaneous percolation declines with a rise in rolling friction and size ratio. However, percolation under vibration has not been comprehensively studied, though in screening the vibration can influence the particle bed and enhance percolation of particles in a vibrated packed bed. Percolation under vibration helps to percolate particles with a large-size ratio. However, little research has been carried out on large size particle percolation than the spontaneous threshold (Bridgwater, J. , Sharpe & Stocker 1969; Hudson, Jansen & Linkson 1969; Kudrolli 2004; Li, J et al. 2010; Rahman et al. 2008; Wilkinson & Edwards 1982).

Particle screening is now routinely used in high-tonnage material separation applications in mineral, metallurgical, food processing and pharmaceutical industries (Esfandiary 2014; Jansen & Glastonbury 1968) (Delaney, Gary W. et al. 2012). In particular, the performance of these screens is found to be not only dependent on the screens but also very much dependent on the properties of the particles they handled. These particle properties include particle shape, particle size distribution, contact mechanics and surface characteristics. Therefore, the widely used macroscopic models in current industrial screening processes cannot be applied to different types of particles because the characteristics of granular particles are highly dynamic owing to the complex interactions between individual particles and screens. The rate of particle passage depends on the probability of passing through the aperture, vibration conditions, material properties, feeding conditions, inclination angle and screen configuration (Cleary, Paul W., Sinnott, Matthew D. & Morrison, Rob D. 2009; Cleary, PW, Wilson & Sinnott 2018; Dong, K, Wang & Yu 2013; Dong, K, Yu & Brake 2009). Different feed flow rate affects the passing of particles along the screen by changing the interaction dynamics between particles and bed depth. Most fine particles pass through the upper portion of the screen for lower feed rates, but these particles are evenly distributed across the screen for higher feed rates (Harzanagh, Orhan & Ergun 2018). The cut size of screening is higher under low vibration conditions and low inclination angle (Davoodi, A. et al. 2019; Harzanagh, Orhan & Ergun 2018; Peng, Feng, et al. 2019; Zhao, L et al. 2011). The small-sized particles block the aperture hole due to better percolation. Conversely, excessive pegging reduces the flow rate and causes screen apertures to become blocked by particles that are similar to the mesh size (Delaney, Gary W. et al. 2012). Small particles pass primarily through the upper deck of the screen.

Moreover, the particle bed of the screen is thicker at the lower deck. The stratification process significantly affects screen performance at the lower deck (Davoodi, Ali et al. 2019). The dimension of screen length affects the performance of screens. Longer screen lengths result in higher screening efficiency (Liu, C et al. 2013; Wang, G & Tong 2011). Dynamic material accumulation in the feeding region also affects the passage of undersized particles where near-mesh sized particles block the apertures of the screen. However, small particles may still travel across the interstitial gaps between large particles near the screen and pass through the apertures of the screen (Li, J et al. 2003; Zhang, B et al. 2016). The segregation ability of banana screens could be significant while being up to three to four times that of standard vibrating screens (Cleary, P et al. 2010; Dong, K, Esfandiary & Yu 2017; Dong, K, Yu & Brake 2009; Gangfeng et al. 2016; Li, Z & Tong 2017; Wills & Finch 2016).

Controlling and optimising screens is essential for application, which requires a fundamental understanding of the screening process. Effective ways to increase screen performance include reducing vibration amplitude/frequency and the incline angle of decks, using cyclical vibration rather than linear vibration and 5-deck banana screens rather than 3-deck banana screens (Dong, K, Yu & Brake 2009). The screening performance improves with the increase in deck length, which can be optimised theoretically. If the inclination of the discharge end is too small and the particle velocity amplitude is small, then the screening process would be ineffective. Considering the theoretical aperture size derived from rectangular slot apertures, a good fit could allow a larger top size of the material to fall through the deck (Asbjörnsson et al. 2016).

Recently, physics-informed machine learning has become a promising means of minimising computational time, discretisation of PDEs, algorithms and higher-dimensional problems of hidden physics. Physics-informed learning integrates mathematical models and databases through machine learning or neural networks. It can design new frameworks, standardised models and new mathematical scales for hidden physics while improving the accuracy (Jordan & Mitchell 2015; Karniadakis et al. 2021; Raissi & Karniadakis 2018; Sarker 2021; Zhang, Y & Ling 2018). By using artificial intelligence and simulation techniques, critical non-linear problems can be solved with minimal experimental cost and time requirements (Laguitton & Leung 1989; Napier-Munn & Wills 2006). Computers can solve high-level critical problems that would take years for humans to solve. For the complex and less understood grinding process, the focus on offline data-driven modelling has increased in recent years. Based on the grinding process training data, various learning algorithms such as case-based reasoning, fuzzy

logic, machine learning, artificial neural networks and genetic algorithms have been used to map the process variables and particle size. Machine learning has been widely used in intelligent fitting, pattern recognition, parameter optimisation, result prediction and error detection during the screening process (Li, Y et al. 2020; Li, Z et al. 2019; Zhang, B et al. 2016). Trained models help to predict results, reduce simulation duration and optimise controlling parameters of the screen. The SVM model was established to anticipate screen sieving efficiency with a cross-validation approach and to optimise parameters (Li, Z et al. 2015; Zhang, B et al. 2016). The predicted performance of machine learning model was better than the existing test/simulation results and the relative error was significant (Li, Z et al. 2019; Zhang, B et al. 2016). For roller mills, the effectiveness of several machine learning methods in predicting the particle size has been examined. The neural network method demonstrated highest accuracy while considering the experimental data, classifier data and clinker flow as input parameters (Pani & Mohanta 2015).

The shape of particles and contact mechanisms between them are important factors for process industries. The particle contact interaction, which is a crucial characteristic of granular matter, can become more complex when simulating differently shaped particles. Granular materials are naturally spherical, non-spherical and irregular in shape and size, which can influence the passing of particles, percolation and screen efficiency (Dong, K, Wang & Yu 2016; Guises et al. 2009; Lu, G, Third, JR & Müller, CR 2015; Zhou, Z-Y et al. 2011). While spherical particles pass with equal probability in any orientation, irregularly shaped near-mesh sized particles must orient themselves in a direction that permits them to pass. Another important consideration is contact force, which can be measured by the discrete element method (DEM) with the help of contact mechanics and overlap between particles of different shapes. Zhu et al. (Zhu, HP et al. 2007) described particle-to-particle and particle-to-fluid interaction forces (Figure 1-1). The calculation of different contact forces has been included in DEM simulations, which makes DEM more applicable to particulate research. For granular materials, ellipsoidal particles in DEM simulations are complex. The major challenge is the implementation of a stable contact detection algorithm with contact forces of elements and formation to DEM (Lin, X & Ng, TT 1995). The structural analysis of non-spherical particles and packings based on Voronoi cells was investigated by Dong et al. (Dong, K, Wang & Yu 2016). With a change in aspect ratio, ellipsoid and cylindrical particles exhibit distinct surface area data. A numerically stable contact detection algorithm based on the geometric potential concept was applied in DEM for ellipsoidal particles. The particle array with ellipsoids achieved lower porosity and a

larger coordination number under the same consolidation procedure (Lin & Ng 1997). A force model for spherical particles moving on a flat plane proposed the presence or absence of rolling friction in DEM. The difference between the two models was largely dependent on the sliding friction coefficient between spheres and the plane (Zhu & Yu 2006). Penetration depth, contact plane and contact point were taken into account in the qualitative comparison of contact force models for ellipsoidal particles. The differences between geometric potential and common normal method indicated that penetration depth and contact normal vectors changed identically with orientation angles while having differences for the contact point (Kildashti et al. 2018).

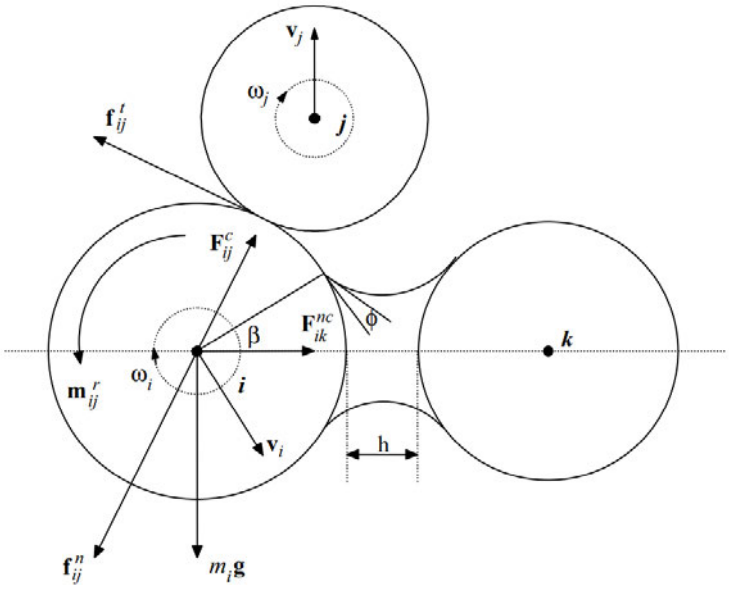

Figure 1-1 Schematic illustration of the forces acting on particle i from contacting particle j and non-contacting particle k (capillary force here) (Zhu, HP et al. 2007).

1.2 Research objectives

The main objective of the present research is to study the industrial screening process of granular materials and provide improved macroscopic models for industrial applications, which includes the following objectives:

a) To develop a DEM study and machine learning model for particle percolation under vibration.

b) To develop a process model of a vibrating screen based on DEM and physics-informed machine learning.
c) To develop a process model for an inclined double-layer vibrating screen based on DEM and machine learning.
d) To develop a logical model for choking judgement of an inclined vibrating screen based on DEM and machine learning.
e) To develop an explicit contact force model for superellipse particles by the Fourier transform and its application in superellipse packing.

The outcomes of this thesis include: (i) the percolation of particles under vibration and the machine learning modelling of percolation velocity to predict the size ratio threshold; (ii) a better understanding of screening process based on local passing of inclined and multi-deck screen and physics informed machine learning modelling to predict the particles passing; (iii) a logical model to predict the choking judgement of screen while combining the numerical results and machine learning and (iv) a novel contact force model for non-spherical particles by Fourier transformation and packing. Figure 1-2 shows the research roadmap of this thesis.

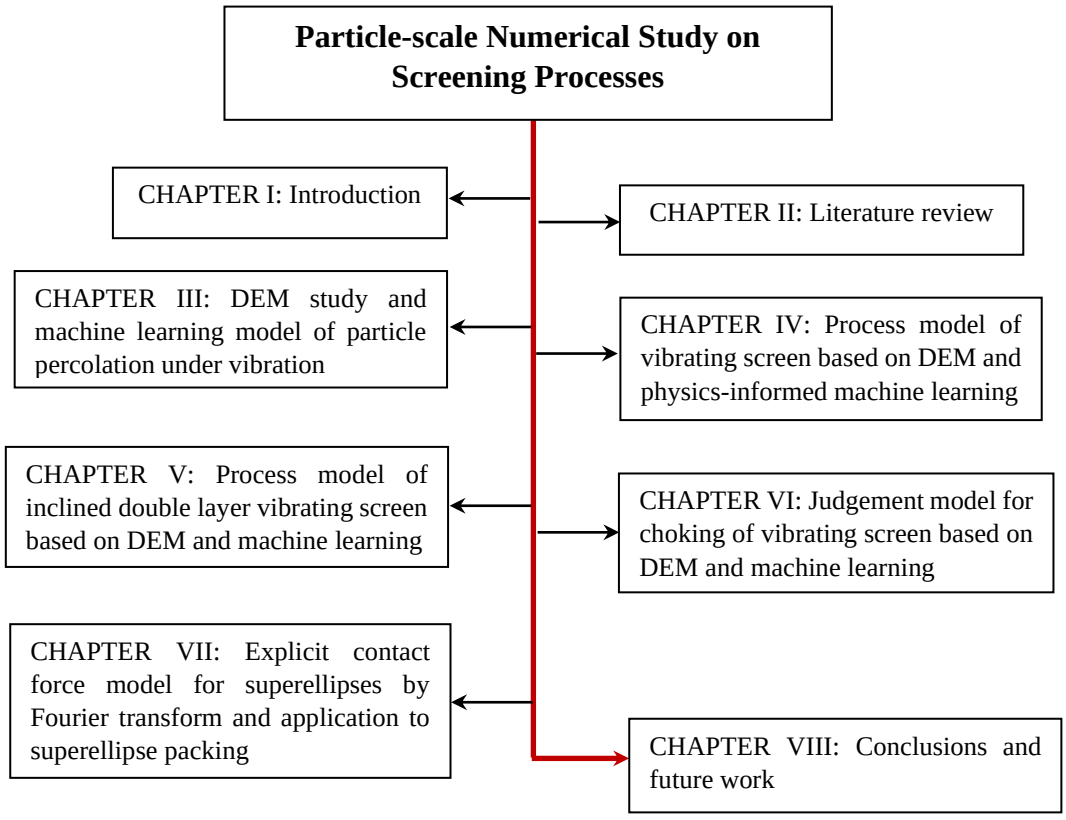

Figure 1-2 Research roadmap of thesis.

1.3 Significance of the research

Sieving and segregation of particles are one of the common and most crucial processes in modern granular industries. The industrial use of granular materials in mining engineering, agricultural materials processing, pharmaceutical industry has been increasing. Different types of industrial screens are also used in industries. The integration of experimental studies, theoretical development, numerical simulation and machine learning modelling could bring a better understanding and representation of cost management for the related industries.

One example can clear lack of the area; spontaneous percolation is well known in inter particles collision and flow investigation. But vibrational percolation is a not well understood process in granular inter particles percolation phenomena in the literature. This process was studied by the DEM model. Based on the simulation results, machine learning models were used to model percolation velocity as a function of vibration conditions and size ratio. Using the machine learning model, the percolation threshold size ratios under different vibration conditions were obtained. These results have demonstrated that spontaneous percolation theory could encompass vibrated beds. This includes the effects of vibration amplitude and frequency on percolation velocity under different size ratios as well as the relationship between percolation and radial dispersion of percolating particles in a vibrated bed. The obtained knowledge can be used in both fundamental research and industrial applications.

Different types of industrial screens (banana screen, horizontal screen, inclined vibrating screen, multi-deck screen) are used in mining and commercial industries for the segregation of materials/products. The screening processes are complicated and difficult to model due to numerous controlling variables in screen processes and screen geometries. To develop a process model for an inclined vibrating screen based on particle passing, the flow and passing of particles through local parts was numerically studied based on the DEM. The process model was proposed to predict the particle passing rate with the help of machine learning modelling. Furthermore, the machine learning model was linked to the DEM simulation results. To analyse screen performance, the machine learning model was then used to predict the passing of particles under different vibration conditions, feeding conditions and screen configurations.

The time-consuming simulation process can be minimised by using process models for industrial screens and other granular processing applications.

On the other hand, the multi-deck screening process is more crucial than a single-layer screen for screen geometry, feeding of different layer materials and controlling variables. To develop a process model for an inclined double-layer vibrating screen, computational and machine learning were studied together. In the proposed model, the flow and sieving could be assumed to be steady for a segment base double-layer screen. A process model was developed by considering the inlet, passing and overflow, local particle properties and operational conditions for a combination of DEM and machine learning. The developed model can be used to predict the sieving performance of double-layer screen without choking while being under different conditions. In particular, the model could be applied with various feed rates, double-layer inclined screen and different apertures under different vibration conditions.

None of the previous studies examined screen choking in detail including the threshold of the controlling variable and the feed rate. Therefore, it is necessary to develop a generalised model that can predict the choking of the screening process. Considering the gap, a decision-making choking logical model for the screening process was also investigated by combining DEM simulation and machine learning classification. To develop a decision-making choking logical model for the screening process, the particle inlet in a region of the screen and the flow controlling variables were considered as dependent variables. The choking logical model was established through machine learning (classification) of data generated by a series of controlled DEM simulations. The choking decision logical model was used to predict the choking condition and threshold of a screening case while considering the feed on the screen, vibration conditions and inclination angle.

The majority of simulation research is for spherical-shaped particles. Irregular or non-spherical-shaped theoretical developments are required. In the final component of this thesis, the contact detection algorithm of superellipse-shaped particles and packing analysis were introduced. With the help of DFT fitting and DEM analysis, the collision of irregularly shaped particles and theoretical concepts can be understood. The discrete solutions as a function of two angles were transformed into the frequency domain by using two-dimensional (2D) discrete Fourier transform (DFT). The transformed terms were sorted according to their magnitudes. Those below a certain value were filtered in the inverse discrete Fourier transform (IDFT). In addition, the packing of superellipses was simulated using the established explicit

force model. The study would help understand the screening process while considering non-spherical particles in future.

1.4 Thesis outline

A critical review of the screening process and related models, including segregation, packing, percolation, screening principles, complex industrial screens, factors affecting screening, theoretical and mathematical models, are presented in **Chapter 2**.

Chapter 3 presents the DEM study and machine learning model of particle percolation under vibration. Both spontaneous and vibrational percolation of particles were studied using DEM. Percolating particles with size ratios lower and higher than the spontaneous threshold were considered. The effects of vibration amplitude and frequency on the percolation velocity and radial dispersion coefficient were analysed. In addition, the correlations between the percolation velocity and the velocity amplitude of the vibration were investigated. Based on the simulation results, machine learning models were used to model percolation velocity as a function of vibration conditions and size ratio. Using the machine learning model, the percolation threshold size ratios under different vibration conditions were obtained.

Chapter 4 develops a process model for particles passing along an inclined vibrating screen using computational and machine learning modelling. The DEM was used to simulate the particle flow along the screen. The existing process models of such screens are normally empirical, which could not consider non-uniform distribution of particles along the whole screen. This study developed a process model for inclined vibrating screens by combining DEM simulation and machine learning. The flow and passage in different segments of the screen were analysed based on the particle-scale information obtained from the simulation and mass continuity. By applying machine learning to this information, a segment model was then developed to predict the passing rates of different-sized particles based on the local conditions. For the prediction of passing rate, a local passing function was formed according to vibration conditions, incline angle and number of particles on the screen deck. Machine learning models (e.g., linear, SVM, GPR) were used to predict the passing of particles while considering DEM findings. The GPR squared exponential model (i.e., machine learning) is best at predicting the results of particles passing through the screen. The process model was then applied to various screen scenarios such as under different feeding conditions, two-deck screens with different inclination angles and vibration conditions. The process model was able to predict both the

overall and local passing of the screen under different operational conditions, which provided not only the partition curve, cut size and probable error to evaluate the overall performance but also guidance for process design, control, minimising simulation time, process and optimisation.

Chapter 5 extends the process model to the inclined double-layer vibrating screen by combining DEM simulation and machine learning. The screening process along the whole screen under different operational conditions was simulated by the DEM. Particle flow and the passage of different layers and segments of the screen were analysed based on the particle-scale information obtained from the simulations. By applying machine learning to the simulated data, a segment model was then developed to predict the passing rates of different-sized particles based on the local conditions of both layers. Supervised machine learning models such as linear, support vector machine (SVM) and Gaussian process regressions (GPR) were used for training the database generated by the DEM. The GPR squared exponential model was found to be the best model. Finally, a process model for the whole screen was developed by linking the segment models. During the development of the segment model, the local flow conditions of different parts of the screen were considered and different operational conditions were applied to different parts of the screen. The process model was then applied to various vibration conditions on both layers and different feeding scenarios. The performance of the screen was analysed in terms of cut size and probable error, which provided guidance for process design, control and optimisation. The process model opens the door for the smart operation of industrial multi-layer screens.

Chapter 6 presents a decision-making logical model of screening for the judgement of screen choking, which is also based on the combination of DEM and machine learning. To build the data model, the particle inlet in a particular area of the screen and the flow-controlling variables were considered as input variables. The logical choking model was established through machine learning of data generated by a series of controlled DEM simulations. The model can predict the threshold of controlling variables and feed of different-sized particles for screen choking or non-choking. The logical model will help to minimise the computational duration and cost of the screening process by predicting the judgement before any screening case. The logical model could also be applied to predict the judgement of choking with the change of vibration condition, feed rate and inclination angle.

Chapter 7 presents an explicit contact force model for superellipses by Fourier transform and application to superellipse packing with the DEM approach. DEM uses first principles to model the motion of each particle. Therefore, if the interactions between particles can be accurately modelled, the simulated results could be reliable. The most general interaction between particles is contact force. However, the method for calculating contact force for non-spherical particles has not been established yet (Lu, Third & Muller 2015; Zhong et al. 2016). The overlap and contact force between non-spherical particles with respect to orientation angles resemble intersecting waves. Therefore, the Fourier series was proposed to establish explicit force models by fitting them to a comprehensive force database. This idea was implemented to elliptical particles and its applicability was determined. The Fourier transform has been used to characterise complex shapes (Shen, Farid & McPeek 2009), despite being used to model the interaction between non-spherical particles. However, it might be challenging to fit a Fourier series with many terms. Conversely, the Fourier transform can be a more general technique to establish Fourier series and the packing of superellipses. The application of such methodology was presented to establish an explicit force model of superellipses and simulation of the particle packing as the first test and is expected to be extended to screening simulation in the future.

Chapter 8 concludes this thesis. Potential future research suggestions are also included.

It should be noted that a description of the DEM model is provided in each chapter. The governing equations are repeated, but the simulation circumstances are unique to each chapter. Chapters are in the form of publication or as preparation for submission.

CHAPTER II: Literature review

2.1 Introduction

Mixing and separation of granular materials according to their size using screens is a crucial process for industries such as mining, agriculture and pharmaceuticals (Cleary, PW 2009; Cleary, Paul W, Sinnott, Matthew D & Morrison, Rob D 2009; Djoković et al. 2017; Dong, K, Wang & Yu 2013; Jansen & Glastonbury 1968; Standish, Bharadwaj & Hariri-Akbari 1986; Wills & Finch 2016). The particles are sieved across a moving mesh surface, where the screen consists of a number of apertures. The particles must be able to arrange themselves above an opening as they pass across the screen. Furthermore, the particle's force must be strong enough to convey it through the opening. Because of the enormous number of variables relating to screen geometries, operational circumstances and particle characteristics, feeding and passing, understanding of this process is currently limited. The performance of process industries might improve as a result of theoretical and experimental understanding of the process, which might also have a significant influence on financial implications (Asmar et al. 2002; Cleary, P et al. 2010; Cleary, Paul W., Sinnott, Matthew D. & Morrison, Rob D. 2009; Djoković et al. 2017; Dong, K, Esfandiary & Yu 2017; Taggart 1945; Wills & Finch 2016; Wolff 1954).

Different industrial screens are used worldwide for different purposes and features of materials. Although efficiency decreases rapidly with fineness, industrial screening is extensively used for separation of particles between 300 mm and 40 μm (Wills & Finch 2016). Banana screens are commonly used in high-tonnage material separation, where capacity and efficiency are critical for granular material segregation (Cleary, P et al. 2010; Cleary, PW 2009; Dong, K, Yu & Brake 2009; Wills & Finch 2016). As one of the most effective methods of material classification, trommel screens are widely used in mining, metallurgy, chemical, construction, environmental protection and other industries (Sinnott, Cleary & Morrison 2017; Stesscl & Cole 1996). Gyratory, grizzly, and horizontal vibrating screens are commonly used for separating fine dry and wet materials during screening (Ardi et al. 2017; Dong, K & Yu 2012; Iwashita & Oda 1998; Li, J et al. 2003; Wolff 1954).

The processing of particles in different industries could be improved through research into the passage and mixing of materials, material properties and contact mechanisms. Theoretical and empirical investigation could improve screen configuration and understanding of sieving (Cleary, PW 2009; Dong, K, Esfandiary & Yu 2017; Dong, K, Yu & Brake 2009). Optimisation and prediction analysis could reduce experimental cost and time requirements (Barrasso, Tamrakar & Ramachandran 2014; Li, Z et al. 2019; Mahdi & Holdich 2017; Zhang, B et al.

2016). Particle screening and innovation in granular material separation could also contribute to cost minimisation, value-addition opportunities, and integrated approaches for industrial applications. Mathematical knowledge of the sieving process, i.e., the probability of particles passing through screens, is crucial to the understanding of the performance of the screen (Standish 1985). The random path model of screens involves the probability of particles passing through the apertures of flat, rotating and dynamic casting screens (Jansen & Glastonbury 1968). Subasinghe et al. (Subasinghe, Schaap, W & Kelly, EG 1989) used a probabilistic method (Weibull distribution) to predict screening results.

A comprehensive literature review is presented while considering different industrial screens, their geometrical comparison, operational conditions, and applications. The performance of screens was found to be not only dependent on the screens but also on the properties of particles they handled. These properties included particle shape, particle size distribution, vibration conditions, mechanics and surface properties. Therefore, the most used macroscopic models cannot be used with different types of particles in industrial screening. The characteristics of granular particles are dynamic owing to the complex interactions between individual particles as well as between particles and screens. Furthermore, machine learning is considered for particulate modelling, optimisation and linking particle-scale analyses with macroscopic screening theories.

2.1.1 General screening processes

A general screening process is show in Figure 2-1. the underflow of particles from the screen is facilitated by the segregation and stratification phenomena and the remaining particles move to the end of the screen (Figure 2-1). The particle mixture initially appears at the top of the screen. The materials or ‘feeds’ are passed through the screen. Some particles segregate through the apertures of the screen and the remaining particles move forward on the screen. After reaching the end of the screen, the materials are collected including the remaining materials from the previous deck of the screen (Asbjörnsson et al. 2016; Cleary, PW 2009; Cleary, Paul W, Sinnott, Matthew D & Morrison, Rob D 2009; Wolff 1954; Zhang, B et al. 2016) (Delaney, Gary W. et al. 2012). If the particle size is small compared to the apertures, there is a good probability they will pass through the screen before being discharged at the end. When the particle size is relatively large, or similar to the apertures, there is a high probability that they will be rejected as overflow. Furthermore, if the particles move quickly, they may bounce from wire to wire and never pass through the apertures (Taggart 1945).

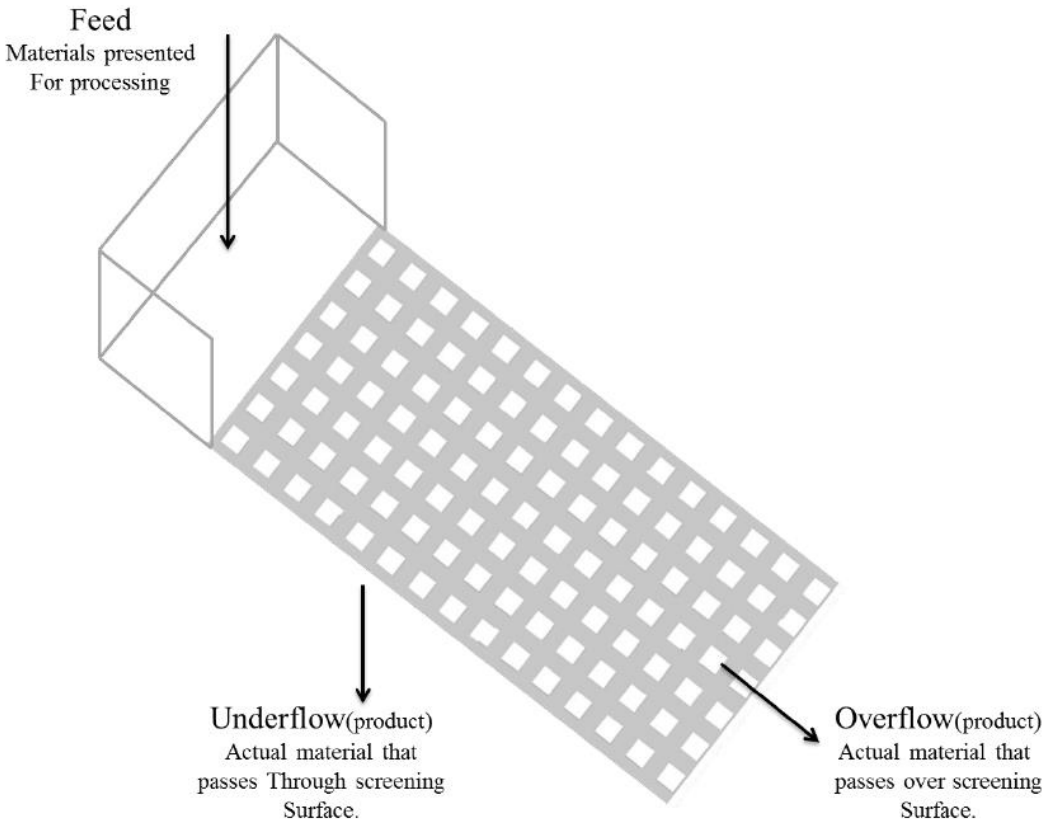

Figure 2-1 Simplified screen (Esfandiary 2014).

During over-feeding, particles tend to spread around the feed box floor and fall onto the screen. The stratification process occurs when the screening surface vibrates, resulting in the material bed developing fluid-like properties. The larger particles rise to the top while the smaller particles pass through the gaps and make their way to the bottom of the bed. The separating process can be performed without stratification. However, there is an ideal bed height for stratification. A thin bed can reduce the effectiveness of screening, whereas a thick bed slows stratification, dampens bed movement, and diminishes separation accuracy.

2.2 Industrial screen and application

Mining industries, pharmaceuticals industries, food, plastics, recycling, and agricultural industries use screening processes for sizing separation (Cleary, PW 2009; Dong, K, Yu & Brake 2009; Jansen & Glastonbury 1968). The screen is usually a surface consisting of several decks and many different size apertures having uniform dimensional shapes. The main goal of the screening process optimisation is for reducing production costs and improving sieving rate.

Screening is also used for grading products, washing, dewatering, segregating, and mixing several materials within defined material size ranges. Various types of industrial screens are available for processing materials. In the agriculture sector, systematic sizing is important for food industries, especially for those that would be heated or cooled, as large differences in sizing may lead to over- or under-processing of the product.

Table 2-1 Industrial screens and configuration (Wills & Finch 2016).

Screen type	Industry application	Size
Banana	Mineral process, sizing, separation, stockpile sizing, mill discharge and manufacturing	2.1 × 5.8 m up to 4.3 × 9.7 m
Horizontal	Trash removal, sizing, stockpile sizing, mill discharge sizing, desliming, drain and rinse	1.2 × 4.8 m up to 4.3 × 9.7 m
Gyratory	Fine particle screening such as dewatering of carbon in gold plants	The nest of sieves up to approx. 2.7 m
Roller	Classifying coarse, moist, sticky or clayey raw materials	1.1 × 2.0 m (approx.)
Trommel	Mineral processing, municipal and industrial waste	7.3 × 16.6 m (approx.)
Grizzly	Minerals, ore, blasted or ripped rock, gypsum, foundry materials and large stone process	

The banana screen (Figure 2-2a) is now widely used in the separation of high-tonnage materials where both capacity and efficiency are important. Banana screens have excellent segregation capacity that is up to three or four times that of regular vibrating screens. The steep configuration of sections allows the feed material to flow rapidly to the end of the screen. Furthermore, compared to a thick slow-moving bed, fine particles screen out more rapidly. A banana screen's slope gets reduced at the discharge end to slow down the existing material and enable more efficient screening of close-range particles.

A gyratory screen (Figure 2-2b) is a machine with vertical and gyratory motion. Gyratory screens are generally used for the separation of fine dry and wet materials. Roller-type screens (Figure 2-2c) are generally used for screening very sticky materials with 3–300 mm particles. Roller screens use a sequence or series of parallel-driven rolls (i.e., circular, elliptical, profiled) and discs to transport oversized particles across the series while the fine materials fall through the gaps between discs/rollers.

Trommel screening is one of the oldest screening methods. Trommel screens (Figure 2-2g) consist of a circular screen that rotates between 35% and 45% of the critical speed. The trommel contains a series of internal baffles and is positioned with a small inclination from horizontal to transfer material to the cylinder. Trommels can be configured to deliver a variety of product sizes by rotating trommel screens from finest to coarsest. Trommels are less expensive, vibration-free and more physically robust than vibrating screens, but typically have lower capacity since only a portion of the screen surface is in use at any given time. Grizzly screens are used to screen very rough materials on an inclined screen. The screens are made from parallel steel bars or rails that are spaced apart and aligned with the flow of materials (e.g., ore). Vibrating grizzly screens (Figure 2-2d) have a circular throw mechanism and are commonly inclined at an angle of 20 degrees. Grizzlies are most used in mineral processing to size the feed for primary and secondary crushers.

Modular screens (Figure 2-2e) are made up of two or more separate screen modules connected in a series to create a larger screen from a collection of smaller pieces. This configuration has the advantage of allowing each screen module to be customised with its screen slope, screen surface type, vibration stroke and frequency. This enables the performance of different portions of the screen to be tuned separately. Horizontal vibrating screens have a horizontal or almost horizontal screening surface and hence require less headroom than inclined screens. Horizontal screens must be vibrated with a double- or triple-shaft vibrator that produces a linear or elliptical vibration. Horizontal screens (Figure 2-2f) are utilised in heavy medium circuits for sizing applications when screening efficiency is crucial. Resonance screens are a form of horizontal screen that consists of a screen frame coupled to a dynamically balanced frame with the same natural resonance frequency as the vibrating screen body via rubber buffers. Resonance screens minimise energy losses, and the quick return motion created by the resonant action gives the deck a lively action that encourages effective screening.

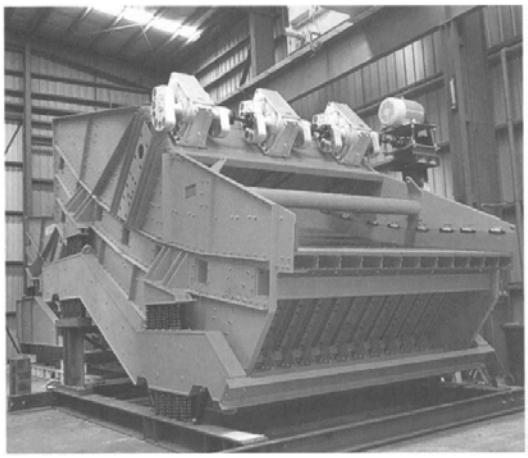

(a) Banana screen

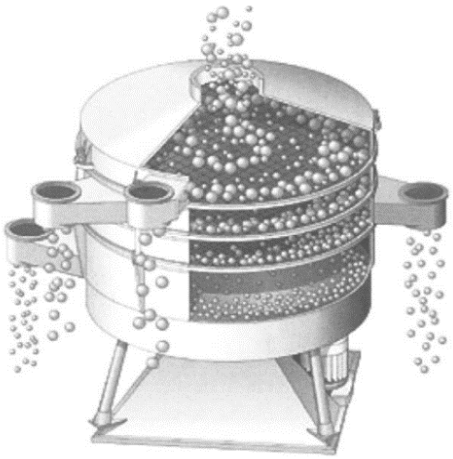

(b) Gyratory screen

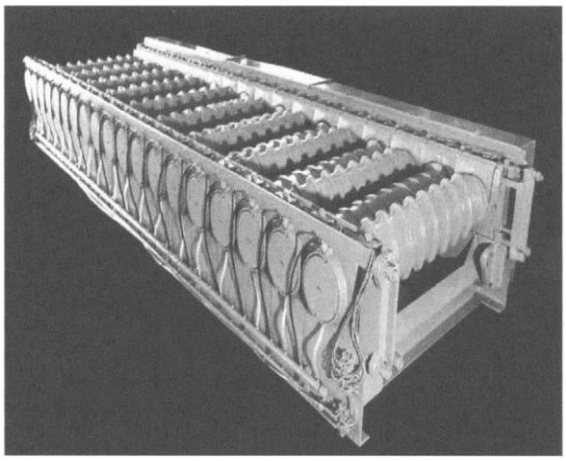

(c) Roller screen

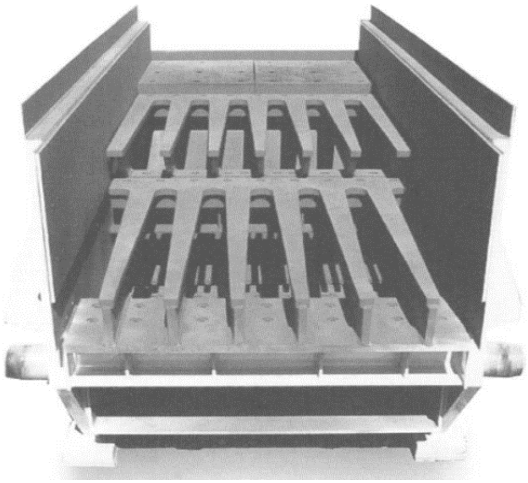

(d) Vibrating grizzly screen

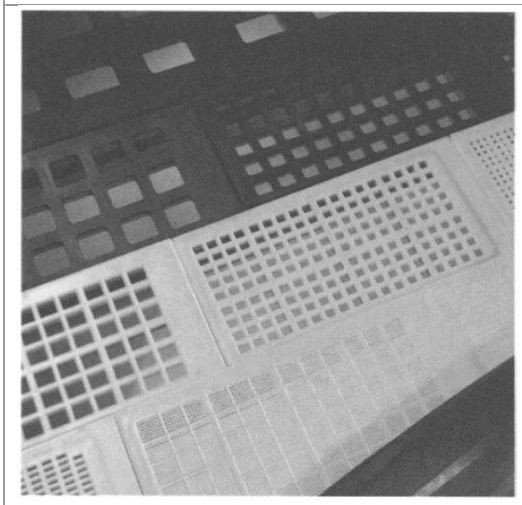

(e) Modular screen

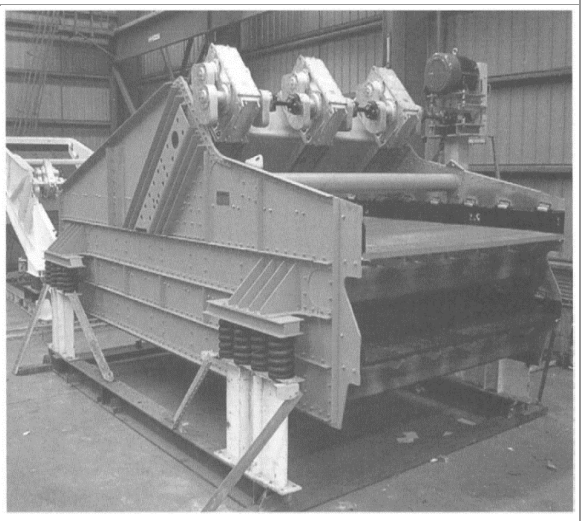

(f) Horizontal screen

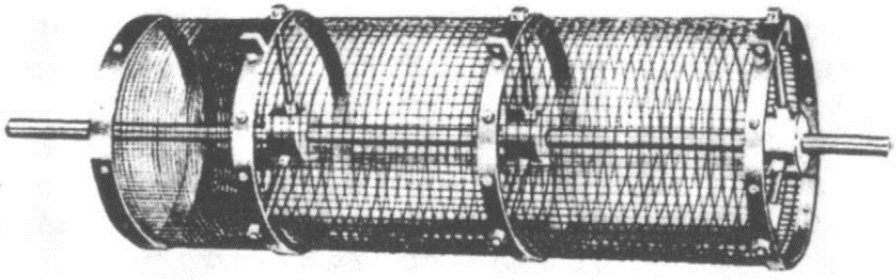

(g) Trommel screen

Figure 2-2 Different types of industrial screens (Wills & Finch 2016).

2.3 Controlling variables of the screening process

The degree of accuracy with which the material is separated into size fractions above or below the aperture size is known as screening efficiency. There are a number of factors that could influence the performance and efficiency of the screen. Figure 2-3 displays some of the variable factors of the screening process.

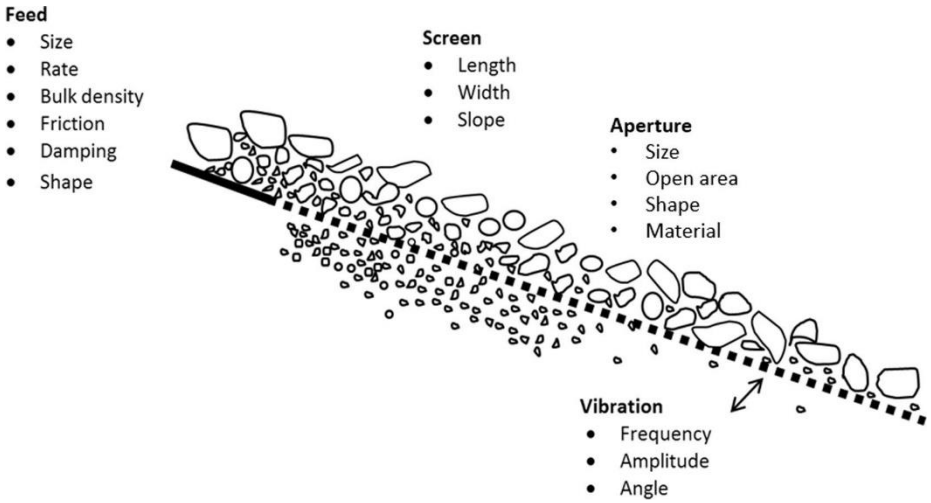

Figure 2-3 Screening process and variables (Ogunmodimu et al. 2021).

2.3.1 Feed rate

One of the major factors in screening is feed rate. The feed rate can change the output in an almost absolute separation. Screening in industry has greater demand for high feed rates for material processing. Therefore, the duration of particles on the screen is short and fine materials may not have sufficient time to reach the screen surface before the scope passes to discharge. Depth of bed is one of the defining factors of sieving performance. For lower feed rates and larger size materials, the flow of materials will be low because the particles tend to have unrestrained motion and the whole screen surface is not being used. For higher flow rates, closeness of the particles tends to restrain bouncing (as in Figure 2-4) and maximise exposure of passing materials to the screen apertures. With segregation or stratification for vibration, small particles pass to the bottom of the bed while large particles rise to the top. When calculating bed depth along the screen, bed depth will be proportional to the feed rate.

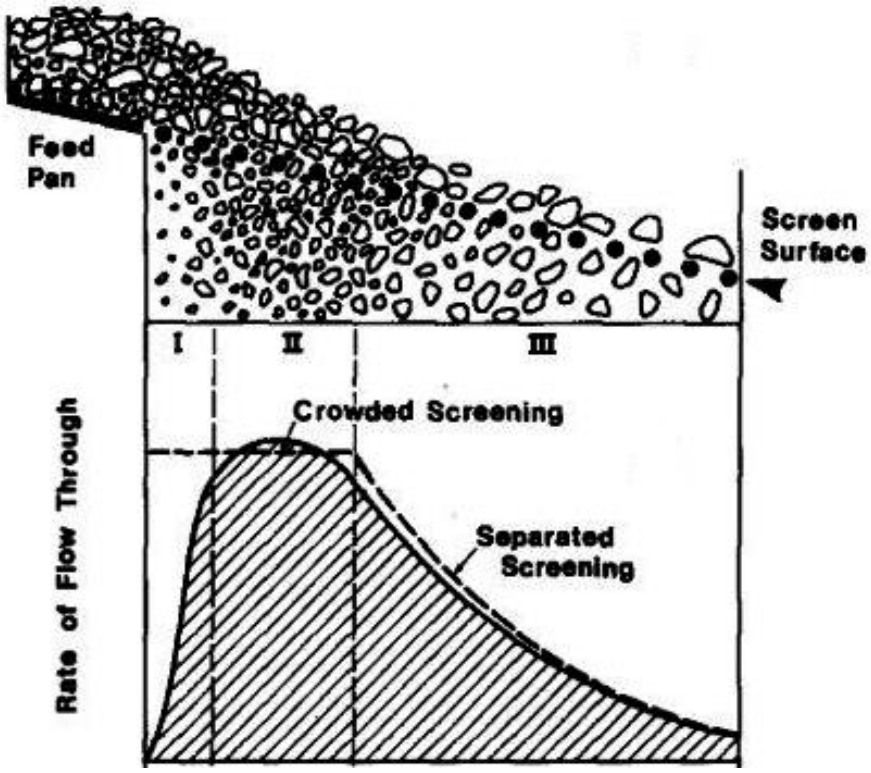

Figure 2-4 Particles feeding along a screening surface (Subasinghe, G, Schaap, W & Kelly, E 1989).

2.3.2 Screen angle

Screening efficiency depends on the passing of particles. The likelihood of materials passing the screen is high when the material reaches the aperture perpendicularly. When a particle approaches with a shallow angle to the aperture, it will face a small effect on the aperture dimension. Near-mesh size particles have less chance to pass through the aperture. The angle of the screen also influences the velocity/speed of particles and duration on the screen. Therefore, the number of particles passing through the screen surface also changes.

Table 2-2 The critical contact angle of a particle passing through the aperture in a single contact (Jansen & Glastonbury 1968).

Aperture shape	Angle of media	Critical contact angle
Square	$<90^0$	$\cos\alpha_\theta = \frac{1+\sqrt{1+8m^2}}{4m}$, α_1 and α_2 are positive roots of: $4m^2(k^2+1)\cos\alpha - 4mk\sqrt{1+k^2}\cos\alpha - (4m^2-1)(k^2-1)\cos^2\alpha + 2mk\sqrt{k-1}\cos\alpha + m^2k^2 = 0$ where $k = \tan\gamma$
Square	90^0	$\alpha = 0^0$
Square	90^0	$\cos\alpha = \frac{1+\sqrt{1+8m^2}}{4m}$
Square	$<90^0$	$k = \cos\gamma$, α_1 and α_2 are positive roots of: $4m^2(k^2+1)\cos\alpha - 4m(k^2-1)\cos^2\alpha - (4m^2-1)(k^2+1)\cos^2\alpha + 2m(k^2+2)\cos\alpha + (m^2k^2-1) = 0$
Square	$<90^0$	ψ is a complex function that decreases with the increase of $\frac{d_p}{D_w}$
Rectangular	90^0	$\cos\alpha = \frac{1+\sqrt{1+8m^2}}{4m}$, $\cos\alpha' = \frac{1+\sqrt{1+8M^2}}{4M}$, $m = \frac{2D_a+D_w-d_p}{D_w+d_p}$, $M = \frac{2D_{ah}+D_w-d_p}{D_w+d_p}$
Rectangular	90^0	$\alpha = 0^0$

Note. k = constant, m = constant, x = weight fraction of material remaining on the screen, W = weight of particles on the screen, $\alpha, \alpha_1, \alpha_2$ = critical contact angle of a particle with a screen wire, θ = critical angle for circular vibration of a screen, γ = angle of incidence of particle path to the screen plane, μ = coefficient of static friction, μ' = coefficient of sliding friction and ω = angular velocity of rotation or vibration coefficient.

2.3.3 Open area

The likelihood of materials passing through a screen depends critically on its open area. The probability of particles passing through the screen aperture is proportional to the percentage of open area, which can be defined as the ratio of the net area of the apertures to the total area of the screening surface. When the open area of the screen deck is covered by the material, the maximum probability of a particle reaching an aperture could be achieved. In general, the open area decreases with the fineness of particles. Very thin and fragile wires or deck construction is needed to increase the open area of a fine screen. The classifiers replace screens for fine aperture sizes due to fragility and low throughput capacity.

Table 2-3 Effect of parameters on the theoretical probability of particle passage through a screen aperture (Jansen & Glastonbury 1968).

Aperture shape	Angle of median	Reflection	Probability of passage in a single contact
Square	$<90^0$	Yes	$\left(\frac{D_a + D_w - (D_w + D_p)\cos\alpha_\theta}{D_a + D_w}\right) \times \left(\frac{D_a + D_w - \left(\frac{D_w + D_p}{2}\right)(\sin(\gamma - \alpha_2) + \sin(\gamma + \alpha_1))}{D_a + D_w}\right)$
Square	90^0	No	$\frac{(D_a - D_p)^2}{(D_a + D_w)^2}$
Square	90^0	Yes	$\frac{D_a + D_w - (D_w + D_p)\cos\alpha_\theta}{D_a + D_w}$
Square	$<90^0$	Yes	$\left(\frac{D_a + D_w - (D_w + D_p)\cos\alpha_\theta}{D_a - D_w}\right) \times \left(\frac{D_a + D_w - \left(\frac{D_w + D_p}{2}\right)\left\{\frac{\sin(\gamma - \alpha_2) + \sin(\gamma + \alpha_1)}{\sin\gamma}\right\}}{D_a + D_w}\right)$
Square	$<90^0$	Yes	$\frac{(D_a + \psi D_w - D_p)[(D_a + D_w)\sin\gamma - \{1 - \psi\}cD_w - D_p]}{\{D_a + D_w\}\{(D_a + D_w)\sin\gamma\}}$
Rectangular	90^0	Yes	$\left(\frac{D_a + D_w - (D_w + d_p)\cos\alpha}{D_a + D_w}\right)\left(\frac{D_a + D_w - (D_w + d_p)\cos\alpha'}{D_{ah} + D_w}\right.$
Rectangular	90^0	No	$\frac{(D_\mu - d_\mu)(D_{\mu'} - d_p)}{(D_a + D_w)(D_{ah} + D_w)}$

Note. D_a = length of the side of a square screen aperture, D_c = diameter of a circular aperture, D_w = diameter of screen wire, d_p = particle diameter, g = gravitational acceleration, h = ratio of shorter side to longer side for a rectangular particle.

2.3.4 Vibration

Vibration modes used on screens include linear, horizontal, elliptical, and circular. The use of an accurate vibration mode assists stratification of feed materials while allowing fines and small particles to pass through the screen layer to the screen surface and larger particles to rise to the top. Excessive vibration intensity causes the particles to bounce, resulting in fewer effective presentations to the screen surface. Higher vibration can be applied to 'cushion' certain materials, which prevents particle bouncing at a high rate of feed.

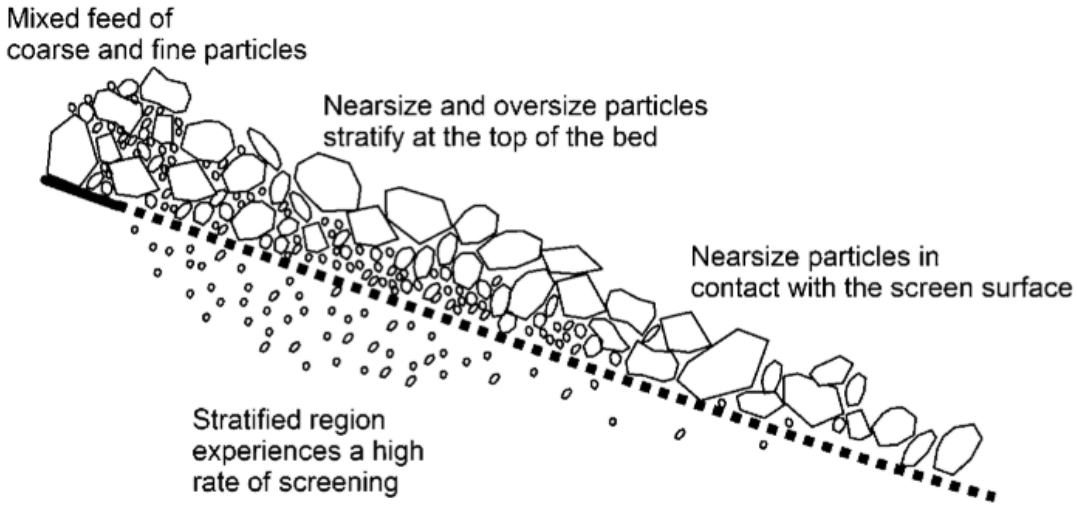

Figure 2-5 Stratification of particles on a screen (Wills & Finch 2016).

2.3.5 Moisture

The quantity of surface moisture in the feed and clay content has a significant impact on screening efficiency. Damp feeds screen poorly because they tend to clump together and 'blind' the apertures. Without taking extra precautions to avoid blinding, screening with aperture sizes less than 5 mm require completely dry material for improved output. Heated decks can be used to break the surface tension of water between the screen wire and the particles.

2.4 General characterization of particles properties

Particulate materials are ubiquitous in many industrial applications such as mining, agriculture, and pharmaceuticals. In many industrial processes, raw materials are handled in granular format to separate materials of different sizes. Screening, also known as sieving, is an operation that utilises mechanisms such as particle-to-particle collision and particle-to-system collision to separate particles according to their sizes (Lin, X & Ng, TT 1995) while achieving mixing (Bridgwater, J. , Sharpe & Stocker 1969), sieving (Dong, K, Yu & Brake 2009) and stratification (Bridgwater, J & Ingram 1971; Rahman et al. 2008) via the passage of free particles through screen apertures (Bridgwater, J. , Sharpe & Stocker 1969; Dong, K, Wang & Yu 2013; Dong, K & Yu 2012; Dong, K, Yu & Brake 2009). Many factors including characteristics of the particles and the environment can affect the structure and dynamics of granular materials. A greater fundamental understanding of these processes through particle-scale studies is required.

2.4.1 Characteristic of particles

Sieving is widely used for powder and granular particle classification. The method utilised is usually based on the size of the materials/particles and independent of other particle properties such as density, moisture, optical properties, arrangement of particles and surface roughness. A collection of macroscopic particles and discrete solids is referred to as granular material and is distinguished by energy loss at the points where the particles interact. The lower size limit for granular particles is 1 μm. Examples of granular materials are coal, nuts, sand, rice, cornflakes, snow, coffee powder, fertiliser, and ball bearings. The properties of powder differ from granular particles according to their size properties. As a result, the powder is more cohesive.

Figure 2-6 Examples of granular materials (Wikipedia).

Granular material is commonly used in the commercial minerals industry, pharmaceutical industry, energy production and agriculture. Different properties of particles such as shape (e.g., sphere, non-sphere, polygonal, hexagonal) and condition (e.g., wet or dry) could influence the screening process. Fernandez studied the particle hydrodynamics (Fernandez et al. 2011) in screening. Other complicated particles were also studied, including the cohesive non-spherical particles (Cleary, PW, Wilson & Sinnott 2018) and rock particles (Cleary, Paul W, Sinnott, Matthew D & Morrison, Rob D 2009; Cleary, Paul W., Sinnott, Matthew D. & Morrison, Rob D. 2009; Zhao, L et al. 2017). Zhao et al. (Zhao, L et al. 2016) analysed the screening of spherical and non-spherical particles and observed the effects of particle shape on the screening process.

2.4.2 Particle size effect on screening process

The difference in the size of the particles could change screening efficiency (Lu, G, Third, JR & Müller, CR 2015; Wang, X et al. 2018). Spherical particles pass with the same probability in any orientation. Near-mesh size particles with irregular shapes arrange themselves in a way that allows them to pass. In some orientations, elongated and slab-like particles might have a limited cross-section for passage and a large cross-section in other orientations. The rate of particle passage varies with the ratio of fine particles and the size. Furthermore, the rate of particle passage depends on the probability of passing through the screen aperture and the amount of free material on the screen surface (Soldinger 1999). The concept of particle size

applies to particles in ecology, colloidal particles, particles related to granular material and particles that form a granular material. Understanding particle size is particularly important in sieving when the particle size is similar to the aperture size and/or the likelihood of passage is low. If apertures are passed or plugged with mesh-sized particles, screening efficiency reduces. Different screens accept different size configurations of materials (Figure 2-7).

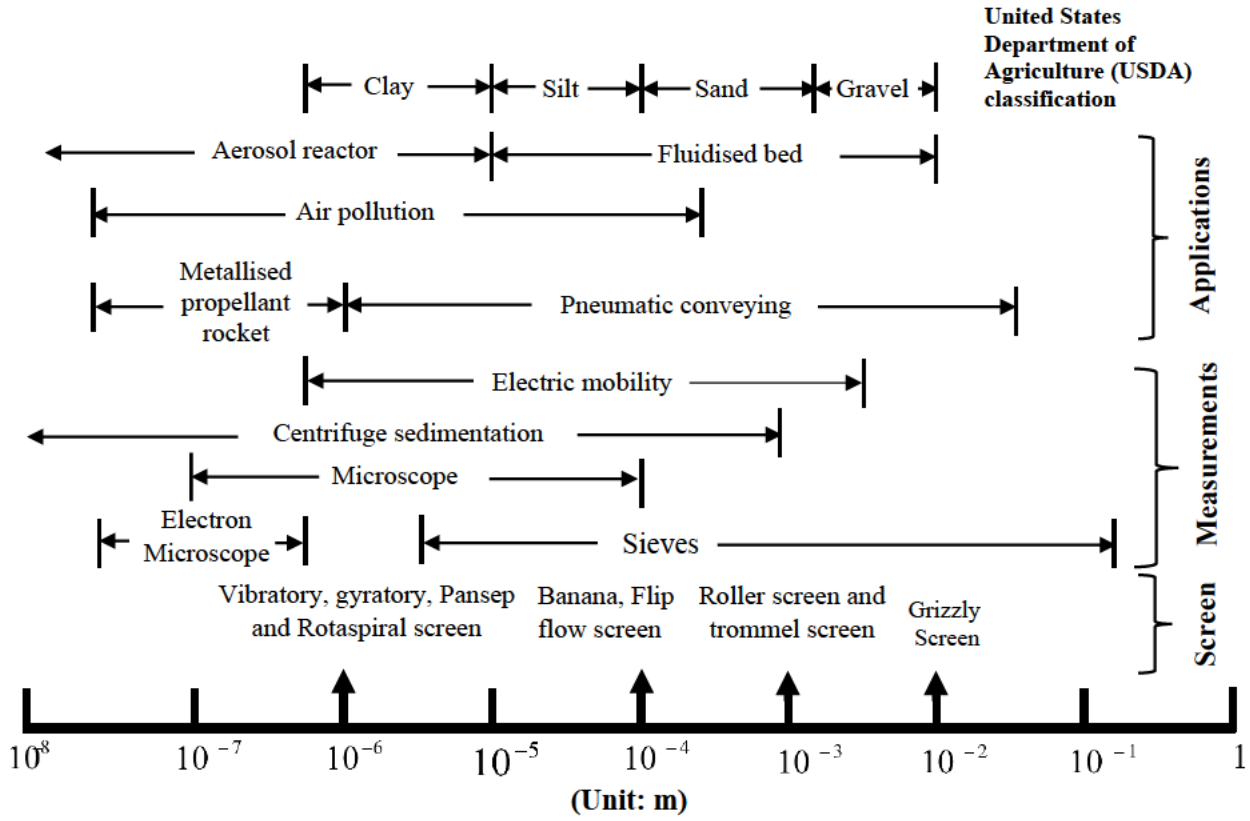

Figure 2-7 Magnitudes of particle sizes in gas-solid systems and minimum size distribution of fine materials with different screen capacity (Fan L. and Zhu 1998; Wills & Finch 2016).

2.4.3 Sieving error

Sieve apertures may be considered as a set of holes that reject or pass particles. The probability of a particle passing through an aperture is determined by the following factors (Dong, K, Esfandiary & Yu 2017; Dong, K, Wang & Yu 2013; Soldinger 1999, 2000) (Davoodi, Ali et al. 2019; Delaney, Gary W. et al. 2012; Standish 1985; Standish & Meta 1985):

- The particle size distribution of the feed: sieving performance could be reduced by a large fraction of near-mesh sized particles. Sieving efficiency could also reduce when there are many fine particles. Before sieve analysis, it is advised to remove fine

particles. The fine particles must travel through the entire nest of the sieve and delay the screening process. Wet sieving may be required as tiny particles tend to stick to larger ones.

- The number of particles on the sieve—The smaller the load or feed, the faster the analysis for the sieve. Feed that is too low leads to errors in weighing and unacceptable percentage losses.
- The physical properties of the particles—Adhesion (i.e., stickiness caused by water) such as from excessive humidity, cohesion (i.e., tendency of particles to stick together and become granular) and other surface phenomena. Coating with powder can diminish cohesivity, which could reduce granule formation.
- The method of shaking the sieve—Optimal sieve motion minimises the risk of aperture blockage and the probability of removing particles.
- Particle size—Large particle sieving is slower than compact particles.
- The geometry of the sieving surface: Fractional open area.

2.5 Evaluation of screening performance

2.5.1 Screening efficiency

Screening efficiency is defined as the ratio of the amount of material that passes through the aperture and discharges with the oversize product to the amount of undersized product fed into the screen initially. The effectiveness of the screen decreases if a higher number of undersized materials are discarded. To improve screening efficiency, the amount of thrown-away undersized material with the large material must be reduced. Various formulae are used to calculate screen efficiency depending on whether the oversize or undersized material fraction from the screen is used. The following information is required to calculate undersized or oversize screen efficiency.

Screen efficiency based on oversized (η_o) material is calculated by:

$$\eta_o = \frac{\mathrm{o}\,[1\ -\ \mathrm{Mo}]}{\mathrm{f}\,[1\ -\ \mathrm{Mf}]} \qquad \text{(Eq. 2.1)}$$

Screen efficiency based on undersized (η_u) material is calculated by:

$$\eta_u = \frac{\mathrm{u}\ \times \mathrm{Mu}}{\mathrm{f}\ \times\ \mathrm{Mf}} \qquad \text{(Eq. 2.2)}$$

where o = mass flow rate of solid in the screen overflow, Mu = mass fraction of undersize in the underflow, f = mass flow rate of solid feed, u = mass flow rate of solid in the screen underflow, Mf = mass fraction of undersize in the feed, Mo = mass fraction of undersize in the overflow.

Overall screen efficiency is calculated by multiplying these two efficiencies together:

$$E = Eo \times Eu \quad \text{(Eq. 2.3)}$$

Efficiency is the ratio of the amount of undersized material obtained by screening to the amount of undersized material available in the feed. It is calculated by the formula:

$$E(\%) = \frac{100(e - v)}{e(100 - v)} \times 100 \quad \text{(Eq. 2.4)}$$

where e = percentage undersize in feed and v = percentage undersize in over product.

The overall efficiency of the screening process can be calculated using (Harzanagh, Orhan & Ergun 2018):

$$E = \frac{c - f}{c(1 - f)} \quad \text{(Eq. 2.5)}$$

where *f* is the fraction of material above the cut size in the feed and *c* is the fraction of material above the cut size in the oversize stream.

2.5.2 Cut point

Figure 2-8 shows the partition curve of oversize materials. The partition curve for an ideal separation is vertical, as in curve 'a', but the partition curve for a real separation of material process is represented in curve 'b' (Figure 2-8). The cut sizes (d_{25}, d_{50} and d_{75}) are also calculated based on the curve analysis. Various parameters can be used to identify deviation from the ideal screening curve. The cut size is always smaller than the apertures with the highest openings. The cut size is normally referred to as d_{50}, i.e. the point on the partition curve at which 50% of particles have a possibility of reporting to the overflow. In an ideal classifier, particles that are larger than the d_{50} cut size will report to the coarse stream and smaller report

to the fine stream. This cannot be achieved in real classifiers. The closer the real partition curve to ideal, the better its classification efficiency.

2.5.3 Ep or probable error

The performance curve is an appropriate way to show the separation sharpness. The numerical figures (i.e., partition curves) are based on the error between the actual curve and the line of perfect separation, which is termed the probable error. Probable error (E_p) is defined as half of the difference between the sizes at which 75% and 25% recovery are observed (Sanders 1978).

$$E_p = 0.5(d_{75} - d_{25}) \qquad \text{(Eq. 2.6)}$$

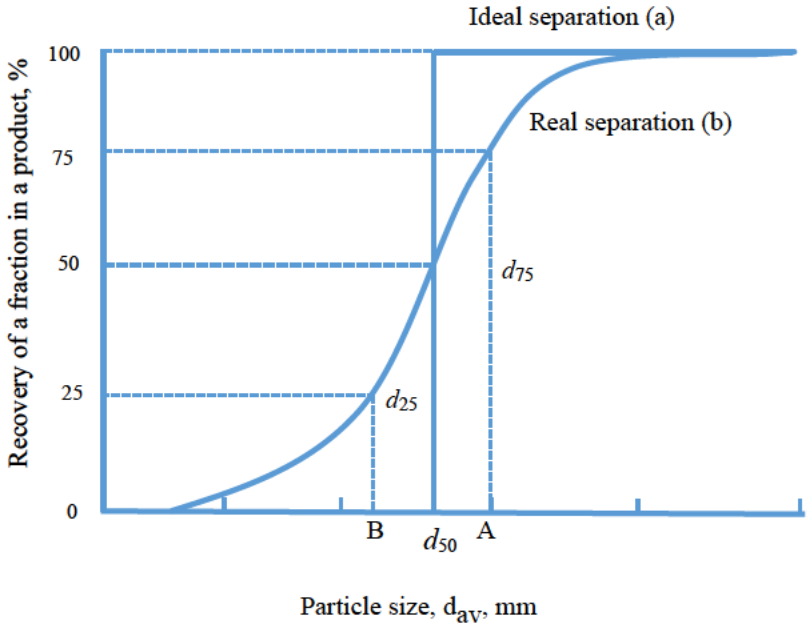

Figure 2-8 Ideal and real partition curves of oversize and undersize particles for the separation process.

2.6 Characterization of the particulate system dynamics

To simulate a particular system of particles, it is crucial to consider particle interaction, force and potential energy distribution that determine dynamics.

2.6.1 Velocity

Velocity is the most common parameter that specifies the dynamics of a particular system of particles. Particulate systems can be defined by the temperature of granules equal to the root

mean square of particle velocity fluctuations, which is similar to thermodynamic temperature. By definition, granular material contains macroscopic granular particles (i.e., limit: 1 μm) that are too large to display any significant thermal motion. The dominant velocity characteristics impose granular particle or material flow, particle motions and collisions between particles. Particle motion is quantified by the temperature and kinetic energy variation of particles. Temperature is the main factor that determines the flow of granular particles, which follows the same formula as the thermodynamic temperature of gas. Continuous input of external energy is required to maintain granular temperature. The amount of granular temperature depends on net energy, which is determined by the generation of energy by external vibration and the dissipation of energy by inelastic collisions. For the random motion of particles, granular temperature specifies the energy per unit mass of materials (Baldassarri et al. 2005).

2.6.2 Forces

For particulate system simulation, the relevant forces can be divided into three general categories: interaction forces, environmental forces and boundary forces. There are two categories of interaction forces that act on interacting particles: contact forces, which act on particles when they are in physical contact and non-contact forces, which take place even when particles are not in physical contact.

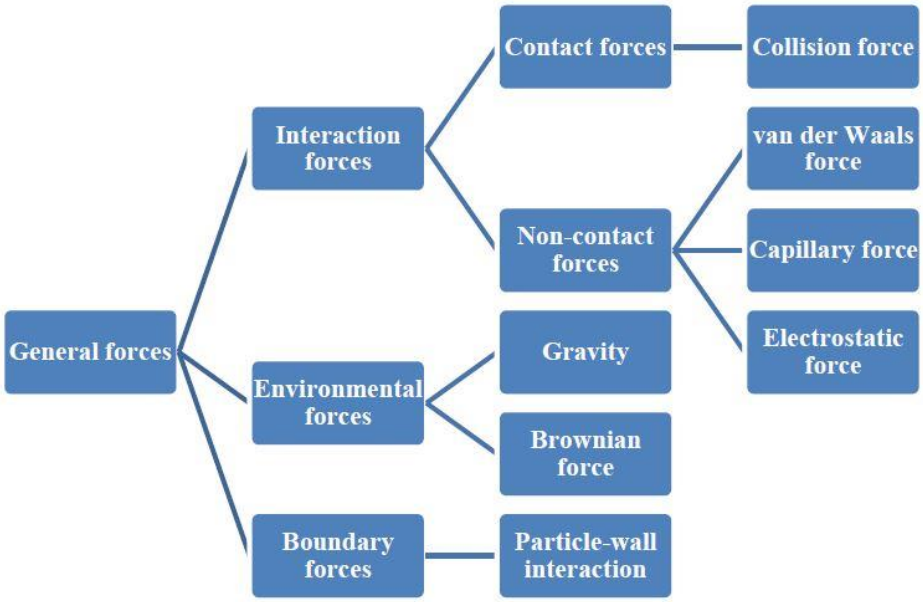

Figure 2-9 Particulate system forces diagram.

In a particulate system, attractive interaction occurs in accordance with van der Waals forces, which originate from the polarisability of atoms that build up on particles. In addition, electrostatic interactions can influence particles. Gravitational force is a common environmental force exerted on particulate systems as a result of the gravitational field.

2.6.3 Energy

The concept of potential energy is used in calculating non-spherical particles (Brito et al. 2018; Mailman et al. 2009). When considering potential energy between two interacting particles, the gradient at the position of each particle can be evaluated to find the force on each particle. The sum of attractive and repulsive forces in interaction is the potential energy. Considering the expression of attraction, the magnitude of the interaction increases with the decline in separation between particles. Therefore, attraction would be the dominant effect at small separations. The Van der Waals energy is reduced at very large distances and repulsion energy decreases exponentially. Therefore, the total interaction energy is always attractive for very small and very large distances. Alternatively, there may be a range of distances over which repulsion forces dominate.

2.7 Macroscopic theories of the screening process

2.7.1 Particles process theory

The process of particle sieving by screening is usually divided into two steps. First, the movement of undersize materials to the deck of the screen and second, materials passing through the apertures. When the material constructs a layer on the surface of the screen, contact between particles and the screen is established. As a result, they may pass through the screen. The top layer can replenish the contact layer and the rate of passing remains constant. This is called crowded screening and can be defined as:

$$\frac{dN}{dt} = -s \qquad \text{(Eq. 2.7)}$$

where the number of particles, N, is on the screen surface, s is the crowded screening rate constant and t is for time. When the materials construct a layer on the surface and do not

interfere with each other, the passing rate is proportional to the amount of material on the surface:

$$\frac{dN}{dt} = -kN \qquad \text{(Eq. 2.8)}$$

The sieving rate is *k* for separated screening. Solving (Eq. 2.8), the remaining particles on the screen represent a function of time:

$$N(t) = -N_0 e^{-kN} \qquad \text{(Eq. 2.9)}$$

Here, N_0 is the number of the initial particles. The orientation of particles for passing and the screen is small. Vibration will influence the movement of particles across the screen surface. The movement of the screen can be expressed by the dimensionless sieve number k_v :

$$k_v = \frac{A(2\pi f)^2}{g} \qquad \text{(Eq. 2.10)}$$

where *f* is screen frequency, *A* is screen amplitude, and *g* is acceleration of gravity. It can be said that k_v is the relationship between acceleration of the screen and *g*. By using (Eq. 2.9), the grade and existing particles, or recovery, of batch stratification can be predicted based on the difference in screen kinetics.

In a mixture containing two particles, N_1 and N_2 , the screen kinetics are respectively k_1 and k_2 , and the grade (*g*) and recovery for the first particle can be derived as:

$$g(t) = \frac{N_1 e^{-k_1 t}}{N_1 e^{-k_1 t} + N_2 e^{-k_2 t}} \qquad \text{(Eq. 2.11)}$$

and recovery:

$$r(t) = e^{-k_1 t} \qquad \text{(Eq. 2.12)}$$

Similar equations can be derived for the second particle on the screen (i.e., oversize or undersize streams).

2.7.2 Probabilistic approach of sieving

Probability and kinematic screening processes are used to analyse the passing of particles via multiple attempts to determine the influence of the feed rate, the effect of operating variables (Dong, K, Wang & Yu 2013; Kapur, Ball & Fuerstenau 1977; Soldinger 1999, 2000; Standish & Meta 1985; Subasinghe, G, Schaap, W & Kelly, E 1989), the particles remaining on the screen and the sieving speed of particles (Ferrara, Preti & Schena 1987; Standish 1985; Standish, Bharadwaj & Hariri-Akbari 1986; Standish & Meta 1985; Subasinghe, Schaap, W & Kelly, EG 1989). By using probability process, it is possible to determine the influence of the feed rate and the change in proportions of fine material (Soldinger 1999, 2000). Moreover, the sieving speed of undersized particles, the relationship between the sieving speed and the remaining materials are described in kinetic (Standish 1985; Standish & Meta 1985) modelling.

The passage rate depends on the probability of particles passing through the apertures and the amount of free material on the screen surface (Soldinger 1999). The sieving process can be described by first-order relationships but can also be described by simple probabilistic analyses. In the case of screening, a probabilistic approach gives the fraction of material retained, Y_d, as (Subasinghe, G, Schaap, W & Kelly, E 1989):

$$Y_d = (1-p)^N \qquad \text{(Eq. 2.13)}$$

where p is the probability of passage of a particle of size, d, in a single attempt, and N is the number of attempts. It is generally assumed that for a vibratory screen with constant frequency and amplitude of vibration, for particles of all sizes, the number of attempts is proportional to the distance travelled along the screen (i.e., N is determined by the product of screen length, L, and the number of attempts per unit N_L, which is regarded as constant). However, as noted above, the rate of segregation determines the amount of a given size of material that is in contact with the screen surface, implying that N_L varies with screen length and particle size. The values of N can be back-calculated using (Eq. 2.13) rearranged as:

$$N = \frac{\ln (Y_d)}{\ln (1-p)} \qquad \text{(Eq. 2.14)}$$

where $p = \frac{[(a+w)cos\varphi - w - d](a-d)}{(a+w)^2 cos\varphi}$, a is the edge of a square aperture, w is the wire diameter, and φ is the inclination of the screen surface to the horizontal.

The probabilistic model is equivalent to a Weibull survival function with two parameters. $Y_d = \exp\{-A(L^B)\}$, A, B = constants, p = the probability of passage in a single attempt; N = the number of attempts and L = screen length (Subasinghe, Schaap, W & Kelly, EG 1989).

Conversely, it is possible to determine the influence of feed rate and varying proportions of fine material:

$$\begin{aligned} &\text{Passage rate: } \dot{P} = k(1 - P) \\ &\text{For bottom layer: } \dot{P} = k \cdot B \end{aligned} \qquad \text{(Eq. 2.15)}$$

where P is the share of the original amount of fine particles that has passed through the apertures in the screen surface (Soldinger 1999) and B is the part of the original amount of fine particles gathered in the bottom layer (Soldinger 1999, 2000).

High-density material has a higher probability of passage. The passage probability of particles can be defined as:

$$k_j = 80(e^{\left(-\frac{\beta d_{50}}{Ap}\right)} - e^{-\beta} d_{50}/Ap) \qquad \text{(Eq. 2.16)}$$

where d_{50} is the mean particle size, Ap is the aperture size and β is the rate factor.

2.7.3 Kinetic of sieving

According to Standish (Standish 1985), for packing and sieving, matter kinetics of sieving is often studied considering the rate of sieving of near-mesh sized particles with the total feed or load on the sieve, which is found to not differ appreciably with time. Thus, the first-order rate law can be expressed as:

$$-\frac{dW}{dt} = kW \qquad \text{(Eq. 2.17)}$$

where the weight of particles is W on the sieve, t is the time of sieving and k is the sieving rate constant. The equation can be used for the random path model of the low probability of particles passing or loading. Eq. 2.17 can also be considered in continuous screening applications because of the distance travelled across the screen (Jansen & Glastonbury 1968) and sieving in the presence of attrition (Gupta, Fuerstenau & Mika 1975). Eq. 2.17 also serves as a foundation for the standard rate technique of sieve analysis and a foundation for the mathematical model

of (Bandemer & Espig 1978), which is widely regarded as the greatest attempt of at an analytical treatment of sieving. Unfortunately, prior understanding of sieve function is required for its application, and the mathematics involved are rather difficult. For sieving different sized particles acting independently it can be written as:

$$-\frac{dW_1}{dt} = k_1 W_1;\ -\frac{dW_2}{dt} = k_2 W_2;\ etc. \qquad \text{(Eq. 2.18)}$$

where k_1 , k_2, etc. are the constants of the sieving rate for each particle size. It should be noted that earlier treatments, which solely included sieving of near-mesh size particles were predicated on the hypothesis that W = const. When sieve residue decreases during the sieving process, and $W \neq$ constant, integrating (Eq. 2.18) for this case and collecting terms for any time results as:

$$\frac{W_1}{W_1} = \left(\frac{W_2}{W_2}\right)^{k_1/k_2} = \left(\frac{W_3}{W_3}\right)^{k_1/k_3} \qquad \text{(Eq. 2.19)}$$

The weights obtained in (Eq. 2.19) provide k ratios. This is done by first redefining (Eq. 2.17) as:

$$-\frac{1}{a_r}\frac{dW_i}{dt} = k_i \frac{W_i}{W} \qquad \text{(Eq. 2.20)}$$

where a_r is the sieve area, W_i/W is the weight fraction of particles of size di on the sieve and k^* is the sieving rate constant with units such as kg/(m^{2}s). Comparing (Eq. 2.17) and (Eq. 2.19) provides the relationship between the two forms of the rate constant:

$$k_i = k^* \frac{a_r}{W} \qquad \text{(Eq. 2.21)}$$

and the overall material balance, including the oversize stream, W_1 is, for any time:

$$W = W_1 + \sum_{1}^{n} W_i \qquad \text{(Eq. 2.22)}$$

Finally, combining (Eq. 2.22) and (Eq. 2.19), substituting the result of (Eq. 2.18), focusing on particles of size $d1$, integrating from $W_{1.0}$ to W_1 and rearranging the equation generates:

$$k_1^* a_r t = W_1 \ln\left(\frac{W_{1.0}}{1}\right) + \sum_1^n W_{i.0} \frac{k_1}{k_i} \times \left[1 - \left(\frac{W_1}{W_{1.0}}\right)^{k_i/k_1}\right] \qquad \text{(Eq. 2.23)}$$

k_1^* can be found constant by solving (Eq. 2.23), and (Eq. 2.19) can be evaluated with k (or k*). The composition of the undersize stream for any level of the weight fraction for passing. For length L, mean velocity down the screen and screening time are related and this relationship completes the identity between the first-order rate law for batch sieving ($-\mathrm{d}W/\mathrm{d}t = kW$) and for continuous screening ($-\mathrm{d}W/\mathrm{d}L = kW$) (Standish & Meta 1985).

2.7.4 Stratification

Stratification can be defined as the fall of undersized particles through the spaces between oversized particles resulting from the vibration of the screen. A well-integrated particle passage and stratification model was proposed by Soldinger (Soldinger 1999, 2000). Stratification is completed when fine particles are in the bottom layer. The particles have no further effect on the screening process. The rate of stratification is related to the number of remaining fine particles.

Thus, the stratification can be described via the first-order rate process as:

$$\dot{S} = c(1 - S) \qquad \text{(Eq. 2.24)}$$

where $\dot{S}$ is the time derivative of $S \rightarrow 1$ down the screen, $S = S_0$ at the initial case, and time $t = 0$ and c denote the rate of stratification. Fine particles such as dust that do not appear in the bottom layer remain on coarser particles. For the constant c, stratification is:

$$S = c(1 - S_0)e^{-c\,t} \qquad \text{(Eq. 2.25)}$$

According to Soldinger (Soldinger 1999), there are two different simultaneous processes during screening. One is stratification and the other is the passage of materials through the aperture in the screen surface. The term “misplaced particles” refers to fine particles that are below the range of the separation limit and coarse particles that are within the fine fraction. Both processes depend on other characteristics. The rate of stratification depends on the proportion of fine particles and the ratio of the particle sizes. Furthermore, the passage depends on the probability that particles will pass through the apertures and the number of fine particles

on the surface of the screen. The stratification rate varies with the proportion of fine material and the ratio of material size. Factors that impact the stratification output (Mosby, 1996) include:

- with more particle size variation, stratification increases.
- when overall particle size is smaller, stratification diminishes.
- particle density differences and shape are less significant than variations in particle size.
- the presence of liquids reduces stratification.

2.7.5 Weibull distribution of particles passing with probabilistic theory

Screening has been described with two first-order rate processes the segregation and passage of particles through the screen (Subasinghe, G, Schaap, W & Kelly, E 1989). The particle size distribution in the bed and vibration condition influence passing through the bed to reach the screen surface. Particle passing through the screen is reported with first-order rate process under conditions of constant probability of passing.

Combining the two processes, the fraction of size *i* retained on the screen after length *L* (Subasinghe, G, Schaap, W & Kelly, E 1989) is:

$$E_{iO} = \frac{[k_{iG}\exp(-k_{iP}L) - k_{iP}\exp(-k_{iG}L)]}{k_{iG} - k_{iP}} \; for\; 0 \le i \le L_G \qquad \text{(Eq. 2.26)}$$

where k_{iG} = rate constant for the size *i* segregating to the screen surface and k_{iP} = rate constant for the size *i* passing through the screen.

k_{iG} and k_{iP} explain that if the particle size is smaller than the screen aperture, the segregation rate of particles decreases. For the near size particles, the passing rate constant increases as the particle size approaches the aperture size. The segregation rate increases and the passing rate constant approaches zero. For intermediate values of d_i/L_A, the value of k_{iG} approaches the value of k_{iP} and a dynamic equilibrium exists between the two processes. With the values of k_{iG} and k_{iP}, the undersize particle size distribution of the screen can be estimated. The Weibull distribution function in the form of a Rosin-Rammler function is adequate to describe the screen products as (Subasinghe, G, Schaap, W & Kelly, E 1989):

$$E_{io} = exp\left[\left(-\frac{L}{B}\right)^{A}\right] \quad \text{(Eq. 2.27)}$$

The constants *A* and *B* were fitted to third-order polynomials.

2.8 Percolation

Percolation is one of the major phenomena in granular material flow analysis. The inter-percolation concept represents the behaviour of connected clusters in a random graph, which can clarify the relocation of smaller materials through an assembly of large materials (Tang, P & Puri 2005) resulting from gravity or another applied force. Inter-particle percolation for mixing (Bridgwater, J. , Sharpe & Stocker 1969) and stratification in sieving (Soldinger 1999) are widely adopted in industrial applications. Industrial materials with low cohesion including sodium carbonate, polymer chips, sand, mineral ores, cement, detergents, fertilizers, coal and food products are important. Comprehensive formation of the material may be minor in certain applications but might be significant in others. Gravity and strain are the major forces that cause small particles in the mixture to pass through larger particles during extensive mixing or percolation. The Flory–Stockmayer theory was the first to illustrate percolation processes (Sahini & Sahimi 1994). In the past, physical models were used to investigate percolation processes such as fluid flow in a porous medium for randomly blocked channels (Broadbent & Hammersley 1957).

Mathematical analysis of percolation has bought novel theories and methods in a range of subjects such as physical science, epidemiology, and complex networks. In geology, percolation refers to the filtration of water through soil and permeable rocks (i.e., porous media). Even though disagreement between physical and numerical experiments still exists, numerical methods have been recently employed to improve the understanding of the inter-particle percolation mechanism.

The study of percolation is based on the fundamental knowledge of particle packing. Packing density, coordination number and radial distribution function are critical to understand particle flow behaviour in a packed bed. The flow of granular media is relevant to a wide range of industrial sectors related to sand, powders, food, coal and ore. Thus, analysis of gravitational flow of granular materials in mining applications has been reported by many authors (Chen, G

1997; Just & Free 1971; Rustan 2000). The flow of granular material is quite complex and not well understood, which makes modelling a difficult task (Campbell 1990; Hutter & Rajagopal 1994; Jaeger, Nagel & Behringer 1996).

2.8.1 Spontaneous percolation

Smaller particles tend to drain through larger particles under the influence of gravity, which is known as the spontaneous inter-particle percolation phenomenon. The ability to control this phenomenon is very critical (Bridgwater, J. , Sharpe & Stocker 1969). Large particles can rise to the top or fall to the bottom depending on their physical properties and density (Kudrolli 2004). The extent of percolation depends on the rate of strain and the relative size of particles (Scott & Bridgwater 1975). Percolation is determined by the gravitational force on particles. Therefore, it is inhibited by cohesive materials. Spontaneous particle percolation has been empirically studied to analyse percolation velocity, dimensionless distance distribution and residence time (Bridgwater, J & Ingram 1971; Bridgwater, J. , Sharpe & Stocker 1969). An experimental study on the dispersion of particles during spontaneous percolation shows that particles disperse radially with a linear trend (Figure 2-10) (Bridgwater, J. , Sharpe & Stocker 1969). Examination of spontaneous inter-particle percolation of small beads through an unconsolidated porous media found that radial or transverse dispersion decreases and longitudinal dispersion increases with the increase in percolating particle density (Lominé & Oger 2009).

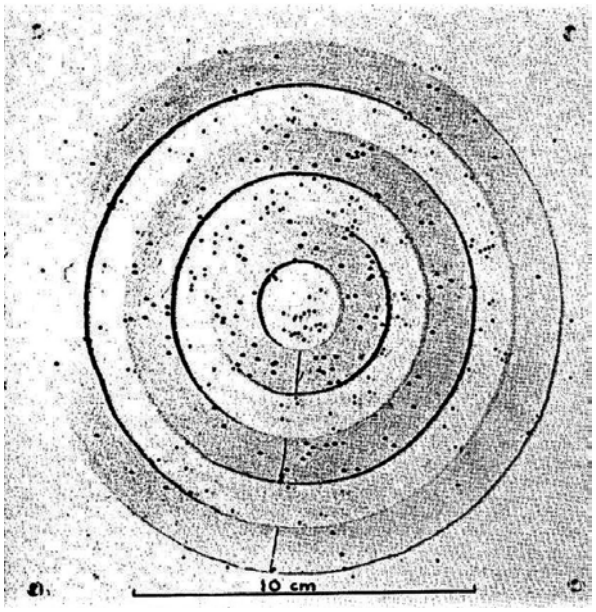

Figure 2-10 Typical dispersion of about 200 × 0.08 cm diameter steel bearing on the target plate. Where plate bed packing is 1.2 cm diameter glass spheres, bed height is 30 cm and bed diameter is 15 cm (Bridgwater, J. , Sharpe & Stocker 1969).

Considering the study of spontaneous percolation of particles from a packed bed, the variation of percolating particle height with time was determined by the coefficient of restitution and the diameter ratio of the percolating particles to the packing (Li, J et al. 2010). The residence time distribution of percolating particles conformed to a diffusive mechanism (Figure 2-11). This could influence percolation velocity while increasing the height in free fall.

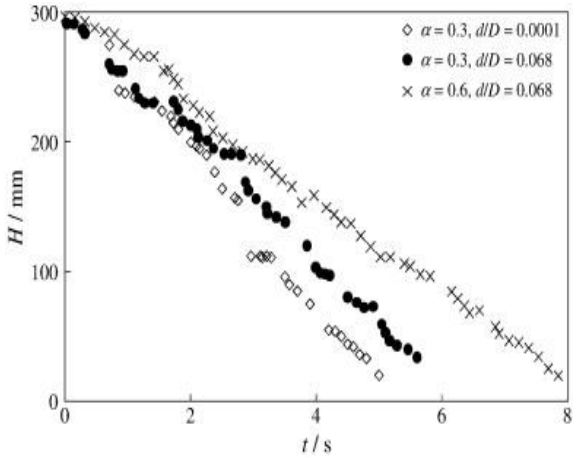

Figure 2-11 Variation of height (*H*) with time (*t*) for a percolating particle under different coefficient of restitution and diameter ratio (Li, J et al. 2010).

2.8.2 Vibration effect on percolation

Vibrated beds are used in a variety of industries to handle bulk materials at large scales. To increase the contact efficiency inside the bed, it is necessary to understand particle percolation and segregation. Vibration helps to percolate particles with large size ratios (Hudson, Jansen & Linkson 1969; Kudrolli 2004). In numerous cases, the gravitational spontaneous percolation approach has been considered (Bridgwater, J. , Sharpe & Stocker 1969; Li, J et al. 2010; Rahman et al. 2008; Wilkinson & Edwards 1982). However, this approach is limited to large-size ratio particle percolation. In vibration percolation, the material bed is influenced by the vibration, which leads to different percolation behaviour. However, no studies have comprehensively considered vibrational percolation for different amplitude, frequency and size ratios. Yu et al. (Yu, AB & Hall 1994) investigated the packing of fine powders subjected to tapping in an experimental setting and linked packing density with material characteristics such as particle shape and size distribution. Hudson et al. (Hudson, Jansen & Linkson 1969) carried

out an experimental analysis on particle segregation by vibration screen. They found that small particles passed through larger packed particles by percolation, which provided a basic concept for particle percolation flow rate and mixing. A linear cohesion contact model was used to study the segregation process of spherical and cubical wet particles under a vertical vibration (Zhao, L-L et al. 2019). Both the spherical and cubical wet particle systems present a hill-shaped segregation pattern. The segregated large particles are uniformly gathered around the cylindrical container wall while the small particles are concentrated in the bottom layer and the middle of the container.

Brazil-nut or reverse Brazil-nut segregation was obtained for different mixtures under vibration. Two experiments are shown in Figure 2-12. Theoretical findings (Breu et al. 2003) also predict a reverse Brazil-nut effect, where large particles sink to the bottom of the container. It is evident that the percolation for the Brazil-nut segregation occurred under vibration.

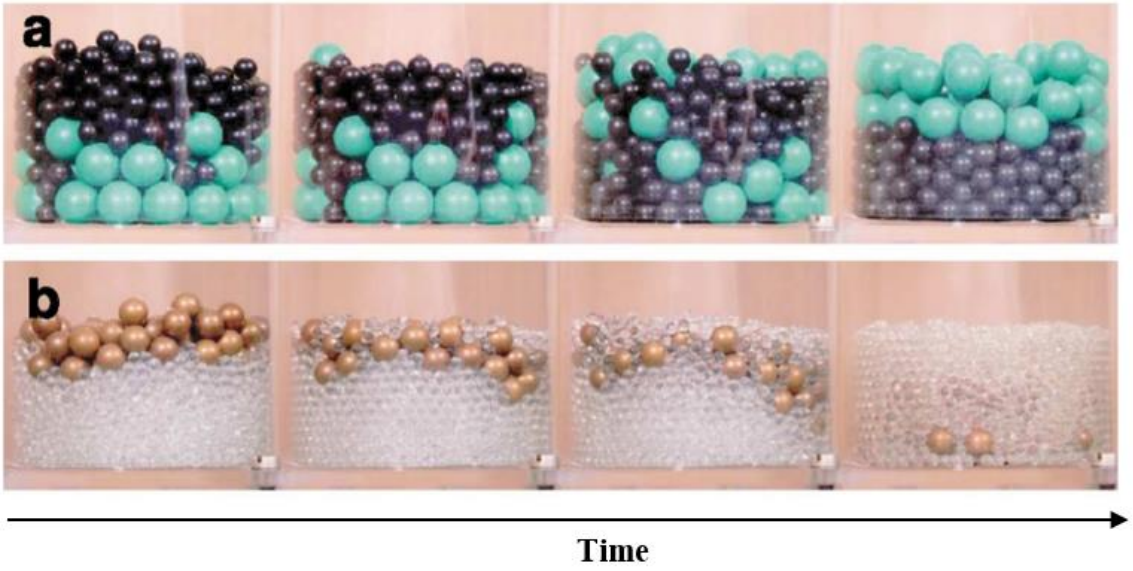

Figure 2-12 Temporal evolution of the system: (a) initially 8 mm glass beads on top of 15 mm polypropylene, which show the classical Brazil-nut effect; (b) 10 mm bronze spheres on 4 mm glass beads showing the reverse Brazil-nut effect (Breu et al. 2003).

2.8.3 Percolation velocity

The dimensionless percolation velocity of a particle moving down through a randomly packed bed of much larger particles under gravity is a function of different variables. According to Bridgwater (Bridgwater, J & Ingram 1971):

$$v = f\ (d, D, \boldsymbol{g}, \rho_s, \rho_e, \alpha, \mu_{st}, \mu_s, \varepsilon) \qquad \text{(Eq. 2.28)}$$

where d and D are the diameters of percolating and packing spheres, $\boldsymbol{g}$ is the gravitational acceleration, ρ_s and ρ_e are the density of percolating and packing spheres respectively, α is the coefficient of restitution, μ_{st} and μ_d are the static and dynamic coefficients of friction between percolating and packing spheres respectively, and ε is the void ratio of packing. So dimensionless percolation velocity will be:

$$\frac{V}{\sqrt{\boldsymbol{g}D}} = f\ (\frac{d}{D},, \rho_s, \rho_e, \alpha, \mu_{st}, \mu_s, \varepsilon) \qquad \text{(Eq. 2.29)}$$

2.8.4 Radial dispersion

Percolating particles also move in the radial direction in the packed bed with a radial dispersion coefficient, E_r, defined by the following equation:

$$\frac{r^2}{4E_r t} = ln\ (\frac{N_0}{N_0 - N}) \qquad \text{(Eq. 2.30)}$$

where N is the number of small particles with centres within the radius r at time t, N_0 is the total number of percolated particles and r is the radius of annular rings containing N percolating particles (Bridgwater, J. , Sharpe & Stocker 1969).

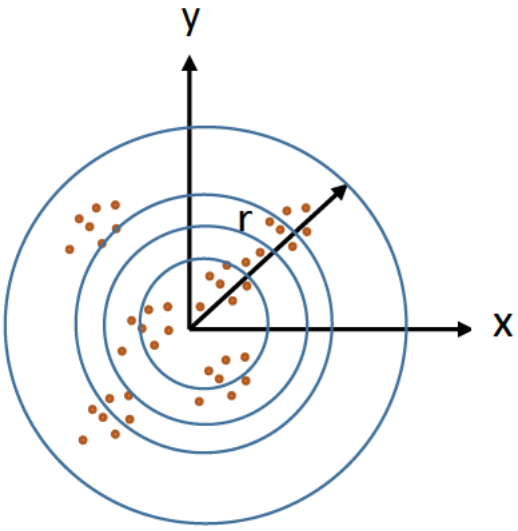

Figure 2-13 Radial dispersion of particles.

2.8.5 Residence time distribution

Residence time distribution shows the pattern of percolating particles' travelling time in the bottom of a packed bed. Mean residence time can be calculated by averaging the total residence time by total percolating particles. Percolation velocity is determined by measuring height and mean residence time. Residence time distributions or cumulative residence time distributions are normally employed to present the percolation time of all percolating particles (Bridgwater, J & Ingram 1971).

2.9 Numerical studies on screening

Screening theories are important to understand the mathematical probability of particulate passage and factors controlling screen performance. The kinetic batch sieving (Standish 1985) and continuous screening methods were developed by Standish et al. (Standish & Meta 1985). They followed the first-order rate law of a mixture for confirmation of sieving and screening conditions. Additional understanding of liquids, particle density, shape, different particle sizes and feed effect on stratification is also important. The screening process of materials depends on how the rate of stratification and rate of passage vary along the screen (Soldinger 1999). Subasinghe et al. (Subasinghe, Schaap, W & Kelly, EG 1989) analysed the prediction of

screening models via the Weibull distribution. The model predicts the screening results of different systems by evaluating the relevant parameters of each system. The nature of the screen surface, particulate materials, random path model of flat and rotating screen as well as dynamics of the casting screen were found to be the most important factors that affect screening performance (Jansen & Glastonbury 1968). Trumic et al. (Trumic & Magdalinovic 2011) described the screening kinetics process of different types of raw materials under a range of influential factors such as dimensions of the screen, particle size distribution of the raw material, particle shape and thickness of the bed.

The screening process is essential for industrial applications. It is beneficial to optimise the operational conditions to improve the efficiency of the process (Cleary, Paul W., Sinnott, Matthew D. & Morrison, Rob D. 2009; Dong, K & Yu 2012; Elskamp et al. 2017; Lu, G, Third, J & Müller, C 2015; Soldinger 2000; Zhao, L et al. 2016). DEM can handle complex geometries and vibrational conditions of screens. DEM can provide comprehensive information on the particle scale that may be difficult to obtain through experimentation. However, for irregular or non-spherical particles, greater conjecture is required to predict factors such as stratification of bed material, blinding of apertures and places where spherical particles fail. Thus, further in-depth systematic studies are required. DEM may generate knowledge to improve the design and control of sieving under a wide range of conditions include linking screen kinetics to operational conditions, screen geometries, particle properties and machine learning.

A pilot-scale DEM study of vibrating screens was undertaken by Harzanagh et al. (Harzanagh, Orhan & Ergun 2018) for spherical and non-spherical particles. The irregular particles provided better predictions and reflection of actual phenomena such as stratification and segregation of particles from spherical particles, in which the spherical particles failed. Furthermore, the impact of inter-particle cohesion on flow and separation efficiency of screens was studied using DEM (Cleary, PW, Wilson & Sinnott 2018). High cohesion was found to reduce the screen performance. Conversely, reducing the vibration and inclination angle of screens enhances sieving performance (Dong, K, Wang & Yu 2013). Dong et al. reported that the shape of apertures could affect particle flow and separation in vibrating screens (Asbjörnsson et al. 2016). The sieving performance was investigated in terms of the particles passage along the screen deck. The research also linked microscopic information with macroscopic sieving performance and focused on design, control as well as optimisation of the screening process.

A non-linear regression model with dependent and independent variables was developed by Li et al. (Li, Z et al. 2019) for non-spherical particles on vibrating banana screens using DEM, which determined optimal vibration conditions. Moreover, the particle bed of the screen remains thicker at the lower deck and the stratification process mainly affects the screen performance in the lower deck (Davoodi, Ali et al. 2019). Most of the fine particles pass through the first panel of the screen aperture for lower feed rates and the particles are evenly distributed across the screen for higher feed rates. The cut size of screening remains higher for low vibration conditions and inclination angle (Davoodi, A. et al. 2019; Harzanagh, Orhan & Ergun 2018; Peng, Feng, et al. 2019; Zhao, L et al. 2011). The dimension of screen length affects the performance of screen, i.e. longer screen lengths provide higher screening efficiency (Liu, C et al. 2013; Wang, G & Tong 2011). The performance of a banana screen can be improved by reducing vibrational frequency, amplitude and inclination angle of decks using a flatter greater than a three-deck banana screen (Dong, K, Yu & Brake 2009). The use of rectangular apertures affects the maximum size of particles passing through the banana screen (Asbjörnsson et al. 2016). For a small inclination of the discharge end, the screening process will be difficult to proceed for the too-small particle velocity amplitude. Moreover, screen efficiency increases with an increase in screen length (Liu, C et al. 2013). With the increase in frequency, amplitude and inclination angle, the bottom deck recovery remains higher than the top deck of industrial multi-deck screens. Excessive reduction in vibration amplitude can reduce screening recovery for reduced particle velocity and a reduction of processed material (Jahani, Farzanegan & Noaparast 2015). Moreover, the velocities of particles remain higher on top decks than on lower decks of the screen while increasing the penetration of fine particles. Conversely, the velocity of particles remains higher for the middle decks of a multi-deck banana screen than for the top and bottom decks (Cleary, Paul W., Sinnott, Matthew D. & Morrison, Rob D. 2009).

Li et al. (Li, Z & Tong 2017) reported DEM simulation sieve analysis of banana screens with the inclination of decks and improved the study by Fibonacci sequence (Cleary, Paul W, Sinnott, Matthew D & Morrison, Rob D 2009). The experimental results showed that the screening performance efficiency of banana screens improved with Fibonacci sequence analysis by about 7%. Elliptical vibration screen-based theoretical and numerical DEM investigation was performed (Yin, Zhang & Han 2016). The elliptical-shaped screen exhibited a relatively high processing capacity with good screening efficiency when compared to the screening performance of different motion traces. To better simulate irregular particles, the

benchmark process model was extended for batch screening of the altered operational case (Elskamp et al. 2016). The banana screen increases the passage rate of fine fractions, and the screening model makes it possible to simulate the behaviour in a particular screen. With the increase in the passage of material, the local wear on the screen cloth increases (Asbjörnsson et al. 2016). Particle passage and recovery by banana screen remains higher for the top deck than the bottom deck (Cleary, PW 2009; Cleary, Paul W., Sinnott, Matthew D. & Morrison, Rob D. 2009; Jahani, Farzanegan & Noaparast 2015) as the top panel bed becomes well-stratified following the lower flow speed of the shallow panel, which gives the particles more time to pass through the screen apertures. Using the developed phenomenological screening process, model optimisation of screen performance under different feeding conditions was adjusted according to the outcome of DEM simulations. The theoretical single deck banana screen process optimisation was analysed for screening efficiency and improved DEM for a dry contact soft-sphere model (Liu, C et al. 2013). The discharge would be small if the screening inclination of the discharge end is small. Green iron ore pellet classification by rolling screen was studied with the help of DEM simulation (Silva et al. 2018). Half of the screen with a very low friction wall could be simulated to save computing effort without significant loss or change of information.

2.10 Artificial intelligence modelling for granular processing

With the advancement of computing and the availability of massive data sets, artificial neural networks or machine learning modelling has the potential to explain complex non-linear relationships between parameters and aid predictions. Supervised machine learning has been used by several researchers for predicting results of numerical simulations (Barrasso, Tamrakar & Ramachandran 2014; Bui, Bui & Rutschmann 2019; He & Tafti 2019; Zhang, S-l et al. 2018; Zhao, Z et al. 2021).

For problems that cannot be solved by data mining and output prediction, an artificial neural network (ANN) can be particularly beneficial. Considering the DEM findings, an ANN model was developed to estimate the porosity of gravel-bed rivers (Bui, Bui & Rutschmann 2019). The results showed that combining DEM and ANN was effective for the study of porosity and fine sediment infiltration process in gravel beds. An ANN was combined with population balance modelling (PBM) as a fundamental component of the kernel function. The coupled model exhibited changes in the average particle size and size dispersion over time as opposed to a constant aggregation rate kernel in the wet granulation process (Barrasso, Tamrakar &

Ramachandran 2014). Using relative neighbour particle locations, existing Reynolds number and void fraction information as inputs to the model by ANN, CFD-DEM simulations of dense fluid-particulate systems improved the drag force prediction accuracy (He & Tafti 2019). A BNN-based particle distribution model was proposed for a vibrating screen (Zhao, Z et al. 2021). Particle distribution could be easily established by specifying the network's excitatory and inhibitory inputs based on the structure of the screen and particle feeding.

Even though physics-informed machine learning is partially understood and has uncertain and high-dimensional contexts, it is used to integrate data and mathematical physics models (Karniadakis et al. 2021). Machine learning, a subset of artificial intelligence, refers to computer learning from data without being explicitly programmed. Neural networks are a specific type of machine learning model, which are used to make brain-like decisions. Physics-informed machine learning (ML) is a wide and open topic. Moreover, the ML model is not like curve fitted. Machine learning models are designed to make the most accurate predictions possible. On the other hand, statistical models are designed for inference about the relationships between variables (Bzdok, Altman & Krzywinski 2018). Data from DEM simulations of particle flow in a rotating drum under different operational circumstances were used to develop a data-driven model (Li, Y et al. 2020). The drum size, rotation speed, filling level and particle–wall friction was considered for the training and the prediction was performed for particle flow in a rotating drum with a limited training data set. The CNN was trained and tested using the discharge DEM result in a hopper bin packing with high accuracy (Chen, S et al. 2018). For the grinding process of particles, neural network and SVR models were tested. The model allowed the identification of anomalous data and real-time prediction of cement Blaine based on the input variables (Pani & Mohanta 2015). Based on the experimental data, a support vector machine (SVM) model was developed to predict sieving performance. The prediction error of the LS-SVM model was tested by testing points, which was significantly less than the neural network and existing adaptive genetic algorithm (Zhang, B et al. 2016). Optimised non-linear regression modelling (PSO-SVM) was applied to the outcomes of linear vibrating screens to predict screening efficiency and solve the complex non-linear screen model (Zhang, B et al. 2016). A novel screening process model was developed considering the local passing of particles for an inclined screen (Arifuzzaman, S. M., Dong, Kejun & Yu, Aibing 2022) and a double-layer vibrating screen (Arifuzzaman, S.M., Dong, Kejun & Yu, Aibing 2022) based on physics-informed machine learning. The model was able to effectively assess the effects of the controlling variables on the sieving performance parameters than the DEM.

2.11 Methodology: Discrete Element Method

Numerical modelling and simulation are popular topics in engineering research for time-consuming, increase the quality of the products, to avoid costly experiments and predict results. Simulation is used in a vast area of engineering for the mathematical knowledge of the problems and computer's computation power to solve real/critical problems in time. The DEM comes under the family of numerical methods that could compute the motion and the effects of a large number of small particles. To save time, cost and risk, numerical simulation of particles has become an ideal option in engineering. In particle physics, numerical simulations provide a vast area to develop ideas and validation of experimental results. DEM was developed by Cundall et al. (Cundall & Strack 1979) to understand rock mechanical problems and applied to granular materials. In the DEM technique, the motion of each particle is governed by Newton's second law and is traced by an explicit numerical scheme (Cundall & Strack 1979).

In recent years, research on discrete particle simulation techniques and computer technology has expanded rapidly across the world. DEM is increasingly used for particle flow modelling. Utilizing DEM modelling, the crushing process of virtual coal particles (Li, Y-W et al. 2019), particle dynamics and information at the particle scale can be understood (Zhu, HP et al. 2007). DEM can also provide both macroscopic and microscopic 'measurements' in granular systems and describe particles of non-spherical shapes (Lu, G, Third, JR & Müller, CR 2015). There are two types of discrete particle simulation for hard-particle and soft-particle models. The soft-sphere method was originally developed by Cundall et al. (Cundall & Strack 1979). In this method, deformation of particles is allowed, which is then used to calculate elastic, plastic and frictional forces between particles. The motion of particles is described by Newton's laws of motion. This model has the ability to handle numerous particle interactions, which is important for modelling quasi-static systems. The forces between particles cannot be explicitly considered in a hard-particle simulation because collisions are processed one at a time rather than instantly. To be specific, the hard-particle method is most useful in simulating rapid granular flows. In particular, the soft-sphere method has been extensively used to study various phenomena such as percolation of particles, particle packing, transport properties, mixing, granulation, heaping/piling process and hopper flow.

2.11.1 Governing equations

Translation and rotation are the two types of motions in the DEM. For the matter of particle movement, the particle can contact neighbouring particles, the system wall and surrounding fluid particles. Momentum and energy are exchanged via those collisions. Therefore, the forces on a particle can be determined by its interaction with contacting particles and vicinal medium in a coarse particle system. For a fine particle system, non-contact forces such as the van der Waals electrostatic forces should also be considered.

The motions are studied for each particle and governed by Newton's second law of motion, as determined by Cundall et al. (Cundall & Strack 1979):

$$m_i \frac{d\boldsymbol{v}_i}{dt} = \sum_j \left(\boldsymbol{F}_{ij}^n + \boldsymbol{F}_{ij}^t\right) + m_i \mathbf{g} \qquad \text{(Eq. 2.31)}$$

and

$$\boldsymbol{I}_i \frac{d\boldsymbol{\omega}_i}{dt} = \sum_j \left(\boldsymbol{T}_{ij} + \boldsymbol{T}_{r,ij}\right) \qquad \text{(Eq. 2.32)}$$

where m_i, v_i, $\boldsymbol{I}_i$ and ω_i are the mass, translational velocity, moment of inertia and angular velocities of particle i respectively. The gravitational acceleration is **g**, where the inertia of particle i is a tensor vector but can be represented by using a body-fixed coordinate system (Džiugys & Peters 2001). $\boldsymbol{F}_{ij}^n$ and $\boldsymbol{F}_{ij}^t$ are the normal and tangential components of the contact force exerted on particle i by particle j. $\boldsymbol{T}_{ij}$ and $\boldsymbol{T}_{r,ij}$ are torques on particle i from particle j resulting from the total contact force (the sum of the normal and tangential forces) and rolling friction. These equations are developed from spherical particle equations and are similar to those adopted in various studies of non-spherical particles.

2.11.2 Force model

Particle contact forces are considered as particle–particle and particle–wall when they are in physical contact. The most common contact force is collision force between particles.

2.11.2.1 Spherical shape particles interaction

Material properties including density, structure and mechanical properties are crucial along with the operating conditions of the component in engineering. Contact point determination is relatively easy for the symmetry of overlap (δ) between two particles. For two colliding

spheres, the calculation is $\delta = R_1 + R_2 - d$, where the radii of the spheres are R_1 and R_2 and the distance between the centres (C_1 and C_2) of the two spheres is d (Figure 2-14). The contact point (P) can be expressed as the midpoint of the line connecting C_1 to C_2. The contact normal vector $\overrightarrow{C_1\ C_2}$ defines the tangential force direction of the contact given by the direction of the relative speed between the two spheres in the plane and perpendicular to $\overrightarrow{C_1\ C_2}$. Normal contact force cannot be induced at any moment during the rotation of the spherical particles. However, the condition is much more complex for irregular / non-spherical particles.

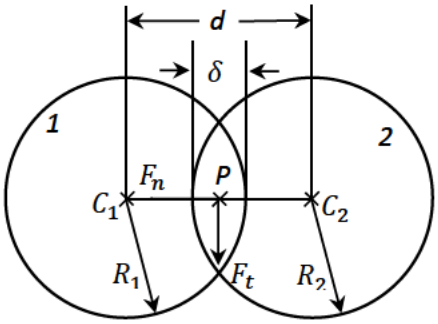

Figure 2-14 Spherical particles conflict (Lu, G, Third, JR & Müller, CR 2015).

2.11.2.2 Non-spherical shape particles interactions

For non-spherical and irregular particles, it can be difficult to define the contact point of the overlap section. For example, the contact point between two colliding particles may be defined as the geometric centre of the overlapping area or as the mid-point of the line that connects the two points of intersection in two-dimensional particles. The physical problem of contact definition introduces particle collision with a flat wall. The contact point will always lie on the surface of the particle's wall (i.e., the wall does not deform during contact).

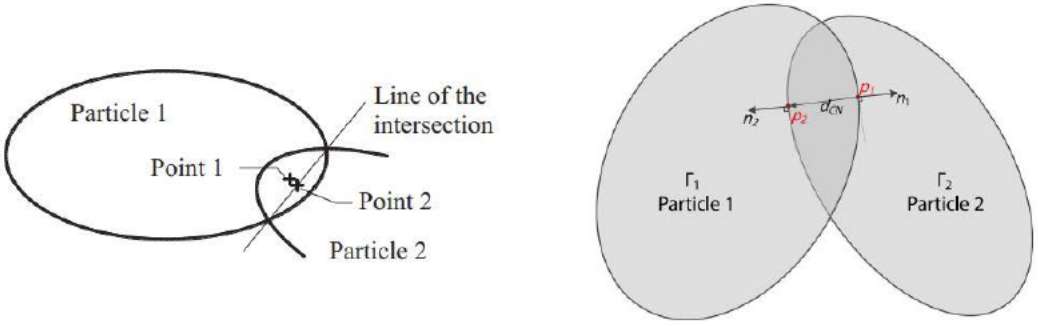

Figure 2-15 Non-spherical particles collide (Kildashti, Dong & Samali 2018).

For non-spherical particles, the concept of normal contact is less precise than for spherical particles. In general, normal contact for non-spherical particles does not pass through the centre of gravity of the particles in contact. For non-spherical particles, the normal contact force deals with the moment and rotation effect. Single-point contact models will not be effective for the result with unphysical behaviour, as direction and magnitude over subsequent time steps may suddenly change for the contact force. In Figure 2-15, particle 2 is in contact with particle 1 (fixed in space) with its two vertices *p1* and *p2*. If it is assumed that the contact force only acts on p1, i.e. the point with the largest overlap between the two particles, particle 2 rotates in the subsequent time and the largest overlap between particles 1 and 2 may move to p2 during the next time. Thus, the point at which the contact force acts suddenly changes from p1 to p2.

2.11.2.3 The collision force

In contact mechanics, contact with particles and the interaction between particles is a complex issue. For the deformation of particles, contact between two particles is not at a single point but through a finite area, which is similar to the contact of two rigid bodies allowed to overlap slightly in the DEM. The calculation of the contact traction distribution across this area as well as the total force and torque acting on a particle are extremely complex because they are dependent on several geometrical and physical variables such as particle shape, material characteristics and particle movement state. To be computationally efficient and suitable for multi-particle systems, the DEM often uses simplified models or equations to calculate the forces and torques generated from particle interaction. A variety of approaches have been recommended for this. In general, linear models are the most intuitive and simple. Cundall et al. (Cundall & Strack 1979) proposed the linear spring–dashpot model. It is the most widely used linear model, where the spring is used for elastic deformation and the dashpot accounts for viscous dissipation.

Normal force $$f_n = -K_n \delta_n \boldsymbol{n}_c - C_n (v_c \cdot \boldsymbol{n}_c) \boldsymbol{n}_c$$ (Eq. 2.33)

Tangential force $$f_t = -K_t V_c^t - C_t (v_c \times \boldsymbol{n}_c) \times \boldsymbol{n}_c$$ (Eq. 2.34)

Hertz (1882) (Hertz 1882) presented a theory to describe elastic contact in the normal direction between two spheres, assuming that normal force and normal displacement had a nonlinear

connection. A generic tangential force model was developed by Mindlin and Deresiewicz (Mindlin 1953), which showed that the force-displacement relationship was influenced by loading history as well as by the change in normal and tangential force or instantaneous displacement rates. It is not often used in DEM applications as the complete Hertz–Mindlin and Deresiewicz model is time-consuming for DEM simulations of granular flows containing a large number of particles. For DEM modelling, many simplified models based on the Hertz, Mindlin and Deresiewicz theories have been established. For example, Walton (Walton 1993) used an approximation of the Mindlin and Deresiewicz contact theory. He used a semi-latched spring force-displacement model in the normal direction and in the tangential direction.

Normal force

$$f_n = \begin{cases} -K_1 \delta_n n_c, \dot{\delta_n} \geq 0 \\ -K_2(\delta_n - \delta_{n0})\boldsymbol{n}_c, \dot{\delta_n} < 0 \end{cases} \quad \text{(Eq. 2.35)}$$

Tangential force

$$f_t = \begin{cases} \acute{f}_t + k_t^0(1 - \frac{f_t - f_t^*}{\mu f_n - f_t^*})^{\frac{1}{3}} \Delta v_c^t \\ \quad if\ \hat{v}_c^t\ in\ initial\ direction \\ \acute{f}_t + k_t^0(1 - \frac{f_t - f_t^*}{\mu f_n + f_t^*})^{\frac{1}{3}} \Delta v_c^t \\ if\ \hat{v}_c^t\ in\ opposite\ direction \end{cases} \quad \text{(Eq. 2.36)}$$

Thornton and Yin (Thornton & Yin 1991) proposed a more complex model to simulate tangential force. A more intuitive model was adopted by Langston et al. (Langston, Tüzün & Heyes 1994). They applied a direct force-displacement relationship for tangential force and Hertz's theory for normal force. The model has been widely used to study the dynamic behaviour of granular materials because of its simplicity and intuitiveness:

Normal force

$$f_n = -\frac{4}{3} E^* \sqrt{R^*} (\delta_n)^{\frac{3}{2}} \boldsymbol{n}_c - C_n \left(8 m^* E^* \sqrt{R^* \delta_n}\right)^{\frac{1}{2}} (v_c \cdot \boldsymbol{n}_c) \boldsymbol{n}_c \quad \text{(Eq. 2.37)}$$

Tangential force

$$f_t = -\mu \left| f_{n,e} \right| (1 - (1 - \frac{|v_c^t|}{\delta_{max}})^{\frac{3}{2}}) \hat{v}_c^t + 2 C_t (1.5 \mu m * \frac{|f_{n,e}| \sqrt{1 - \frac{|v_c^t|}{\delta_{max}}}}{\delta_{max}})^{\frac{1}{2}} (v_c \times \boldsymbol{n}_c) \boldsymbol{n}_c \quad \text{(Eq. 2.38)}$$

The inter-particle forces act at the point of contact between particles rather than at the mass centre of a particle while generating torque that rotates the particle. In general, two components of the tangential and asymmetrical normal traction distributions contribute to the torque. In

comparison to the tangential component, determining the contribution of the normal component, also known as rolling friction torque, is extremely difficult. Numerous DEM models assume rolling friction torque to be insignificant. However, torque demonstrated to have a major effect in several situations that involve the transition between static and dynamic states such as the development of the shear band (Iwashita & Oda 1998, 2000) and heaping (Zhou, YC et al. 1999).

Rolling friction torque	$\boldsymbol{m}_r = -k_r\theta_r - C_r d\theta_r/dt$	(Eq. 2.39)
Tangential forces torque	$\boldsymbol{m}_t = \boldsymbol{R} \times \boldsymbol{f}_t$	(Eq. 2.40)

and movement of a single particle on a plane (Zhou, YC et al. 1999; Zhu & Yu 2006):

Rolling friction torque	$\boldsymbol{m}_r = -\min\{\mu_r\lvert f_n\rvert, \acute{\mu}_r\lvert\omega_n\rvert\}\hat{\omega}_n$	(Eq. 2.41)
Tangential forces torque	$\boldsymbol{m}_t = \boldsymbol{R} \times \boldsymbol{f}_t$	(Eq. 2.42)

2.11.2.4 Non-contact forces

When fine particles and/or moisture are present, noncontact inter-particle interactions can have a substantial impact on particle packing and flow behaviour. In the past, empirical indexes such as the Hausner ratio, angle of repose and shear stress were often used to assess inter-particle forces (Hausner 1972). Although these indices can help explain particle behaviour in some cases, general quantitative application is still problematic. These issues can be solved by DEM because such forces can be considered directly. Non-contact forces frequently involve a mixture of three fundamental forces—the van der Waals force, capillary force and electrostatic force—all of which can act simultaneously or sequentially to varying degrees.

2.11.2.5 The capillary force

The capillary force between particles is a long-distance attractive force that might be observed. The amount of the force is proportional to the inverse of the inter-particle distance. It acts on particles that have menisci with nearby particles. Capillary force is largely related to surface tension at solid/liquid/gas contact. The force of reduced hydrostatic pressure in the bridge itself was developed by Zhu et al. (Zhu, HP et al. 2007):

$$F^l = 2\pi\gamma R sin(\varphi)\sin(\varphi+\theta) + \pi R^2 \Delta p sin^2(\varphi) \quad \text{(Eq. 2.43)}$$

Where θ is the contact angle, φ is the half-filling angle and γ is the liquid surface tension. The Laplace–Young equation, which states that the mean curvature of the meniscus profile is constant and proportional to Δp, could be used to calculate the decline in hydrostatic pressure in the bridge Δp. Liquid distribution among particles must be established to simulate capillary force in DEM simulations. Muguruma et al. (Muguruma, Tanaka & Tsuji 2000) assumed that liquid can transport among particles and distribute evenly among all gaps than the rupture distance. Conversely, Mikami et al. (Mikami, Kamiya & Horio 1998) considered that liquid is uniformly distributed among particles and liquid movement between particles can be ignored if the viscosity of the liquid is low. By combining these two assumptions, Yang et al. (Yang, Zou & Yu 2003) considered that liquid was uniformly spread and couldn't be transferred between particles by mixing. A liquid bridge is formed when the particle gap is smaller than the rupture distance. The liquid assigned to a particle is equally dispersed among its liquid bridges. The idea of the DEM is to track the trajectory and rotation of each element in a time-stepping simulation and to determine its location as well as orientation followed by computing the interactions between the elements and their surroundings. The element positions could be altered as a result of the interactions. In general, elements are individual particles, but they can also represent clusters.

The fundamental DEM approach for dynamic Newtonian analysis is discussed in the following sections. The positions of particles are first recorded. These are used to determine particle interactions and subsequently used to analyse the following dynamics. Particle positions and velocities are calculated at regular intervals while other calculations such as contact force are only recorded during a contact. When applying DEM to the system, there are several key stages as below:

- Searching the system for all particles and referencing them.
- Calculating forces and moments for all particle–particle and particle–wall interactions using interaction laws.
- Determining particle motion by employing Newton's second law (i.e., accelerations, velocities and positions).

The input parameters for running the simulations could be divided into three categories: the vessel geometrical data, particle physical properties and desired output. The size and shape of the vessel are determined by geometrical data including the number of sections, diameter, height and angle of inclination of each section. Each model defines the position of the walls in relation to a global coordinate system.

CHAPTER III: DEM study and machine learning model of particle percolation under vibration

3.1 Introduction

Granular materials are important to various industries. However, they often consist of particles of different sizes. Many industrial processes involve classification of particles according to size, which has received much research attention (Cleary, PW 2000; Cleary, PW, Wilson & Sinnott 2018; Dong, K et al. 2010; Dong, K & Yu 2012; Feng, YQ & Yu 2007, 2010; Peng et al. 2018). Inter-particle percolation is a basic process that results in segregation of particles of different sizes (Bridgwater, J & Ingram 1971; Bridgwater, J. , Sharpe & Stocker 1969; Zhu et al. 2009). The process of small particles passing through an assembly of larger particles (Tang, P & Puri 2005) is widely encountered in industrial applications for mixing (Bridgwater, J. , Sharpe & Stocker 1969; Takabatake et al. 2018; Tsugeno et al. 2021) and sieving (Soldinger 1999).

Early in the 1970s, mono-size small particles percolating through a packed bed of mono-size large particles was studied by physical experimentation (Scott & Bridgwater 1975). Later, numerical models were also employed and studies were extended to a much wider range of controlling variables in percolation (Bridgwater, J, Cooke & Scott 1978; Bridgwater, J. , Sharpe & Stocker 1969; Zhou, H et al. 2016; Zhu et al. 2009), particularly with the DEM (Cundall & Strack 1979). Percolation velocity was found to be dependent on both particle properties and operational conditions. The key particle property is the size ratio of small to large particles. The size ratio needs to be lower than 0.154 to allow spontaneous percolation under gravity (Bridgwater, J, Cooke & Scott 1978; Zhu et al. 2009). Below this threshold, percolation velocity increases with decreasing size ratio. Other particle properties also affect the percolation velocity including density, restitution coefficient and friction coefficient (Bridgwater, J, Cooke & Scott 1978; Zhu et al. 2009). The distribution of residence time of percolating particles has also been well studied (Bridgwater, J, Cooke & Scott 1978; Bridgwater, J. , Sharpe & Stocker 1969; Rahman et al. 2008; Williams & Shields 1967). Percolating particles have been found to move in the radial direction, which can be modelled as a dispersion process (Zhu et al. 2009). Table 3-1 summarises the effects of controlling variables on percolation found in the literature.

Most previous studies have focused on spontaneous percolation, which is limited by particle size ratio. In fact, vibration is normally used to facilitate particle segregation (Chen, F, Jelagin & Partl 2020; Hudson, Jansen & Linkson 1969; Kudrolli 2004; Qiao, Dong & Duan 2021; Qiao

et al. 2021). Under vibration, voids between large particles in the bed are increased, and the movement of large particles affects the percolation of small particles. Therefore, vibration and spontaneous percolation lead to different percolation behaviours. However, percolation behaviour in a vibrated bed has received limited research attention, so the effects of key variables, including vibration amplitude and frequency, and size ratio, are not yet well understood. Although the segregation of granular particles in mixtures under vibration has been examined (Breu et al. 2003; Dai, B-B et al. 2021; Qiao, Dong & Duan 2021; Qiao et al. 2021; Windows-Yule 2016), many previous studies have focused on analysing segregation parameters, and few have analysed percolation parameters in a vibrated bed.

Table 3-1 List of studies on particle percolation.

Controlling variables	Percolation parameters	Effects
Size ratio	Percolation velocity	Decreases with increasing size ratio (Bridgwater, J, Cooke & Scott 1978; Zhou, H et al. 2016; Zhu et al. 2009) (Hudson, Jansen & Linkson 1969; Kou et al. 2020; Li, J et al. 2010; Rahman et al. 2008)
Particle density		Increases with increasing particle density (Zhou, H et al. 2018) (Lominé & Oger 2009)
Restitution coefficient or damping coefficient		Increases with increasing damping coefficient or decreasing restitution coefficient (Kou et al. 2020; Li, J et al. 2010; Rahman et al. 2008; Zhou, H et al. 2018; Zhu et al. 2009)
Friction		Decreases with increasing friction (Kou et al. 2020; Zhou, H et al. 2016; Zhou, H et al. 2018)
Cohesion		Increases with increasing cohesive force (Zhou, H et al. 2018)
Particle shape		Percolation velocity of cubic particles is lower than that of spherical particles (Kou et al. 2020)
Size ratio	Radial dispersion	Decreases with increasing size ratio (Bridgwater, J. , Sharpe & Stocker 1969; Kou et al. 2020; Rahman et al. 2008)
Particle density		Radial/transverse dispersion decreases, and longitudinal dispersion increases when particle density increases (Hudson, Jansen & Linkson 1969; Lominé & Oger 2009; Zhou, H et al. 2018)
Particle shape		Radial dispersion of cubic particles is lower than that of spherical particles (Kou et al. 2020)

Cohesive force		Increases with increasing cohesive force (Zhou, H et al. 2018)

Machine learning is increasingly being used to model granular systems (Chen, S et al. 2018; He & Tafti 2019; Liao et al. 2021; Zhao, Z et al. 2021). Applications include artificial neural network (ANN) modelling for drag forces (He & Tafti 2019), biological neural network (BNN) modelling for particle distribution on mechanical screens (Zhao, Z et al. 2021), deep learning modelling for granular flow in hoppers (Chen, S et al. 2018) and support vector regression (SVR) for particle flow in rotating drums (Li, Y et al. 2020). These studies show that data models are very effective for complex granular systems, while different models may be suitable for different problems (Chen, S et al. 2018; Li, Y et al. 2020; Liao et al. 2021; Zhao, Z et al. 2021). A major advantage of using data models to predict the collective behaviour of granular particles is that they are much less time-consuming than numerical simulations. However, it is worth noting that data modelling studies largely rely on data obtained by numerical simulations.

The aim of the present study was to model the effects of vibration on particle percolation. The percolation of small particles in a vibrated bed of large particles was examined by using DEM simulations. Percolating particles with size ratios lower and higher than the spontaneous threshold were both considered. The effects of vibration amplitude and frequency on percolation velocity and radial dispersion coefficient were analysed. In addition, the correlations between percolation velocity and velocity amplitude of vibration were investigated. Further, based on the simulation results, machine learning was used to model the percolation velocity as a function of both vibration conditions and size ratio. Using the machine learning model, the percolation threshold size ratios under different vibration conditions were obtained.

The study is organised as follows: Section 3.2 describes the numerical model and simulation conditions; Section 3.3 validates the model by comparing it with experimental studies; Section 3.4 discusses the simulation results and presents the machine learning model for percolation velocity to calculate percolation threshold size ratios under different vibration conditions; and Section 3.5 concludes the study.

3.2 Methodology

3.2.1 Governing equations

In the present study, both spontaneous and vibrational percolation were investigated using DEM simulations. In the DEM, the motion of each particle is governed by Newton's second law (Cundall & Strack 1979). For a spherical particle i, its translational motion and rotational motion are respectively determined by:

$$m_i \frac{d\mathbf{v}_i}{dt} = \sum_j (\mathbf{F}_{ij}^n + \mathbf{F}_{ij}^t) + m_i \mathbf{g} \quad \text{(Eq. 3.1)}$$

$$I_i \frac{d\boldsymbol{\omega}_i}{dt} = \sum_j (\mathbf{M}_{ij} + \mathbf{M}_{r,ij}) \quad \text{(Eq. 3.2)}$$

where $\mathbf{v}_i$ and $\boldsymbol{\omega}_i$ are the translational and angular velocities of particle *i* respectively; m_i and I_i are the mass and moment of inertia of particle *i* respectively; $\mathbf{g}$ is the gravitational acceleration; $\mathbf{F}_{ij}^n$ and $\mathbf{F}_{ij}^t$ are the normal and tangential contact forces respectively. Here, the simplified Hertz–Mindlin and Deresiewicz models are used to calculate these forces as determined by (Langston, Tüzün & Heyes 1995; Zhu, H et al. 2007):

$$\boldsymbol{F}_{ij}^n = \left[(2E/3(1-\tilde{\sigma}^2))\sqrt{\bar{R}}\delta_n^{3/2} - \gamma_n \left(m^*(3E/(1-\tilde{\sigma}^2))\sqrt{\bar{R}}\delta_n^{1/2}\right)^{1/2} \left(\boldsymbol{V}_{ij}.\hat{\boldsymbol{n}}_{ij}\right)\right]\hat{\boldsymbol{n}}_{ij} \quad \text{(Eq. 3.3)}$$

$$\boldsymbol{F}_{ij}^s = -\mu_s \left|\boldsymbol{F}_{ij}^n\right| \left[1 - \left(min\left(\delta_s, \delta_{s,max}\right)/\delta_{s,max}\right)^{3/2}\right]\hat{\boldsymbol{\delta}}_s \quad \text{(Eq. 3.4)}$$

where E is Young's modulus, $\tilde{\sigma}$ is the Poisson ratio, γ_n is the normal damping coefficient, and μ_r and μ_s are the rolling and sliding friction coefficients respectively, δ_n is the relative normal displacement, δ_s is the total tangential displacement $\delta_{s,max}$ is the maximum δ_s when the particles start to slide and $\hat{\boldsymbol{\delta}}_s$ is its unit vector; $\bar{R} = R_i R_j/(R_i + R_j)$, where R_i and R_j are the radii of the two particles respectively; $m^* = m_i m_j/(m_i + m_j)$; $\delta_{s,max} = \mu_s[(2-\tilde{\sigma})/2(1-\tilde{\sigma})]\delta_n$ and $\hat{\boldsymbol{n}}_{ij} = (\boldsymbol{R}_i - \boldsymbol{R}_j)/|\boldsymbol{R}_i - \boldsymbol{R}_j|$.

In Eq. (Eq. 3.2), $\mathbf{M}_{ij}$ is torque resulting from the contact force, and $\mathbf{M}_{r,ij}$ is the rolling resistance torque between two contact particles caused by elastic hysteretic losses or viscous dissipation, which can be determined by:

$$\mathbf{M}_{r,ij} = -\mu_{r,ij} R_i \left| \boldsymbol{F}_{ij}^{n} \right| \hat{\boldsymbol{\omega}}_i \qquad \text{(Eq. 3.5)}$$

where $\hat{\boldsymbol{\omega}}_i = \boldsymbol{\omega}_i / |\boldsymbol{\omega}_i|$. Further details can be found in (Zhou, YC et al. 1999; Zhu, H et al. 2007). In this work, only dry coarse particles are considered, hence the van der Waals force and capillary force are not included.

Particle and wall interactions can also be calculated with the above equations (Eq. 3.3 and (Eq. 3.4), in which the equivalent radius of the wall is regarded as infinitely large. The wall is modelled as a plane with the same material properties as the particles. Under vibration, the position and velocity of the wall are updated at every timestep, and the values are used to calculate particle–wall interactions. The time step is determined by $dt = 0.1\sqrt{m/k}$, where m is the mass of a particle and k is the estimated spring constant when the normal overlap is 10% of the particle diameter. This is based on the natural period of oscillation of the equivalent spring when using the Hertz contact force model (Hertz 1882). In a multi-size system, the time step is calculated for each type of particle and the minimum time step is used. Simulations were conducted using the university in-house DEM program, which has been validated for various systems (Amirifar et al. 2018, 2019; Dong, K, Wang & Yu 2013).

3.2.2 Simulation conditions

The setup used in the simulations is shown in Figure 3-1, which consists of a packed bed of large spherical particles and small spherical percolating particles. It should be noted that in simulating spontaneous percolation, and to be consistent with the experimental study, the large particles were packed into a cylindrical container (Bridgwater, J & Ingram 1971). Further, in simulating percolation in a vibrated bed, the periodic boundary conditions were used along x and y axes to avoid possible convection resulting from vibration, which can cause abrupt changes of segregation in vibrated beds (Qiao, Dong & Duan 2021; Qiao et al. 2021).

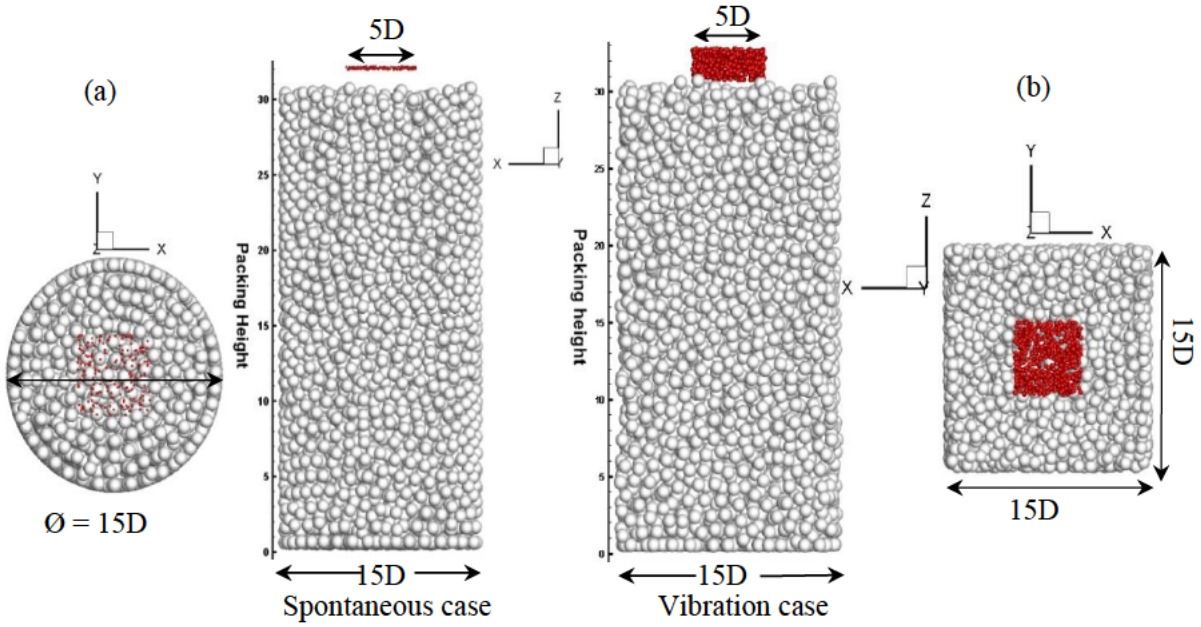

Figure 3-1 Schematics of the models for percolation in: (a), static bed; and (b), vibrated bed.

The simulation process is shown in Figure 3-2. First, large particles were randomly generated and settled under gravity to form a high packed bed. Second, small (i.e., percolating) particles were randomly generated on top of the packed bed. In simulating spontaneous percolation, the packed bed was static. In simulating percolation under vibration, the bed was vibrated at 0.70 s. The vibration applied to the bottom wall was a sinusoidal vertical vibration governed by $z = A\sin(2\pi ft)$. During a simulation, the position, velocity and forces on each particle were recorded every 0.01 s. After a small particle had passed through the packed bed, it was removed and recorded for later analyses. It is worth noting that a small number of particles may become jammed in the bed and not pass even after a long time, especially in spontaneous percolation.

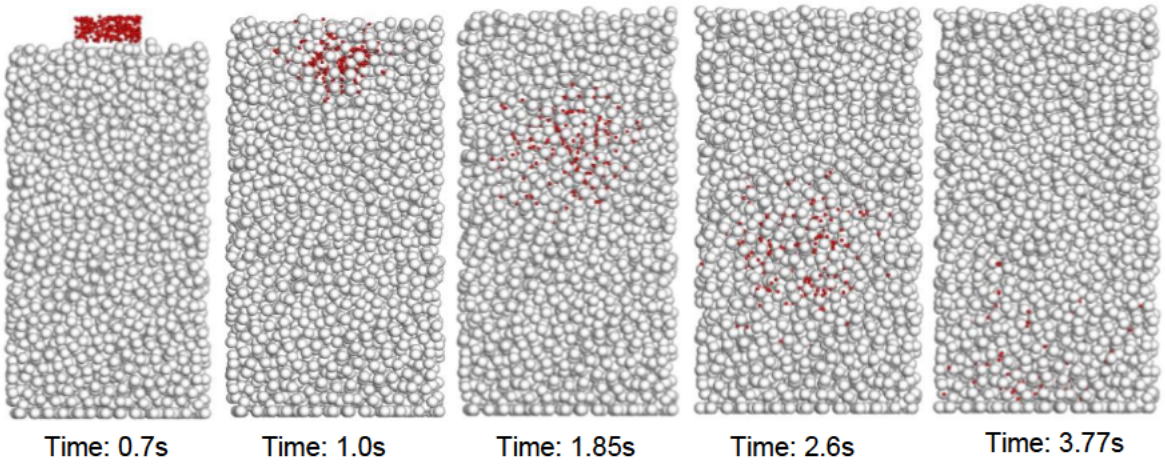

Figure 3-2 Snapshots of the simulated percolation process under vibration, where A= 0.10D, f = 15.0Hz and d/D = 0.17.

The simulation conditions are listed in Table 3-2. Although not specifically discussed here, the material properties are the same as those used in previous studies (Amirifar et al. 2018, 2019) including studies that used the same contact force model (Zhou, Z-Y et al. 2011). Briefly, the particle parameters are largely based on those of glass beads and have been previously calibrated by comparing experimental packing fractions and coordination numbers of static and vibrated beds consisting of spherical particles (Amirifar et al. 2019; An et al. 2016; An et al. 2021; Dong, K, Wang & Yu 2016; Tian, Dong & Yu 2014; Yi et al. 2011) and non-spherical particles (Arifuzzaman et al. 2020; Dong, K, Wang, C & Yu, A 2015; Kildashti, Dong & Samali 2019; Wang, C, Dong & Yu 2015). Notably, because the present work focuses on the effects of vibrational conditions and size ratio, other material properties are kept constant (unless reproducing specific experiments). The effects of material properties found in previous studies are summarised in Table 3-1.

Table 3-2 Parameters used in DEM simulations.

Simulation parameter	Value
Large particle size, D (cm)	1.17
Number of large particles, N_D	5000
Percolate particle size, d (cm)	0.05–0.30
Percolate particles number, N_0	500

Young's modulus, E (kg/(cm/s^2))	1e^7
Density of particle, ρ (kg/m^3)	2980 (Ballotini spheres (Hudson, Jansen & Linkson 1969))
Sliding friction coefficient, μ_s	0.3
Rolling friction coefficient, μ_r	0.0001
Damping coefficient, γ_n	0.3
Vibration amplitude, *A/D*	0.01–1.5
Vibration frequency, *f* /Hz	1, 5, 10, 15, 20, 30, 35
Size ratio, *d/D*	0.043–0.256

3.3 Model validation

3.3.1 Spontaneous percolation

To validate the DEM model, simulations were first performed under similar conditions to the spontaneous percolation experiments conducted by Bridgwater et al. (Bridgwater, J & Ingram 1971): packed bed ~31 cm in height, large particle number (N_D) = 4000, large particle diameter (D) =1.17 cm, small particle number (N_0) = 171 and small particle diameter (d) = 0.08 cm. As percolating particles of different materials were used in the experiments, in simulations different densities were used for the percolating particles in different cases. The normal damping coefficient was also calibrated to match the restitution coefficient determined in the experimental study (see Table 3-3).

The dimensionless percolation velocity, according to the experimental study, was defined as:

$$V_p = \frac{\langle v_{p,i} \rangle}{\sqrt{gD}} \qquad \text{(Eq. 3.6)}$$

where $v_{p,i}$ is the mean velocity of a percolating particle passing through the packed bed, g is the gravitational acceleration and D is the diameter of the large particles. V_p is the mean value of $v_{p,i}$.

Table 3-3 Simulation conditions for spontaneous percolation.

Experiment number	Percolating particles material	Density (kg/m^3)	Coefficient of restitution	Normal damping coefficient
S1	Steel	7850	0.92	0.035
S2	Iron	7874	0.88	0.05
S3	Glass	2500	0.84	0.089
S4	Resin	1080	0.69	0.12
S5	Lead	11350	0.19	0.41

The simulated and measured percolation velocities are compared in Figure 3-3. For each case, simulation was repeated three times and the mean value was used. The errors of the simulation were small (see error bars in Figure 3-3). Further, the simulated V_p was generally in agreement with the experimental data for different percolating particles (Figure 3-3). The two points with relatively large deviations may be because the effects of other material properties, such as the sliding friction coefficient and rolling friction coefficient (Li, J et al. 2010; Zhou, H et al. 2016; Zhu et al. 2009). Previous studies have shown that these properties affect percolation; however, not in experimental study (Bridgwater, J & Ingram 1971). Similarly, large deviations for one or two points have been reported in other numerical studies (Li, J et al. 2010).

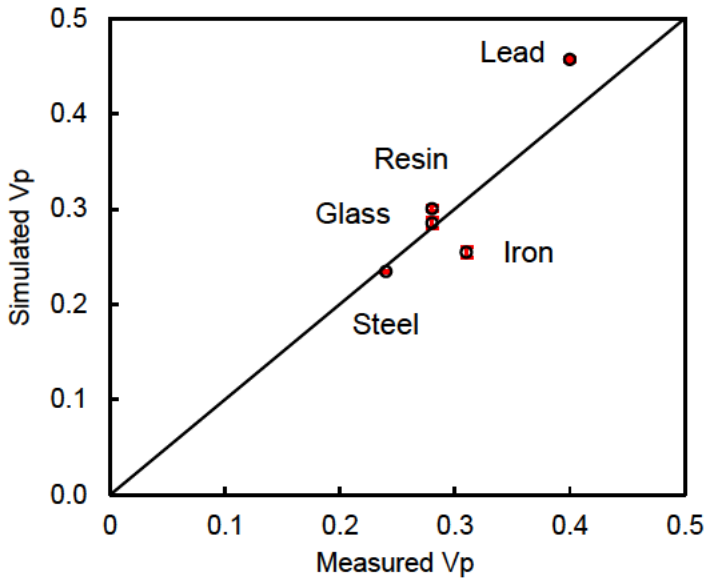

Figure 3-3 Simulated percolation velocity versus measured percolation velocity in Ref (Bridgwater, J & Ingram 1971). Simulation conditions for different cases are listed in Table 3-3.

3.3.2 Brazil-nut and reverse Brazil-nut segregations under vibration

The model was also used to simulate segregation experiments, like those conducted by Breu et al. (Breu et al. 2003), in which granular mixtures of two types of particles with different sizes and densities were vibrated and Brazil-nut or reverse Brazil-nut segregation was obtained for different mixtures. In the present study, two experiments were simulated using the DEM program, as shown in Figure 3-4. Using the experimental conditions for Brazil-nut segregation, the simulation demonstrated exactly the Brazil-nut segregation; while using the experimental conditions for the reverse Brazil-nut segregation, the simulation demonstrated exactly the reverse Brazil-nut segregation. The two simulations using the DEM program matched well with the experimental results, and comparisons between different scenarios demonstrated the validity of the DEM program. For validation of the vibration case, the DEM program (Amirifar et al. 2018) was validated by an experimental study that focused on self-assembly of granular spheres under vibration. Moreover, the DEM program has also been successfully used in various other studies including on packing (Zhou, Z-Y et al. 2011), sedimentation (Dong, K, Yu & Brake 2009), screening (Dong, K, Yu & Brake 2009), mixing (Halidan et al. 2018), burden distribution (Liu, S et al. 2015) and screw feeding process (Li, X et al. 2020).

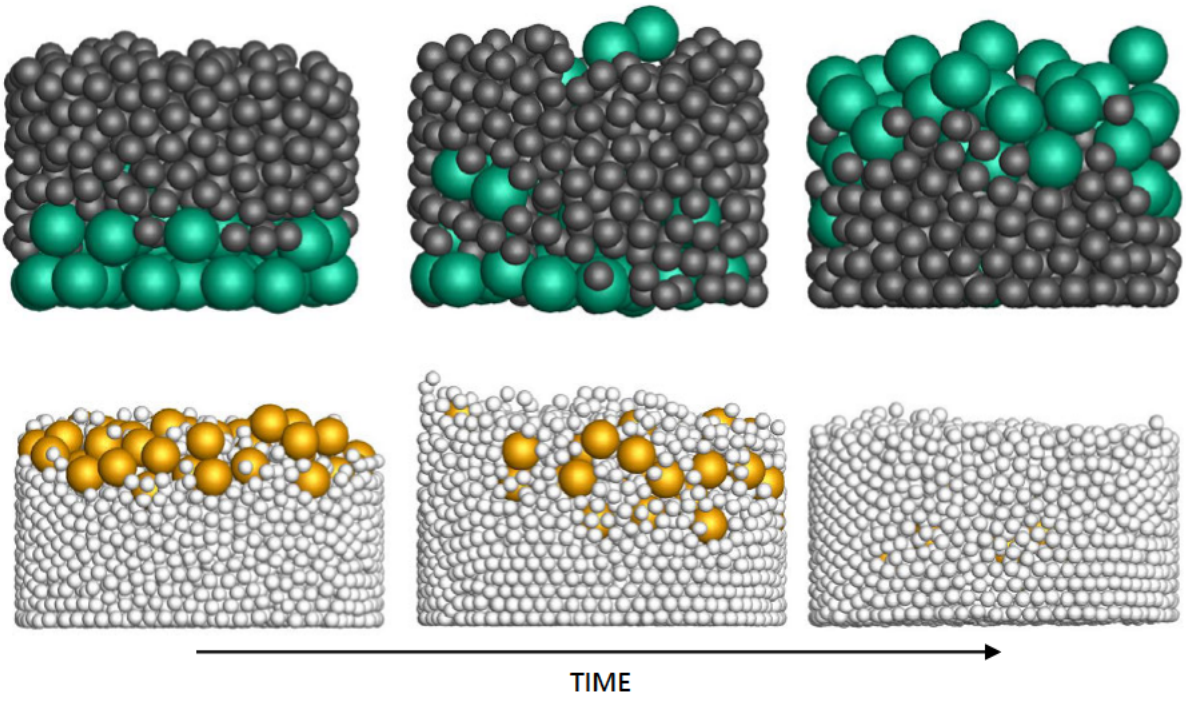

Figure 3-4 Temporal evolution of the simulated vibrated binary mixtures based on experiments by Breu et al. (Breu et al. 2003): (a), a mixture of 8 mm glass beads (density: 2500 kg/m^3) and 15 mm polypropylene beads (density: 1500 kg/m^3), which shows the Brazil-nut segregation after vibration (A = 4mm, f = 20Hz); (b), a mixture of 10 mm bronze spheres (density: 8900 kg/m^3) and 4 mm glass beads (density: 2500 kg/m^3), which shows the reverse Brazil-nut segregation after vibration (A = 2mm, f = 30Hz).

3.4 Results and discussion

3.4.1 Effects of controlling variables on percolation velocity

As discussed above, percolation velocity is a function of a number of variables even in a static packed bed (Bridgwater, J & Ingram 1971; Li, J et al. 2010; Rahman et al. 2008; Zhu et al. 2009). The present work focuses on the effects of vibration conditions with different size ratios (d/D).

3.4.1.1 Percolating particles with *d/D* lower than spontaneous percolation threshold

First, the effect of vibration on percolation was studied with d/D much lower than the spontaneous percolation threshold of 0.154. Figure 3-5a and Figure 3-5b show the variations of V_p with changes in vibration frequency (f) and amplitude (A) respectively, for d/D = 0.085. Figure 3-5a shows that under a constant (A), there is a slight increase of V_p when f is just above 0. However, when f > 5 Hz, V_p decreases with increasing f, showing an adverse effect of high f. Similar results can be found in Figure 3-5b: after A > 0.01 D, V_p decreases monotonically with increasing A. This is in accordance with previous studies in low-head screens, in which sieving performance decreased with an increase of vibration amplitude or frequency in the vertical direction (Dong, K & Yu 2012). Percolating particles are also affected by vertical vibration and may have more upwards movement than in a static bed. It is worth noting that the results of the present study show fluctuations, which is a common feature of properties of vibrated particle beds (Amirifar et al. 2018; Qiao, Dong & Duan 2021), indicating certain disordered behaviours of granular particles under vibration.

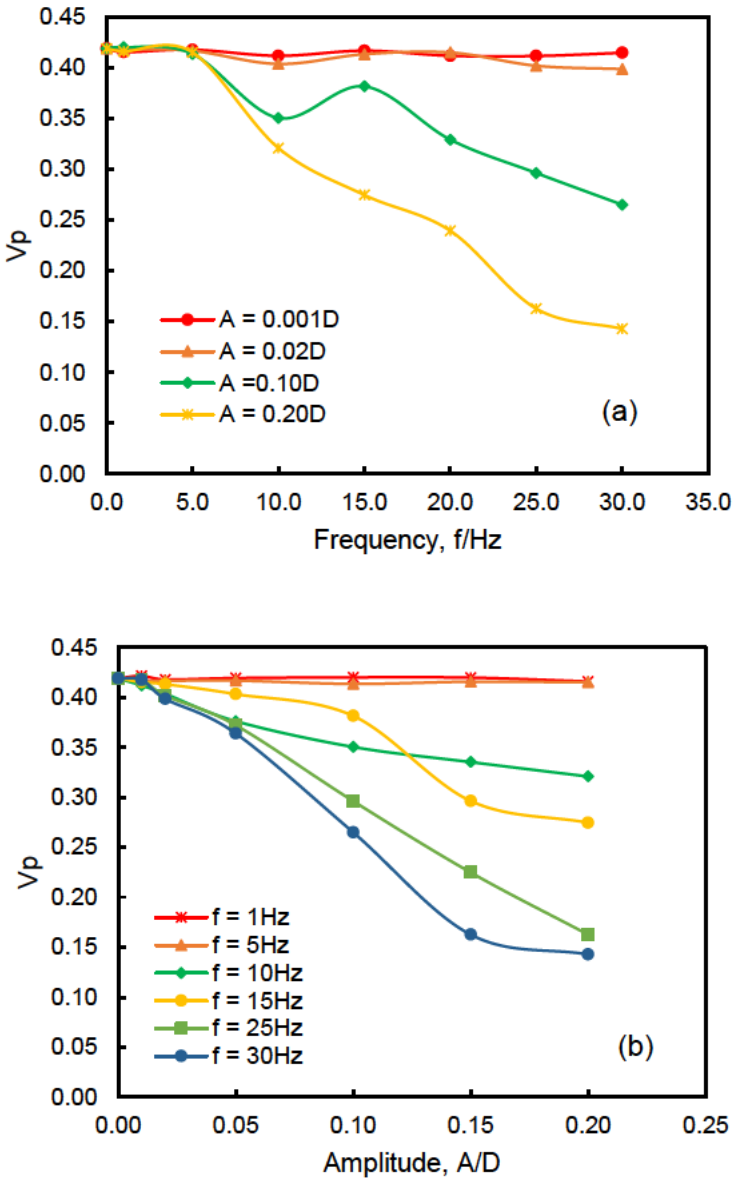

Figure 3-5 Percolation velocity as a function of: (a) vibration frequency and (b) vibration amplitude, with $d/D = 0.085$.

Figure 3-6 illustrates V_p as a function of the velocity amplitude V_b for $d/D = 0.085$. The results with the same f are plotted with the symbols of the same shape. The velocity amplitude V_b is a dimensionless parameter, determined by $V_b = 2\pi(\frac{A}{D})f\sqrt{\frac{D}{g}}$. This parameter has been found to be related to structural changes in vibrated beds (Amirifar et al. 2018, 2019; Tai & Hsiau 2004). Velocity amplitude has also been found to be related to the segregation degree and velocity in vibrated beds (Qiao, Dong & Duan 2021; Qiao et al. 2021). Therefore, velocity amplitude is investigated in the present study. Figure 3-7 shows that all the data points nearly fall on one

curve, indicating that under a given d/D, V_p can be effectively correlated with V_b as the combined effects of A and f. Again, some points show relatively higher deviations from the fitted line. These disordered behaviours thus cause the complex behaviours of percolating particles.

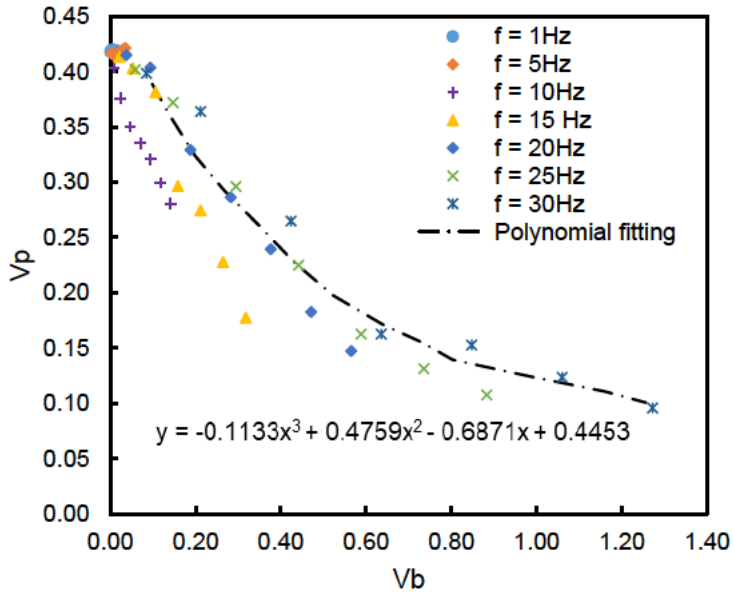

Figure 3-6 Percolation velocity as a function of V_b (d/D = 0.085).

Figure 3-7 further demonstrates the comprehensive dependence of V_p on A and f under d/D = 0.085. The contour plot can be approximately divided by different curves corresponding to different V_b, which confirms that V_p can be reasonably correlated with V_b under d/D = 0.085. It is worth noting that V_p remains the highest in a small range of low A and f, which is close to that of spontaneous percolation.

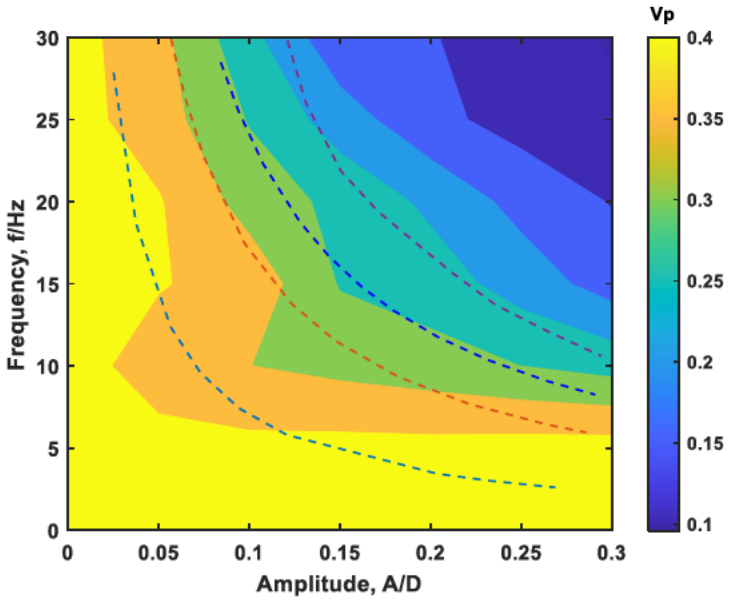

Figure 3-7 Percolation velocity as a function of vibration amplitude and frequency with $d/D = 0.085$. Curves are hyperbolas defined by $V_b = 0.152$, $V_b = 0.37$, $V_b = 0.52$ and $V_b = 0.74$ respectively, from left to right.

3.4.1.2 Percolating particles with *d/D* higher than the spontaneous threshold

Figure 3-8 shows the variation of V_p against V_b for $d/D = 0.171$. As d/D was higher than the spontaneous threshold, small particles had difficulty percolating without vibration. Therefore $V_p = 0$ when $V_b = 0$. However, with a slight increase of V_b, V_p increased dramatically to the maximum and then decreased with further increasing V_b. Interestingly, different series of data with different A can also fall on one curve, which indicates that V_b can still be an effective parameter to correlate V_p for this d/D. However, the correlation is different from that of $d/D = 0.085$, as shown in Figure 3-5. The data are more scattered when V_b is small and V_p is near the highest value, showing that the effect of vibration is more complex in this region. Generally, the results show that to facilitate percolation of particles with a size ratio just higher than the spontaneous threshold, vertical vibration with V_b lower than 0.15 can be effective. However, vibration that is too strong decreases the percolation velocity, which is similar to the discussion above.

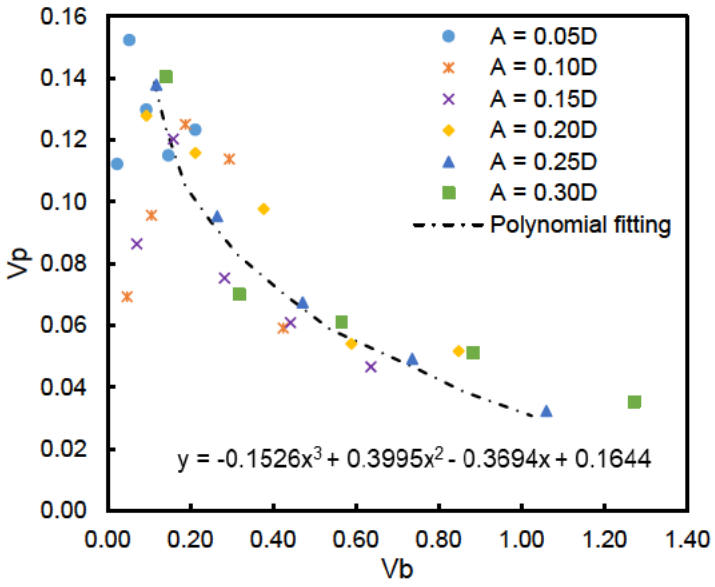

Figure 3-8 Percolation velocity as a function of V_b, with $d/D = 0.171$.

Figure 3-9 shows V_p as a function of A and f together under $d/D = 0.171$. When A and f are both high, the contour plot can still be approximately divided by curves of different V_b. However, when either A or f is small, the maximum V_p regions appear in the low A and high f region and the low f and high A region. Note that there is a non-percolation region in the figure where $V_p = 0$. According to the figure, for this size ratio, the favourable vibration conditions for percolation are low A and medium f.

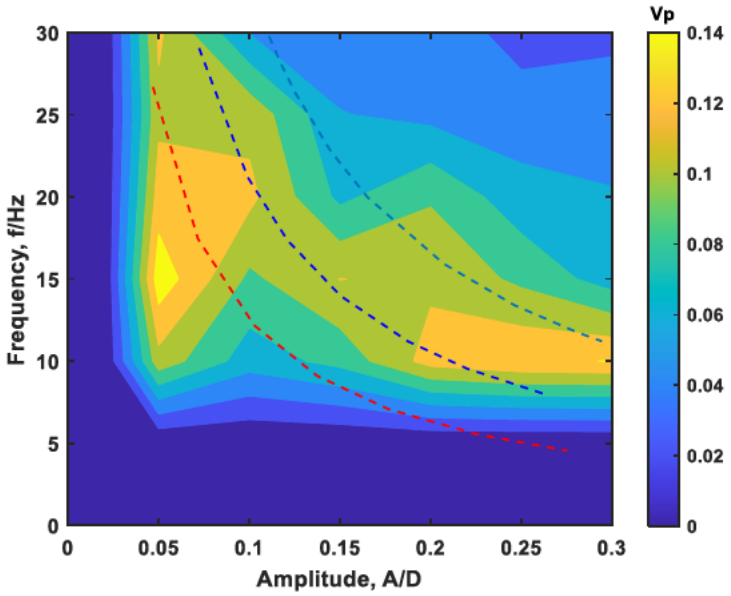

Figure 3-9 Percolation velocity as a function of A and f, with $d/D = 0.171$. Curves are hyperbolas defined by $V_b = 0.27$, $V_b = 0.46$ and $V_b = 0.72$ respectively, from left to right.

For even larger percolating particles with d/D = 0.256, it was found that particles cannot percolate when either A or f is too low. At higher A and f, particles may percolate, but the vibrated bed can be fluidised, so V_p fluctuates significantly with the changes of A and f. This indicates that if d/D is too high, vertical vibration is not an effective way to help percolate particles. Extreme fluctuation of the data render the effects of A and f on V_p not meaningful and hence they are not discussed here.

To compare the effects of vibration conditions on different sized percolating particles, Figure 3-10 plots V_p as a function of A or f for different size ratios. Figure 3-10 further shows that the effect of vibration is different for different size ratios. If d/D is lower than the spontaneous threshold of 0.154, increasing A or f generally decreases V_b, although a slight increase may be achieved at very low A and f. On the contrary, if d/D is higher than 0.154, certain A and f are required to enable percolation, but too high A or f causes V_b to decrease again. Even with proper vibration, V_p is still dominated by d/D, that is, if d/D is higher than 0.154, vibration cannot increase V_p to a comparable value to if d/D is lower than 0.154, and the effects of A and f on V_p are rather small when d/D reaches 0.214.

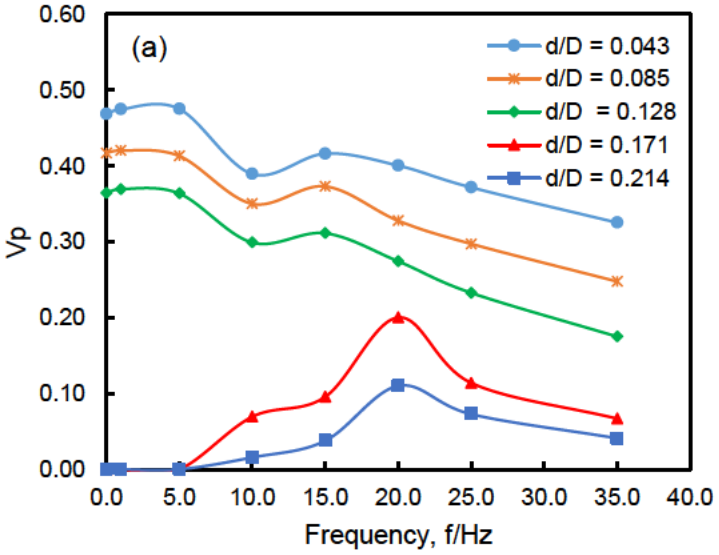

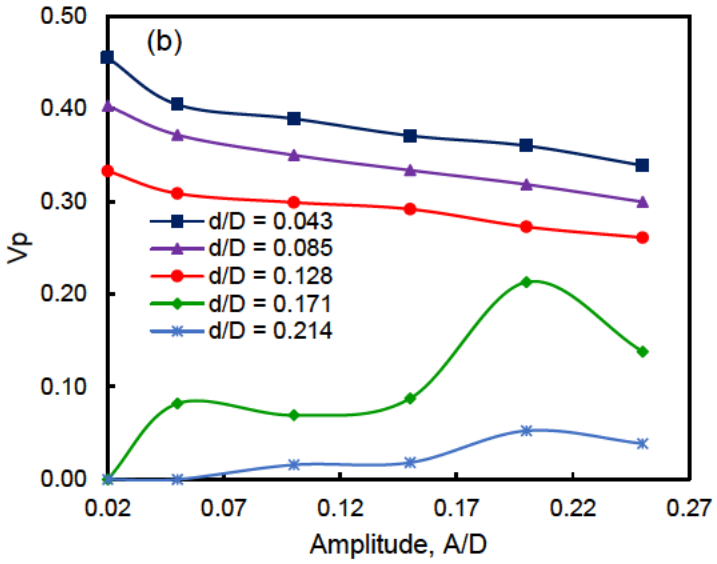

Figure 3-10 (a), Percolation velocity against vibration frequency at different size ratios with A=0.1D; (b), percolation velocity against vibration amplitude at different size ratios with f=10Hz.

3.4.2 Effects of variables on radial dispersion during percolation

As discovered in spontaneous percolation (Bridgwater, J. , Sharpe & Stocker 1969), percolating particles also disperse radially when falling through the packed bed. Radial dispersion can be described by:

$$\frac{r^2}{4E_r\Delta t} = \ln\left(\frac{N_0}{N_0 - N}\right) \qquad \text{(Eq. 3.7)}$$

where E_r is the radial dispersion coefficient, N_0 is the total number of percolating particles and N is the number of percolating particles that have centres within radius r at percolation time Δt.

Figure 3-11 illustrates the radial distribution of percolating particles on the XY plane at different times. At $\Delta t = 0s$, particles start to percolate and are concentrated in the centre region. With increasing time, particles gradually move away from the centre, showing radial dispersion.

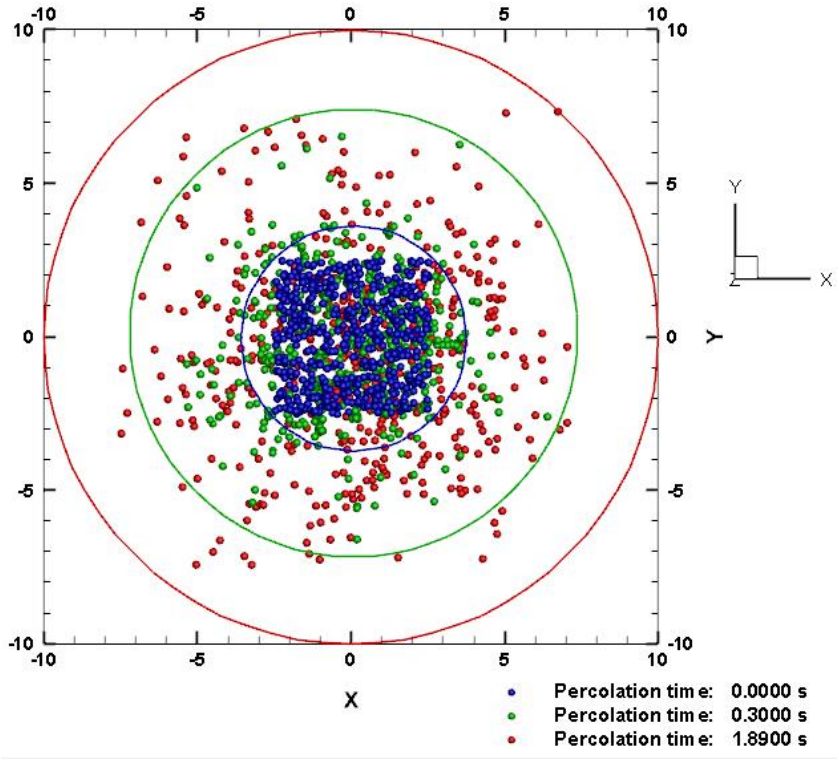

Figure 3-11 Radial dispersion of percolating particals (f =10 Hz, d = 0.1 D, A = 0.1 D), where blue particles and cycle are for Δt = 0s, green particles and cycle for Δt = 0.3s, and red particles and cycle for Δt = 1.89s. The three cycles enclose all particles at the corresponding times respectively.

If the radial dispersion model is observed, the plot of r^2 versus $\ln[N_0/(N_0-N)]$ will be a straight line with a gradient of $4E_r\Delta t$ (Bridgwater, J. , Sharpe & Stocker 1969), where r is the radius of the circular region on the XY plane enclosing all percolating particles at Δt. Then the radial dispersion coefficient can be calculated using (Eq. 3.7. Figure 3-12 shows r^2 versus $\ln[N_0/(N_0-N)]$ under different vibration conditions, which indicates that the radial dispersion model is still applicable to particle percolation in a vibrated bed, while dispersion is obviously affected by the vibration conditions. Here, Δt = 1.89 s is used for all cases.

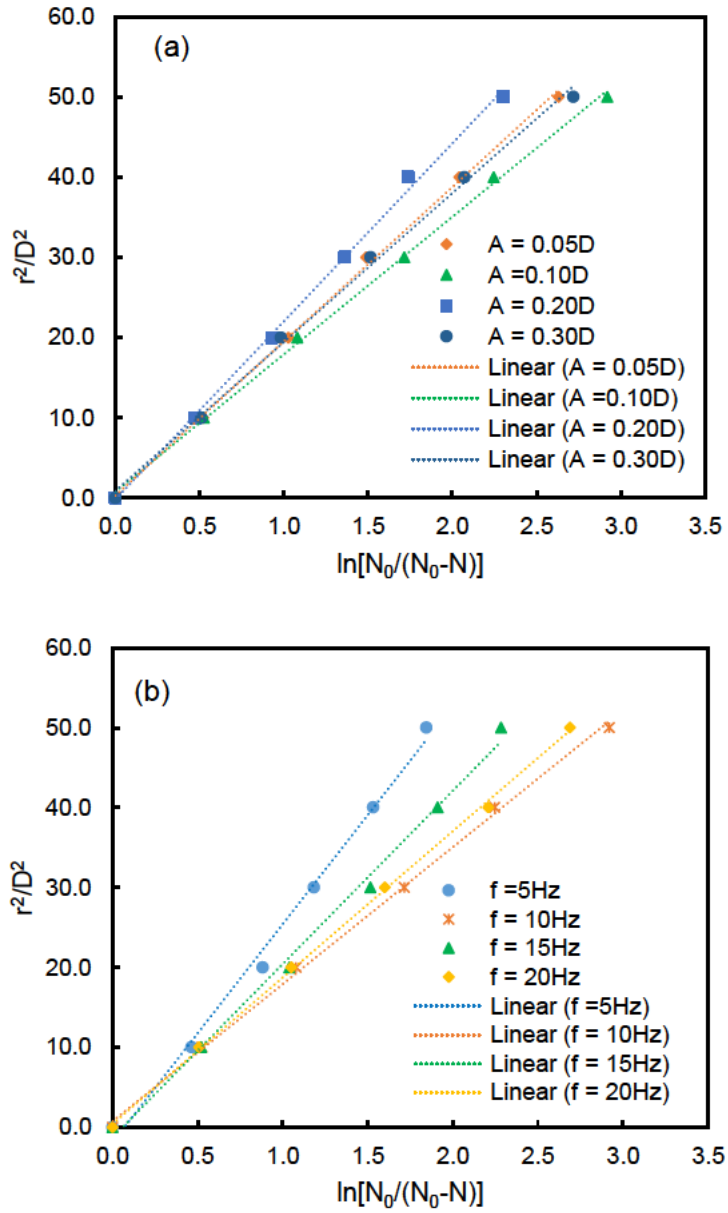

Figure 3-12 r^2 versus ln[N0/(N0-N)]: (a), under different A when f = 10 Hz, d/D=0.085; and (b), under different f when A = 0.10D, d/D = 0.085.

Figure 3-13 (a) shows the radial dispersion coefficient (E_r) at different vibration conditions. E_r for spontaneous percolation is 1.79 cm^2/s for d/D = 0.085, while it is generally higher under vibration, as shown Figure 3-13. However, E_r decreases with increasing f when f is small, which shows that at this stage, increasing vertical vibration can suppress the radial dispersion. But after f increases over 10 Hz, E_r fluctuates with the further increase of f. If vertical vibration is relatively strong, it may also induce significant radial movements of large particles (shown in supplementary information), hence the radial dispersion of small particles may also be

increased with the collisions of large particles. This finding indicates that in a screening process, vertical vibration may be helpful to the fast dispersing of small undersize particles (Dong, K & Yu 2012).

Figure 3-13 (b) shows E_r for percolating particles of different size ratios. E_r is generally lower for percolation particles of larger sizes, while when d is above 0.1D, E_r does not decrease significantly with the further increase of d. A higher f can increase E_r only when d is very small. This finding indicates that very small size particles in the screen process may disperse much faster than other particles, which may result in the complicated variation of the particle size distribution in the packed bed on the screen (Dong, K & Yu 2012).

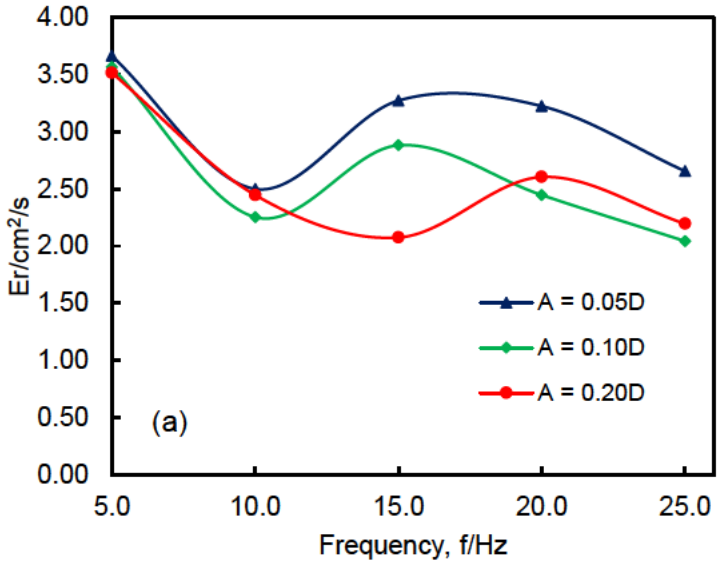

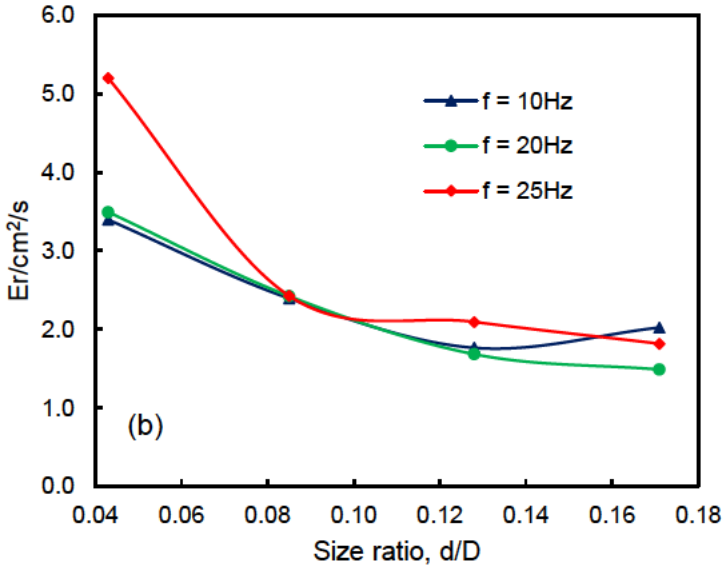

Figure 3-13 Radial dispersion coefficient as a function of: (a), vibration amplitude under different vibration frequency when d/D = 0.085; and (b), particle size ratio under different vibration frequencies when A = 0.1D.

Since percolation velocity and radial dispersion represent the movments of percolating particles along the vertical and horizontal directions respectively, their correlations are further investigated. As shown in Figure 3-14 (a), E_r generally increases with increasing V_p, showing that the movements of particles along different directions are largely correlated. However, when V_p is smaller than 0.3, E_r does not have a clear correlation with V_p. In the above discussion it has been known that V_p normally is small when vibration is too strong. Under such condition, the vibrated particles may move more isotropically and thus E_r increases more significantly. Interestingly, in Figure 3-14 (b), E_r shows a similar correlation with V_p for different size ratios. Generally, a lower d/D results in a higher E_r, which agrees with that of the spontaneous percolation (Bridgwater, J. , Sharpe & Stocker 1969; Rahman et al. 2008). In addition, under small d/D, percolating particles have both higher V_p and E_r; whereas when d/D is close or even higher than the spontaneous threshold of 0.154, E_r remains low. This further indicates that in a screening process, vertical vibration is effective to disperse small undersize particles, but it is not effective to disperse relatively large undersize particles.

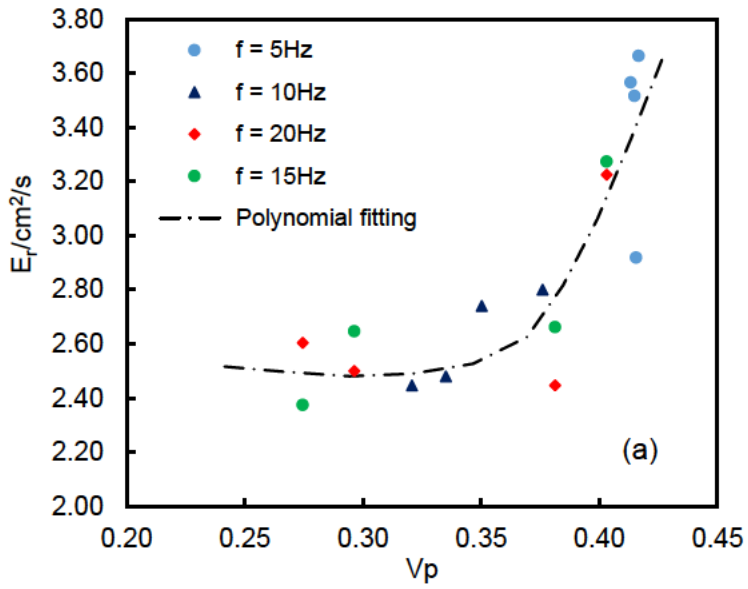

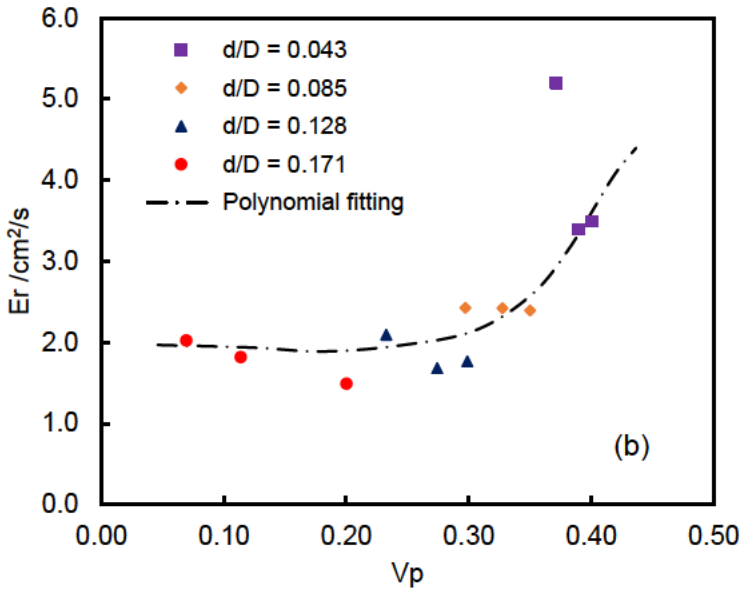

Figure 3-14 Radial dispersion coefficient as a function of percolation velocity with (a), d/D = 0.085, and (b), A = 0.10D. Data points are obtained under different vibration frequencies and amplitudes.

3.4.3 Modelling percolation velocity by machine learning

The above results show that percolation velocity has complex dependence on vibration amplitude and frequency and particle size ratio, which is not easily modelled by conventional means. For example, in Figure 3-6 and Figure 3-8 it can be seen that the polynomial fitting equations between V_b and V_p are rather different with different size ratios. Hence, machine learning was exploited to model V_p as a function of A, f and d/D together. There were, in total, 291 cases used for training machine learning models available in MATLAB. To develop a data model, the data are normally randomly split for training and testing. Different ratios can be used to divide the data but in general the training data should be larger than the testing data. To guarantee accuracy of the model while avoiding over-fitting, a commonly used ratio is 70% for training and 30% for testing (Efron & Tibshirani 1997; Nguyen et al. 2021; Toleva 2021). The root mean square error (RMSE) values for different machine learning models are listed in Table 3-4. The best RMSE score among the models was 0.032027 for the Gaussian process regression (GPR) model with exponential kernel. There was good agreement between the predicted results with the training GPR model and the simulated results of the testing cases (Figure 3-15). It is worth noting that a number of cases with V_p = 0 were included in the training data to effectively set the boundary of the model.

Table 3-4 Performance of the machine learning models for percolation velocity.

Machine learning model	RMSE
Linear regression	0.10424
Interaction linear regression	0.07837
Robust linear regression	0.10593
Stepwise linear regression	0.077992
Rational quadratic GPR	0.033167
Squared exponential GPR	0.3246
Matern 5/2 GPR	0.034696
Exponential GPR	0.032027
Linear SVM	0.10843
Quadratic SVM	0.081038
Cubic SVM	0.065501
Fine Gaussian SVM	0.065503
Medium Gaussian SVM	0.050047
Coarse Gaussian SVM	0.089968

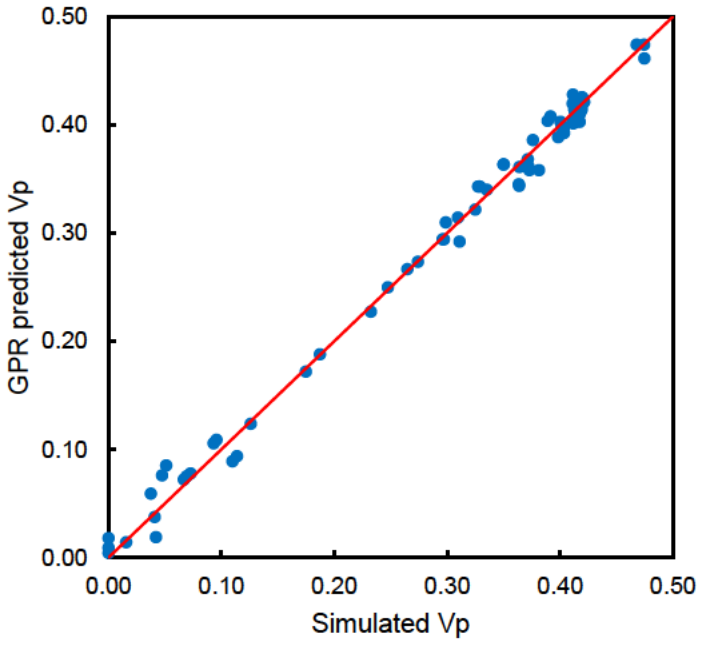

Figure 3-15 Gaussian process model (GPR) predicted percolation velocity versus simulated percolation velocity for the testing cases (30%). The GPR model is trained by using 70% simulation cases.

In brief, GPR models are nonparametric, kernel-based, probabilistic models for supervised machine learning. A GPR model addresses the question of predicting the value of a response variable y_{new}, given new input vector x_{new}, and the training data $\{y=f(x), x\in\mathbb{R}^d\}$, which is assumed to be a Gaussian process with zero mean function and covariance function $k(x, x')$. A GPR model then considers the following equation:

$$y = h(x)^T\beta + f(x) \quad \text{(Eq. 3.8)}$$

where $h(x)$ is a set of basic functions that transform the original feature vector x in $\mathbb{R}^d$ into a new feature vector $h(x)$ in $\mathbb{R}^p$, and β is a vector of coefficients. Then, an instance of response y can be modelled as:

$$P(y_i|f(x_i), x_i) \sim N(y_i|h(x_i)^T, \beta + f(x_i), \sigma^2) \quad \text{(Eq. 3.9)}$$

where σ^2 is the noise variance, and the covariance function is usually parameterised by a set of kernel parameters θ, so $k(x, x')$ is often written as $k(x, x'|\theta)$. The exponential covariance kernel function used in the GPR is determined by:

$$k(x_i, x_j|\theta) = \sigma_f^2 \exp\left(-{}^{r_{ml}}/_{\sigma_l}\right) \quad \text{(Eq. 3.10)}$$

where $r_{ml} = \sqrt{(x_i - x_j)^T((x_i - x_j)}$.

The expected value of prediction y_{new} at a new point x_{new} given y, X and parameters β, θ and σ^2 can be determined by (Rasmussen & Williams 2006):

$$y_{new} = h(x_{new})^T\beta + \sum_{i=1}^{n} \alpha_i\, k(x_{new}, x_i|\theta) \quad \text{(Eq. 3.11)}$$

where $\alpha = (K(X, X|\theta) + \sigma^2 I_n)^{-1}(y - H\beta)$. A detailed algorithm of the model can be found in the MATLAB document (MATLAB 2021a).

It is worth noting that other machine learning models can also be used to model segregation and vibration behaviours of granular particles. The machine learning model selected here was chosen because of its good performance with the data.

3.4.4 Application of GPR model: effect of vibration conditions on percolation threshold

As discussed above, the percolation threshold size ratio is d/D = 0.154 for spontaneous percolation; however, with vibration particles larger than 0.154D can also percolate. It is interesting to know how the threshold changes with vibration conditions. Using the GPR model, V_p can be more easily predicted as a function of d/D under given vibration amplitude and frequency, as shown inFigure 3-16. Here, all the simulated results were added to the training set to improve the accuracy of the GPR model.

For spontaneous percolation where A = 0 and f = 0, V_p decreases with increased d/D, and reaches zero when d/D = 0.154. Therefore, 0.154 is the spontaneous percolation threshold. By applying the same concept to percolation in a vibrated bed, given A and f, V_p also generally decreases with increased d/D and reaches zero at a certain value, which can be regarded as the percolation threshold (Figure 3-16). In practice, however, it is difficult to obtain exact zero V_p in the machine learning model. Therefore, here, the value of d/D corresponding to V_p = 0.01 was considered the percolation threshold under such vibration conditions.

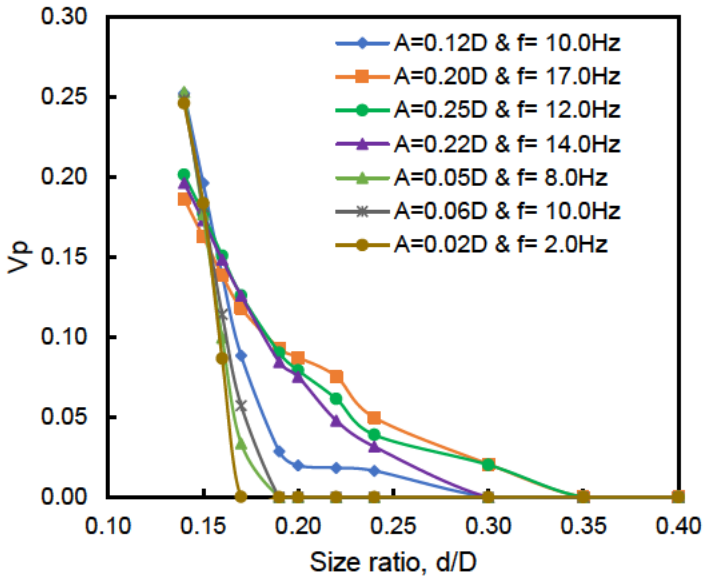

Figure 3-16 Percolation velocity as a function of size ratio (d/D) under different vibration conditions, predicted by the trained GPR model.

By using the trained GPR model, threshold size ratios with a matrix of A ={0.02, 0.04,0.05, 0.07, 0.08, 0.09, 0.10, 0.13, 0.15}(unit: D) and f={ 1, 3, 5, 7, 8, 9, 12, 14, 15}(unit: Hz) were calculated, and the results are shown in Figure 3-17. It is evident that increasing vibration enabled percolation of particles larger than 0.154 D. Moreover, with the contours of the threshold size ratio as a function of A and f, the vibration conditions for percolating particles of a particular size ratio can be easily identified, which may guide related operations. It is worth noting that the effects of other material properties could be included in the model, although in the present work the focus is the effect of vibration.

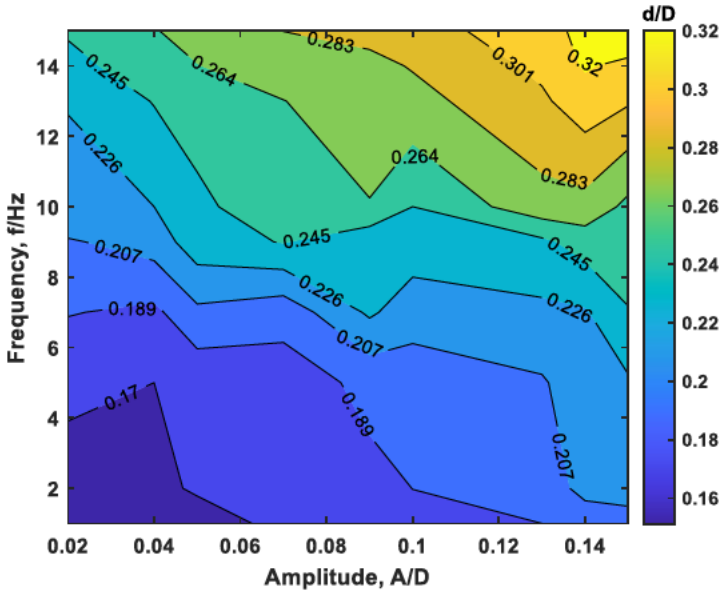

Figure 3-17 Percolation threshold size ratio as a function of vibration amplitude and frequency, based on the results predicted by the trained GRP model.

3.5 Conclusions

In the present study, percolation of small particles through a packed bed of large particles under sinusoidal vertical vibration was investigated using a validated DEM model. The effects of vibration amplitude (A) and vibration frequency (f) on the percolation of particles with different size ratios (d/D) was studied in terms of percolation velocity (V_p) and radial dispersion. Machine learning was used to model percolation velocity on the basis of the DEM data. The major conclusions drawn are as follows:

- For *d/D* smaller than the spontaneous threshold of 0.154, vertical vibration has an adverse effect on percolation and V_p decreases with increasing *A* and *f*. For *d/D* slightly larger than 0.154, vertical vibration can enable percolation that does not occur spontaneously. However, V_p increases with increasing *A* and *f* only when their values are relatively small. When *A* and *f* increase beyond certain values, V_p decreases with further increase of *A* and *f*.
- Under a given *d/D*, V_p can be reasonably correlated with vibration velocity amplitude V_b, though the data shows certain fluctuations. The contour plot of V_p as a function of *A* and *f* can more comprehensively identify optimised vibration conditions for percolation velocity. Conversely, the contour plot also demonstrates that the dependency of V_p on the controlling variables is complex and not easily modelled by conventional methods.
- The radial movement of percolating particles in the vibrated bed follows the radial dispersion model established for spontaneous percolation. Similar to the effects of vibration conditions on V_p, radial dispersion can be increased by vertical vibration when *A* and *f* are small. However, radial dispersion can be supressed by vibration when *A* and *f* are large. There is a positive correlation between the radial dispersion coefficient E_r and V_p when V_p is relatively high. These findings are helpful to the design of screening processes.

Machine learning was here applied to DEM simulated results. The Gaussian process regression model was found to be the best for modelling percolation velocity as a function of *A*, *f* and *d/D* together. Using a trained GPR model, the percolation threshold as a function of vibration condition was established for the studied system.

These results have extended spontaneous percolation theory to encompass vibrated beds. This includes the effects of vibration amplitude and frequency on percolation velocity under different size ratios, and the relationship between vertical (percolation) and horizontal (radial dispersion) motion of percolating particles in a vibrated bed. This knowledge may be used to guide and model related processes such as screening and sieving. Machine learning is also shown to be effective for modelling proposed parameters in current theories of particle segregation. Therefore, supported by DEM simulation data, the combination of machine learning, DEM and percolation theory may be further explored to model related industrial processes such as sieving and mixing.

It is worth noting that in the machine learning model, input variables can include other controlling variables, such as other particle properties and system dimensions. Generally, more input variables result in higher dimensional data space in the machine learning model, which also requires much larger data sets. Therefore, for the application of the machine learning model to a specific system, the input variables need to be carefully considered to balance model capability with data size. For example, if the model is to be applied to a sieve shaker, whether particle properties should be considered depends on whether different particle mixtures are to be used in real applications. Further, greater understanding of the effects of vibrational conditions and size ratio on percolation behaviour could enhance qualitative guidance for process design.

Nomenclature

A	Vibration amplitude
d	Percolating particle diameter
D	Packing particle diameter
E	Young's modulus
E_r	Radial dispersion coefficient
f	Vibration frequency
$\boldsymbol{F}_{ij}^{n}$	Normal contact force
$\boldsymbol{F}_{ij}^{t}$	Tangential contact force
$\boldsymbol{g}$	Gravitational acceleration
$h(x)$	Basis function
H	Vector of explicit basis function
$\boldsymbol{I}$	Moment of inertia of particle
m	Mass of particle
N	Number of percolating particles within radius r at time t
N_D	Number of large particles
N_0	Number of percolating particles
r	Radius describing dispersion
r_{ml}	Euclidean distance between x_i and x_j
R_i	Radius of particle i
R_j	Radius of particle j
t	Time

V_b	Vibration velocity amplitude
V_p	Percolation velocity
x_i	Predictor value
x_{new}	New input vector
y_i	Response (target) value
y_{new}	Response variable

Greek letters

β	Vector of coefficient
γ_n	Normal damping coefficient
δ_n	Relative normal displacement
δ_s	Total tangential displacement
θ	Kernel parameter
ρ	Particle density
$\tilde{\sigma}$	Poisson ratio
σ^2	Noise variance
σ_f	Signal standard deviation
σ_l	Characteristic length scale
μ_r	Rolling friction coefficient
μ_s	Sliding friction coefficient
ω	Particle angular velocity

Subscripts

i	Particle *i*
j	Particle *j*
i j	Between particles *i* and *j*

Abbreviations

GPR	Gaussian process regression
ML	Machine learning
RMSE	Root mean square error

CHAPTER IV: Process model of vibrating screen based on DEM and physics-informed machine learning

4.1 Introduction

Screens have been used to separate particles according to their sizes for a long time. They are widely used in various industrial sectors, from conventional civil, mineral processing and agriculture, to contemporary sectors such as pharmaceuticals and recycling (Dong, K, Wang & Yu 2013; Dong, K, Yu & Brake 2009). However, screening processes are complex and difficult to model because they involve many controlling variables. These variables can be generally divided into three categories: (i) screen geometry, such as aperture sizes and shapes (Asbjörnsson et al. 2016; Wolff 1954; Zhang, B et al. 2016); (ii) operational conditions, such as vibration and inclination angle; and (iii) particle properties, such as particle size distribution (Cleary, PW 2009; Dong, K, Yu & Brake 2009; Jansen & Glastonbury 1968) and moisture level (Wills & Finch 2016). The effects of these variables are complex and often interplay with each other. For example, using weaker vibration normally increases particle residence time and hence the passing of particles (Dong, K, Wang & Yu 2013; Dong, K, Yu & Brake 2009); however, if the vibration is too weak, undersized particles may not be able to percolate through the particle bed on the screen, and slow flow of particles can lead to screen choking (Esfandiary 2014; Jansen & Glastonbury 1968). Another example is that particle size distribution may have critical effects as apertures in the screen can be more easily blocked by near-mesh size particles (Delaney, Gary W. et al. 2012).

Although screening processes are complex, there are various process models proposed in the literature. Most models are based on probability theory (Dong, K, Wang & Yu 2013; Kapur, Ball & Fuerstenau 1977; Soldinger 1999, 2000; Standish & Meta 1985; Subasinghe, G, Schaap, W & Kelly, E 1989) and the kinetic approach (Ferrara, Preti & Schena 1987; Standish 1985; Standish, Bharadwaj & Hariri-Akbari 1986; Standish & Meta 1985; Subasinghe, Schaap, W & Kelly, EG 1989) and typical examples are listed in Table 4-1. In general, probability models consider the passing of particles resulting from a series of collisions of particles with the screen mesh, and in each collision a particle has a certain probability of passing through the aperture while the overall passing rate is the likelihood function for multiple attempts. This type of model normally ignores the effect of particle–particle interactions. Conversely, kinetic models (Standish 1985; Standish & Meta 1985) focus on modelling how fast undersize particles can be sieved and the relationship between sieving speed and the remaining materials. The passage rate depends on the probability that particles will pass through apertures and the amount of free

material on the screen surface (Soldinger 1999). Very few models consider both passing and material flow along a screen (Soldinger Stafhammar 2002).

Table 4-1 List of screening process models in the literature.

Model/study	Note	Mathematical model
Probability model (Soldinger 1999, 2000)	Possible to determine the influence of feed rate and varying proportions of fine material	Passage rate: $\dot{P} = k(1 - P)$ For bottom layer: $\dot{P} = k \cdot B$ where P is share of the original amount of fine particles that has passed through apertures in the screen surface (Soldinger 1999), B is the part of the original amount of fine particles gathered in the bottom layer (Soldinger 1999, 2000)
Probability model (Calanog & Geiger 1973)	The probability of passage is considerably smaller for cube shaped particles than spheres	The probability of passing of a particle, $P = (a - d)^2/a^2$, $a =$ screen opening and $d =$ particle diameter
Probability model (Davoodi, Ali et al. 2019)	High-density material has a higher probability of passage	Passage probability: $k_j = 80(e^{\left(-\frac{\beta d_{50}}{Ap}\right)} - e^{-\beta} d_{50}/Ap)$ where d_{50} is the mean particle size, Ap is the aperture size, and β is the rate factor
Kinetic and probabilistic model (Subasinghe, Schaap, W & Kelly, EG 1989)	The probabilistic model is equivalent to a Weibull survival function with two parameters	Weibull survival function , $Y_d = \exp\{-A(L^B)\}$, A and B are constants; L is the screen length, $Y_d =$ fraction of material of size detained on the screen at a position L along the screen.
Probabilistic model (Subasinghe, G, Schaap, W & Kelly, E 1989)	To predict screening results covering different particle sizes, screen lengths, and different vibratory systems, with reasonable accuracy	The fraction of material retained: $Y_d = (1 - p)^N$, where p is the probability of passage in a single attempt; N is the number of attempts $p = \frac{[(a+w)cos\varphi - w - d](a-d)}{(a+w)^2 cos\varphi}$, where a is the edge of a square aperture, w is the wire diameter, and $\varphi$is the inclination of the screen
Kinetic plus probability model (Ferrara, Preti & Schena 1987)	It is possible to obtain a single equation for screen oversize efficiency, which is valid for crowded, separate or mixed conditions and therefore very useful for characterising the	Kinetics of the process: $\partial w(X, l)/\partial l = -k(X) f(X, l)$ where w(X, l) dX is the per unit width for particles of size from X to X+dX in layer l, $f(X, l)$ is the particle concentration. Probability of passage: $k(X) = w_c np(X)$ where w_c is the critical flow rate and n the number of particle presentations per unit

	screening process with few parameters	length, $p(X) = (D - X)^2/(D + B)^2$, D is the mesh aperture (square) and B the wire diameter
Kinetic model (Standish, Bharadwaj & Hariri-Akbari 1986) (Standish 1985)	The effect of operating variables on the kinetic constants	$-\frac{dW}{dt} = kW$, where W is the weight of particles on the sieve, k is the sieving rate constant
Probability model (Dong, K, Wang & Yu 2013)	Interactions between particles and screen deck	The probability of remaining particles $P(N) = (1 - p)^N$, particles passing, $p = \frac{(a-d)(\mathrm{acos}(\theta)-d)}{(a+b)^2\cos(\theta)}$, the weight percentage passing, $W_p = 1 - (1 - p)^N$

In recent decades, numerical simulations have played an increasing role in understanding particle-scale behaviour in screening processes. In particular, the DEM has been used to study various screening processes (Asbjörnsson et al. 2016; Cleary, PW 2009; Davoodi, A. et al. 2019; Dong, K, Esfandiary & Yu 2017; Elskamp et al. 2016; Harzanagh, Orhan & Ergun 2018). With the help of particle-scale information provided by DEM simulation, the complex dynamics of particle flow (Lu, G, Third, JR & Müller, CR 2015; Zhu, HP et al. 2007) and particle passing have been investigated (Asbjörnsson et al. 2016; Davoodi, A. et al. 2019; Dong, K, Wang & Yu 2013; Harzanagh, Orhan & Ergun 2018; Zhao, L et al. 2011). However, DEM simulations require very high computational effort to study industrial scale screens with a large number of particles (Hoomans, Kuipers & van Swaaij 2000; Yan, Z et al. 2015). Thus, there have been attempts to link DEM studies with process models based on probability theory (Dong, K, Esfandiary & Yu 2017; Dong, K, Wang & Yu 2013); however, complex particle–particle interactions remain difficult to model.

For solving complex problems with high-dimensional data, artificial intelligence has been found to be advantageous in many fields (Laguitton & Leung 1989; Napier-Munn & Wills 2006). Based on training data, various learning algorithms can be used to explore the mapping of the process variables, which can fit non-linear relationships in complicated granular systems (Barrasso, Tamrakar & Ramachandran 2014; Chen, S et al. 2018; Dai, W, Liu & Chai 2015; Li, Y et al. 2020, 2021; Pani & Mohanta 2015; Zhang, B et al. 2016). Artificial intelligence has also been increasingly used to study screening processes (Chen, Z et al. 2021; Li, Z et al. 2019; Li, Z et al. 2015; Shanmugam et al. 2021; Zhang, B et al. 2016; Zhao, Z et al. 2021), including modelling the effect of moisture content on coal sieving (Shanmugam et al. 2021), distribution

of particles on a vibrating screen (Zhao, Z et al. 2021) and intelligent fitting and controlling of parameter optimisation for screening processes (Li, Y et al. 2020; Li, Z et al. 2019; Zhang, B et al. 2016). Recently, physics-informed machine learning (i.e., kernel-based regression, neural networks) has emerged as a promising alternative of deep neural networking to avoid the need for large training databases. Integration of mathematical models and databases has enabled higher-dimensional problems of PDEs to be solved, faster training of database, new scalable mathematics, better accuracy and modelling of hidden physics (Karniadakis et al. 2021).

Using these methods, it has been found that the sieving behaviours in different parts of the screen are different because of variations in the packed bed structure on the screen (Jiang, H, Zhao, Duan, Yang, et al. 2017; Jiang, H, Zhao, Qiao, et al. 2017). A screening process can be optimised by varying the conditions in different parts, such as with banana screens or 'varied amplitude' screens (Jiang, H, Zhao, Duan, Liu, et al. 2017; Jiang, H, Zhao, Duan, Yang, et al. 2017; Jiang, H, Zhao, Qiao, et al. 2017). These studies indicate that screening behaviour should be considered based on local flow conditions. With this idea, the present study aimed to develop a segment-based process model by combining the DEM and machine learning. Assumptions included that on a screen segment, the local flow is steady and the relationship between local passing rate and local flow conditions can be modelled. Such relationships would be too complex to derive theoretical models, hence the model developed here used a combination of DEM and machine learning. The segments could then be linked by using mass continuity. Different operational conditions can be set for different segments to model multi-deck screens using the universal local passing function. Moreover, the ML predicts the local flow and passing on a vibrating screen and the partition curve is predicted by the link of local flows base on physics laws. The DEM model has been validated by good agreement with experimental data.

The study is structured as follows: Section 4.2 addresses the DEM methodology and inclined screen simulation conditions. The process model of an inclined screen with segment-wise analysis is also defined in Section 4.3. In Section 4.4, process modelling is combined with machine learning to predict various feeding and vibration conditions and model optimisation. Section 4.5 concludes the study.

4.2 Methodology

4.2.1 DEM Simulation

4.2.1.1 Governing equations

The DEM is used to simulate screening processes at the particle-scale and generate data for machine learning. In the DEM, the motion of each particle is governed by Newton's second law (Cundall & Strack 1979). For a spherical particle i, its translational motion and rotational motion are respectively determined by:

$$m_i \frac{d\boldsymbol{v}_i}{dt} = \sum_j (\boldsymbol{F}_{ij}^n + \boldsymbol{F}_{ij}^s) + m_i \mathbf{g} \qquad \text{(Eq. 4.1)}$$

$$\boldsymbol{I}_i \frac{d\boldsymbol{\omega}_i}{dt} = \sum_j (\boldsymbol{R}_{ij} \times \boldsymbol{F}_{ij}^s - \mu_r R_i \left|\boldsymbol{F}_{ij}^n\right| \hat{\boldsymbol{\omega}}_i) \qquad \text{(Eq. 4.2)}$$

where $\boldsymbol{v}_i$, $\boldsymbol{\omega}_i$, m_i and $\boldsymbol{I_i}$ are respectively the translational and angular velocities, the mass and the moment of inertia of particle i, $\boldsymbol{g}$ is the gravitational acceleration, $\boldsymbol{R}_{ij}$ is the vector pointing from the centre of particle i to its contact point with particle j. $\boldsymbol{F}_{ij}^n$ and $\boldsymbol{F}_{ij}^s$ are the normal and tangential contact forces respectively, which can be determined as (Brilliantov et al. 1996; Langston, Tüzün & Heyes 1995):

$$\boldsymbol{F}_{ij}^n = \left[\frac{2}{3}\frac{Y}{1-\tilde{\sigma}^2}\sqrt{\bar{R}}{\xi_n}^{3/2} - \gamma_n \frac{Y}{1-\tilde{\sigma}^2}\sqrt{\bar{R}}\sqrt{\xi_n}(\boldsymbol{v}_i \cdot \hat{\boldsymbol{n}}_{ij})\right]\hat{\boldsymbol{n}}_{ij} \qquad \text{(Eq. 4.3)}$$

$$\boldsymbol{F}_{ij}^s = -\mu_s|\boldsymbol{F}_n|[1-(1-\frac{min(\xi_s, \xi_{s,max})}{\xi_{s,max}})^{3/2}]\hat{\boldsymbol{\xi}}_s \qquad \text{(Eq. 4.4)}$$

where Y is Young's modulus, $\tilde{\sigma}$ is the Poisson ratio, γ_n is the normal damping coefficient, μ_s is the sliding friction coefficient, ξ_s is the total tangential displacement and $\bar{R} = R_i R_j/(R_i+R_j)$, $\xi_{s,max} = \mu_s[(2-\tilde{\sigma})/2(1-\tilde{\sigma})]\xi_n$, $\hat{\boldsymbol{n}}_{ij} = (\boldsymbol{R_i} - \boldsymbol{R_j})/\left|\boldsymbol{R_i} - \boldsymbol{R_j}\right|$. The second term of the torque results from the rolling resistance between two contact particles resulting in elastic hysteretic losses or viscous dissipation, where μ_r is the rolling friction coefficient and $\hat{\boldsymbol{\omega}}_i = \boldsymbol{\omega}_i/|\boldsymbol{\omega}_i|$ (Zhou, YC et al. 1999; Zhu, HP et al. 2007). The above equations calculate the interaction between particles and the system wall (i.e., the contact between particles and a finite polygon surface). Van der Waals force and capillary force between particles are not considered because

the coarse particles are dry. The wall is modelled as a plane with the same material properties as the particles. Under vibration, the position and velocity of the wall are updated in every time step, and the values are used to calculate the particle–wall interactions. The time step is determined by $dt = 0.1\sqrt{m/k}$, where m is the mass of a particle and k is the estimated spring constant when the normal overlap is 10% of the particle diameter. This is based on the natural period of oscillation of the equivalent spring when using the Hertz contact force model (Hertz 1882). In a multi-size system, the time step is calculated for each type of particle and the minimum time step is used. Simulations were conducted by our in-house DEM program, which has been used and validated in various systems in our previous studies (Amirifar et al. 2018, 2019; Dong, K, Wang & Yu 2013; Dong, K, Yu & Brake 2009).

4.2.1.2 Simulation conditions

In the present study, a screen with an incline similar to a previous study was considered (Dong, K, Wang & Yu 2013). The deck consisted of a flat surface uniformly perforated with square apertures 3.5 × 3.5 mm spaced 3.0 mm apart. The left side of the deck was the feed end, while the right side was the discharge end. The length, width and thickness of the deck were 600 mm, 26 mm and 2 mm respectively. Periodic boundary conditions were applied in the *x*-direction (i.e., front and rear) to reduce computational effort. The feed particles fell and hit the vibrating screen deck, particles passing through the deck to report to the underflow or flowing along the screen to the discharge end and reporting to the overflow (Figure 4-2). The particle size distribution, material properties and feed rate are listed in Table 4-2. The simulation data were collected only at the steady flow state, when the inlet flow rate was balanced with the sum of the underflow and overflow rates for particles of each size, with some fluctuations.

Table 4-2 List of parameters used in the simulations.

	d_1	d_2	d_3	d_4	d_5	d_6	d_7
Particle size, d_i (mm)	1.10 to 1.25	1.3 to 1.45	1.50 to 1.73	1.8 to 2.05	2.5 to 2.55	3.05 to 3.2	3.65 to 3.75
Feed rate n_i (num/s)	n_1	n_2	n_3	n_4	n_5	n_6	n_7
	3300 to 5300	2050 to 3300	1250 to 2000	1000 to 1500	400 to 950	200 to 1250	100 to 200

Particle density, (kg/m^3)	7500						
Young's modulus (N/m^2)	1×10^7						
Damping coefficient, γ_n	Particle-particle:2×10^{-4}; particle-wall: 2×10^{-4}						
Sliding friction coefficient, μ_s	Particle-particle: 0.3; particle-wall: 0.5						
Rolling friction coefficient, μ_r	Particle-particle: 0.01; particle-wall: 0.01						
Vibration frequency (Hz), f	20, 25, 30, 35, 40, 50 and 60						
Vibration amplitude (mm), A	1.5, 2.0, 2.5 and 3.0						
Vibration motion	Sinusoidal, both along y and z directions.						
Incline angle (°), θ	7, 9, 11, 13, 15, 17 and 22						

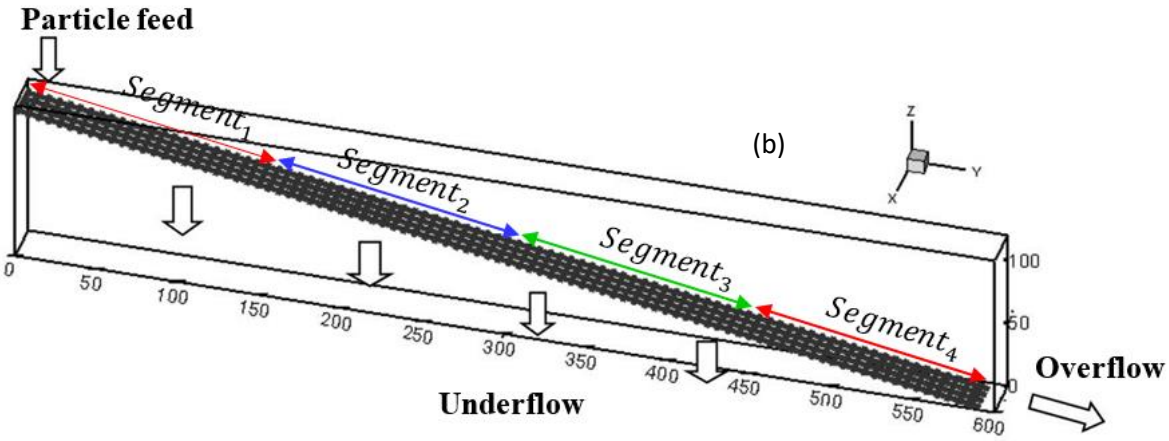

Figure 4-1 Schematic of the simulated screen.

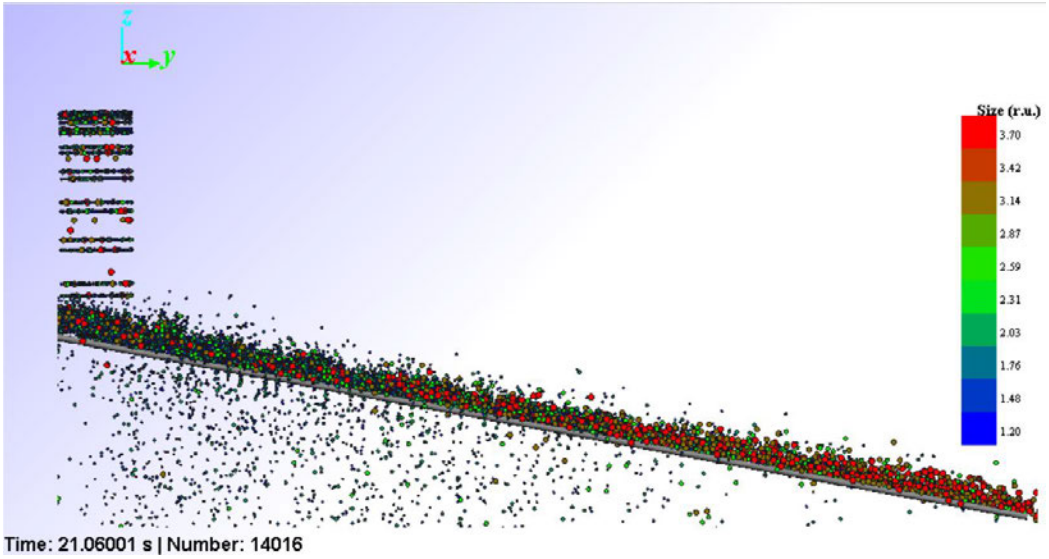

Figure 4-2 Snapshot of simulation using the inclined vibrating screen with steady state (A = 2 mm, f = 30 Hz and θ = 11°).

4.3 Process model of screen based on physics-informed machine learning

Here a process model for vibrating screens is proposed based on physics-informed machine learning, using the inclined screen described above. As discussed previously, the passing of particles varies in different positions of the screen deck due to the difference in local conditions. Therefore, the local conditions of segments of the inclined screen were considered. As shown in Figure 4-3a, under steady state on segment j of the screen, particle passing behaviour was assumed to be uniform. In particular, input flow $\{d_i, I_i\}^j$, overflow $\{d_i, O_i\}^j$ and passing flow $\{d_i, P_i\}^j$ of this segment were all constants, where d_i is the particle size of the ith component in the particle mixture, and I_i, O_i and P_i are the flow rates of the input flow, overflow and passing of the ith component respectively. The superscript j refers to the segment number j.

The passing rate was assumed to be dependent on the input flow, vibration conditions and inclination angle, so a function to predict the passing rate $\{P_i\}$ is:

$$\{d_i, P_i\}^j = f_P\left(\{d_i, I_i\}^j, A, f, \theta\right) \quad \text{(Eq. 4.5)}$$

where $f_P\left(\{d_i, I_i\}^j, A, f, \theta\right)$ is defined as the local passing function. It is worth noting that this function may also be dependent on other variables, which could be extended in future work. The particle size distribution was considered as discrete rather than continuous, for more flexibility in describing different mixtures. Although discrete forms may involve a large number of variables in the equation, this can be readily accommodated by a data model.

The input flow, overflow and passing flow of a segment should satisfy mass continuity, which is determined by:

$$\{d_i, O_i\}^j = \{d_i, I_i\}^j - \{d_i, P_i\}^j \quad \text{(Eq. 4.6)}$$

Considering mass continuity between segments, the overflow of upstream segment j-1 should be equal to the input flow of segment j, and overflow of segment j equal to input flow of downstream segment j + 1, thus:

$$\{d_i, I_i\}^j = \{d_i, O_i\}^{j-1} \quad \text{(Eq. 4.7)}$$

$$\{d_i, O_i\}^j = \{d_i, I_i\}^{j+1} \quad \text{(Eq. 4.8)}$$

The model is illustrated in the flow chart in Figure 4-3b. If the inclined vibrating screen is divided into different segments with the local passing function $f_P\left(\{d_i, I_i\}^j, A, f, \theta\right)$ in (Eq. 4.5), the sieving process can be predicted from the feed end to the discharge end, with the feed rate as the initial input flow of the first segment. However, f_P has many input variables, which include particle properties and operational conditions, making the relationship is very complicated and non-linear. It would be difficult to develop this function in a conventional way. Therefore, in the present work, this function is developed by applying machine learning to the database generated by DEM simulation.

For each simulation of the inclined screen described in Section 4.3, and in accordance with previous studies (Dong, K, Wang & Yu 2013; Standish 1985), the whole screen was divided into four segments from the feed end to the discharge end (Figure 4-2b). For each segment, input flow $\{d_i, I_i\}$, output flow (overflow) $\{d_i, O_i\}$ and passing flow $\{d_i, P_i\}$ were calculated using the average of the DEM simulation data at the steady state. Then, different machine learning models were applied to the data, and the model with the highest accuracy was selected, which will be discussed in the following section. It is worth noting that the data from different segments were combined in the machine learning model training, so the model observes the assumption that f_p depends only on local flow conditions.

After f_p was modelled by machine learning, it was used in the process model described by Eqs (Eq. 4.5–(Eq. 4.8). A MATLAB program was developed to calculate $\{P_i\}$ on the first segment according to $\{I_i\}$, A, f and θ; then, the inlet for the second segment was calculated by (Eq. 4.6) and ((Eq. 4.7), and the passing rate $\{P_i\}$ for the second segment was predicted using the machine learning model of f_p but with the conditions of the second segment. The third and remaining segments were modelled using a similar procedure. It is worth noting that for each segment, not only $\{I_i\}$ was different but also A, f and θ could be different on a multi-deck screen. These results are shown in detail in the following section.

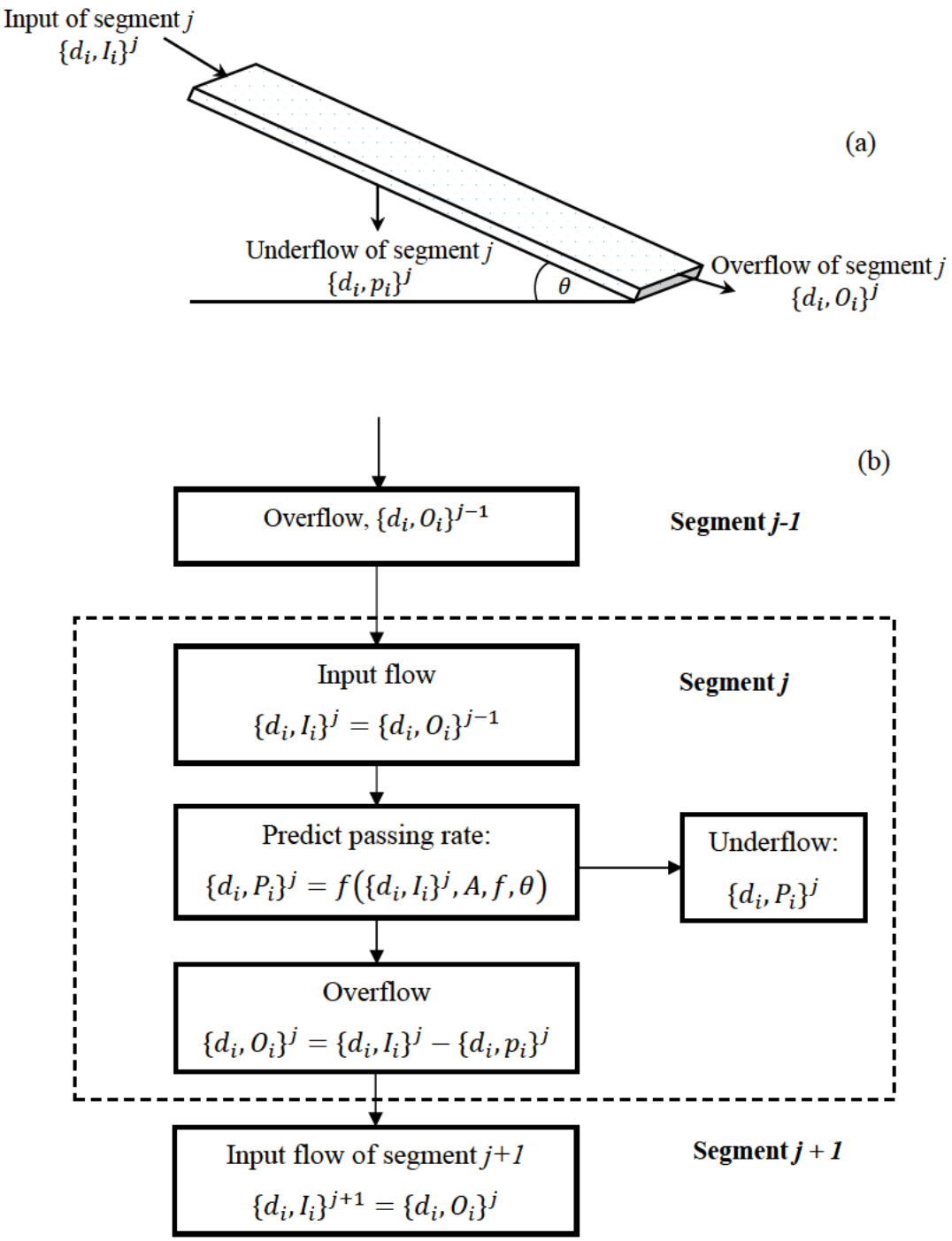

Figure 4-3 (a) Particles flow of a segment j ; (b) Process model flowchart.

4.4 Results and discussion

4.4.1 Machine learning of local passing function f_P

As described above, the local passing function f_p is used to predict by training machine learning models with the DEM simulation data. The input variables are $\{d_i\}$, $\{I_i\}$ A, f, and θ for a segment. The simulated inclined screen is divided into four segments. For the first segment, $\{I_i\}$ is the feed rate $\{n_i\}$, while for other segments, $\{I_i\}$ is calculated using (Eq. 4.8). The output variables of the model are $\{P_i\}$. The variables and their ranges are listed in Table 4-3. The total training data contains 900 sets of data obtained in 225 cases, as each simulation contains 4 sets. The data is trained with linear, SVM (Vapnik 1995) and GPR regression (Rasmussen & Williams 2006) ML models. The detailed algorithm of the models can be found in the MATLAB document (MATLAB 2021a, 2021b).

The R-squared values of the considered models are listed in Table 4-4, from which it can be seen that the squared exponential GPR regression model is the best model with very high accuracy (R-squared is higher than 0.96). The DEM and ML results of particles passing (P_1, P_2, P_3, P_4, P_5 and P_6) of vibrating inclined screen are shown in Figure 4-4.

Table 4-3 Input and output variables used for process model database.

Input	Used values	Output	
A (mm)	1.5 , 2.0, 2.5 and 3.0	P_1 (num /s)	underflow of d_1
f (Hz)	20, 25, 30, 35, 40, 50, 60	P_2 (num /s)	underflow of d_2
θ (º)	7, 9, 11, 13, 15, 17, 22	P_3 (num /s)	underflow of d_3
d_1 (mm)	1.1, 1.2, 1.25	P_4 (num /s)	underflow of d_4
d_2 (mm)	1.3, 1.4, 1.45	P_5 (num /s)	underflow of d_5
d_3 (mm)	1.5, 1.68, 1.73	P_6 (num /s)	underflow of d_6
d_4 (mm)	1.8, 2.0, 2.05		
d_5 (mm)	2.5, 2.55		
d_6 (mm)	3.05, 3.15, 3.2		
d_7 (mm)	3.65, 3.70, 3.75		
I_1 (num /s)	4.08 - 5327.7		
I_2 (num /s)	5.28- 3301.74		
I_3 (num /s)	9.52 - 2029.28		
I_4 (num /s)	15.36 - 1523.52		
I_5 (num /s)	22.14 - 923.82		
I_6 (num /s)	30.16 - 1266.3		
I_7 (num /s)	100 - 200		

Table 4-4 Performance of the machine learning models for particles passing along the screen.

Machine learning model	R^2 of P_1	R^2 of P_2	R^2 of P_3	R^2 of P_4	R^2 of P_5	R^2 of P_6	Average
Linear regression	0.94	0.93	0.89	0.83	0.64	0.60	0.805
Interaction linear regression	0.98	0.98	0.96	0.93	0.79	0.79	0.905
Robust linear regression	0.94	0.92	0.89	0.83	0.64	0.58	0.8
Stepwise linear regression	0.98	0.97	0.96	0.93	0.78	0.76	0.897
Rational Quadratic GPR	0.99	0.99	0.98	0.97	0.89	0.87	0.948
Squared exponential GPR	**0.99**	**0.99**	**0.98**	**0.97**	**0.97**	**0.96**	**0.977**
Matern 5/2 GPR	0.99	0.99	0.98	0.97	0.97	0.95	0.975
Exponential GPR	0.99	0.99	0.98	0.96	0.89	0.86	0.945
Linear SVM	0.94	0.92	0.88	0.80	0.61	0.52	0.778
Quadratic SVM	0.98	0.97	0.95	0.91	0.76	0.75	0.887
Cubic SVM	0.99	0.98	0.98	0.95	0.83	0.79	0.92
Fine Gaussian SVM	0.89	0.87	0.87	0.86	0.78	0.76	0.838
Medium Gaussian SVM	0.98	0.98	0.96	0.93	0.78	0.72	0.892
Coarse Gaussian SVM	0.95	0.94	0.90	0.82	0.57	0.42	0.767

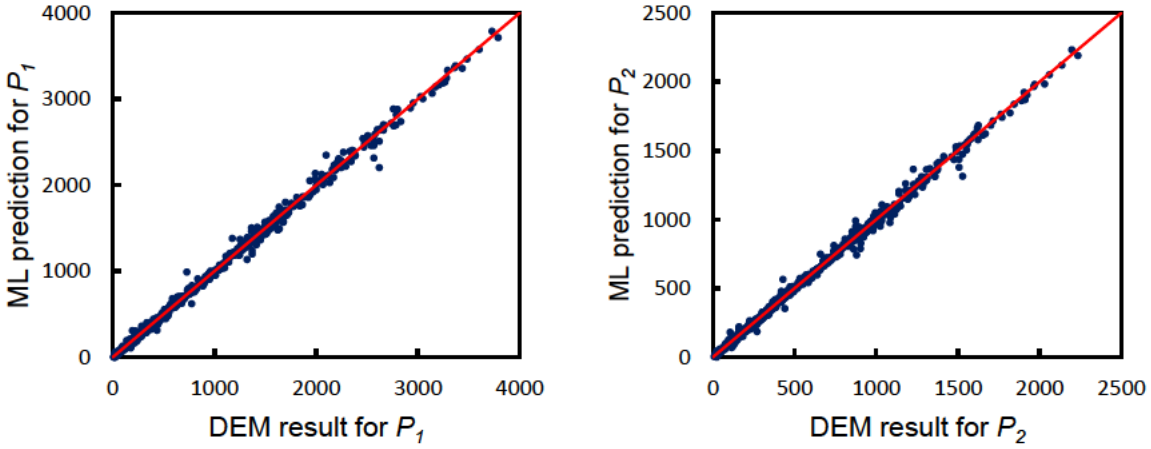

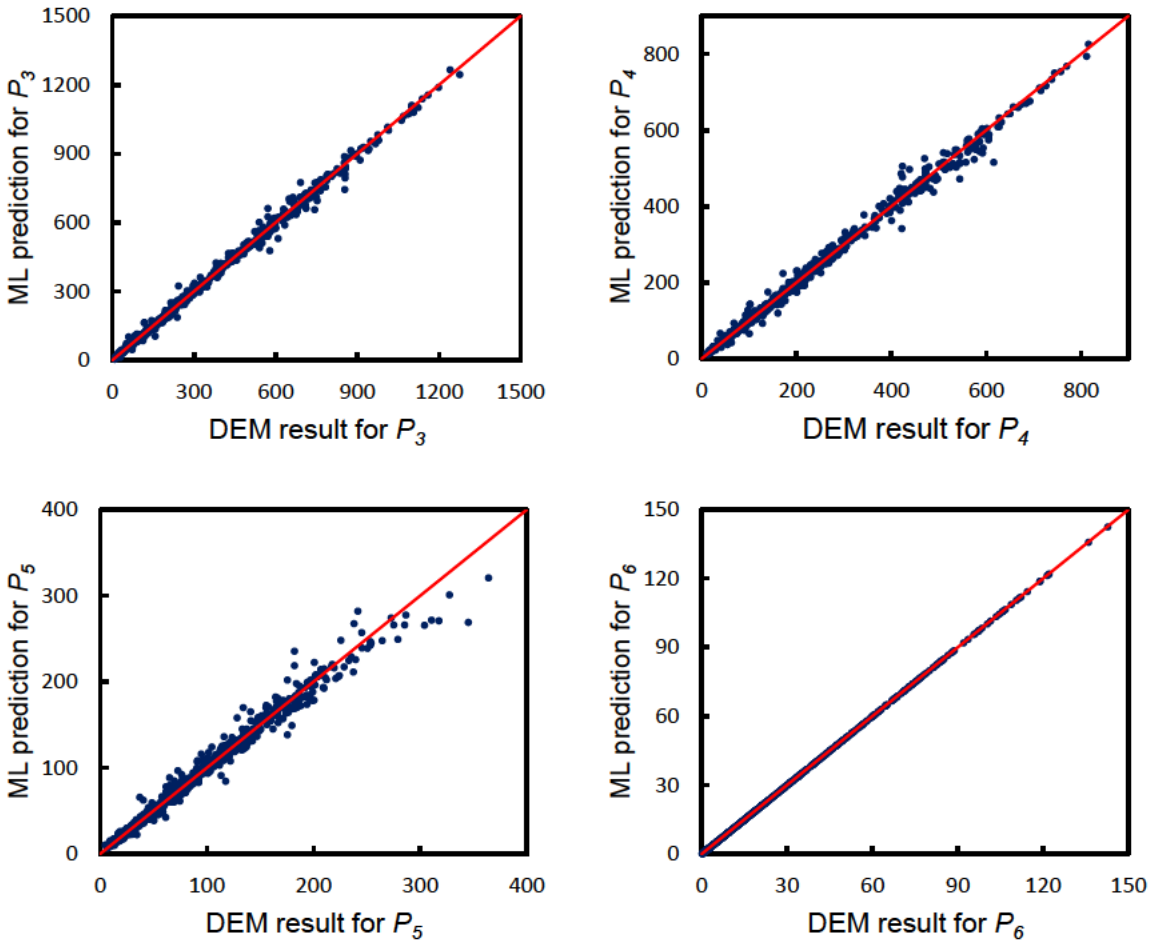

Figure 4-4 DEM and ML predicted local passing flow rates (unit: num/s).

4.4.2 Full process model for inclined screen

After f_p is developed, the simulated incline screen with four segments can be fully modelled using the method described in Section 4.3 and Figure 4-3 (b). With the passing rate of each size particles obtained from the model, the partition curve for the overflow of the whole screen can be obtained, which can be used to evaluate the sieving performance. This curve shows the percentage of particles reporting to the overflow as a function of particle size. The partition number normally increases from a lower value to 100% with increasing particle size. The cut sizes, d_{25}, d_{50} and d_{75} refer to the particle sizes where the partition numbers are 25%, 50% and 75% respectively. Probable error (E_p) is defined as half of the difference between d_{25} and d_{75}. In general, higher cut size d_{50} and lower E_p mean better sieving performance.

Figure 4-5 compares the partition curves obtained from the process model and DEM simulation. It can be seen under various vibration conditions, the results from the process model

match well with the DEM results, which shows the process model is very accurate and universal.

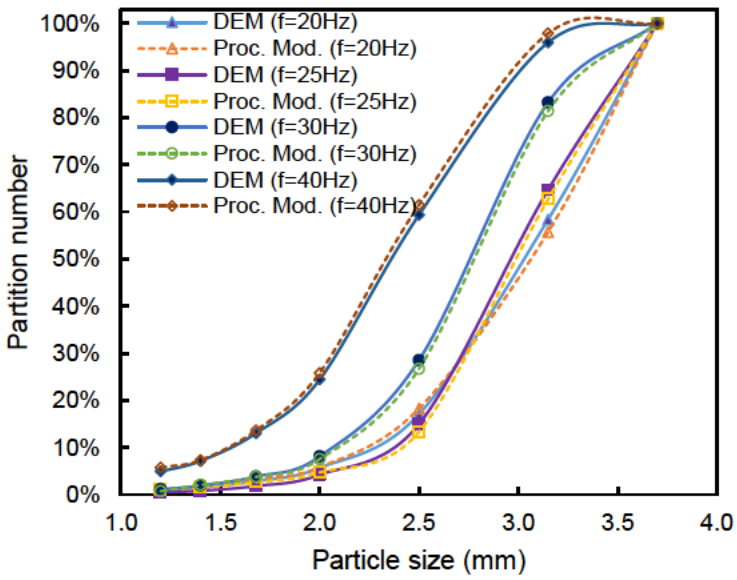

Figure 4-5 Comparison of overflow partition curves obtained from DEM and process model under different vibration frequencies, where A = 2.5mm, θ=11° and feed condition is as simulation.

Then, the process model was used to study the effect of particle size distribution on screen performance. Here, three size distributions were considered (Table 4-5). Figure 4-6 shows the cumulative distributions and volume ratios of different sized particles of different size distributions. In Feed 1, the volume ratios of different size particles were similar. The particle size was considered based on the screen aperture size. For instance, small undersize particles were smaller than the aperture size, medium size particles were larger than undersize particles and smaller than near-mesh size particles (i.e., with sizes near the aperture mesh size). In Feed 2, the volume ratios of small undersize particles decreased, while the volume ratios of medium to near-mesh size particles increased. In Feed 3, the volume ratios of near-mesh size particles were dominant. Correspondingly, from Feed 1 to Feed 3, medium size feeding materials increased, while the total volume was kept similar. It is worth noting that $\{d_i\}$ and $\{I_i\}$ can be varied across a reasonable range in the machine learning model. However, if the set values are too different from the training data range, the machine learning model may be invalid (e.g., if the particle size of a component increases from undersize to oversize, or if the feed number is too high and lead to screen choking). These deficiencies can be overcome by including more

data in a wider range of conditions in the machine learning model. Here, $\{d_i\}$ and $\{I_i\}$ were varied within the range of the training dataset, and the screen checked for choking under the considered conditions.

Table 4-5 List of feeding materials with different particle size distributions.

	Component *i*	1	2	3	4	5	6	7
	Category	small undersize	small undersize	small undersize	medium undersize	medium undersize	near-mesh undersize	oversize
	Feed Size (mm), d_i	1.1	1.33	1.67	2	2.5	3.1	3.7
Feed-1 (total feed rate = 39347.70348 mm^3/sec)	Feed Rate (num/sec), n_i	5300	3300	2000	1500	800	550	200
	Volume ratio	9.39%	10.33%	12.40%	15.97%	16.63%	21.80%	13.48%
Feed-2 (40663.76377 mm^3/sec)	Feed Rate (num/sec), n_i	4400	3200	1900	1200	950	700	200
	Volume ratio	7.54%	9.69%	11.39%	12.36%	19.11%	26.85%	13.04%
Feed-3 (41457.69214 mm^3/sec)	Feed Rate (num/sec), n_i	3300	2050	1250	1200	745	1100	200
	Volume ratio	5.55%	6.09%	7.35%	12.12%	14.70%	41.39%	12.79%

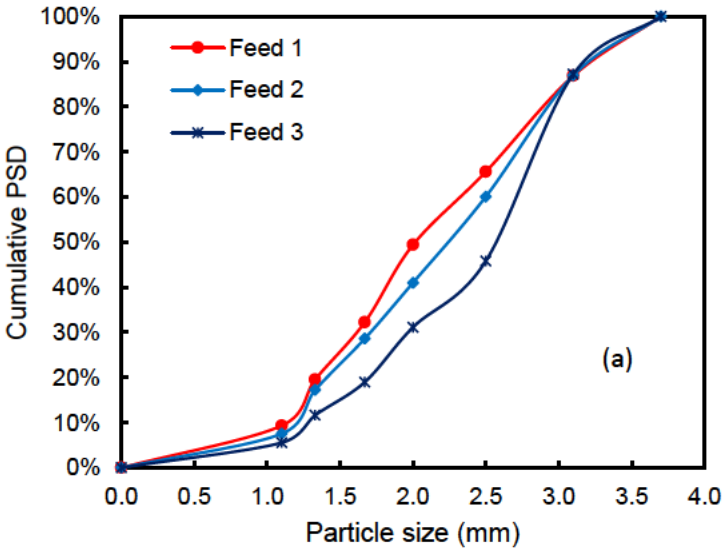

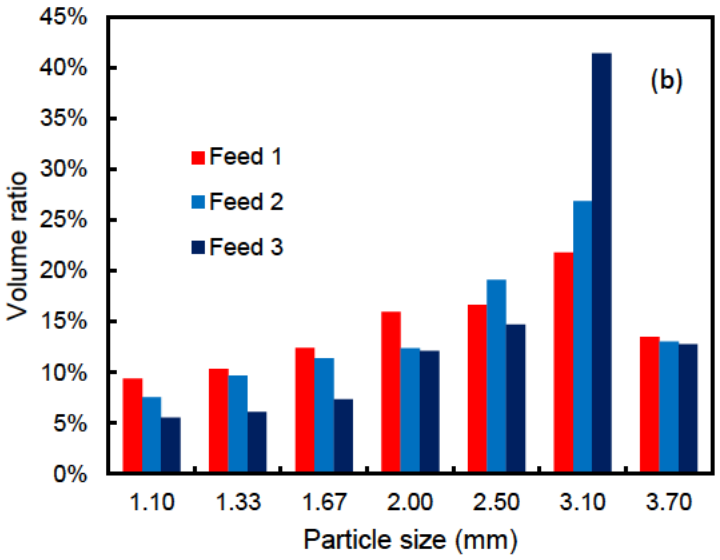

Figure 4-6 (a) Cumulative particle size distribution, and (b) volume ratio of each particle size for different feed conditions.

Figure 4-7 shows E_p and d_{50} of the overflow partition curve under the three feed conditions. As the volume ratio of small particles decreases and that of medium particles increases, d_{50} decreases but E_p increases, showing worse performance. In the corresponding partition curves in Figure 4-7b, the decrease of the passing rate of medium particles is more obvious than that of small particles. This may be because a large number of medium particles are more likely to crowd and dynamically cover the surface of the screen mesh, resulting in particles have less chances to collide with mesh and pass, and such a blocking effect could be more significant on medium particles than small particles. This aligns with the observations in a previous studies (Li, J et al. 2003; Zhang, B et al. 2016), which show that the local passing function developed from machine learning can consider interactions between different sized particles, which is an improvement from previous probability models (Dong, K, Esfandiary & Yu 2017; Dong, K, Wang & Yu 2013).

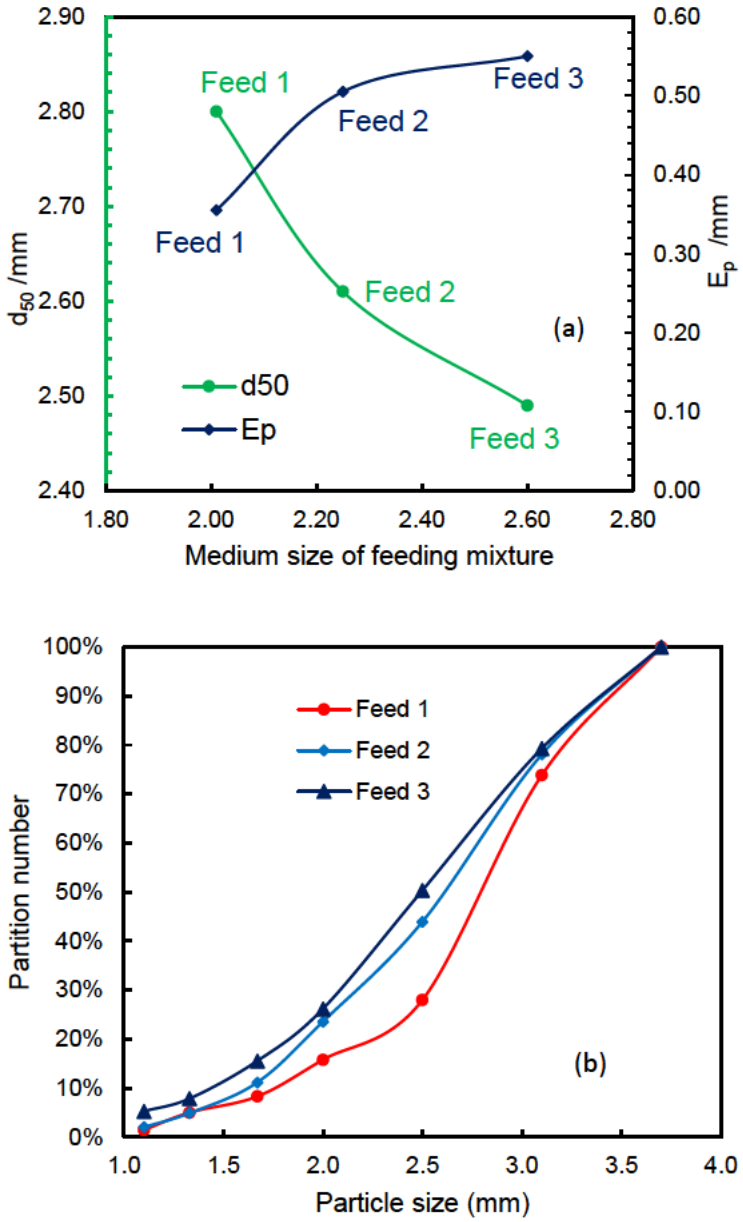

Figure 4-7 (a), E_p and d_{50} as a function of feed medium size, and (b), overflow partition number under different feed conditions.

Figure 4-8 further shows E_p and d_{50} as a function of the vibration frequency under different feed conditions. In general, d_{50} decreases while E_p increases with increasing vibration frequency, indicating that under all three feed conditions, the passing rate is lower with increasing vibration, which is in accordance with previous studies (Dong, K, Wang & Yu 2013; Harzanagh, Orhan & Ergun 2018) and is largely because stronger vibration can increase the bouncing of particles. However, for Feed 3, with the largest portion of medium particles, E_p shows small fluctuations between $f = 25$ Hz and $f = 30$ Hz, which may be because the passing

of medium particles benefits at a certain high vibration frequency. Regarding larger particles, vibration to loosen the particle also needs to be stronger. Such fluctuations show that the data model can capture the complicated combined effects of particle size and vibration conditions on passing, which is difficult to describe with an explicit function.

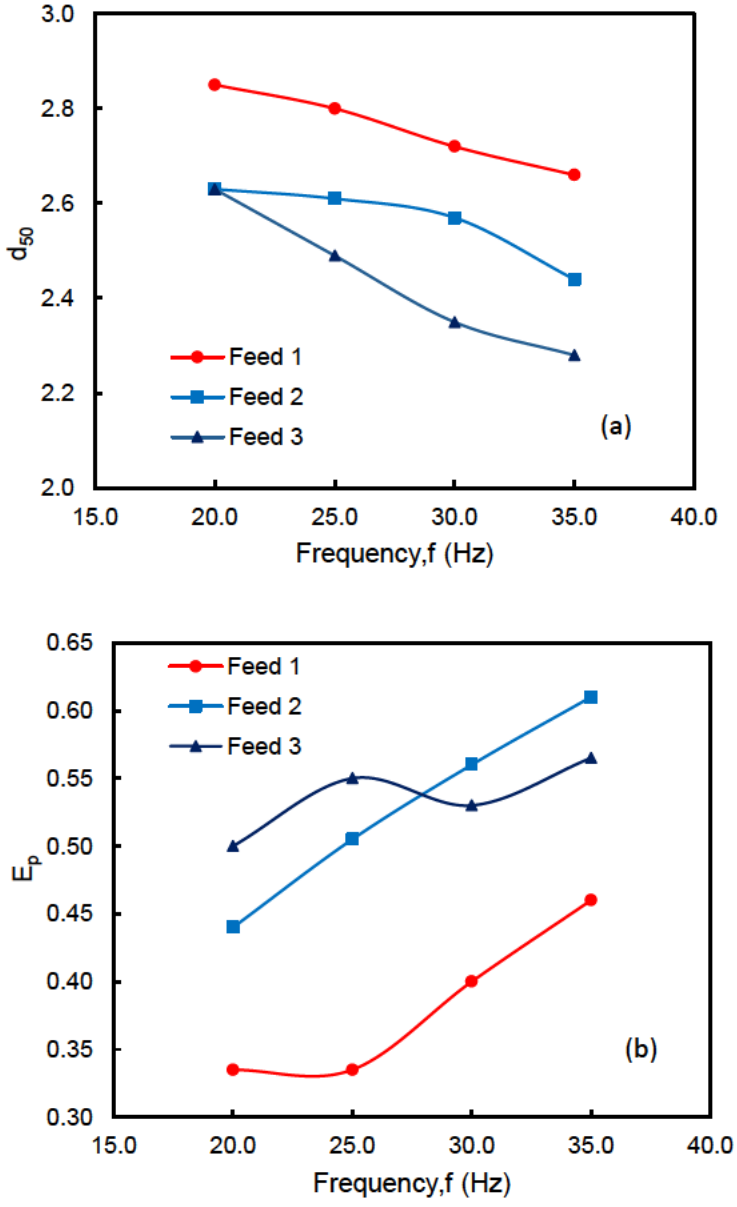

Figure 4-8 d_{50} and E_p as a function of vibration frequency under different feeding conditions.

Figure 4-9 shows d_{50} and E_p as a function of vibration amplitude for various feeding conditions. For example, d_{50} decreased with increased A (Figure 4-9a), which aligns with previous studies (Harzanagh, Orhan & Ergun 2018) and d_{50} of Feed 1 was high among the feed conditions. Conversely, the E_p of Feed 1 was low among the feed conditions and increased with increased

A (Figure 4-9b), largely owing to increased bouncing of particles for strong amplitude. The E_p of Feed 2 increased with increased *A* and decreased for *A* =1.5 mm. E_p of Feed 3 increased gradually with increased *A* and showed a similar trend as Feed 2. The passing of medium and larger particles was not effective for strong amplitude. Lower vibration frequency and/or amplitude was effective for particles passing from the screen.

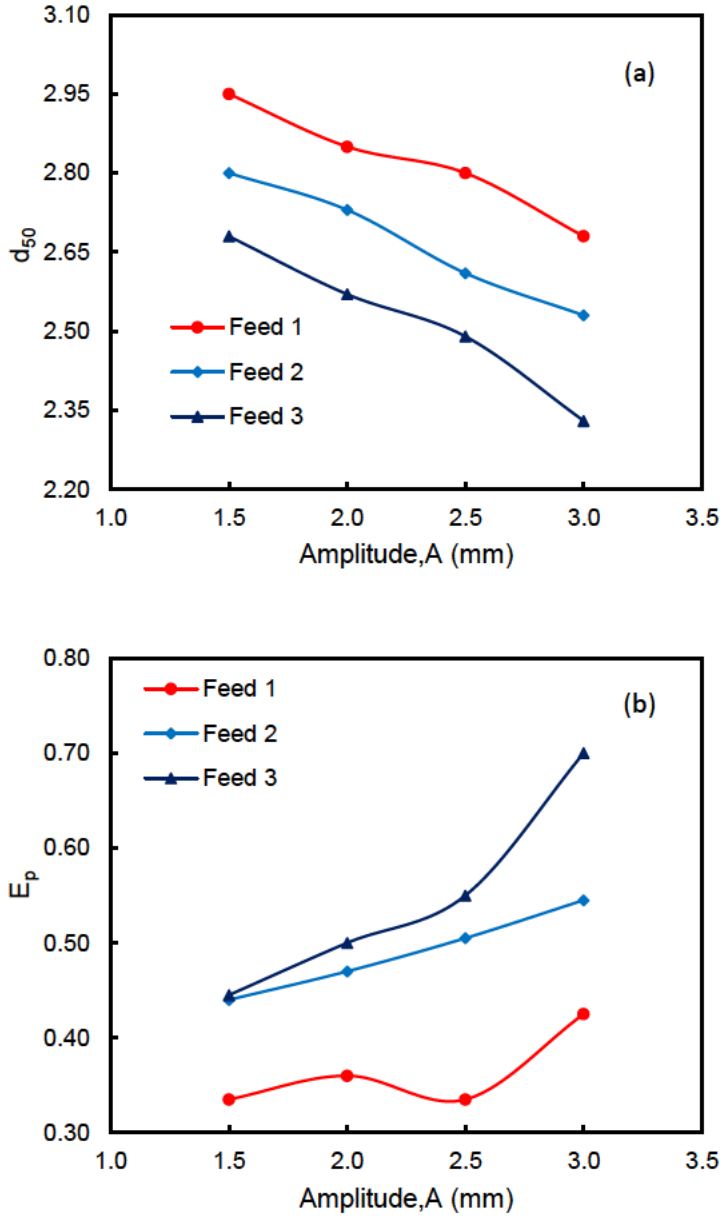

Figure 4-9 d_{50} and E_p as a function of vibration amplitude under different feeding conditions.

Figure 4-10 shows E_p and d_{50} as a function of screen inclination angle under different feed conditions, d_{50} gradually decreased with increased inclination angle (Figure 4-10a) and d_{50} was

maximum at lower inclination angles under all feed conditions. For Feed 1, d_{50} was higher among the feed conditions. Further, E_p increased with increasing inclination angle (Figure 4-10b; (Dong, K, Wang & Yu 2013). For Feed 1 and Feed 2, E_p was lower with an increase of inclination angle. The E_p of Feed 3 increased gradually. However, for Feed 3 with the largest portion of medium particles, E_p showed small fluctuations for $\theta = 15°$ and $\theta = 17°$, which may be because medium particles pass better with greater inclination angle, as for larger particles, the inclination to loosen the particle bed will also need to be stronger.

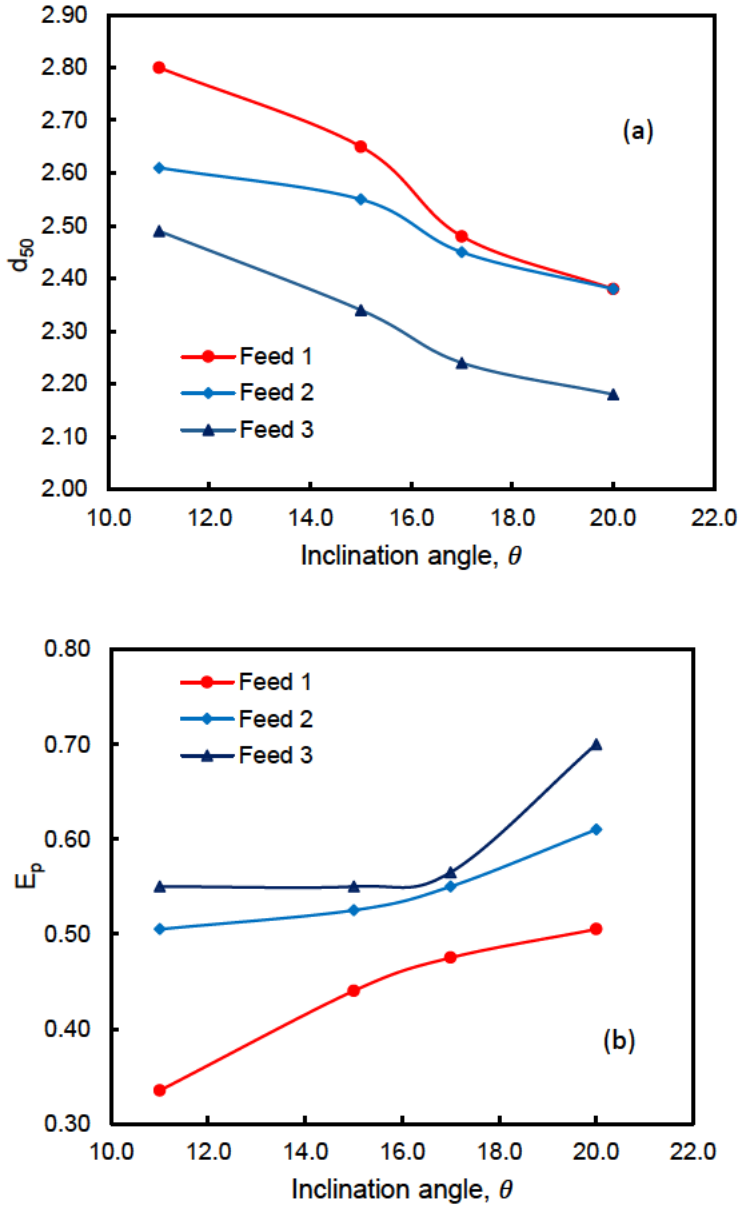

Figure 4-10 d_{50} and E_p as a function of inclination angle under different feeding conditions.

4.4.3 Application to complicated screens

Though the database for training is from the simulation of the simple incline screen, if our assumptions for the local passing function hold, the process model can actually be used for screens with different vibration conditions and incline angles at different segments, which are similar to multi-deck screens and variable vibration amplitude/frequency screens. In the following, we will apply the process model to these kinds of screens.

4.4.3.1 Varied inclination angle

Banana screens or multi-deck screens with different slopes are commonly used in high-tonnage material separation applications. Generally, the inclination angle of the deck is around 30–40° at the feed end of the screen, and reduces to around 0–15° with three to five decks (Dong, K, Yu & Brake 2009). The steep deck at the feed end allows the feed material to rapidly spread over the first part of the screen, while the flat deck at the discharge end slows the particles to increase their residence time and improve screening efficiency (Dong, K, Yu & Brake 2009; Napier-Munn & Wills 2006; Wills & Finch 2016).

Here, the process model was applied to two-deck screens with the same screen mesh and similar feeding materials as the incline screen, so that the local passing function obtained in the above study could still be used, while the different segments gained different inclination angles. As shown in Figure 4-11, the incline screen is "bent" into two equal-length decks. The first deck consisted of segments 1 and 2, which have the same inclination angle θ_1; the second deck consisted of segments 3 and 4, which have the same inclination angle θ_2. According to the design of banana screens, θ_1 should be larger than θ_2. The process model was applied to two-deck screens with different θ_1 and θ_2 values. Some cases were also compared with the DEM simulation, and a simulation snapshot of one of these cases is shown in Figure 4-11b.

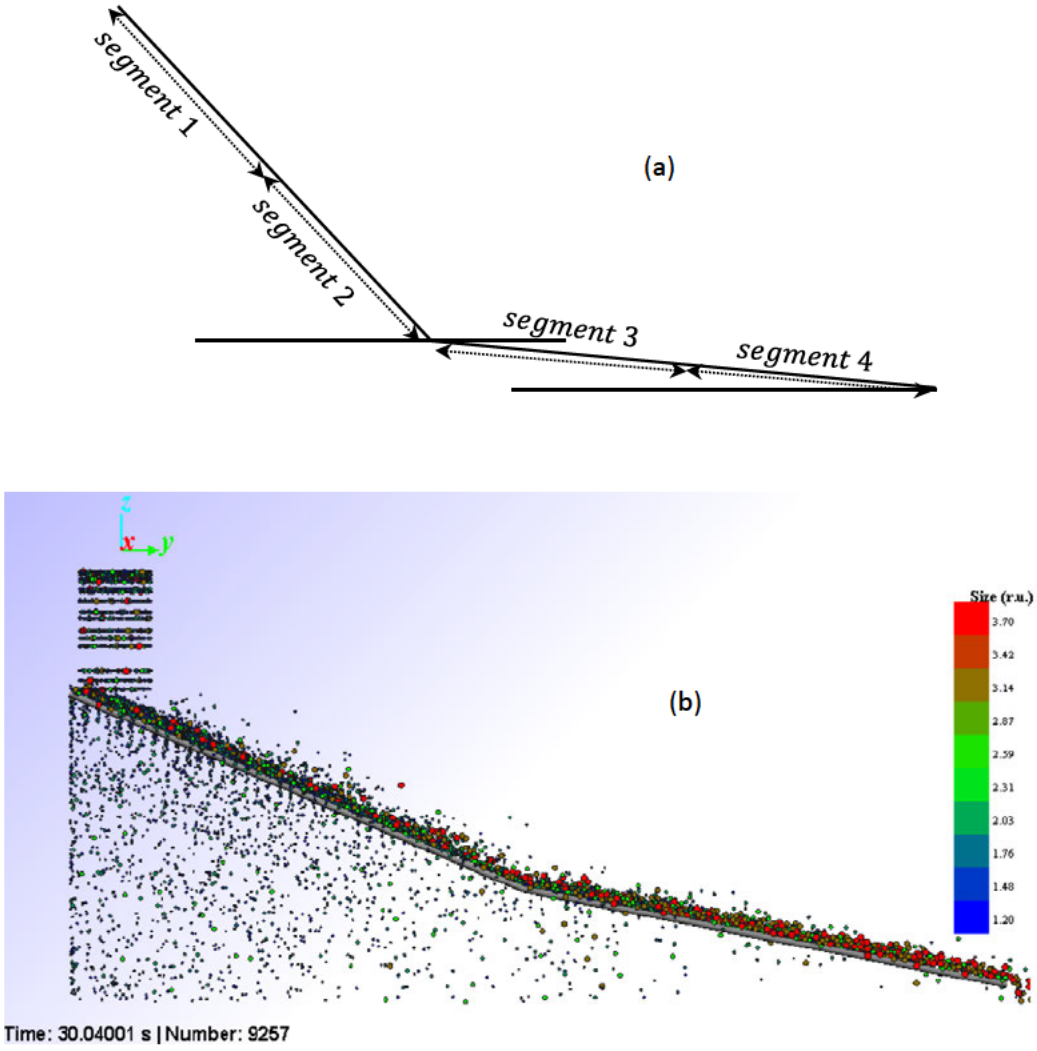

Figure 4-11 (a) Schematic design of multi-deck/banana screen, (b) simulation snapshot of screen with varied inclination angle (where $\theta 1 = 23°$, $\theta 2 = 11°$, $f = 25$ Hz and $A = 2.5$ mm).

Figure 4-12 shows the overflow partition curves for two two-deck screens obtained from DEM and the process model. For the same two-deck screen, the process model result is in good agreement with the DEM result.

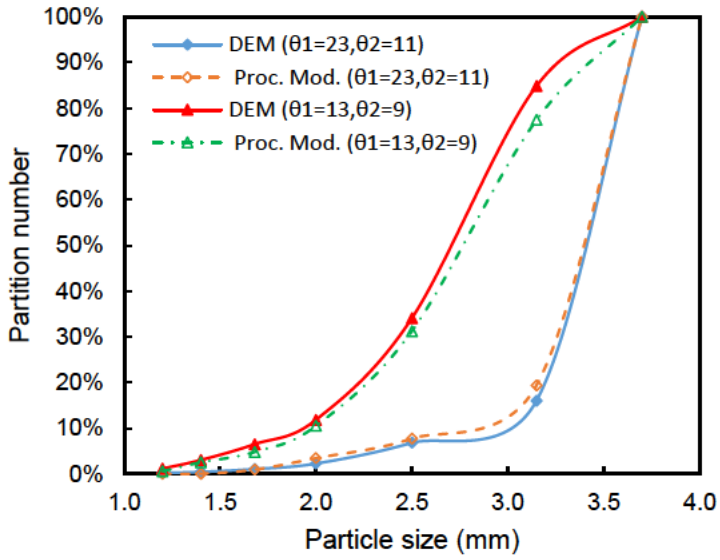

Figure 4-12 Overflow partition curve for varied inclination angle and comparison between DEM and ML results (A = 2.5mm and f = 20Hz).

To maintain the validity of the data model, ranges θ_1 and θ_2 should be within the range of the training data. First, $\theta_1 + \theta_2 = 22°$ and θ_1 were set to 11, 13, 14 and 15 degrees respectively; correspondingly, θ_2 was set to 11, 9, 8 and 7 degrees respectively. The overflow partition curves for different combinations θ_1 and θ_2 are shown in Figure 4-13. The curve shifts leftwards with increasing θ_1, showing a general decrease of passing as the first deck became steeper, even though the second deck became flatter (i.e., θ_2 decreased). This trend indicates that under the considered scenarios, a steeper first deck and flatter second deck is not an effective way to increase overall passing.

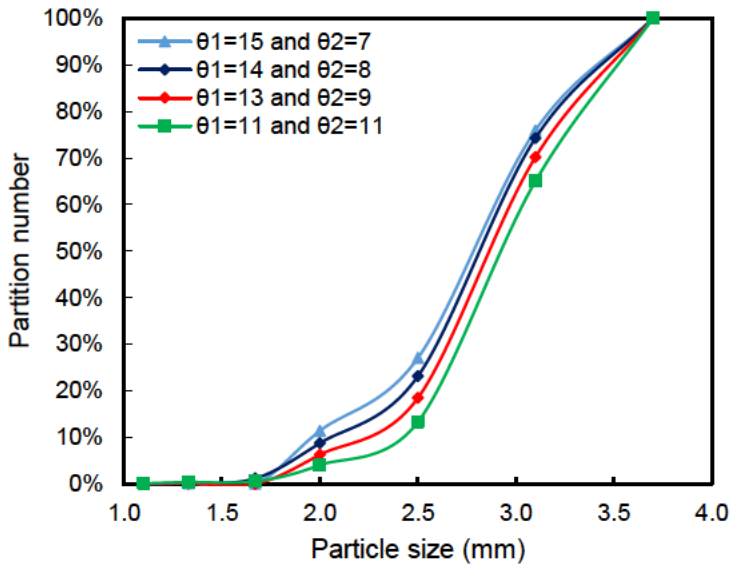

Figure 4-13 Overflow partition curves for different combination inclination angle of multi-deck screen. (θ_1+ θ_2 = 22°, A =1.5mm, f = 20Hz).

The quantitative changes of the screening performance parameters d_{50} and E_p are further shown in Figure 4-14. As can be seen, d_{50} decreases monotonically with the increase of θ_1. However, E_p initially decreases with increased θ_1, then increases, resulting from changes in d_{25} and d_{75}. From the partition curves it can be seen that the decrease in passing rate of small particles is more significant than that of large particles; therefore, the partition curve becomes slightly steeper with increasing θ_1. However, when θ_1 is very large, the decrease of the passing rate of small particles also reduces, and hence E_p increases.

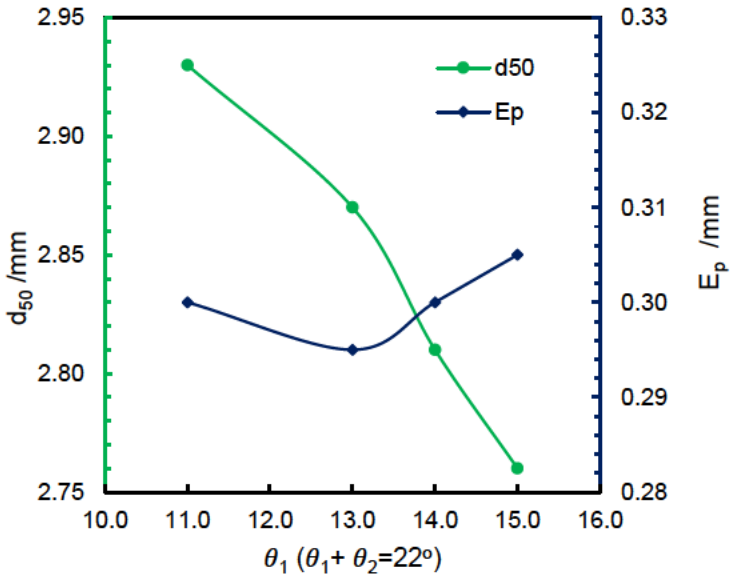

Figure 4-14 d_{50} and E_p as a function of θ_1 (for A = 1.5mm, f=20Hz and θ_1+ θ_2=22°).

Figure 4-15 shows the overflow partition curves of another series of combinations under the constraint $\theta_1 + \theta_2 = 34°$. Regardless, a steeper first deck leads to lower overall passing rates for all particle sizes, although the second deck is flatter. The best performance for the lowest θ_1 can also be reflected in the corresponding highest d_{50}. However, E_p shows more complicated changes, similar to the previous series. With increasing θ_1, E_p initially decreases because the decrease of the passing rate of small particles is higher than that of large particles, then E_p increases when θ_1 is very high and the partition curve becomes the least steep. In general, the complicate change of E_p indicates that the effect of θ_1 (with corresponding change of θ_2) on the passing of different size particles is complicated, while the increase of θ_1 will be more effective on small size particles initially.

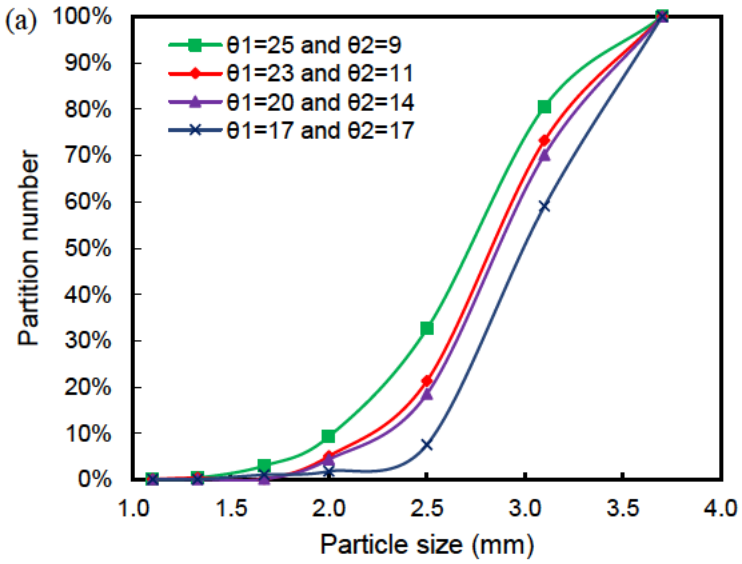

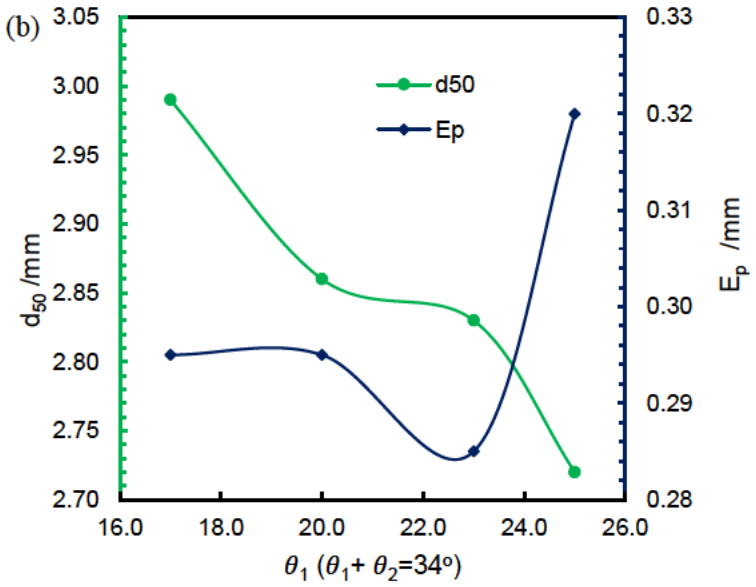

Figure 4-15 Process model predicted two-deck screen sieving performance as a function of the inclination angle of the first deck (f = 20Hz, A =1.5mm, $\theta_1+\theta_2$=34°): (a) overflow partition curves, and (b) d_{50} and E_p.

4.4.3.2 Varied vibration conditions

Vibration conditions may be set differently for different parts of the screen to achieve optimal operation (AstecMobileScreens 2008; Jiang, H, Zhao, Duan, Liu, et al. 2017; Jiang, H, Zhao, Duan, Yang, et al. 2017; Jiang, H, Zhao, Qiao, et al. 2017). In the process model, different vibration conditions were set for each segment. Initially, the model was applied to a screen with two decks under different vibration conditions. As shown in Figure 4-16, the original incline screen was divided into two separate decks. The first deck consisted of original segments 1 and 2, while the second deck consisted of original segments 3 and 4. The vibration amplitude and frequency for the first deck were A_1 and f_1 respectively, while those for the second deck were A_2 and f_2 respectively. Both A_1 and A_2 and f_2 and f_1 could differ. Because of the different vibrations, the second deck had to be lower, and a virtual vertical baffle was set at the left side of the second deck to avoid particle leakage. For both decks, the inclination angle was fixed at 11°, and the feeding materials were fixed to that of Feed 1 (Table 4-5).

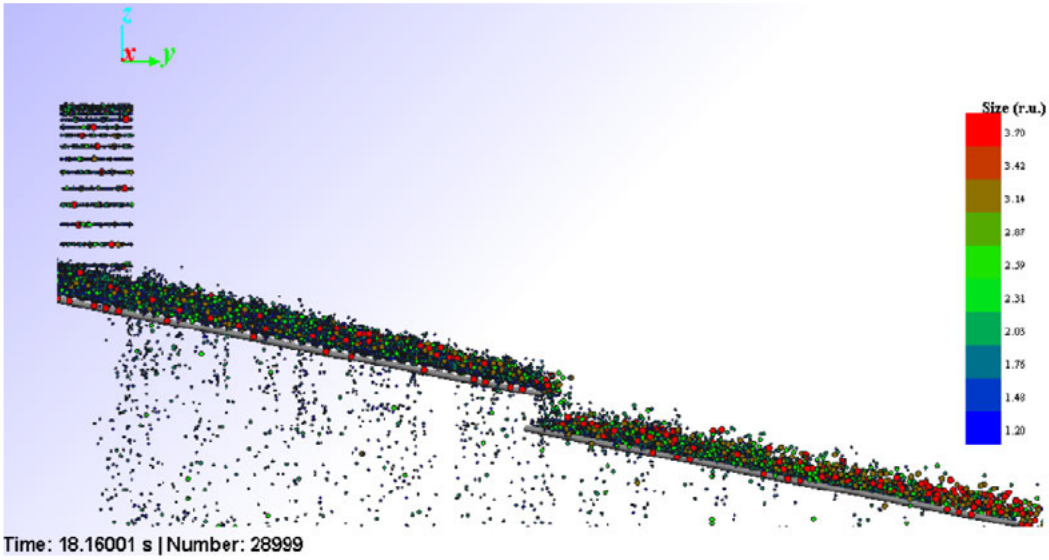

Figure 4-16 Simulation snapshot of varied vibration screen (where, f_1=14Hz, f_2=16Hz, A = 2.5mm and θ=11°.

Figure 4-17 shows the overflow partition curves for the screen under different conditions obtained from DEM and the process model. The good agreement demonstrates the effectiveness of the process model for modelling this kind of screen. Some discrepancies are probably due to that the two decks are disconnected and the abrupt falling of particles from the first deck to the second deck may bring some errors.

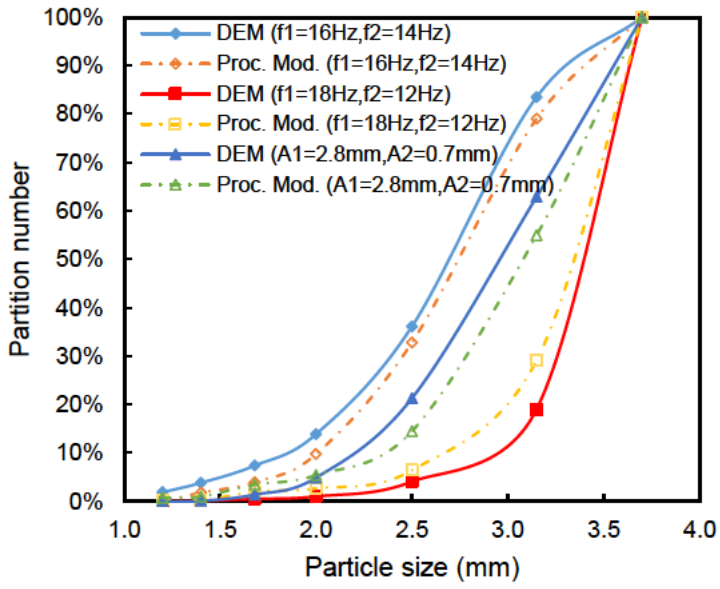

Figure 4-17 Comparison of overflow partition curves for varied vibration screens obtained from DEM and process model (where, θ = 11°).

By using constant vibration frequency (f_2), screen performance decreased with increased frequency (f_1). Lower frequency is effective for a better sieving, as is indicated by decreased d_{50} with increased f_1 and E_p. For $f_1 = f_2 = 15$, sieving was less effective for continuous flow, likely because particle flow and bounce behaviour change under varied vibration conditions.

Next, the process model was used to assess different vibration conditions applied to the two decks. To make the results comparable, $A_1 = A_2$ and $f_1 + f_2$ = constant or $f_1 = f_2$ and $A_1 + A_2$ = constant. The overflow partition curves under different vibration combinations are shown in Figure 4-18. Generally, screen performance is worse with higher vibration amplitude or frequency of the first deck, although that of the second deck was lower corresponding to the constraint.

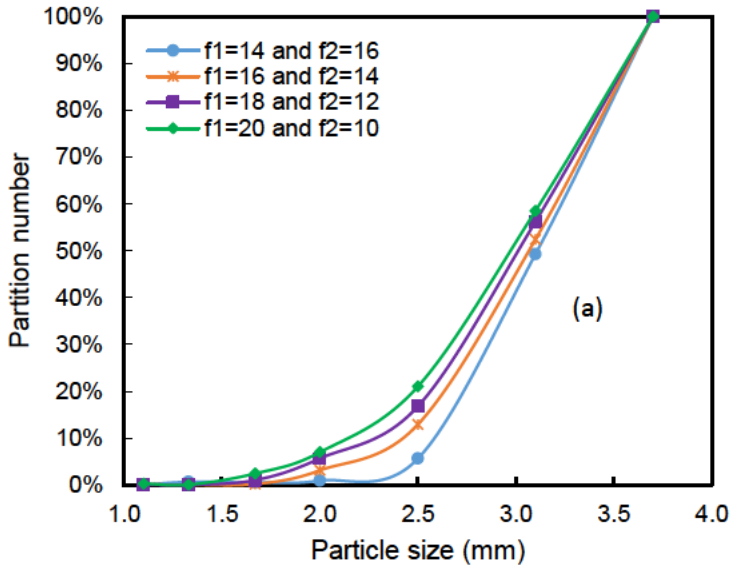

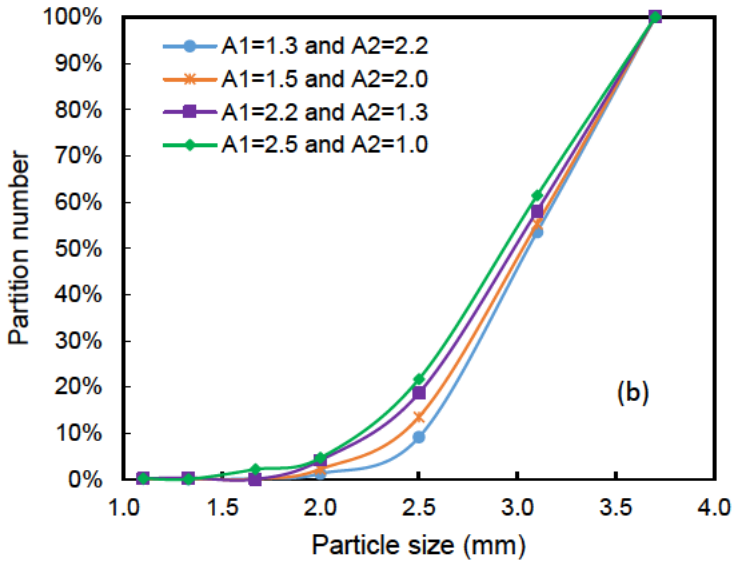

Figure 4-18 Overflow partition curves for varied vibration screen predicted by process model: (a) f_1 and f_2 vary under $f_1 + f_2 = 30$Hz and $A_1 = A_2 = 1.5$ mm, and (b) A_1 and A_2 vary under $A_1 + A_2 = 3.5$mm and $f_1 = f_2 = 20$Hz.

Figure 4-19 presents an overview of the vibration condition effects of the varied vibration screen. In particular, d_{50} decreased and E_p increased with increasing f_1 and A_1 (Figure 4-19a and Figure 4-19b respectively (Dong, K, Wang & Yu 2013). The changes were monotonical and consistent, without any obvious fluctuations like the effects of inclination angle. These results indicate that in the two-deck screens considered, performance was largely controlled by the first deck and deteriorated by increasing A and f similar to screen incline (Dong, K, Wang & Yu 2013; Zhang, B et al. 2016; Zhao, L et al. 2011). Although the second deck had decreased vibration amplitude and frequency, which improve the passing rate of the second deck, the compensation cannot meet the performance loss of the first deck. Therefore, the overall performance decreased.

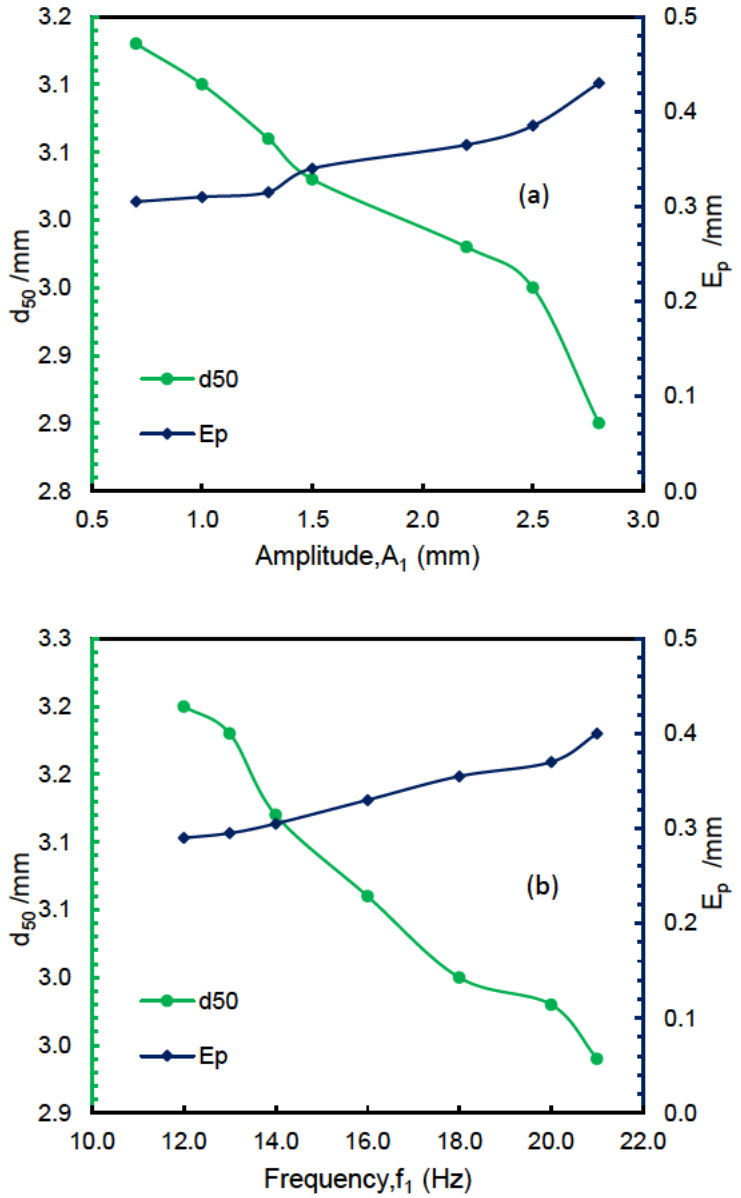

Figure 4-19 E_p and d_{50} of varied vibration screen as a function of: (a) vibration amplitude of the first deck, under $A_1 + A_2 = 3.5$mm and $f_1 = f_2 = 20$Hz; and (b) vibration frequency of the first deck, under $f_1 + f_2 = 30$Hz and $A_1 = A_2 = 3.5$mm.

4.5 Conclusions

In the present study, a physics-informed machine learning process model was developed for an inclined vibrating screen and then applied to other screens with different inclination angles or vibration conditions in different segments of the screen. Assuming in a segment the flow was macroscopically steady in each segment, and the passing of particles was dependent only on

local conditions, machine learning was used to construct the local passing function based on the particle size distribution of the inlet flow, vibration conditions and inclination angle of the segment. The data used for the machine learning were obtained from DEM simulation. With the data model of the local passing function, the process model was developed using mass continuity between segments.

The process model can predict the overflow partition curve in good agreement with DEM for the original simulated inclined screen under different operational conditions. However, the model was able to assess the effects of the controlling variables on the sieving performance parameters much more efficiently than the DEM. Thus, if training data were obtained on-site, the model could be used for real applications.

In addition, the model was very flexible in handling different operational conditions in different parts of the screen, which could be used to model complex multi-deck screens with different vibration conditions and/or different slopes on different decks. It is worth noting that in constructing these different screens, the machine learning based local passing function was the same as that obtained from the original incline screen.

This work paves the way for combining DEM simulation, data modelling and process modelling to guide smart design and control of industrial screens.

Nomenclature

A	Vibration amplitude
A_1	Combination vibration amplitude for upper segment
A_2	Combination vibration amplitude for lower segment
d_i	Particle size (mm)
E_p	Probable error
f	Vibration frequency
f_1	Combination frequency for upper deck
f_2	Combination frequency for lower deck
f_P	Local passing rate function
$\boldsymbol{F}_{ij}^{n}$	Normal contact force
$\boldsymbol{F}_{ij}^{t}$	Tangential contact force
$\boldsymbol{g}$	Gravitational acceleration

$\boldsymbol{I}$	Moment of inertia of the particle
I_i	Feed particles rate from a segment
m	Mass of particle
n_i	Number of feed particles rate
O_i	Overflow rate from a segment or feed to the downstream segment
P_i	Particles passing rate
R^2	Coefficient of determination
R_i	Radius of particle *i*
R_j	Radius of particle *j*
t	Time
Y	Young's modulus

Greek letters

γ_n	Normal damping coefficient
ξ_n	Relative normal displacement
ξ_s	Total tangential displacement
θ	Inclination angle of the screen
θ_1	Combination inclination angle upper deck
θ_2	Combination inclination angle lower deck
ρ	Density (kg/m^3)
$\tilde{\sigma}$	Poisson ratio
μ_r	Rolling friction coefficient
μ_s	Sliding friction coefficient
ω	Particle angular velocity (s^{-1})

Subscripts

i	Particle *i*
j	Particle *j*
i j	Between particles *i* and *j*

Abbreviations

ANN	Artificial neural network

DEM	Discrete element method
GPR	Gaussian process regression
SVM	Support vector machine

CHAPTER V: Process model of inclined double layer vibrating screen based on DEM and machine learning

5.1 Introduction

Screens are commonly used worldwide for the separation and sizing of materials according to the size, especially for granular materials in a variety of industrial sectors including mining and pharmaceuticals (Dong, K, Wang & Yu 2013; Dong, K, Yu & Brake 2009; Li, Z & Tong 2017; Qiao et al. 2018; Wolff 1954; Xiong et al. 2017). The screening processes are complicated and difficult to model while considering numerous controlling variables in screen processes and screen geometries (Asbjörnsson et al. 2016; Wolff 1954; Zhang, B et al. 2016).

The multi-layer screen could perform size separation in mineral processing applications such as ore, coal, fine materials and granular materials (Makinde, Ramatsetse & Mpofu 2015; Wills & Finch 2016). The multi-layer screen is used for high-tonnage materials where both capacity and efficiency are comparatively important (Makinde, Ramatsetse & Mpofu 2015; Peng, Jiang, et al. 2019). The multi-layer screen is known as the vibrating screen while having more than one screening layer. The feed is introduced to the top coarse screen on a multi-layer screen, where the undersize fall to the lower screen layer due to the different screen surface structures. As a result, it produces a range of sized fractions than a single screen. The steep configuration and layers of sections induce the rapid flow of feed materials at the end of the multi-layer screen while simultaneously separating fine materials. The multi-layer screen's segregation capacity is significant, which was reported to be three or four times that of regular vibrating screens (Dong, K, Wang & Yu 2013; Dong, K, Yu & Brake 2009; Makinde, Ramatsetse & Mpofu 2015; Peng, Jiang, et al. 2019; Wills & Finch 2016).

The process is more critical than a single-layer screen while considering screen geometry, feeding of materials in different layers and controlling variables. The fine particles screen out more rapidly than a thick bed. At the discharge end of the multi-layer screen, the slope of screen reduces to slow down the existing material, to sieve the fine materials and to enable a better screening efficiency of the close-range particles (Cleary, PW, Wilson & Sinnott 2018; Dong, K, Wang & Yu 2013; Dong, K, Yu & Brake 2009; Makinde, Ramatsetse & Mpofu 2015; Napier-Munn & Wills 2006; Peng, Jiang, et al. 2019; Wills & Finch 2016).

Fundamental models of particles passing through screen meshes are based on probability theory (Dong, K, Wang & Yu 2013; Kapur, Ball & Fuerstenau 1977; Soldinger 1999, 2000; Standish & Meta 1985; Subasinghe, G, Schaap, W & Kelly, E 1989) or the kinetic approach (Ferrara, Preti & Schena 1987; Standish, Bharadwaj & Hariri-Akbari 1986; Subasinghe, Schaap, W & Kelly, EG 1989). The probabilistic approach has been used to predict screening

results of different particle sizes, screen lengths and vibration conditions with reasonable accuracy (Subasinghe, G, Schaap, W & Kelly, E 1989). By using probability process, it is possible to determine the influence of the feed rate and the change in proportions of fine material (Soldinger 1999, 2000). The rate of passage depends on the probability that the particles will pass through the apertures and the amount of free material on the screen surface (Soldinger 1999). Moreover, the sieving speed of undersized particles, the relationship between the sieving speed and the remaining materials are described in kinetic (Standish 1985; Standish & Meta 1985) modelling. At very low vibrations, the screening process is known to lose efficiency because of choking (Esfandiary 2014). Furthermore, the probability of a particle passing through a screen is considerably lower for cube-shaped particles than spheres (Calanog & Geiger 1973). It is possible to obtain a single equation for screen efficiency, which would be valid for crowded, separate and mixed conditions, which would very useful for characterising the screening process with few parameters (Ferrara, Preti & Schena 1987).

The screening process includes complex particle–particle and particle–wall interactions, which are difficult to study empirically. Recently, research on discrete particle simulation techniques and computer technology has expanded rapidly worldwide. The DEM is becoming more popular for modelling particle flow. For example, the DEM can model particle dynamics and obtain information at the particle scale (Zhu, HP et al. 2007). The DEM can also provide both macroscopic and microscopic view in granular systems and can consider particles with non-spherical or irregular shapes (Lu, G, Third, JR & Müller, CR 2015). The primary limitation of the DEM is its high computational requirements. To minimise runtimes, the number of particles needs to be kept as small as possible. It is especially important to keep array sizes small for neighbouring particles (Asmar et al. 2002; Zhu et al. 2008).

Many opportunities and challenges exist for the application of artificial intelligence (AI) in mineral processing. AI modelling can help to minimise the complex and computational requirements, solve critical non-linear problems and store data. Artificial neural network (ANN) modelling has been applied to rotating drums to predict particle flow characteristics and vibrating screen performance (Li, Y et al. 2021; Shanmugam et al. 2021; Zhao, Z et al. 2021). Machine learning modelling has also been used to predict particle flow in rotating drums (Li, Y et al. 2020), monitor particle size in the grinding process (Pani & Mohanta 2014, 2015) and control parameters of ball mill prediction (Tang, J et al. 2010). Similarly, SVM modelling has been used to predict screen performance and optimise operation parameters (Li, Z et al.

2019; Li, Z et al. 2015; Zhang, B et al. 2016). Machine learning results often show a good fit with empirical results. The machine learning model also helps to identify abnormal data and determine estimation errors between test results and data drives.

In recent work (Arifuzzaman, S. M., Dong, Kejun & Yu, Aibing 2022), a process model was used to examine inclined vibrating single-layer screens to better understand the sieving process. In the present study, a process model is proposed that combines DEM results and machine learning modelling of inclined double-layer screens to further understand the local sieving process. The proposed model assumes steady flow across a double-layer screen. The process model considers the inlet, passage, overflow, local particle properties and operational conditions. The developed model could be used to predict sieving performance under different conditions. In particular, the model could be applied with various feed rates, screen inclines, aperture shapes and vibration conditions.

The study is structured as follows: Section 5.2 represents the DEM methodology and screen simulation conditions. The process model of an inclined double-layer screen and deck-to-deck local function analysis is defined in Section 5.3. In Section 5.4, a double-layer screening process model with various feeding and vibration conditions is optimised and underperforming machine learning prediction studies are demonstrated. The conclusions are presented in Section 5.5.

5.2 Simulation method and conditions

5.2.1 Discrete element method (DEM)

For particle flow along an inclined double layer screen, the DEM was used to trace the motion of individual particles according to mutual interactions. In the DEM, the motion of each particle is governed by Newton's second law (Cundall & Strack 1979). For a spherical particle i, its translational motion and rotational motion are respectively determined by:

$$m_i \frac{d\boldsymbol{v}_i}{dt} = \sum_j (\boldsymbol{F}_{ij}^n + \boldsymbol{F}_{ij}^s) + m_i \mathbf{g} \qquad \text{(Eq. 5.1)}$$

$$\boldsymbol{I}_i \frac{d\boldsymbol{\omega}_i}{dt} = \sum_j (\boldsymbol{R}_{ij} \times \boldsymbol{F}_{ij}^s - \mu_r R_i \left|\boldsymbol{F}_{ij}^n\right| \hat{\boldsymbol{\omega}}_i) \quad \text{(Eq. 5.2)}$$

where $\boldsymbol{v}_i$, $\boldsymbol{\omega}_i$, m_i and $\boldsymbol{I}_i$ are the translational and angular velocities, mass and moment of inertia of particle i respectively, $\boldsymbol{g}$ is the gravitational acceleration, $\boldsymbol{R}_{ij}$ is the vector pointing from the centre of particle i to the contact point with particle j. $\boldsymbol{F}_{ij}^n$ and $\boldsymbol{F}_{ij}^s$ are the normal and tangential contact forces respectively, which can be determined as (Brilliantov et al. 1996; Langston, Tüzün & Heyes 1995):

$$\boldsymbol{F}_{ij}^n = \left[\frac{2}{3}\frac{Y}{1-\tilde{\sigma}^2}\sqrt{\bar{R}}\xi_n{}^{3/2} - \gamma_n \frac{Y}{1-\tilde{\sigma}^2}\sqrt{\bar{R}}\sqrt{\xi_n}(\boldsymbol{v}_i \cdot \hat{\boldsymbol{n}}_{ij})\right]\hat{\boldsymbol{n}}_{ij} \quad \text{(Eq. 5.3)}$$

$$\boldsymbol{F}_{ij}^s = -\mu_s|\boldsymbol{F}_n|[1-(1-\frac{min(\xi_s,\xi_{s,max})}{\xi_{s,max}})^{3/2}]\hat{\boldsymbol{\xi}}_s \quad \text{(Eq. 5.4)}$$

where Y is Young's modulus, $\tilde{\sigma}$ is the Poisson ratio, γ_n is the normal damping coefficient, μ_s is the sliding friction coefficient, ξ_s is the total tangential displacement and $\bar{R} = R_i R_j/(R_i+R_j)$, $\xi_{s,max} = \mu_s[(2-\tilde{\sigma})/2(1-\tilde{\sigma})]\xi_n$, $\hat{\boldsymbol{n}}_{ij} = (\boldsymbol{R_i} - \boldsymbol{R_j})/\left|\boldsymbol{R_i} - \boldsymbol{R_j}\right|$. The second term of the torque results from the rolling resistance between two contact particles resulting in elastic hysteretic losses or viscous dissipation, where μ_r is the rolling friction coefficient and $\hat{\boldsymbol{\omega}}_i = \boldsymbol{\omega}_i/|\boldsymbol{\omega}_i|$ (Zhou, YC et al. 1999; Zhu, HP et al. 2007). The above equations ((Eq. 5.1-(Eq. 5.4) calculate the interactions between particles and the system wall (i.e., contact between particles and a finite polygon surface). Van der Waals force and capillary force between particles are not considered because the coarse particles are dry. The wall is modelled as a plane with the same material properties as the particles. Under vibration, the position and velocity of the wall are updated in every time step, and the values are used to calculate the particle–wall interactions. The time step is determined by $dt = 0.1\sqrt{m/k}$, where m is the mass of a particle and k is the estimated spring constant when the normal overlap is 10% of the particle diameter. This is based on the natural period of oscillation of the equivalent spring when using the Hertz contact force model (Hertz 1882). In a multi-size system, the time step is calculated for each type of particle and the minimum time step is used. Simulations were conducted using the university in-house DEM program, which has been validated for various systems (Amirifar et al. 2018, 2019; Dong, K, Wang & Yu 2013; Dong, K, Yu & Brake 2009).

5.2.2 Simulation condition

In the present study, an inclined double layer screen was considered (Dong, K, Wang & Yu 2013). The deck consisted of a flat surface uniformly perforated with (i) top layer (L1) square apertures of size 3.5 × 3.5 mm spaced 3.0 mm apart and (ii) rectangular apertures of size 3.5 × 1.75 mm spaced 3.0 mm apart. The left side of the deck was the feed end while the right side was the discharge end. The length, width (in the x-direction), and thickness of the deck were 600 mm, 26 mm and 2 mm, respectively. Periodic boundary conditions were applied in the *x*-direction (i.e., front and rear) to reduce computational effort. The screening study was initiated by discharging the mixture of particles (d_i) and feeding to the top deck of the inclined double-layer screen (Figure 5-1). The screen was then vibrated under the vibrational conditions. The particle size distribution, material properties and feed rate of the particles are listed in Table 5-1. Step 1, the feed particles fall and hit the vibrating screen (L1) deck, particles pass through the decks and report to the underflow, or flow along the screen to exceed the discharge end and report to the overflow, as shown in Figure 5-1. Step 2, the particles fall from the top layer (L1) as the feed for the bottom layer (L2). Similarly, particles pass through the decks from the bottom layer and report to the underflow, or flow along the screen to exceed the discharge end and report to the overflow, as shown in Figure 5-1b. The simulated data were only collected at the steady state in this analysis. Periodic boundary conditions were applied in the x-direction (i.e., front and rear) to reduce the computational effort.

Table 5-1 List of parameters used in the simulations.

	d_1	d_2	d_3	d_4	d_5	d_6	d_7
Particle size, d_i (mm)	1.10 to 1.25	1.3 to 1.45	1.50 to 1.73	1.8 to 2.05	2.5 to 2.55	3.05 to 3.2	3.65 to 3.75
Feed rate n_i (num/s)	n_1	n_2	n_3	n_4	n_5	n_6	n_7
	3300 to 5300	2050 to 3300	1250 to 2000	1000 to 1500	400 to 950	200 to 1250	100 to 200
Particle density, (kg/m^3)	7500						
Young's modulus (N/m^2)	1×10^7						
Damping coefficient, γ_n	Particle-particle:2×10^{-4}; particle-wall: 2×10^{-4}						

Sliding friction coefficient, μ_s	Particle-particle: 0.3; particle-wall: 0.5
Rolling friction coefficient, μ_r	Particle-particle: 0.01; particle-wall: 0.01
Vibration frequency (Hz), f	20, 25, 30, 35, 40, 50 and 60
Vibration amplitude (mm), A	1.5, 2.0, 2.5 and 3.0
Vibration motion	Sinusoidal, both along y and z directions.
Incline angle (°), θ	7, 9, 11, 13, 15, 17 and 22

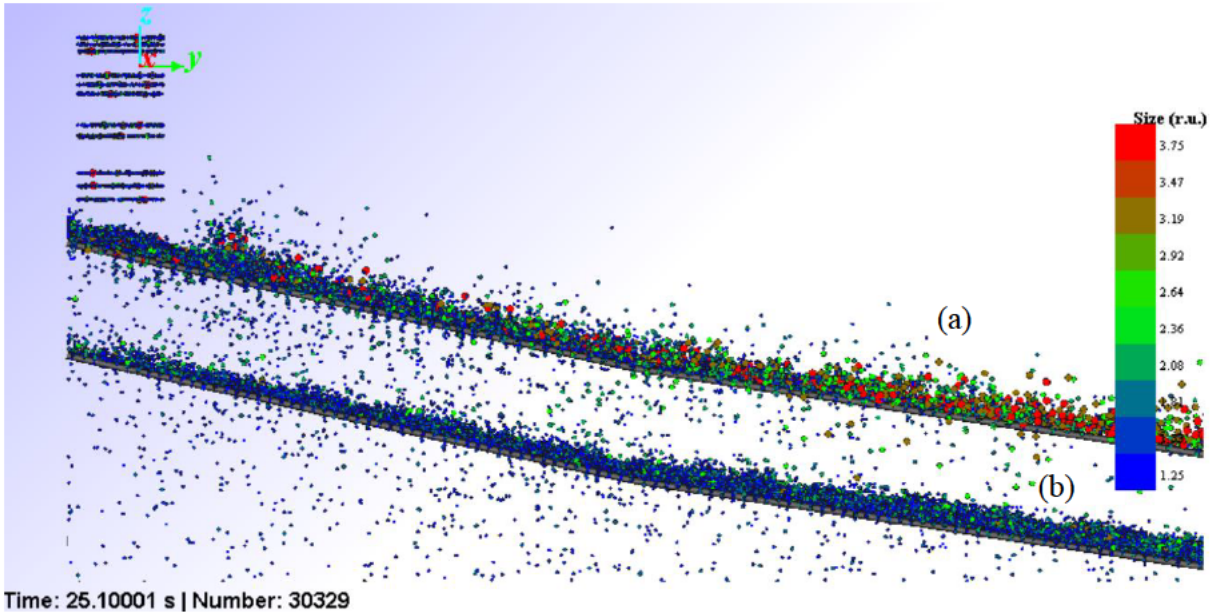

Figure 5-1 Snapshots of simulation using double layer inclined screen with local part or deck with steady state condition, (a) top layer (L1) : A_1 =2 mm, f_1=30Hz, θ =11° and (b) bottom layer (L2): A_2 =2.5 mm, f_2 =25Hz, θ =11°.

5.3 Process model based on machine learning

Here, a process model of an inclined double layer screen based on machine learning was proposed. As shown in Figure 5-3, under the steady state, particle passing behaviour was assumed to be uniform and steady in segment j of the screen. In particular, the input flow $\{d_i, I_i\}^j$, overflow $\{d_i, O_i\}^j$ and passing flow $\{d_i, P_i\}^j$ were all constant, where d_i is the particle size of the ith component in the particle mixture, and I_i, O_i and P_i are the flow rates of the input flow, overflow and passing of the ith component, respectively. The superscript j refers to the segment number j. If particle passing rate is assumed to be dependent on the input flow,

vibration conditions, inclination angle and aperture size, then a function to predict the passing rate $\{P_i\}$ can be determined by:

$$\{d_i, P_i\}^j = f_P\left(\{d_i, I_i\}^j, A, f, \theta\right) \quad \text{(Eq. 5.5)}$$

Where $f_P\left(\{d_i, I_i\}^j, A, f, \theta\right)$ is defined as the local passing rate function. For a multi-layer screen with different apertures in each layer, the passing rate is also dependent on the aperture dimensions. Theoretically, the local passing rate function should also include aperture dimensions as variables. But to obtain a comprehensive function, numerous cases with different aperture dimensions should be simulated. For the double layer screen in the present work, the local passing rate function for the single top layer inclined screen was already developed (Arifuzzaman, S. M., Dong, Kejun & Yu, Aibing 2022). The bottom layer screen had decreased the aperture dimensions. Therefore, another local passing rate function was trained for this layer. Hence, there were two local passing rate functions, $f_{P1}\left(\{d_i, I_i\}^j, A_1, f_1, \theta\right)$ and $f_{P2}\left(\{d_i, I_i\}^j, A_2, f_2, \theta\right)$, for the top and bottom layer screens, respectively.

The input flow, overflow and passing flow should satisfy mass continuity, which is determined by:

$$\{d_i, O_i\}^j = \{d_i, I_i\}^j - \{d_i, P\}^j \quad \text{(Eq. 5.6)}$$

Considering mass continuity between the segments, the overflow of upstream segment *j*-1 should be equal to the input flow of segment *j*, and the overflow of segment *j* equal to the input flow of the downstream segment *j* + 1, that is:

for the top layer screen,

$$\{d_i, I_i\}^{j,L1} = \{d_i, O_i\}^{j-1,L1} \quad \text{(Eq. 5.7)}$$

$$\{d_i, O_i\}^{j,L1} = \{d_i, I_i\}^{j,L1} - \{d_i, P\}^{j,L1} \quad \text{(Eq. 5.8)}$$

and for the bottom-layer screen,

$$\{d_i, I_i\}^{j,L2} = \{d_i, O_i\}^{j-1,L2} + \{d_i, P_i\}^{j,L1} \quad \text{(Eq. 5.9)}$$

$$\{d_i, O_i\}^{j,L2} = \{d_i, I_i\}^{j,L2} - \{d_i, P_i\}^{j,L2} \quad \text{(Eq. 5.10)}$$

The model is further illustrated in layer screen with segment-wise in Figure 5-2. If the vibrating screen is divided into different segments and the local passing rate functions have been obtained, $f_{P1}\left(\{d_i, I_i\}^j, A_1, f_1, \theta\right)$ and $f_{P2}\left(\{d_i, I_i\}^j, A_2, f_2, A_x, A_y, \theta\right)$, the sieving process from feed end to discharge end can be predicted, with the feed rate as the initial input flow of the first segment. In this process model, two local passing functions are considered for the double layer screen. Ideally, the aperture size can be included in the function, but it needs considerable data for different apertures. In this work, only two apertures were considered, and hence two functions were used.

However, f_p has many input variables, such as particle properties and operational conditions, which makes the relationship very complex and non-linear. It would be very difficult to develop this function in a conventional way. In this work, the function was built by applying machine learning to the database generated by DEM simulation. Each screen layer was divided into four segments from the feed end to the discharge end (Figure 5-2b). For each segment of the top layer screen, its input flow rate $\{d_i, I_i\}^{j,L1}$, output flow (i.e., overflow) rate $\{d_i, O_i\}^{j,L1}$ and passing flow rate $\{d_i, P\}^{j,L1}$ were calculated as the mean value in the steady state. Similarly, for each segment of the bottom layer screen, its input flow rate $\{d_i, I_i\}^{j,L2}$, output flow rate $\{d_i, O_i\}^{j,L2}$ and passing flow rate $\{d_i, P_i\}^{j,L2}$ were calculated. Different machine learning models were then applied to the data. The model with the highest accuracy was used, which will be discussed in the following section. Different segments were combined together in the machine learning model training. Therefore, the model has the assumption that f_p depends only on local flow conditions.

After f_{p1} and f_{p2} were modelled by machine learning, they were used in the process model described by (Eq. 5.5) – (Eq. 5.10). A MATLAB program was developed to calculate $\{P_i\}$ on the first segment according to the given $\{I_i\}$, A_1, f_1, A_x, A_y and θ; then, the inlet for the second segment was calculated by (Eq. 5.7) – (Eq. 5.8), and the passing rate $\{P_i\}$ for the second segment was predicted using the machine learning model of f_{p1} but with the conditions for the second segment. The third and remaining segments were modelled using a similar procedure. To calculate $\{P_i\}$ for the bottom layer, the top layer of passing particles was considered on the first segment according to the given $\{I_i\}$, A_2, f_2, A_x, A_y and θ; then, the inlet for the second segment was calculated by (Eq. 5.9)–(Eq. 5.10) considering the top layer passing and upper stream flow of particles to the lower deck. The passing rate $\{P_i\}$ for the second segment was

predicted using the machine learning model of f_{p2} but with the conditions for the second segment. The third and remaining segments were modelled using a similar procedure.

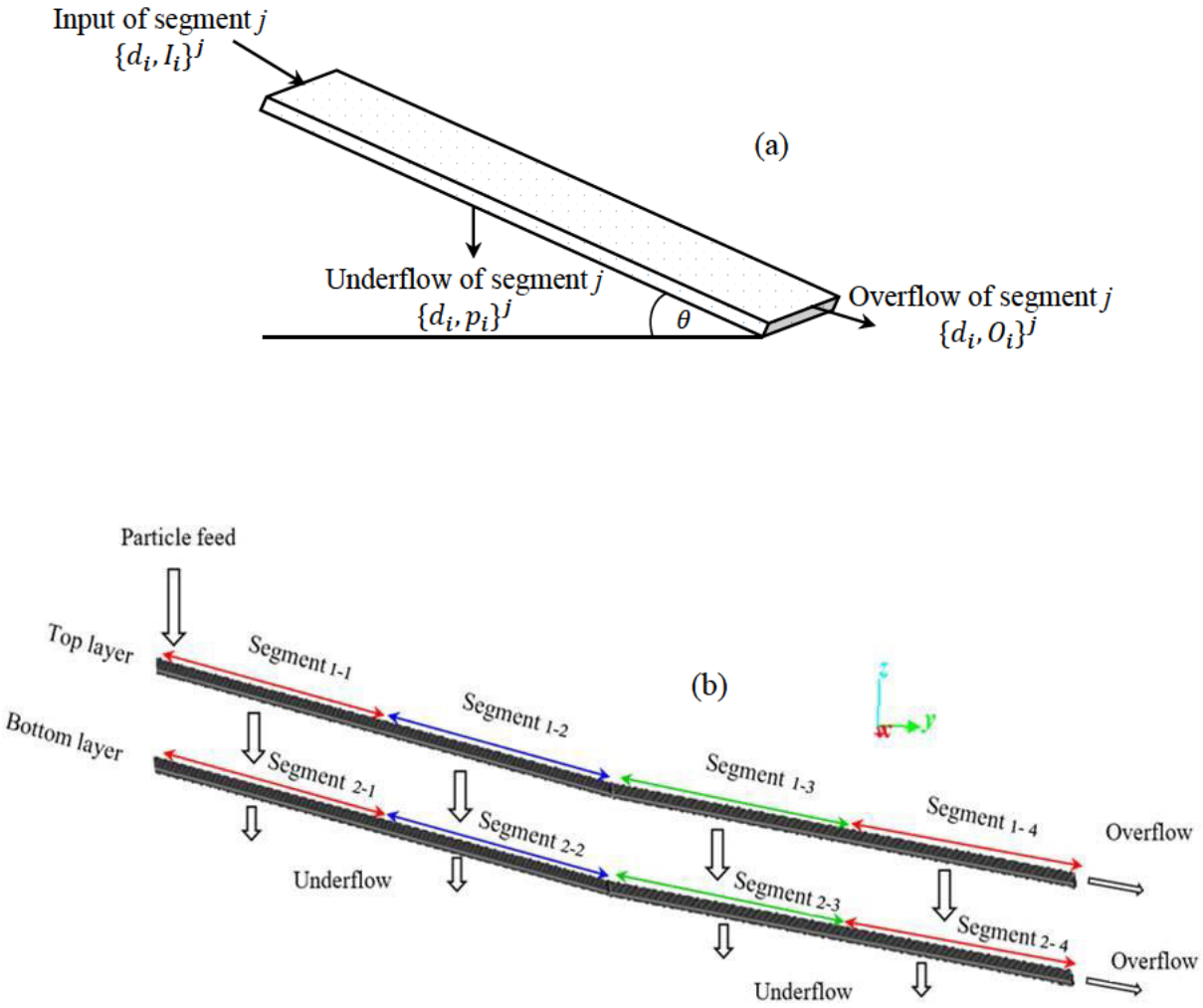

Figure 5-2 Schematics of (a) particle flow of segment j of the model inclined screen and (b) the double layer screen by segment.

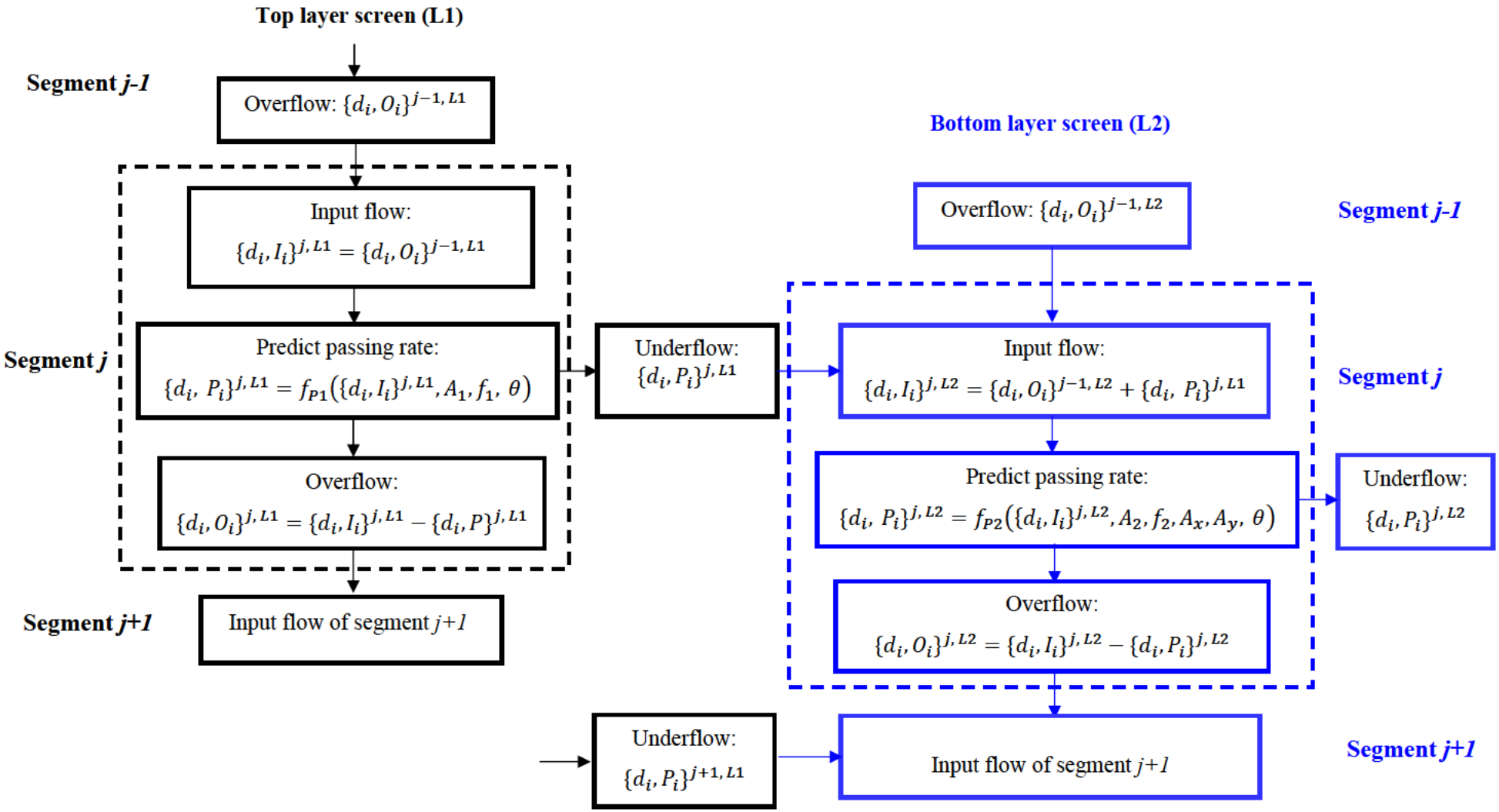

Figure 5-3 Process model flow chart of screening with segment-wise for double layer screen

5.4 Results and discussion

5.4.1 Machine learning model of process model for particles passing

As described above, the local passing functions f_{p1} and f_{p2} were used for prediction by training machine learning models with the DEM simulation data. The input variables were $\{d_i\}$, $\{I_i\}$, A and f for both layers of a segment. The simulated inclined screen was divided into four segments. For the first segment, $\{I_i\}$ was the feed rate $\{n_i\}$, while for other segments $\{I_i\}$ was calculated using (Eq. 5.7) – (Eq. 5.10). The output variables for the training were $\{P_i\}$. The variables and their ranges are listed in Table 5-2. The total training data contained (i) 640 sets of data for the top layer, obtained from 160 cases and (ii) 480 sets of data for the bottom layer, obtained from 120 cases, each simulation with four sets. The database was trained with linear, SVM and GPR regression machine learning models. The GPR models are nonparametric kernel-based probabilistic models for supervised machine learning. The GPR models work well on small datasets and can provide uncertainty measurements on predictions as well as allow prediction without prior fitting. The comparison of DEM and machine learning results of particles passing through the double-layer vibrating inclined screen are shown in Figure 5-4. Table 5-3 and Table 5-4 represent the performance of the machine learning models for particles passing along the screen. The squared exponential GPR model demonstrated higher accuracy in predicting results.

Table 5-2 Input and output variables used for process model database.

Top layer input	Used values	Output	Underflow
A_1	1.5, 2.0, 2.5 and 3.0	P_1	underflow of d_1
f_1	20, 25, 30, 40, 50, 60	P_2	underflow of d_2
θ	11	P_3	underflow of d_3
d_1	1.1, 1.2, 1.25	P_4	underflow of d_4
d_2	1.3, 1.4, 1.45	P_5	underflow of d_5
d_3	1.5, 1.68, 1.73	P_6	underflow of d_6
d_4	1.8, 2.0, 2.05		
d_5	2.5, 2.55		
d_6	3.05, 3.15, 3.2		
d_7	3.65, 3.70, 3.75		
n_1	4.08 - 5327.7		
n_2	5.28- 3301.74		
n_3	9.52 - 2029.28		
n_4	15.36 - 1523.52		
n_5	22.14 - 923.82		

n_6	30.16 - 1266.3		
n_7	100 - 200		
Bottom layer input	Used values	Output	Underflow
A_2	2.0, 2.5, 3.0, 3.5	P_1	underflow of d_1
f_2	20, 25, 30, 35, 40	P_2	underflow of d_2
θ	11	P_3	underflow of d_3
d_1	1.1, 1.2, 1.25		
d_2	1.3, 1.4, 1.45		
d_3	1.5, 1.68, 1.73		
d_4	1.8, 2.0, 2.05		
d_5	2.5, 2.55		
d_6	3.05, 3.15, 3.2		
d_7	3.65, 3.70, 3.75		
n_1	686.56 – 4391.86		
n_2	445.64 – 2846.08		
n_3	254.72 – 1862.18		
n_4	160.92 - 1645.92		
n_5	43.5 – 778.2		
n_6	2.16 - 506.48		

The R-squared values of the considered models are listed in Table 5-3 and Table 5-4, from which it can be seen that the squared exponential GPR regression model is the best model with very high accuracy (average R-squared is 0.95 for the top layer and 0.91 for the bottom layer).

Table 5-3 Performance of the machine learning models for particles passing along the screen of top layer.

Machine learning model for top layer (L1)	R^2 of P_1	R^2 of P_2	R^2 of P_3	R^2 of P_4	R^2 of P_5	R^2 of P_6	Average
Linear regression	0.94	0.93	0.90	0.83	0.62	0.53	0.792
Interaction linear regression	0.98	0.98	0.96	0.93	0.80	0.74	0.898
Robust linear regression	0.94	0.93	0.89	0.83	0.61	0.51	0.785
Stepwise linear regression	0.98	0.98	0.96	0.93	0.78	0.72	0.892
Rational Quadratic GPR	0.99	0.99	0.98	0.97	0.89	0.76	0.93
Squared exponential GPR	0.99	0.99	0.99	0.97	0.89	0.89	**0.95**
Matern 5/2 GPR	0.99	0.99	0.98	0.96	0.89	0.76	0.928
Exponential GPR	0.99	0.99	0.98	0.96	0.88	0.75	0.925
Linear SVM	0.93	0.91	0.88	0.80	0.57	0.48	0.762
Quadratic SVM	0.98	0.97	0.96	0.92	0.76	0.72	0.885
Cubic SVM	0.99	0.99	0.98	0.96	0.85	0.75	0.92
Fine Gaussian SVM	0.91	0.92	0.92	0.90	0.81	0.74	0.867
Medium Gaussian SVM	0.98	0.98	0.97	0.94	0.79	0.68	0.89
Coarse Gaussian SVM	0.95	0.94	0.91	0.82	0.54	0.38	0.757

Table 5-4 Performance of the machine learning models for particles passing along the screen of bottom layer.

Machine learning model for bottom layer (L2)	R^2 of P_1	R^2 of P_2	R^2 of P_3	Average
Linear regression	0.55	0.45	0.40	0.467
Interaction linear regression	0.62	0.51	0.50	0.543
Robust linear regression	0.44	0.26	0.08	0.26
Stepwise linear regression	0.66	0.46	0.50	0.54
Rational Quadratic GPR	0.87	0.79	0.73	0.797
Squared exponential GPR	0.95	0.91	0.87	**0.91**
Matern 5/2 GPR	0.87	0.81	0.72	0.8
Exponential GPR	0.85	0.78	0.70	0.777
Linear SVM	0.48	0.39	0.25	0.373
Quadratic SVM	0.72	0.63	0.57	0.64
Cubic SVM	0.57	0.54	0.58	0.563
Fine Gaussian SVM	0.61	0.54	0.43	0.527
Medium Gaussian SVM	0.61	0.55	0.52	0.56
Coarse Gaussian SVM	0.41	0.36	0.22	0.33

Figure 5-4 compares the partition curves obtained from the process model and DEM simulation. Under various vibration conditions, the results from the process model aligned well with the DEM results for both layers, which indicates that the process model is very accurate and universal.

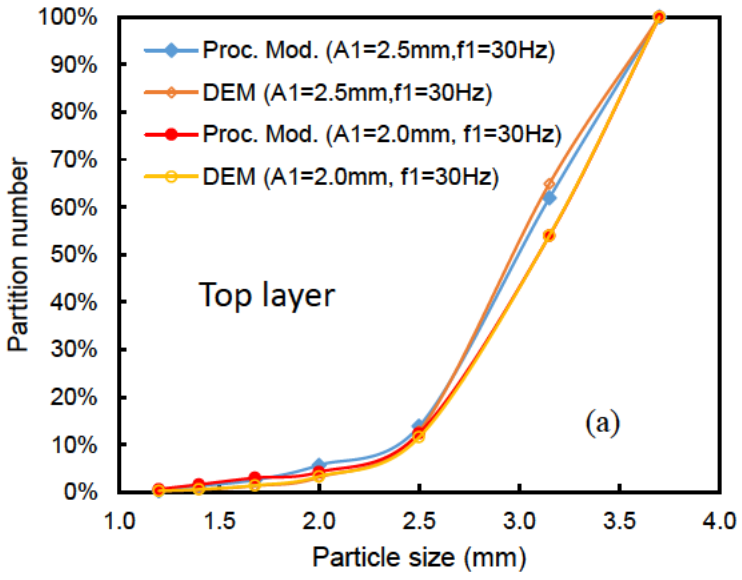

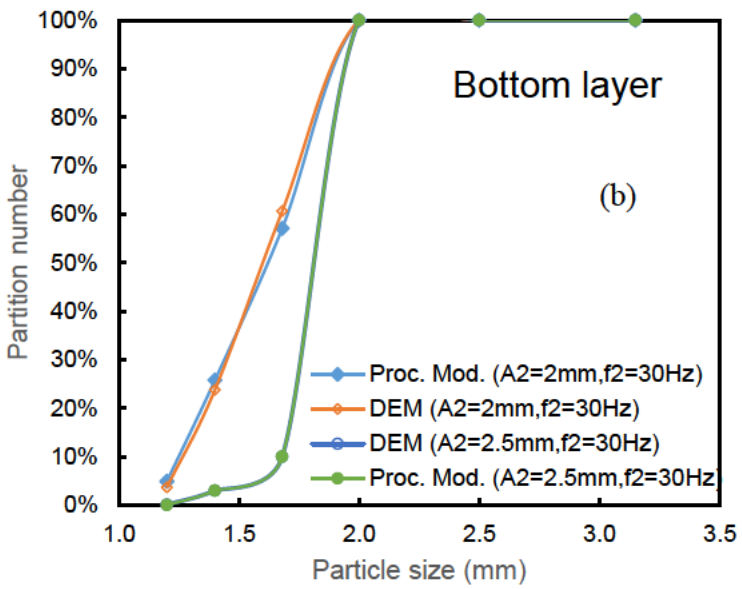

Figure 5-4 (a) Validation of ML and DEM results for top layer (L1) screen (where, A_2= 2.5mm and f_2=30Hz); and (b) validation of ML and DEM results for bottom layer (L2) screen (where, A_1= 2.0mm and f_1=30Hz)

5.4.2 Full process model for double layer inclined screen

The process model is further used to study the effect of particle size distribution on the screening performance. Three size distributions as listed in Table 5-5 are considered. In Feed-1, the volume ratios of different-sized particles were similar (Arifuzzaman, S. M., Dong, Kejun & Yu, Aibing 2022). In Feed-2, the volume ratios of small undersize particles decreased while the volume ratios of medium to near-mesh size particles increased. In Feed-3, the volume ratios of the near-mesh size particles were dominant. Considering Feed-1 to Feed-3, the medium size of the feeding materials increased while the total volume is kept constant. For large-size feed particles report to the top deck product, as they should since they are larger than the holes in the top deck. Very little finer material is retained on the top deck. Almost all this material passed through the bottom deck.

Table 5-5 List of feeding materials with different particle size distributions.

	Component *i*	1	2	3	4	5	6	7
	Category	small undersize	small undersize	small undersize	medium undersize	medium undersize	near-mesh undersize	oversize
	Feed Size (mm), d_i	1.1	1.33	1.67	2	2.5	3.1	3.7
Feed-1	Feed Rate (num/sec), n_i	5300	3300	2000	1500	800	550	200

(total feed rate = 39347.70348mm^3/sec)	Volume ratio	9.39%	10.33%	12.40%	15.97%	16.63%	21.80%	13.48%
Feed-2 (40663.76377 mm^3/sec)	Feed Rate (num/sec), n_i	4400	3200	1900	1200	950	700	200
	Volume ratio	7.54%	9.69%	11.39%	12.36%	19.11%	26.85%	13.04%
Feed-3 (41457.69214mm^3/sec)	Feed Rate (num/sec), n_i	3300	2050	1250	1200	745	1100	200
	Volume ratio	5.55%	6.09%	7.35%	12.12%	14.70%	41.39%	12.79%

Figure 5-5 shows E_p and d_{50} as a function of various feeding conditions against f_1 for the top layer screen from machine learning. In Figure 5-5a, E_p gradually increased with the increase in frequency (f_1) to a maximum of 40 Hz. E_p was lower at 30 Hz for Feed 2 and Feed 3 conditions. This is probably for the particle and aperture size of the top layer, where $f_1 < 25$ Hz helped to pass larger particles. Particles contacts with the number of larger-than-aperture sized particles helped them pass through the screen. High vibration conditions increased particle bounce and d_{50} was higher for Feed 3, which resulted in a high particle passing rate that decreased with the increase in vibration frequency (Figure 5-5b). Further, d_{50} was lower for Feed 2 and increased with increased vibration frequency at the top layer.

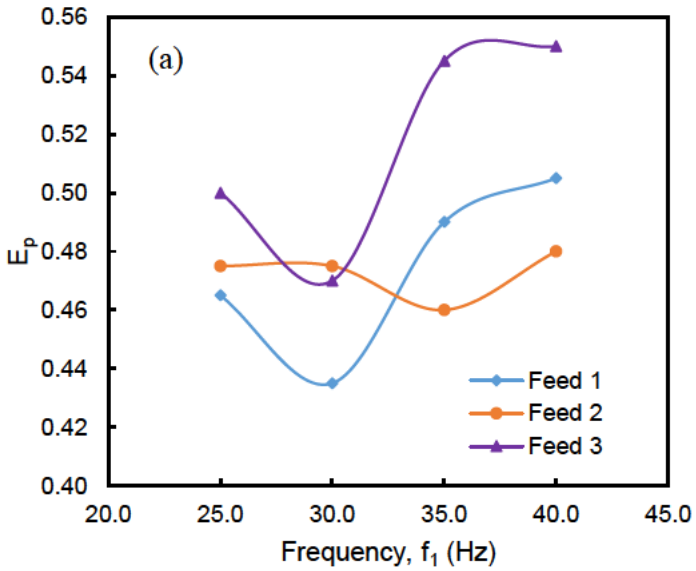

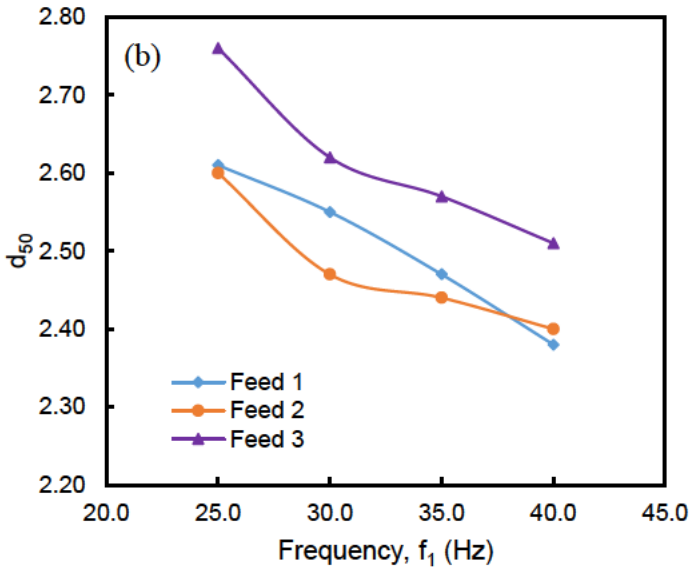

Figure 5-5 E_p and d_{50} as a function of vibration frequency (f_1) under different feeding conditions (where, A_1 = 2.0mm, A_2 = 3.5mm and f_2 = 25Hz).

Figure 5-6 shows the E_p and d_{50} as a function of particles passing along the screen for various feeding conditions against A_1. Particle passage was higher for Feed 3 than the other feed conditions. The value of E_p decreased with the increase in A_1. The particle passing rate changed for Feed 2 and Feed 3, and E_p was higher than the undersized feed condition. Conversely, d_{50} increased with the decline in vibration amplitude (Figure 5-6b). For Feed 1 and Feed 2, d_{50} was lower than Feed 3. This could be attributed to the collision of large particles that creates gaps to facilitate percolation of particles. For higher amplitude (3.5 mm), d_{50} was the lowest for all feed cases. Thus, lower vibration frequency/amplitude was more effective for particles to pass from the screen.

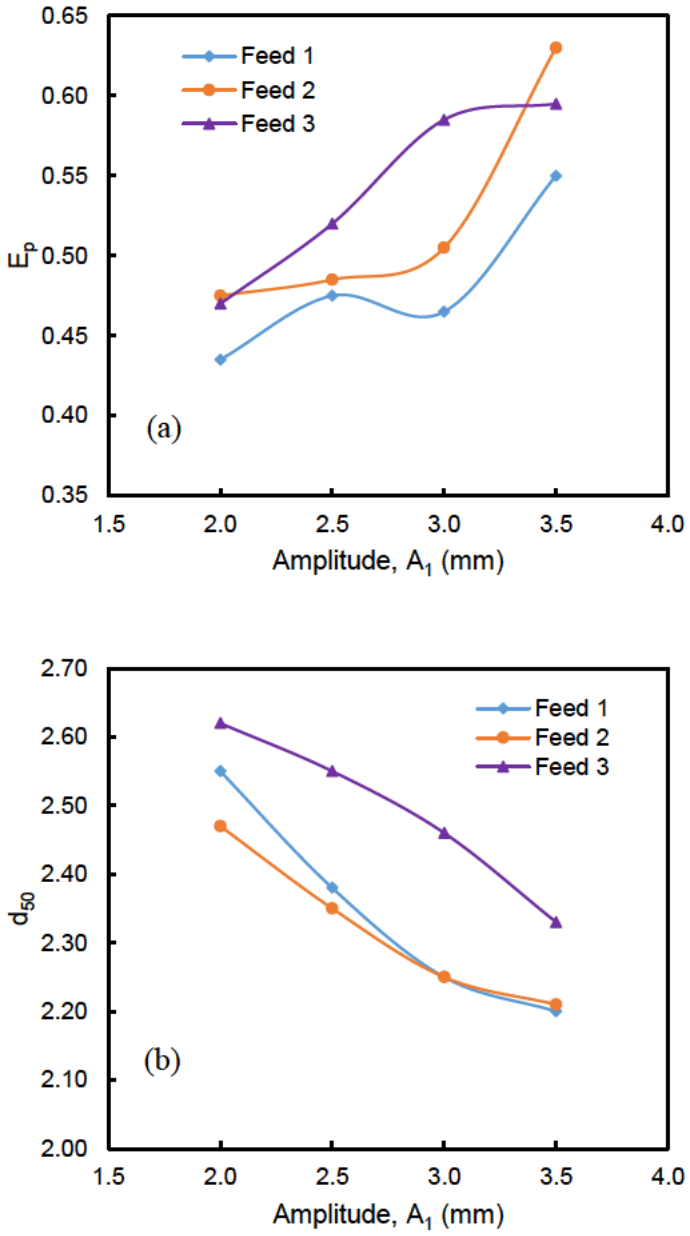

Figure 5-6 E_p and d_{50} as a function of vibration amplitude (A_1) under different feeding conditions (where, f_1 = 30Hz, A_2 = 3.5mm and f_2 = 25Hz).

Figure 5-7 shows the E_p and d_{50} as a function of various feeding conditions against f_2 for the bottom layer screen with machine learning. In Figure 5-7a, E_p gradually increased with the increase in frequency (f_2) to a maximum of 40 Hz for Feed 1. E_p was lower for Feed 2 than for other feeding conditions. This could be attributed to the aperture size of the bottom layer, through which only $d_i < 1.75$ sized particles can pass. Furthermore, contact between small particles and larger than aperture-sized particles help them to pass through the screen. For near-mesh size and larger particles, E_p was lower for the higher f_2 and highest at low frequency. High

vibration increases particle bounce, which could be attributed to the higher d_{50} for Feed 2 and Feed 3. It resulted in higher particle passing rates that decreased with the increase in vibration frequency (Figure 5-7b). Furthermore, d_{50} was lower for Feed 1 and increased with the increase in vibration frequency of the bottom layer. As particles were smaller than the screen aperture, there is less opportunity to pass through the screen.

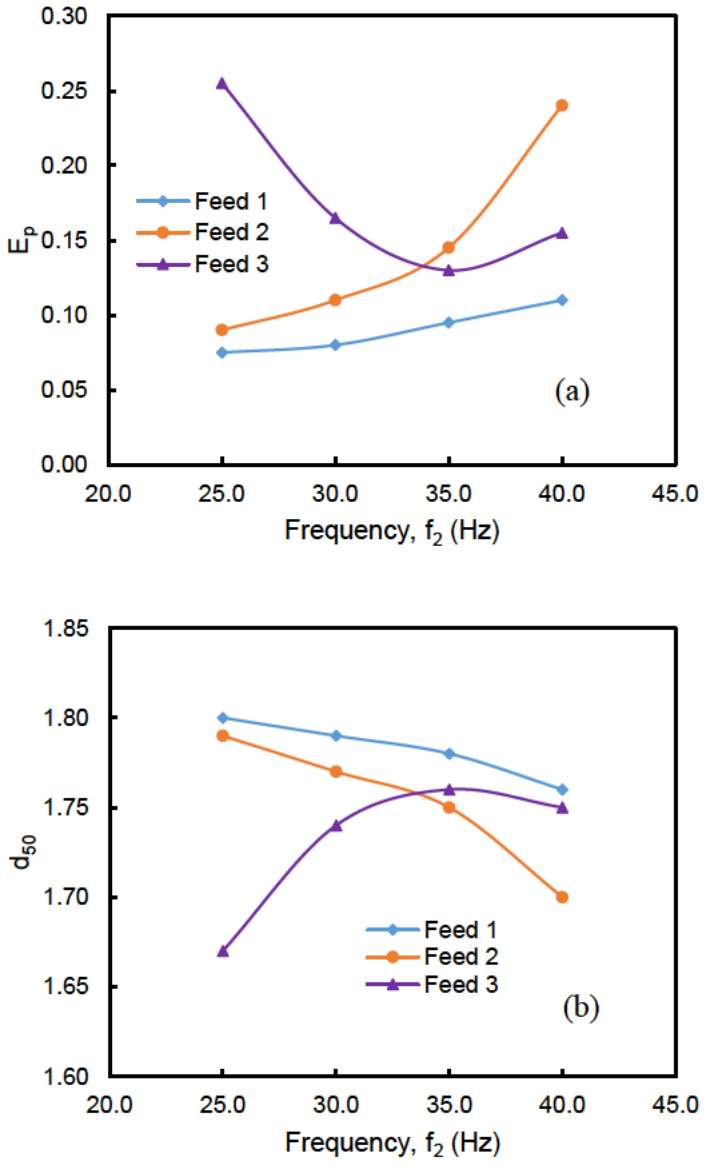

Figure 5-7 E_p and d_{50} as a function of vibration frequency (f_2) under different feeding conditions (where A_1 = 2.0mm and f_1 = 30Hz).

Figure 5-8 shows the E_p and d_{50} as a function of particles passing along the screen for various feeding conditions against A_2. For Feed 2, the particle passing rate was higher than the other feed conditions such as the lower value of E_p and higher A_2. E_p decreased initially and then increased at A_2 = 3.5 mm. It further decreased gradually and was found to be lowest for A_2 = 3.0 mm and highest for 3.0 mm. Feeding condition affected bottom layer sieving. The passing of particle rate changed while considering the aperture shape and the collision with particles in Feed 2 and Feed 3. On the other hand, d_{50} increased with the increase in amplitude (Figure 5-8b). For Feed 1 and Feed 2, d_{50} was higher than Feed 3 for 2.5 mm and 3.0 mm. At higher amplitude (3.5 mm), the d_{50} decreased. Thus, lower vibration frequency/amplitude was more effective for particles passing through the screen. The particles whose size was close to the mesh aperture size of the screen mesh faced difficulty with the accumulation of particles in the top layer (Li, J et al. 2003; Zhang, B et al. 2016). In the present study, the opposite phenomena indicated changes in the bottom layer passing with the change in aperture shape and size distribution.

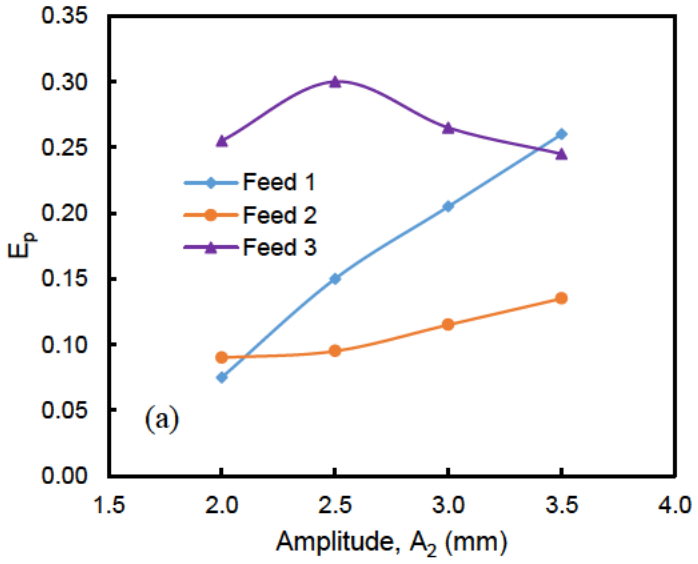

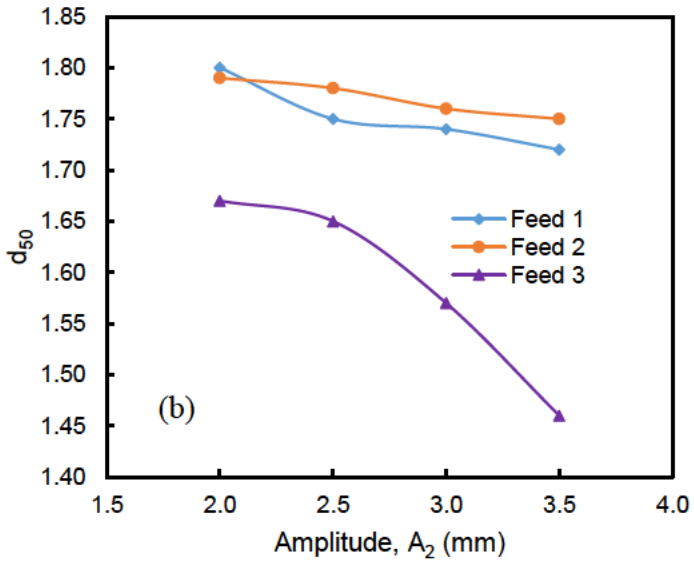

Figure 5-8 E_p and d_{50} as a function of vibration amplitude under different feeding conditions (where, A_1 = 2.0mm and f_1 = 30Hz).

5.4.3 Effect of vibration on double layer screen

By developing the local passing rate functions, f_{p1} and f_{p2}, for a double layer inclined screen, the full sieving process model could be divided into four segments on each layer (Figure 5-3). With the passing rate of each sized particle obtained from the model, the partition curve for the overflow of the whole screen was obtained, which was then used to evaluate sieving performance. This curve shows the percentage of particles reporting to the overflow as a function of particle size. Figure 5-9 shows the overflow partition curve of screen performance of the double layer screen with different amplitude (A_1), where the vibration condition of the bottom layer was fixed. Both layers of the screen exhibited reduced performance with increased A_1.

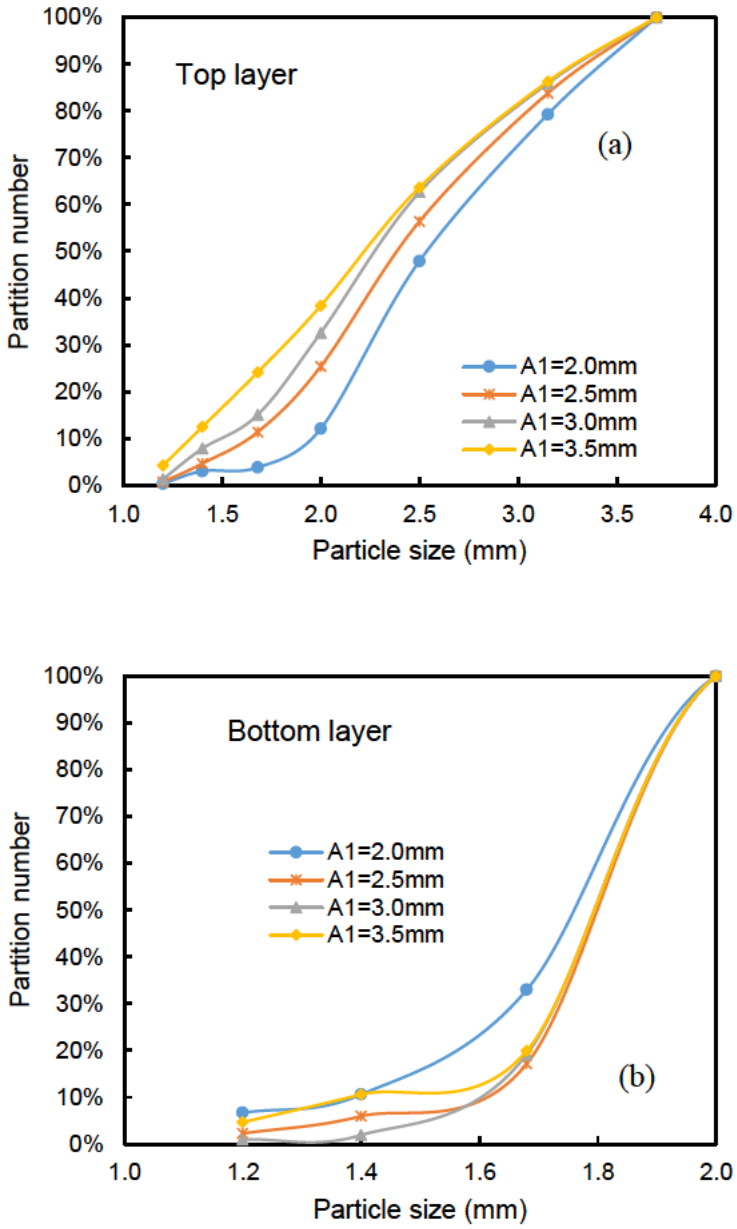

Figure 5-9 Effect of vibration amplitude on double layer screen (a) top layer; and (b) bottom layer (where, f_1 = 30Hz, A_2 = 3.5mm and f_2=25Hz).

Figure 5-10 shows the overflow partition curve of screen performance of the bottom layer with different vibration frequency (f_1). The double layer screen performance decreased with increased vibration frequency (f_1).

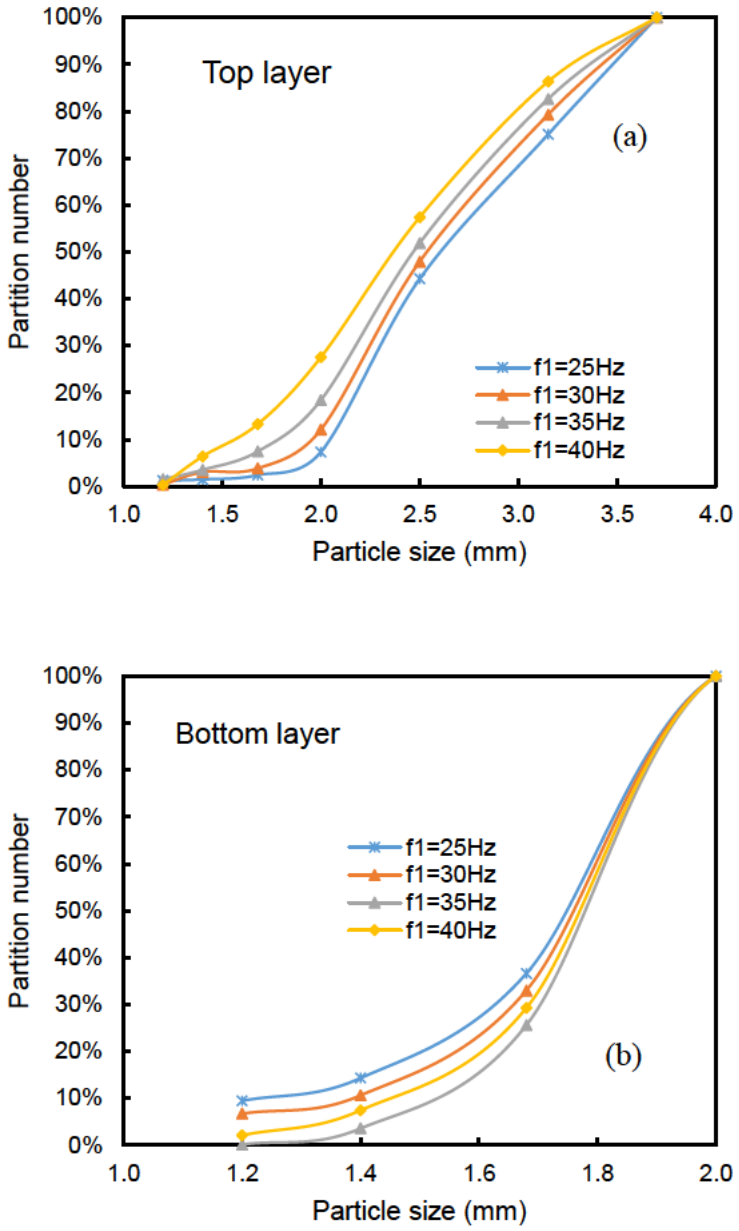

Figure 5-10 Effect of vibration frequency on double layer screen (a) top layer and (b) bottom layer (where, A_1 = 2.0mm, A_2 = 3.5mm and f_2=25Hz).

5.4.4 Effect of vibration on the bottom layer of double layer screen

The process model is further used to study the effect of vibration on the change in vibration condition for the bottom layer. The vibration condition of the top layer remained constant. The process model demonstrated similar screen performance for the bottom layer compared to top layer. The feeding condition is different for bottom layer screen. The small undersized particles passed through a small aperture (d_i <1.75). Figure 5-11 shows the overflow partition curve of

screen performance of the bottom layer with the change in amplitude (A_2). Particles smaller than the screen aperture find more opportunities to pass through the screen. The performance of the bottom layer screen decreased with the increase in vibration amplitude (A_2) and the performance decreased for the higher value of A_2 = 3.5mm (Yan, H et al. 2020).

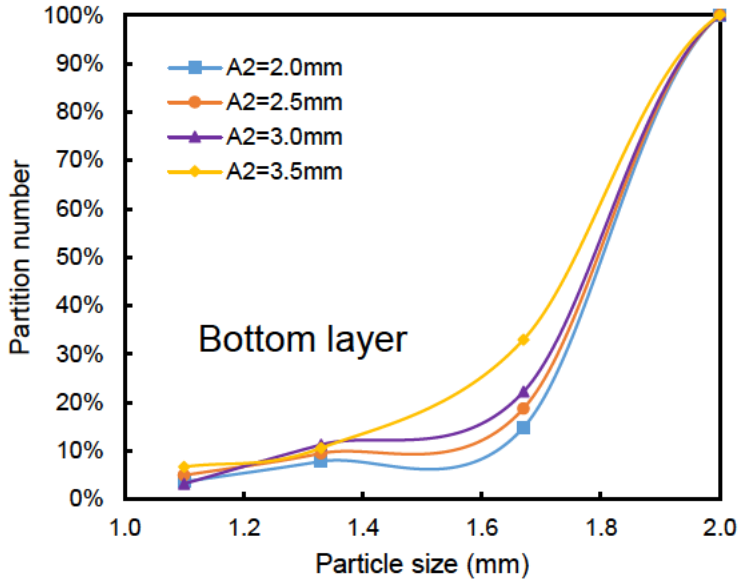

Figure 5-11 Effect of vibration frequency on bottom layer (L2) screen (where, L1 vibration condition: A_1 = 2.0mm and f_1=30Hz)

Figure 5-12 shows the overflow partition curve of screen performance of the bottom layer with the change in frequency (f_2), where top layer vibration conditions and the inclination angle are fixed. The performance of bottom layer screen decreased with the increase in vibration frequency (f_2). High vibration condition is not effective for particles to pass along the bottom layer.

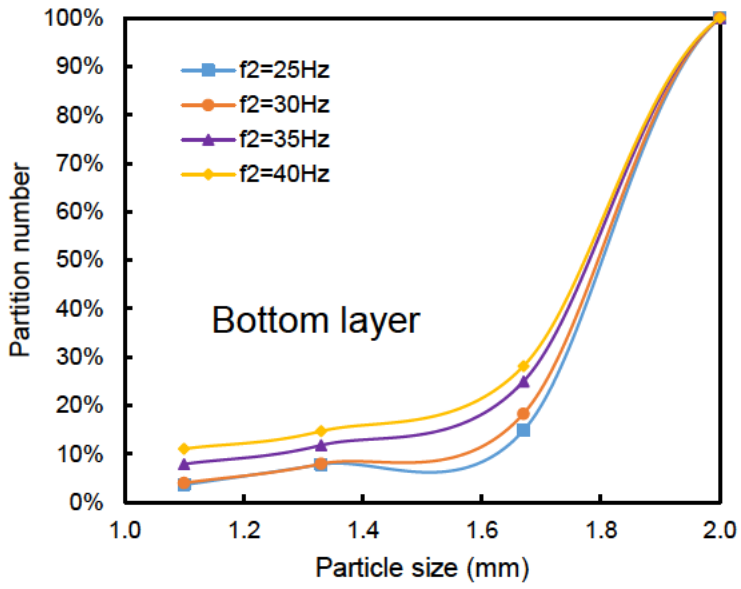

Figure 5-12 Effect of vibration amplitude on bottom layer (L2) screen (where, L1 vibration condition: (a) A_1 = 2.0mm and (b) A_1 =2.5mm for f_1 =30Hz).

5.5 Conclusions

DEM and machine learning modelling of multi-layers screen can provide detailed quantitative predictions about how particles pass through the overall screen, each layer and each segment of each layer. A process model of particle passing was proposed here that considered machine learning modelling based on DEM results. Machine learning and process models can optimise inclined double layer vibrating screens with various feeding scenarios, vibration conditions for both layers, aperture shapes and feed conditions. The major conclusions drawn are as follows:

- The proposed process model is (Chapter 4) further developed successfully for the inclined double layer screen performance by predicting the local passing rate of particles. Machine learning modelling helps to optimise the time-consuming simulation process by quickly predicting results and providing a proper understanding of the local passing of a double-layer screen.
- The inlet for the bottom layer is considered the passing particles from the top layer and the upper stream particles flow to the lower layer. The particle passing decreases with the increases in vibration condition due to the presence of large amounts of undersized

particles in feed. For medium undersized particles, the passage is better than the large number of mesh-sized particles.

- The screen performance decrease with the increase of amplitude/frequency for top layer. On the other hand, screen performance of bottom layer increases with the increase of amplitude/frequency of top layer and again decreases for the higher value. Similarly, bottom layer screen performance decreases with the increase of frequency/amplitude.

Nomenclature

A_1	Vibration amplitude for top layer
A_2	Vibration amplitude for bottom layer
d_i	Particle size (mm)
D_i	Screen deck
E_p	Probable error
f_1	Frequency for top layer
f_2	Frequency for bottom layer
$\boldsymbol{F}_{ij}^{n}$	Normal contact force
$\boldsymbol{F}_{ij}^{t}$	Tangential contact force
$\boldsymbol{g}$	Gravitational acceleration
$\boldsymbol{I}$	Moment of inertia of the particle
I_i	Feed particles rate from a segment
m	Mass of particle
n_i	Number of feed particles rate
O_i	Overflow rate from a segment or feed to the downstream segment
P	Function of passing rate
P_i	Particles passing rate
R_i	Radius of particle i
R_j	Radius of particle j
t	Time
Y	Young's modulus
Greek letters	
γ_n	Normal damping coefficient

ξ_n	Relative normal displacement
ξ_s	Total tangential displacement
θ	Inclination angle of the screen
ρ	Density (kg/m^3)
$\tilde{\sigma}$	Poisson ratio
μ_r	Rolling friction coefficient
μ_s	Sliding friction coefficient
ω	Particle angular velocity (s^{-1})

Subscripts

i	Particle *i*
j	Particle *j*
i j	Between particles *i* and *j*

Abbreviations

ANN	Artificial neural network
DEM	Discrete element method
GPR	Gaussian process regression
ML	machine learning
RMSE	Root mean square error
SVM	Support vector machine

CHAPTER VI: Judgement model for choking of vibrating screen based on DEM and machine learning

6.1 Introduction

Screening is a common method of granular or particle material size classification. The performance of screening depends on the stratification and passing of particles. Screens have many adjustable controlling parameters and are considerably less well understood (Asbjörnsson et al. 2016; Cleary, PW 2009; Cleary, Paul W, Sinnott, Matthew D & Morrison, Rob D 2009; Davoodi, A. et al. 2019; Dong, K, Esfandiary & Yu 2017; Dong, K et al. 2010; Dong, K, Wang & Yu 2013; Dong, K, Yu & Brake 2009; Elskamp et al. 2016; Harzanagh, Orhan & Ergun 2018; Jansen & Glastonbury 1968; Soldinger 1999). Choking of screen is one of the common obstacles for a quality sieving/performance of screen. In general, the choking problem occurs for large amounts of inlets, lower value of vibrational conditions, mesh-design of screen, configuration of screen, distribution of particles, packed bed, and inclination angle (Arifuzzaman, S. M., Dong, Kejun & Yu, Aibing 2022; Davoodi, Ali et al. 2019; Delaney, Gary W. et al. 2012; Dong, K, Yu & Brake 2009).

The particles accumulate on the screen for the lower value of vibration condition and inclination angle, which makes the screening process unsteady or choke (Dong, K, Yu & Brake 2009). The choking of screen also depends on the rate of passage probability that the particles will pass through the apertures and the amount of free material on the screen surface (Soldinger 1999). Size distribution of particles along the screen is one of the vital factors screen performance. The feed also has properties which will affect the efficiency of screen operation or choking and these include, feed flow rate, feed solids, and the amount of near sized material in the feed (Meyers & Mylec 2000). The presence of large amount near aperture sized particles is not effective for better screening and the apertures in the screen become blocked by near-mesh-sized particles, and choking occurs (Delaney, Gary W. et al. 2012). High-density material has a higher probability of passage (Davoodi, Ali et al. 2019). Packing of bed is one of the vital factors for screen choking. Too thick a bed depth preventing stratification and restricting access of finer particles to the screen surface (Meyers & Mylec 2000). At very low vibration, the screening process is known to lose efficiency because of choking (Esfandiary 2014). Lengthways straight wires and enlacements form long rectangular mesh; self-cleaning ability is created by the oscillation of the lengthways wires avoiding the screen choking and due the large free open area the screen has high sorting performance (WovenWireScreens).

For particle scale investigation, discrete element method (DEM) is a popular method that can enhance resolution to view distinct physical properties. Higher resolution provides alternatives to time-consuming physical testing in the initial stages of screen design (Davoodi, A. et al.

2019). Some process models of screening linking DEM modelling have analysed particle–particle interaction (Dong, K, Esfandiary & Yu 2017; Dong, K, Wang & Yu 2013) using probability theory. Conversely, DEM simulation is significantly limited and time consuming (Hoomans, Kuipers & van Swaaij 2000; Yan, Z et al. 2015) for particle numbers and properties, and calculation with explicit scheme.

Advances in artificial intelligence modelling are used in mineral processing to minimise computational power, duration of simulation and data storage. Many opportunities and challenges exist for the application of artificial intelligence in granular processing. Recent research (Barrasso, Tamrakar & Ramachandran 2014; Dai, W, Liu & Chai 2015; He & Tafti 2019; Karniadakis et al. 2021; Li, Y et al. 2021; Li, Z et al. 2019; Mahdi & Holdich 2017; Mishra 2021; Shanmugam et al. 2021; Zhang, B et al. 2016; Zhao, Z et al. 2021) includes data-driven modelling using machine learning (ML) and neural networks on simulated or experiment results. Artificial neural network modelling has been applied in coal preparation to know the permeability of porous media (Mahdi & Holdich 2017), to predict particle flow characteristics in rotating drums (Li, Y et al. 2021), and to predict the screening efficiency of coal with varying moisture content (Shanmugam et al. 2021). Machine learning modelling has been used to predict sustainable value in the mineral processing industry (Li, Y et al. 2020; Li, Z et al. 2019; Li, Z et al. 2015; Pani & Mohanta 2015; Zhang, B et al. 2016), to predict particle flow in rotating drums (Li, Y et al. 2020), to monitor particle size (Pani & Mohanta 2014, 2015), to control parameter prediction of ball mills (Tang, J et al. 2010), and to know the percolation velocity and threshold of particles under vibration conditions (Arifuzzaman et al. 2022). Physics-informed machine learning presents an alternative to deep neural networking to avoid training big databases. The modelling helps understanding of the hidden physics, new frameworks and standardised benchmarks, as well as new mathematics (Arifuzzaman, S. M., Dong, Kejun & Yu, Aibing 2022; Karniadakis et al. 2021). The physics-informed supervised machine leaning model is able to predict the overflow partition curve directly and local passing of screen (Arifuzzaman, S. M., Dong, Kejun & Yu, Aibing 2022). Classification learning is a supervised machine learning concept which basically categorizes a set of data into category and the classifier has been used for the classification of sand particles (Li, L & Iskander 2022).

However, there are few studies proposed a quantitative model of screen choking with considering wide range of operational conditions and inlet of screen. Taking into account the gap of modelling for choking of screen, a model is needed to investigate the choking of screen with considering the operational conditions and feed. With this idea, this paper focuses to

develop a decision-making logical model for choking of screen by combining DEM simulation and machine learning. The particle inlet in a section of a screen and the flow controlling variables are regarded as dependent variables to construct the database. The machine learning (ML) database is generated by a series of controlled DEM simulations to create the choking logical judgement model. The choking judgement of a screen can be predicted by the logical model with considering the feed on the screen, vibration condition, and inclination angle. The logical model also be modelled to predict the vibration condition threshold, inclination angle, and the complex feed threshold for choking judgement. The rest of the study is structured as follows: Section 6.2 describes the DEM methodology and the inclined vibrating screen simulation condition. The choking judgement model of screen based on machine learning are defined in Section 6.3. In Section 6.4, the judgement of choking of screen for vibration condition and feed threshold analysis underperforming machine learning prediction studies are demonstrated, and Section 6.5 concludes the paper.

6.2 Simulation method and conditions

6.2.1 Discrete element method (DEM)

For particles flow along the inclined double layer screen, the discrete element method was used to trace the motion of individual particles in a considered system according to their mutual interaction. In DEM, the motion of each particle is governed by Newton's second law (Cundall & Strack 1979). For a spherical particle i, its translational motion and rotational motion are respectively given by:

$$m_i \frac{d\boldsymbol{v}_i}{dt} = \sum_j (\boldsymbol{F}_{ij}^n + \boldsymbol{F}_{ij}^s) + m_i \mathbf{g} \qquad \text{(Eq. 6.1)}$$

$$\boldsymbol{I}_i \frac{d\boldsymbol{\omega}_i}{dt} = \sum_j (\boldsymbol{R}_{ij} \times \boldsymbol{F}_{ij}^s - \mu_r R_i \left|\boldsymbol{F}_{ij}^n\right| \hat{\boldsymbol{\omega}}_i) \qquad \text{(Eq. 6.2)}$$

where $\boldsymbol{v}_i$, $\boldsymbol{\omega}_i$, m_i and $\boldsymbol{I}_i$ are, respectively, the translational and angular velocities, the mass and the moment of inertia of particle i, $\boldsymbol{g}$ is the gravitational acceleration, $\boldsymbol{R}_{ij}$is the vector pointing from the centre of particle i to the contact point of it with the particle j. $\boldsymbol{F}_{ij}^n$ and $\boldsymbol{F}_{ij}^s$ are the normal and tangential contact forces respectively, which can be given as (Brilliantov et al. 1996; Langston, Tüzün & Heyes 1995):

$$\boldsymbol{F}_{ij}^{n} = \left[\frac{2}{3}\frac{Y}{1-\tilde{\sigma}^2}\sqrt{\bar{R}}{\xi_n}^{3/2} - \gamma_n \frac{Y}{1-\tilde{\sigma}^2}\sqrt{\bar{R}}\sqrt{\xi_n}(\boldsymbol{v}_i \cdot \hat{\boldsymbol{n}}_{ij})\right]\hat{\boldsymbol{n}}_{ij} \quad \text{(Eq. 6.3)}$$

$$\boldsymbol{F}_{ij}^{s} = -\mu_s|\boldsymbol{F}_n|[1-(1-\frac{min(\xi_s,\xi_{s,max})}{\xi_{s,max}})^{3/2}]\hat{\boldsymbol{\xi}}_s \quad \text{(Eq. 6.4)}$$

where Y is the Young's modulus, $\tilde{\sigma}$ is the Poisson ratio, γ_n is the normal damping coefficient, μ_s is the sliding friction coefficient, ξ_s is the total tangential displacement, and $\bar{R} = R_iR_j/(R_i+R_j)$, $\xi_{s,max} = \mu_s[(2-\tilde{\sigma})/2(1-\tilde{\sigma})]\xi_n$, $\hat{\boldsymbol{n}}_{ij} = (\boldsymbol{R_i} - \boldsymbol{R_j})/|\boldsymbol{R_i} - \boldsymbol{R_j}|$. The second term of the torque results from the rolling resistance between two contact particles due to elastic hysteretic losses or viscous dissipation, where μ_r is the rolling friction coefficient and $\hat{\boldsymbol{\omega}}_i = \boldsymbol{\omega}_i/|\boldsymbol{\omega}_i|$ (Zhou, YC et al. 1999; Zhu, HP et al. 2007). The above equations calculate the interaction between particles and the system wall (the contact between particles and a finite polygon surface). The Van der Waals force and the capillary force between particles are not taken into account because the coarse particles are dry. The wall is modelled as a plane with the same material properties of the particles. Under vibration, the position and velocity of the wall are updated in every timestep, and the values are used in calculating the particle-wall interactions. The time step is determined by $dt = 0.1\sqrt{m/k}$, where m is the mass of a particle and k is the estimated spring constant when the normal overlap is 10% of the particle diameter. This is based on the natural period of oscillation of the equivalent spring when using the Hertz contact force model. In a multi-size system, the time step is calculated for each kind of particles and the minimum time step is used. Simulations are conducted by our in-house DEM program, which has been used and validated in various systems in our previous studies (Amirifar et al. 2018, 2019; Dong, K, Wang & Yu 2013; Dong, K, Yu & Brake 2009).

6.2.2 Simulation condition

In this study, an inclined screen similar to that used in our previous study is considered (Arifuzzaman, S. M., Dong, Kejun & Yu, Aibing 2022; Dong, K, Wang & Yu 2013). A simulation starts with no particles on the screen. With the increase of time, more and more particles are fed from the feed side of the screen and fall on the vibrating screen deck. The particles in the considered simulation domain will increase with time at first, but then the simulation will enter either the steady flow state or unsteady flow state. The steady flow state means the inlet flow rate is generally balanced with the sum of the underflow and overflow

rates for particles of each size, although there are small fluctuations, as shown in Figure 6-1 (a) and (b). The particle size distribution, material properties and feed rate are given in Table 6-1. These parameters have been validated in our previous study in terms of the percentage passing distribution and the average particle residence time (Arifuzzaman, S. M., Dong, Kejun & Yu, Aibing 2022; Dong, K, Wang & Yu 2013). Consequently, the particle number of each size particles will no longer increases with time in average. On the other hand, the unsteady flow state means the total outflow cannot balance the inlet flow, so particles in the system keep increasing, and chocking happens as shown in Figure 6-1 (c) and (d).

The particle size distribution is a major fact for the choking of screen, which deals with the passing of particles, collision among particles and screen, and flow of particles etc. For simulation, the feed conditions are divided the undersize particles into three categories (Arifuzzaman, S. M., Dong, Kejun & Yu, Aibing 2022) to predict partition number: small undersize particles, medium undersized particles, and near-mesh undersize particles and more details can be found in section 6.4.2. The process model (Arifuzzaman, S. M., Dong, Kejun & Yu, Aibing 2022) needs to consider logical model to predict the partition curves for several feeding, otherwise it cannot consider chocking.

Table 6-1 List of parameters used in the simulations.

	d_1	d_2	d_3	d_4	d_5	d_6	d_7
Particle size, d_i (mm)	1.10 to 1.25	1.3 to 1.45	1.50 to1.73	1.8 to 2.05	2.5 to 2.55	3.05 to 3.2	3.65 to 3.75
Feed rate n_i (num/s)	n_1	n_2	n_3	n_4	n_5	n_6	n_7
	3300 to 5300	2050 to 3300	1250 to 2000	1000 to 1500	400 to 950	200 to 1250	100 to 200
Particle density, (kg/m^3)	7500						
Young's modulus (N/m^2)	1×10^7						
Damping coefficient, γ_n	Particle-particle:2×10^{-4}; particle-wall: 2×10^{-4}						
Sliding friction coefficient, μ_s	Particle-particle: 0.3; particle-wall: 0.5						
Rolling friction coefficient, μ_r	Particle-particle: 0.01; particle-wall: 0.01						
Vibration frequency (Hz), f	8, 10, 12, 14, 15, 18, 20, 25, 29, 30, 35, 40, 50 and 60						
Vibration amplitude (mm), A	0.7, 1, 1.5, 2.0, 2.5, 3.0 and 3.50						
Vibration motion	Sinusoidal, both along y and z directions.						
Incline angle (°), θ	5, 6, 7, 9, 10, 11, 13, 15, 17 and 22						

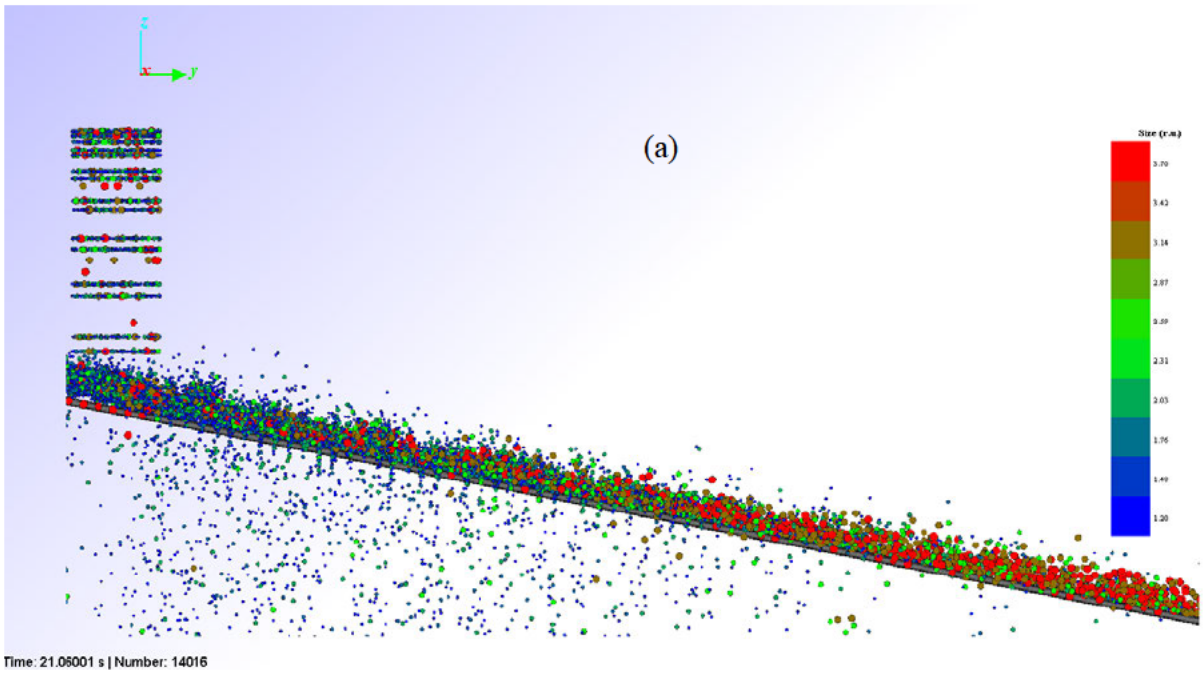
(a)
Time: 21.06001 s | Number: 14016

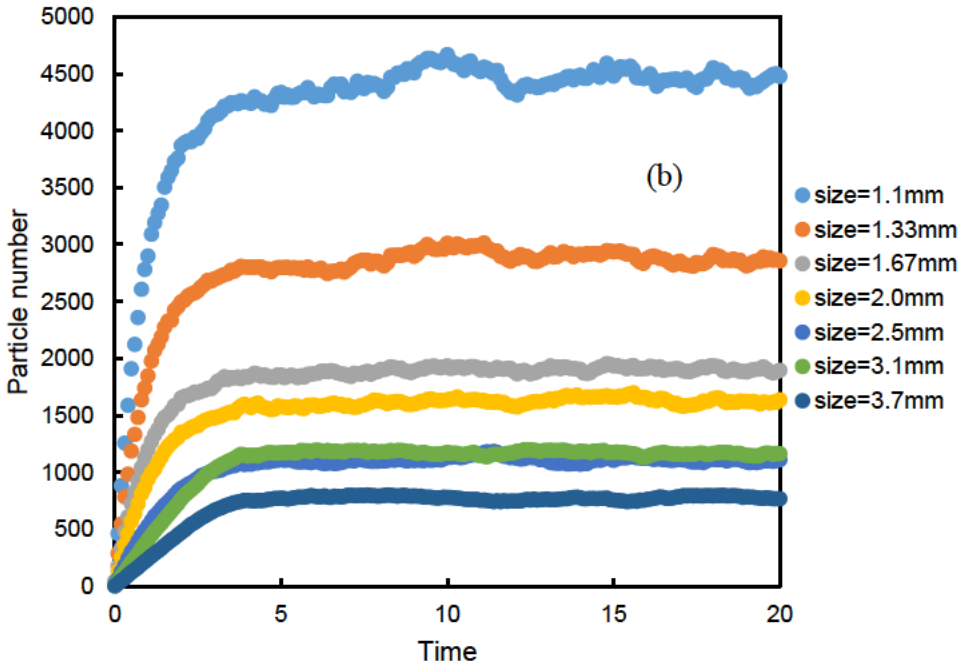
(b)
Particle number
Time
0
500
1000
1500
2000
2500
3000
3500
4000
4500
5000
0
5
10
15
20
size=1.1mm
size=1.33mm
size=1.67mm
size=2.0mm
size=2.5mm
size=3.1mm
size=3.7mm

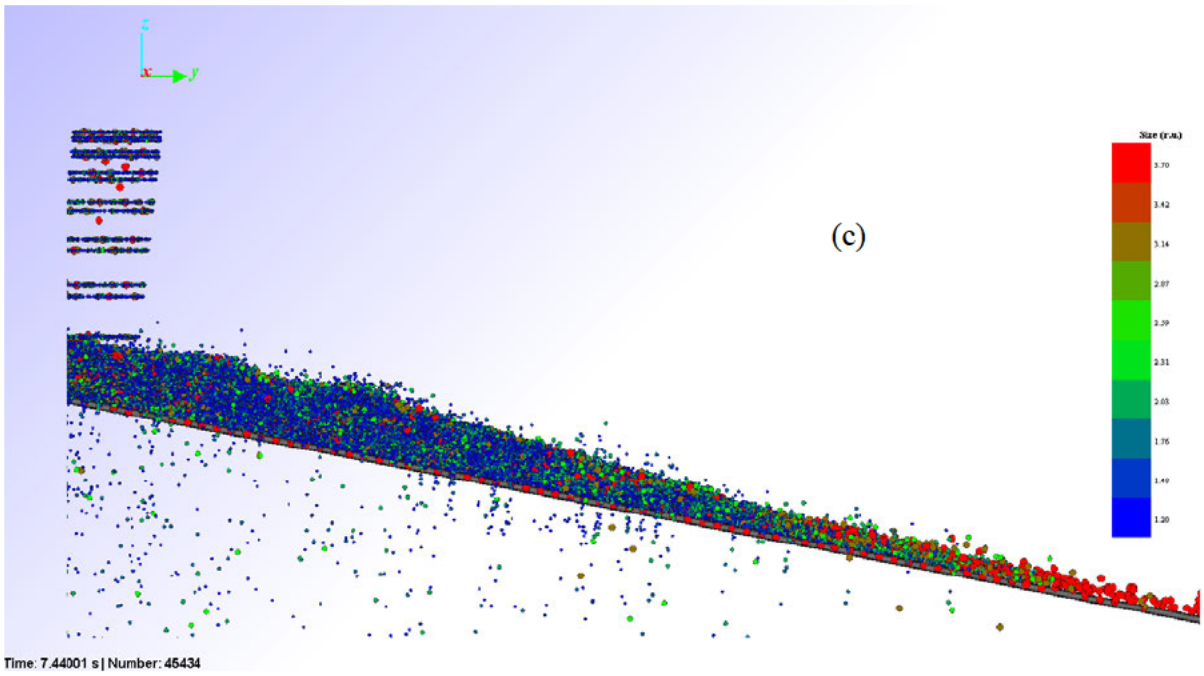

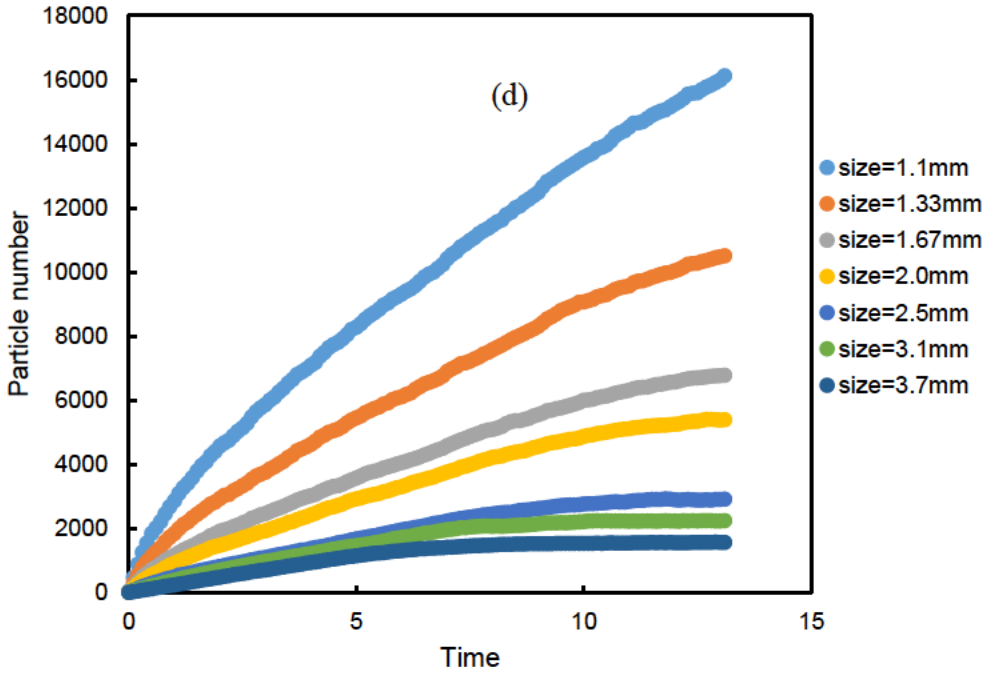

Figure 6-1 (a) Snapshot of simulation using the inclined vibrating screen under steady state flow (A = 2 mm, f = 30Hz and $\boldsymbol{\theta}$ =11°), (b) overflow of particles along the inclined screen for non-choking case; (c) snapshot of simulation using the inclined vibrating screen under steady state flow (A =1.5 mm, f = 25Hz and $\boldsymbol{\theta}$ =5°), and (d) overflow of particles along the inclined screen for choking case.

6.3 Machine learning decision model for choking judgement

Here, we propose a logical judgement model for choking of an inclined vibrating screen based on machine learning. In particular, the input flow $\{d_i, I_i\}$ of the screen, where d_i is the particle size of the *i*th component in the particle mixture, and I_i is the flow rate of the input flow of the *i*th component, respectively. We assume choking is dependent on the input flow, vibration conditions and inclination angle; then, a function (δ) to predict the choking status can be given by:

$$\delta = \delta(\{di, Ii\}, A, f, \theta) \quad \text{(Eq. 6.5)}$$

It can be seen that δ has many input variables, which include both particle properties and operational conditions. Therefore, the relationship is complicated and non-linear. It will be extremely challenging to develop this function in a conventional way. In this study, we build this function by applying the database generated by DEM simulation.

6.4 Results and discussion

6.4.1 Machine learning model of choking condition prediction for inclined vibrating screen

As described above Section 6.3, the logical choking function δ is used to predict choking by machine learning with the DEM simulation data. The input variables are $\{d_i\}$, $\{I_i\}$ *A, f,* and θ for screening. The output variables of the model is choking condition {δ}. The total training data contains 331 simulation cases. The data are trained with linear, SVM, KNN, ESD, Tree and GPR regression ML models. The detailed algorithm of the models can be found in the MATLAB document (MATLAB 2022). The accuracy percentage of the considered models are listed in Table 6-3, from which it can be seen that the Cubic SVM regression model is the best model with very high accuracy (%).

Table 6-2 Input and output variables used for logical model database.

Input	Used values	Output / judgement

A (mm)	0.7 - 3.5	Choking / non-choking
f (Hz)	8 - 60	
θ (°)	5 - 22	
d_1 (mm)	1.1 - 1.25	
d_2 (mm)	1.3 - 1.45	
d_3 (mm)	1.5 - 1.73	
d_4 (mm)	1.8 - 2.05	
d_5 (mm)	2.5 - 2.55	
d_6 (mm)	3.05 - 3.2	
d_7 (mm)	3.65 - 3.75	
I_1 (num /s)	15.2 - 18500.75	
I_2 (num /s)	17.76- 9932.32	
I_3 (num /s)	20.72 - 7525.42	
I_4 (num /s)	48.6 - 4782.23	
I_5 (num /s)	42.64 - 2452.65	
I_6 (num /s)	20.14 - 1664.54	
I_7 (num /s)	100 - 200	
Number of cases	(193 not-choking and 138 choking)	

Table 6-3 Performance of the machine learning models and accuracy to predict the choking of screen.

Model of Classification Learner	Accuracy (%)
Linear discriminant	84.3
Linear SVM	85.4
Fine Tree	82.2
Medium Tree	85.2
Coarse Tree	91.3
Linear SVM	85.3
Quadratic SVM	86.9
Cubic SVM	**97.8**
Fine Gaussian SVM	88.2
Medium Gaussian SVM	81.4
Coarse Gaussian SVM	73.2
Fine KNN	75.3
Medium KNN	81.5
Coarse KNN	74.5
Cosine KNN	76.2
Cubic KNN	81.3
Weighted KNN	84.5
Ensemble Boosted Trees	85.5
Ensemble Bagged Trees	85.5
Ensemble Subspace Discriminant	88.5
Ensemble Subspace KNN	85.4
Ensemble RUS Boosted Threes	85.7

Figure 6-2 provides the confusion matrix to understand the performance of the trained ML classifier model. In Figure 6-2 (a), the top row shows 93% of the none-chocking cases from simulation data are correctly classified, while the other 7% none-chocking cases are falsely predicted as positive. The bottom row shows 75% of the choking cases from simulation data are correctly classified, while the other 25% cases are falsely predicted as negative. The confusion matrix shows summary rows underneath in Figure 6-2 (b). Positive predictive values are shown in green for the correctly predicted results in each class, and false discovery rates are shown below it in red for the incorrectly predicted results in each class. Table 6-4 shows some false positive and negative cases with DEM results and classification model. The positive predictive values (PPV) and true positive rate (TPR) are defined as,

$$\text{PPV} = \frac{\text{Number of true positives}}{\text{Number of true positives} + \text{Number of false positives}} \qquad \text{(Eq. 6.6)}$$

$$\text{TPR} = \frac{\text{True positive}}{\text{True positive} + \text{false negaitive}} \qquad \text{(Eq. 6.7)}$$

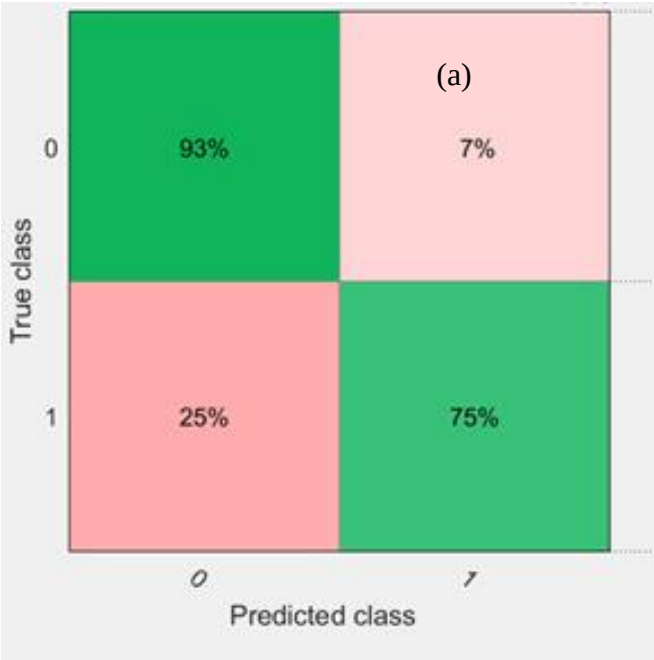

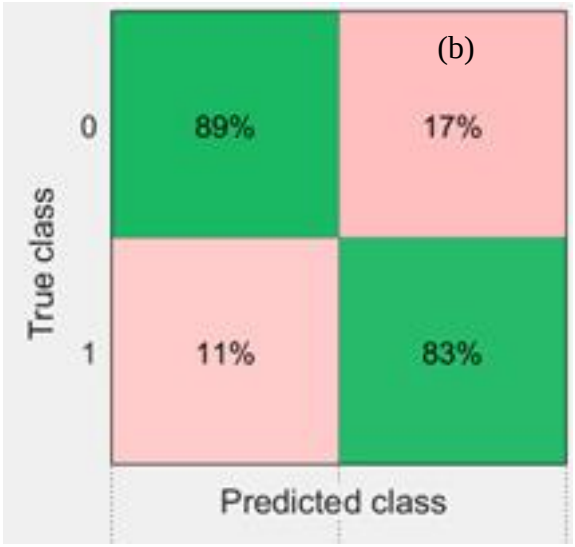

Figure 6-2 Confusion matrix of trained model (1= choking, 0 = not choking)

Table 6-4 Some false positive and negative cases with DEM results and classification model.

Case no	DEM result	Judgement model result	Matching
1. A=2.5mm, f=40Hz, θ = 5^o	0	1	False positive
2. A=2.5mm, f=20Hz, θ = 5^o	1	0	False negative
3 A=2.5mm, f=12Hz, θ = 11^o	1	0	False negative
4. A=1.5mm, f=20Hz, θ = 13^o	1	0	False negative
5. A=1.5mm, f=14Hz, θ = 11^o	1	0	False negative
6. A=2mm, f=20Hz, θ = 9^o	0	1	False positive
7. A=3mm, f=40Hz, θ = 5^o	0	1	False positive
8. A=1.5mm, f=20Hz, θ = 11^o	0	1	False positive
9. A=2.5mm, f=26Hz, θ = 11^o	1	0	False negative
10. A=3.5mm, f=40Hz, θ = 5^o	0	1	False negative

Figure 6-3 illustrates the numbers of simulation results with confusion matrix instead of percentages. The confusion matrix shows the trained classification model; the classifier has performed well and classified the screen results of this true class correctly. Among 331 simulation results, 288 cases are well classified.

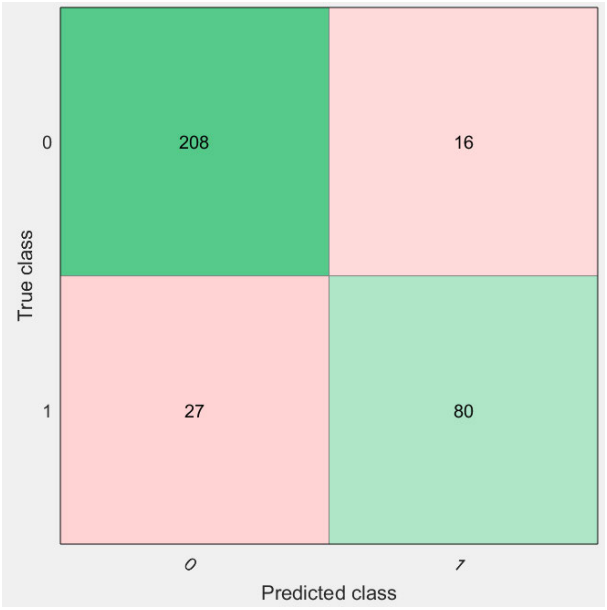

Figure 6-3 Confusion matrix simulation results observation (1= choking, 0 = not choking)

Figure 6-4 shows the receiver operating characteristic curve with true and false positive rates. The ROC curve shows the true positive rate versus false positive rate for the trained classifier (Cubic SVM). The larger area under the curve values indicates the classifier performance. A false positive rate of 0.25 indicates that the Cubic SVM classifier assigns 25% of the simulation results incorrectly to the positive class. The true positive rate of 0.93 indicates that the classifier assigns 93% of the results correctly to the positive class.

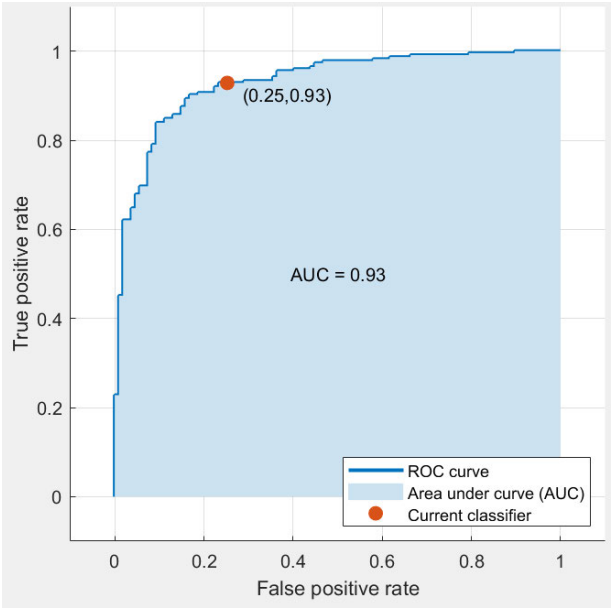

Figure 6-4 Receiver operating characteristic curve after training the database.

6.4.2 Application of ML model: Judgement of choking in screening

6.4.3 Judgement of choking for inclined vibrating screen

The trained model is used for the prediction of choking judgement by using the logical choking function δ. The Choking judgement model is used to obtain the ranges of operational conditions that cause choking and do not cause choking respectively, including vibration amplitude and frequency and the inclination angle. It is also tested under different particle size distributions. Here we consider three size distributions as listed in Table 6-5 (Arifuzzaman, S. M., Dong, Kejun & Yu, Aibing 2022). Here we divide the undersize particles into three categories: (i) small undersize particles, whose sizes are less than 50% of aperture size; (ii) medium undersized particles, whose sizes are equal to or greater than 50% but smaller than 85% of aperture size; and (iii) near-mesh undersize particles, whose sizes are equal or greater than 85% but less than 100% of aperture size. The category of each size component is given in Table 6-5.

Table 6-5 List of feeding materials with different particle size distributions.

	Component *i*	1	2	3	4	5	6	7
	Category	small undersize	small undersize	small undersize	medium undersize	medium undersize	near-mesh undersize	oversize
	Feed Size (mm), d_i	1.1	1.33	1.67	2	2.5	3.1	3.7
Feed-1 (total feed rate = 39347.70348mm^3/sec)	Feed Rate (num/sec), n_i	5300	3300	2000	1500	800	550	200
	Volume ratio	9.39%	10.33%	12.40%	15.97%	16.63%	21.80%	13.48%
Feed-2 (40663.76377 mm^3/sec)	Feed Rate (num/sec), n_i	4400	3200	1900	1200	950	700	200
	Volume ratio	7.54%	9.69%	11.39%	12.36%	19.11%	26.85%	13.04%
Feed-3 (41457.69214mm^3/sec)	Feed Rate (num/sec), n_i	3300	2050	1250	1200	745	1100	200
	Volume ratio	5.55%	6.09%	7.35%	12.12%	14.70%	41.39%	12.79%

Figure 6-5 (a) shows the choking judgement phase diagram of the screen with the change of vibration frequency and inclination angle for Feed-1. For the lower vibration frequency (f < 20Hz), the screening shows choking and even with the larger inclination angle. For 20Hz ≤ f < 25Hz, the screening shows choking for lower inclination angle ($\theta = 5^o$), which is the

inclination threshold of choking under the vibration condition. To remove the choking problem of the screening, higher values of inclination angle ($\theta > 5°$) and the vibration frequency are required. Figure 6-5 (b) shows the choking judgement phase diagram of screening with the change of vibration amplitude and inclination angle. For the lower vibration amplitude (A =2mm), the screening chokes for the lower values of inclination angle and the choking removed with the increase of inclination angle (Dong, K, Yu & Brake 2009). For A > 2mm, the screening does not choke for $\theta = 5°$. Higher vibration amplitude and inclination angle are able to remove the choking of screen and this is mainly due to the increase of particle velocity and flow rate.

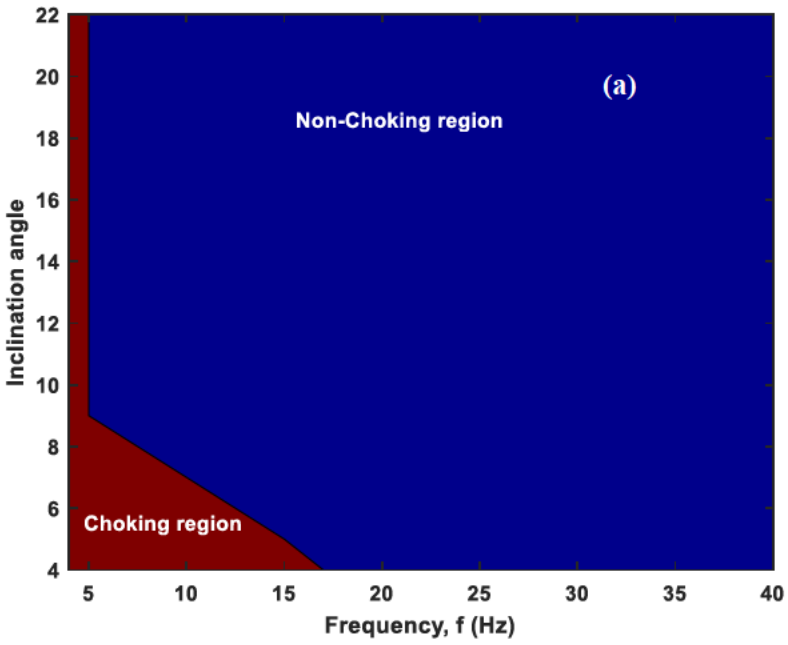

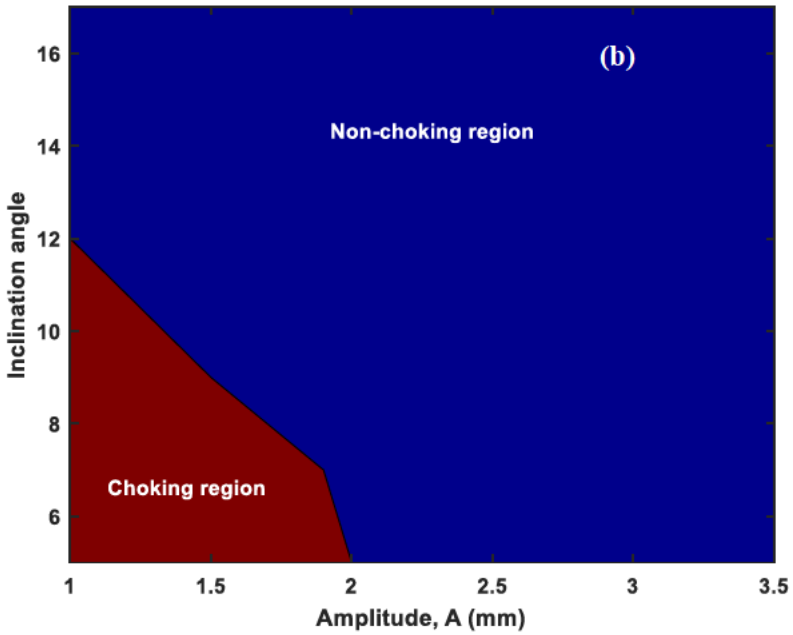

Figure 6-5 Choking judgement phase diagram for Feed-1, (a) the choking and non-choking cases of screen are the function of inclination angle and vibration frequency (f), A = 2.0mm, and (b) the choking and non-choking cases of screen are the function of inclination angle and vibration amplitude (A), f = 20Hz..

Figure 6-7 (a) shows the choking judgement phase diagram of screening with the change of vibration frequency and inclination angle for Feed-2. For the lower vibration frequency ($f <$ 25Hz), the screening shows choking with an increase of inclination angle ($\theta \leq 12°$). For 20Hz $\leq f <$ 35Hz, the screening shows choking for lower inclination angle ($\theta \leq 10°$), which is the inclination threshold of choking under the vibration condition. Higher vibration frequency able to remove the choking problem of screen, even in lower inclination angle. For the Feed-2, there is no choking for the inclination angle $\theta > 12°$. This is probably because that the combination of higher inclination angle and frequency increase the flow velocity of particles and remove the blocking of medium undersize particles to the apertures. In contrast, Figure 6-7 (b) provides the choking condition phase diagram of the screening process with a change of vibration amplitude and inclination angle. For a lower vibration amplitude, the screening process shows choking for lower values of inclination angle, and the choking condition is removed with an increase in amplitude. The blocking effect could be more significant for medium undersized particles than for small undersized particles. For $A > 2$ mm, the screening process chokes for $\theta < 13°$, and better sieving is achieved for a higher inclination angle and amplitude. For medium undersized particles, the threshold of inclination angle is higher than in Feed-1.

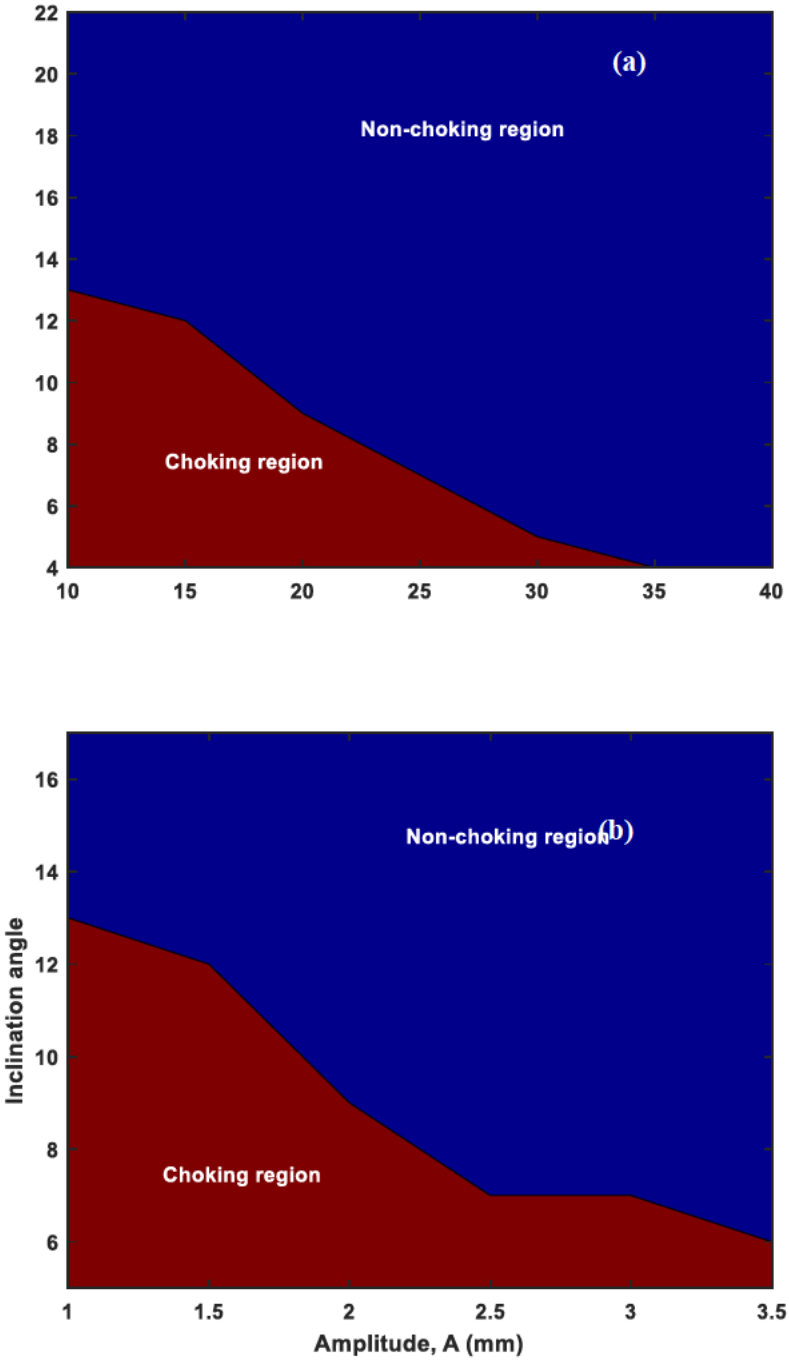

Figure 6-6 Choking judgement phase diagram for Feed-2, (a) the choking and non-choking cases of screen are the function of inclination angle and vibration frequency (f), A = 2.0mm, and (b) the choking and non-choking cases of screen are the function of inclination angle and vibration amplitude (A), f = 20Hz.

Figure 6-7 (a) shows the choking condition phase diagram of the screening process with a change of vibration frequency and inclination angle for Feed-3. A higher vibrational frequency can remove the choking problem of the screen, and $\theta < 12°$ is the inclination threshold. By using near-mesh undersized particles in the feed, the choking region decreases in comparison with Feed-2 because of greater percolation of undersized particles. In Figure 6-7 (b), shows the choking condition phase diagram of the screening process with a change of vibration amplitude and inclination angle. The choking region is also lower than Feed-2. A higher vibrational amplitude can remove the choking condition of the screening process.

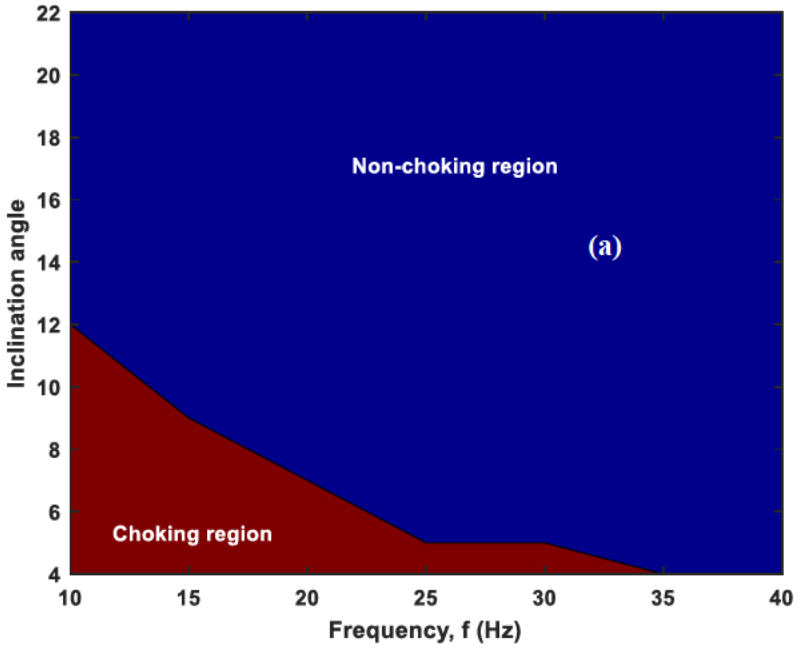

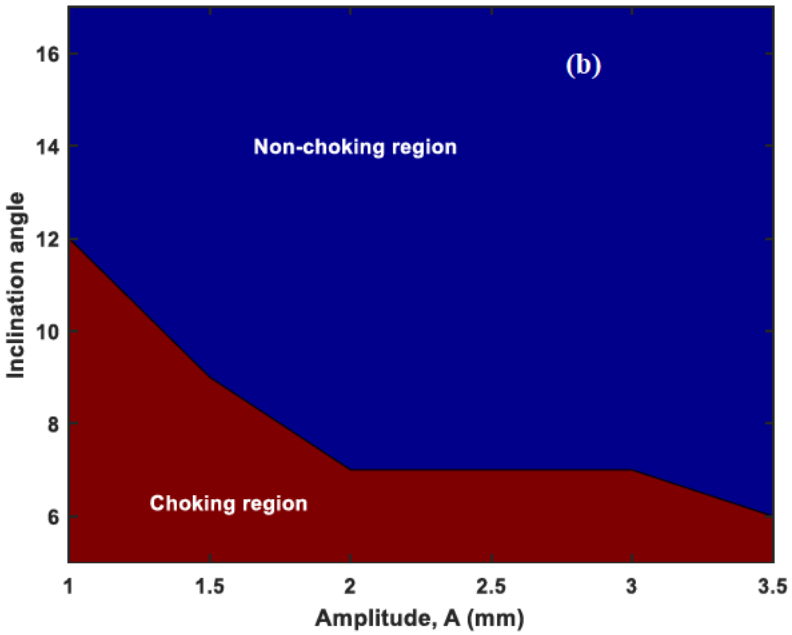

Figure 6-7 Choking judgement phase diagram for Feed-3, (a) the inclination angle as a function of vibration frequency (f), A = 2.0mm, and (b) the inclination angle as a function of vibration amplitude (A), f = 20Hz.

Figure 6-8 shows the comparison of three types of feed for choking and non-choking judgement with the change of vibration amplitude, frequency, and inclination angle. There are three lines in Figure 6-8 (a), below the line shows the choking region and upper region from the line shows the non-choking region. Similarly, the choking and non-choking regions for Feed-2 and Feed-3 show in Figure 6-8. It can be seen that small under sized particles' (Feed-1) non-choking region is highest among the feeds in Figure 6-8 (a). On the other hand, the choking region is maximum for the Feed-2 than Feed-3 for the change of vibration amplitude and inclination angle. The possible reason is the inclination angle of screen and the presence of large number of medium undersize particles covers screen apertures, less chances for particles to collide with the screen mesh and pass, and screen faces a blocking. Figure 6-8 (b) shows the comparison of three types of feed for choking and non-choking judgement with the change of vibration amplitude and frequency. It can be seen that small under sized particles' (Feed-1) non-choking region is highest among the feeds. But, the choking region is maximum for the Feed-3 than Feed-2 for the change of vibration amplitude and frequency. The possible reason is the vibration condition and the presence of large number of near-mesh undersize particles, less chances for particles to collide with the screen mesh and pass, and screen faces a blocking.

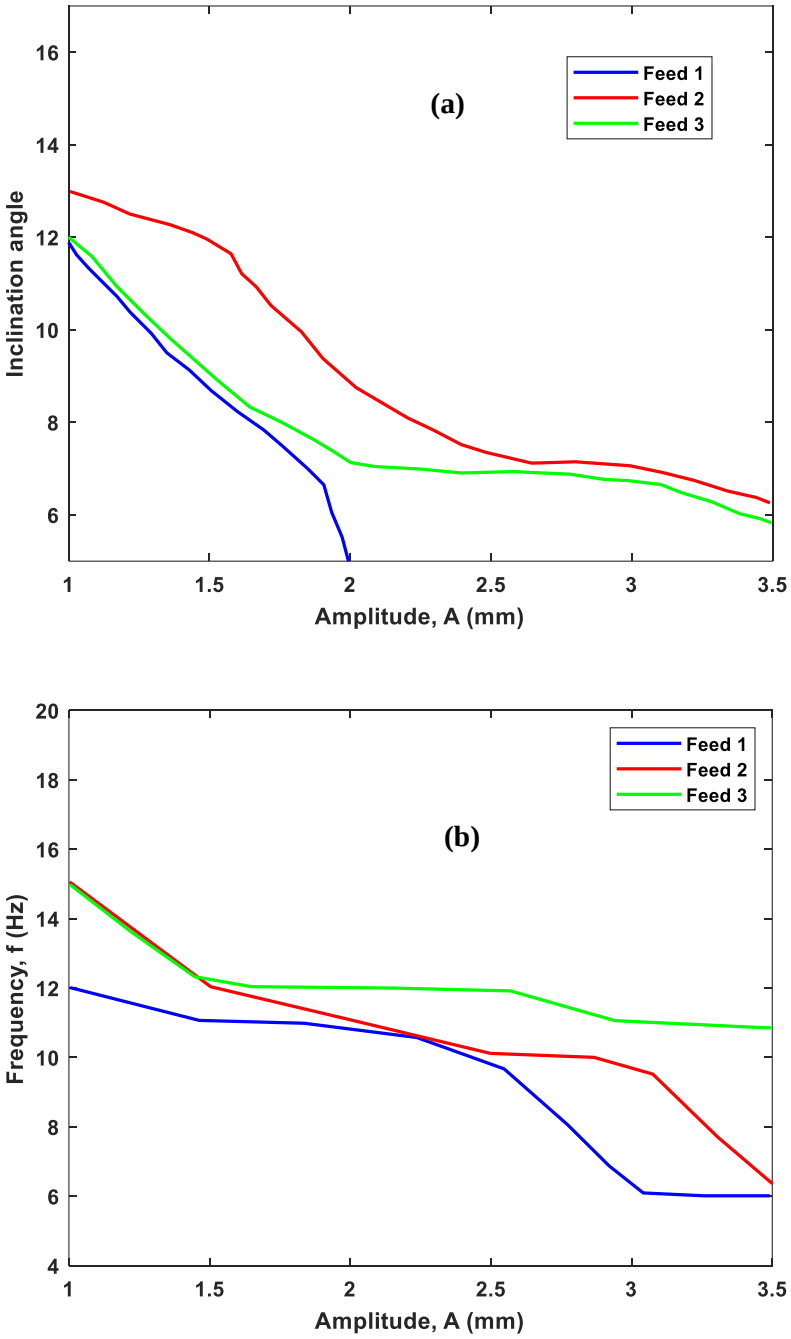

Figure 6-8 Choking judgement phase diagram comparison for three types of feed; (a) variation of inclination angle and vibration amplitude (f = 20Hz); (b) variation of vibration frequency and amplitude ($\theta = 11^{o}$).

Figure 6-9 shows the snapshots of simulation for Feed-2 and Feed-3 for A = 1.8 mm, f = 20 Hz and θ=11º. The packed bed on the screen for these two feed conditions, from which we can see why Feed-2 is the worst with more medium undersize particles, but Feed-3 is better than Feed-2, although with more near-mesh size particles. Which is also satisfying the Figure 6-9 conditions.

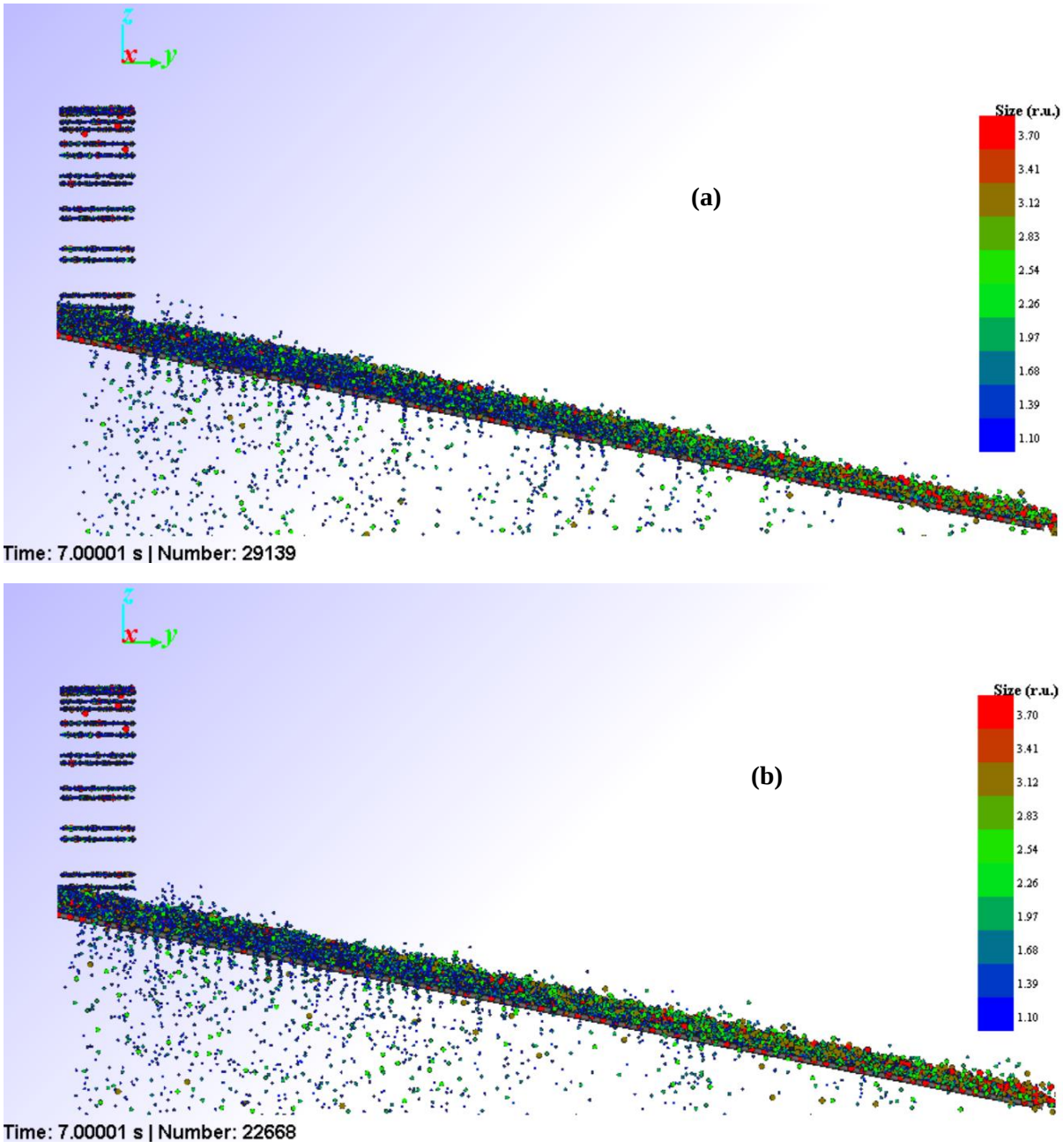

Figure 6-9 Snapshot of simulation of the inclined vibrating screen; (a) Feed-2 and (b) Feed-3 for A = 1.8 mm, f = 20 Hz and θ =11º.

Figure 6-10 shows the combination phase diagram of process model (Arifuzzaman, S. M., Dong, Kejun & Yu, Aibing 2022) and choking judgement model; where D_{50} and Ep are the function of vibration frequency and amplitude. Figure 6-10 (a) shows the phase diagram for D_{50} as a function of A and *f*. The process model predicts the partition curves for various vibration conditions and helps to predict the D_{50} and Ep. On the other hand, the choking judgement model predicts the choking and non-choking results for the various vibration conditions. The combination of both model helps to understand the choking and non-choking cases, D_{50} and Ep for different vibration frequency and amplitude. Moreover, D_{50} increases with the increase of A and *f*. Lower A and *f* are not effective for a better screen performance and creates choking condition. Figure 6-10 (b) shows the phase diagram for Ep as a function of A and *f*. The Ep is maximum for the lower values of A and *f*, which is notifying in the choking region. The combination of process model and choking judgement model helps to define the Ep, choking, and non-choking region easily. The phase diagram also justifies both model prediction of Ep and choking judgement that lower vibration is not effective for better screen performance.

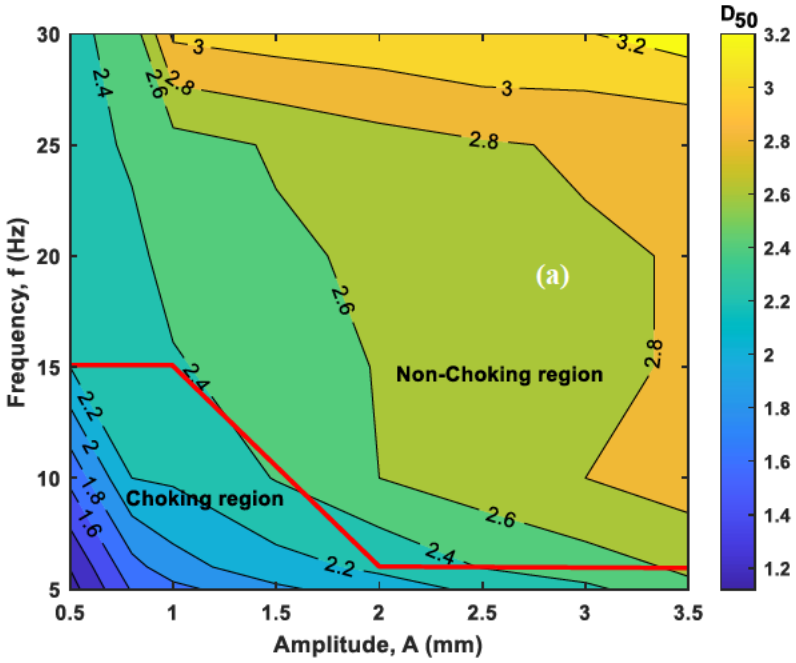

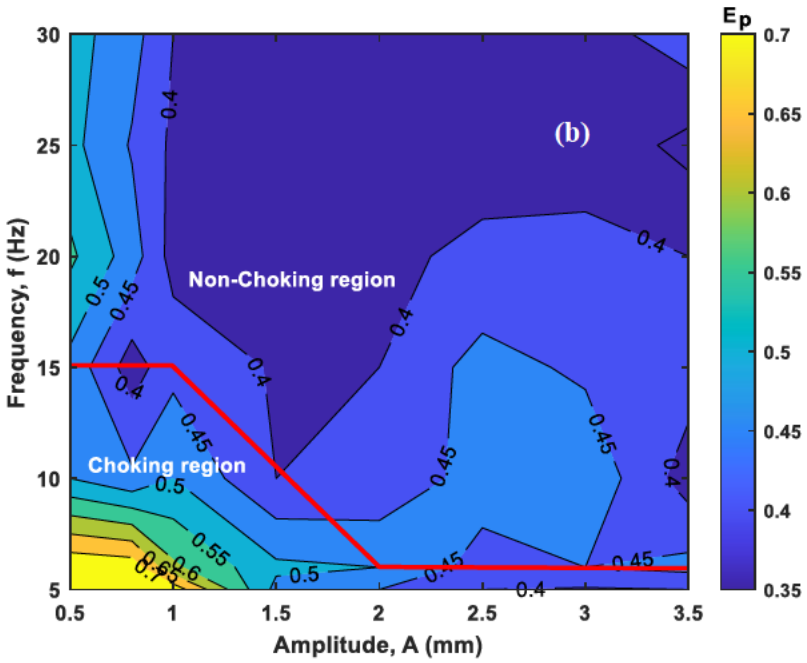

Figure 6-10 Combination phase diagram of process model (Arifuzzaman, S. M., Dong, Kejun & Yu, Aibing 2022) and choking judgement model; (a) D_{50} is a function of vibration amplitude and frequency; (b) Ep is a function of vibration amplitude and frequency, where red line divides the choking and non-choking region. (For 39347.70348mm^3/sec and θ =11°)

6.4.4 Choking and threshold of feeding

As previously discussed, a higher feed rate will cause screen chocking. In practice, the particle size distribution of feeding materials will not change. Here we use the judgement model to get the threshold of the total feed rate for chocking under given vibration amplitude and frequency, the inclination angle, and particle size distribution. The total particle volumetric feed rate is defined as C, given by:

$$C = \sum_i \frac{\pi}{6} n_i {d_i}^3 \qquad \text{(Eq. 6.8)}$$

The feed threshold of chocking is denoted as C_T, and defined as: if $C>=C_T$, chocking will happen; if $C<C_T$, chocking will not happen.

It is very important to know the feed threshold for choking of screen by the use of choking judgement model. The logical model is trained with various feed rate with choking and non-choking screen cases. The feed threshold (C_T) of choking can be defined with a total particle

volume, which makes unsteady flow of particles, and the inlet will be greater than the sum of outlet and passing of particles. Using the logical choking model, it can more easily predict the feed threshold (C_T) under the condition $\{d_i, I_i\}, A, f$, and θ by starting from a non-chocking case, and gradually increase C until the model predicts chocking.

In Figure 6-11, the feed threshold (C_T) is as a function of A and f. The feed threshold increases with the increase of vibration frequency and amplitude. Larger vibration conditions is suitable to avoid the choking of screen. However, it is time consuming to obtain the exact feed threshold from simulation and the machine learning model helps to predict the feed threshold easily with the choking judgement. But, the judgement of choking for various feed can be predicted by logical choking model with a short time. Therefore, here the value of C corresponding to 0.1 is considered as the feed threshold under such vibration conditions. Moreover, the contours of the feed threshold (C_T (mm^3/sec)) as a function of A and f, the vibration conditions for choking of a particular mixture/inlet can be easily identified, which can be a guidance for the related operations.

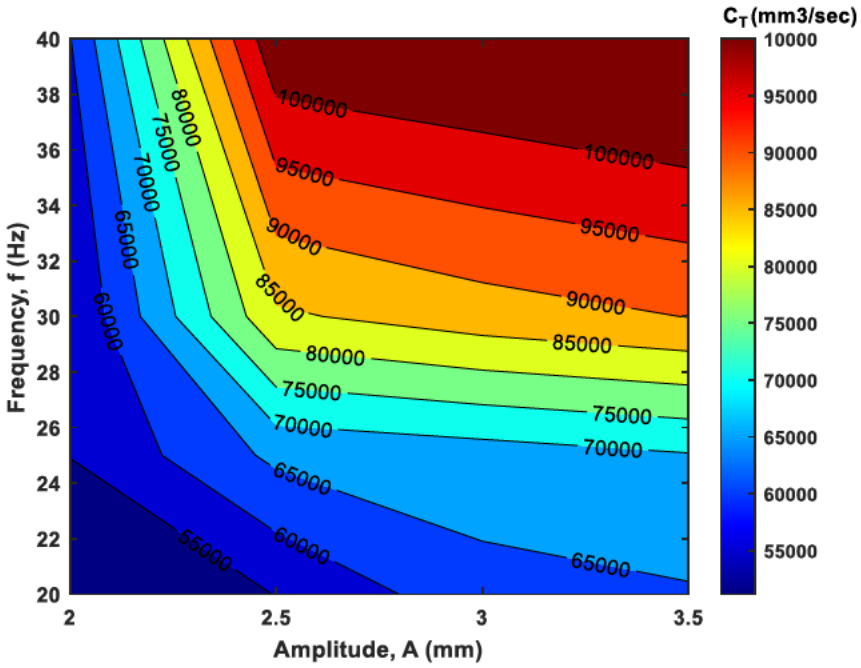

Figure 6-11 Feed threshold (C_T) of choking as a function of vibration amplitude and frequency, based on the results predicted by the logical model for Feed-1 and θ =11°.

Figure 6-12 shows the DEM simulation of particles flow to valid the ML prediction of choking threshold for feeding change. From the Figure 6-11, A value from the Figure 6-11 has been chosen for the feeding threshold C_T = 85777.994 mm^3/sec for the specific controlling variable A = 2.8mm, f = 31Hz and θ =11°. To valid the feeding threshold for the choking, we choose the point as a bit lower and higher than threshold, but not exactly at the threshold are simulated as shown in Figure 6-12 and the feed is considered as Table 6-5. In Figure 6-12(a), the particles flow along the screen remains steady state and shows non-choking for C= 84597.56 mm^3/sec. On the other hand, the flow of particles is slow for C = 86564.95 mm^3/sec in Figure 6-12 (b). A large amount of particles are on screen and lower flow along the screen for the choking, which valid the feeding threshold C_T = 85777.994 mm^3/sec as the Figure 6-11.

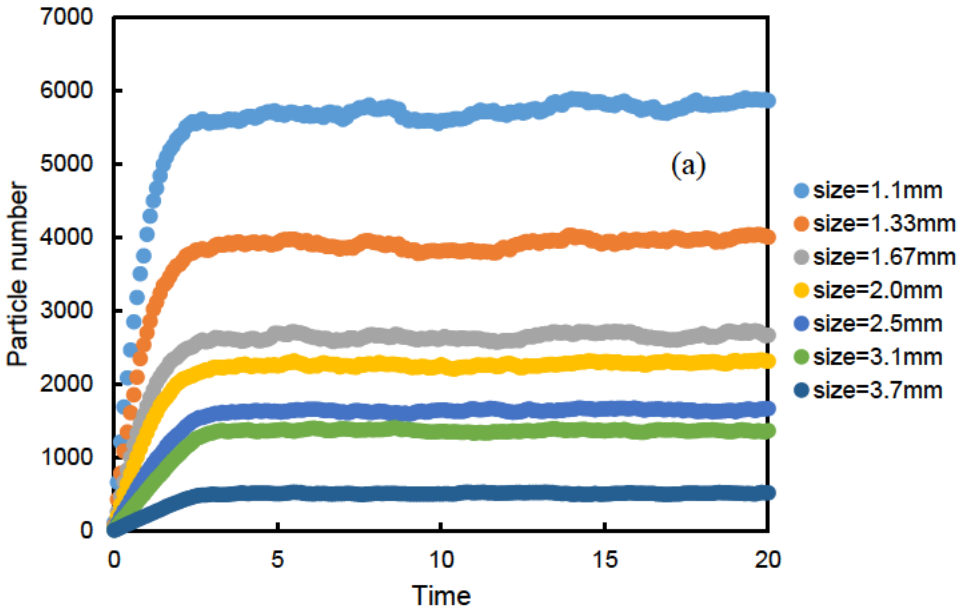

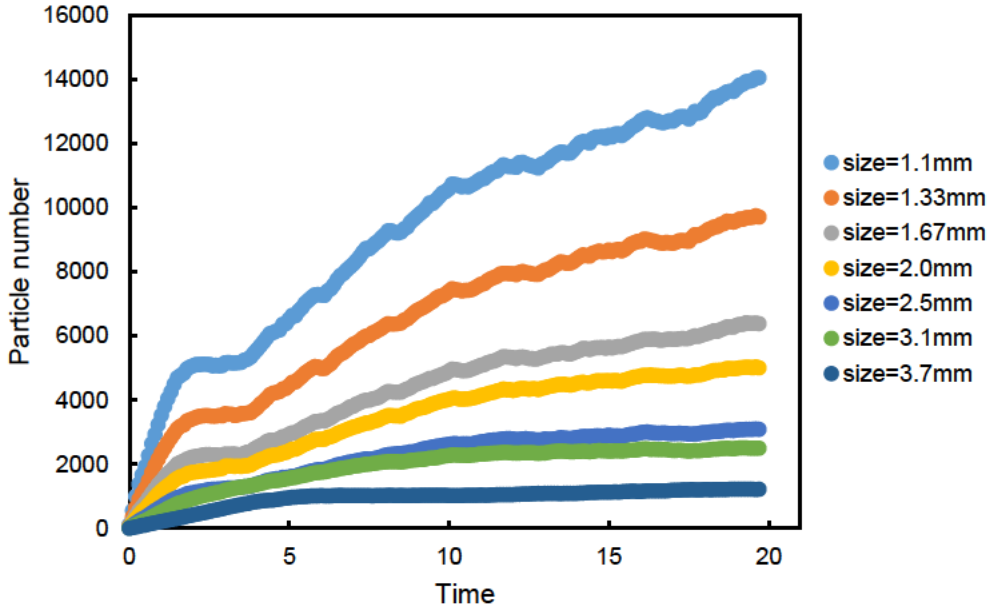

Figure 6-12 Overflow of particles of non-choking and choking cases for validation with DEM simulation and ML feed threshold (C_T) of choking; (a) for C= 84597.56 mm^3/sec, and (b) for C= 86564.95 mm^3/sec (θ =11°) for, A = 2.8mm, f = 31Hz and θ =11°.

In Figure 6-13, we considered C = Feed-3, the choking of screen for various feed of particles distribution can also be predicted by logical choking model with a short time. Moreover, the contours plot of the feeding threshold (C_T) as a function of A and f and feeding threshold increases with the increase of A and f.

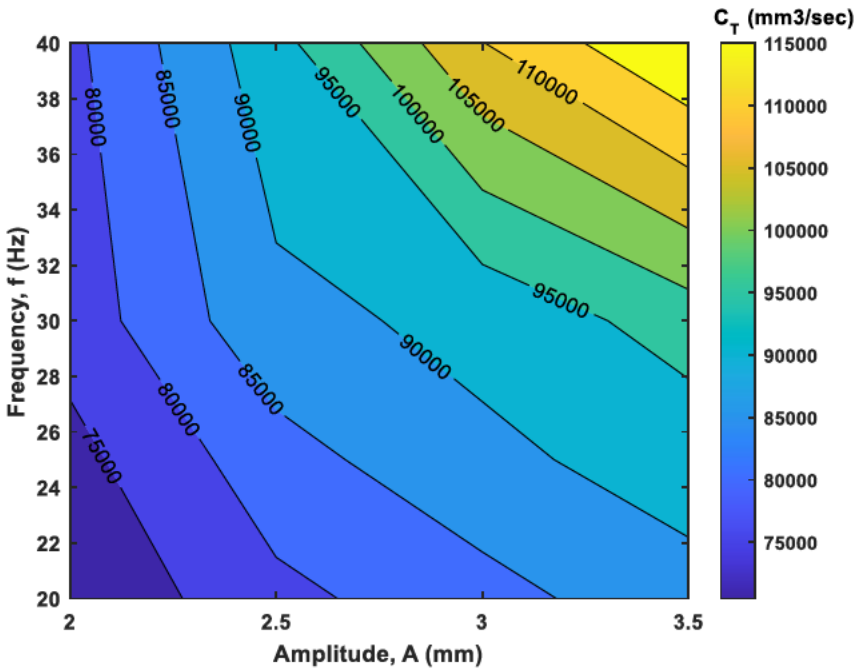

Figure 6-13 Feed threshold (Tc) of choking as a function of vibration amplitude and frequency, based on the results predicted by the logical model for C15 = Feed-3 and θ =11°.

Figure 6-14 shows the DEM simulation of particles flow to valid the ML prediction of feeding threshold for choking. From the Figure 6-13, we choose a feeding threshold C_T = 90377.77 mm^3/sec for the specific controlling variable A = 2.8mm, f = 30Hz and θ =11°. To valid the feeding threshold for the choking, we choose the point as a bit lower and higher than threshold are simulated as shown in Figure 6-14. In Figure 6-14 (a), the particles flow along the screen remains steady state and shows non-choking for C= 89134.04 mm^3/sec. On the other hand, the flow of particles is slow for C= 91621.5 mm^3/sec in Figure 6-14 (b), which valid the Figure 6-13 feed threshold C_T = 90377.77 mm^3/sec.

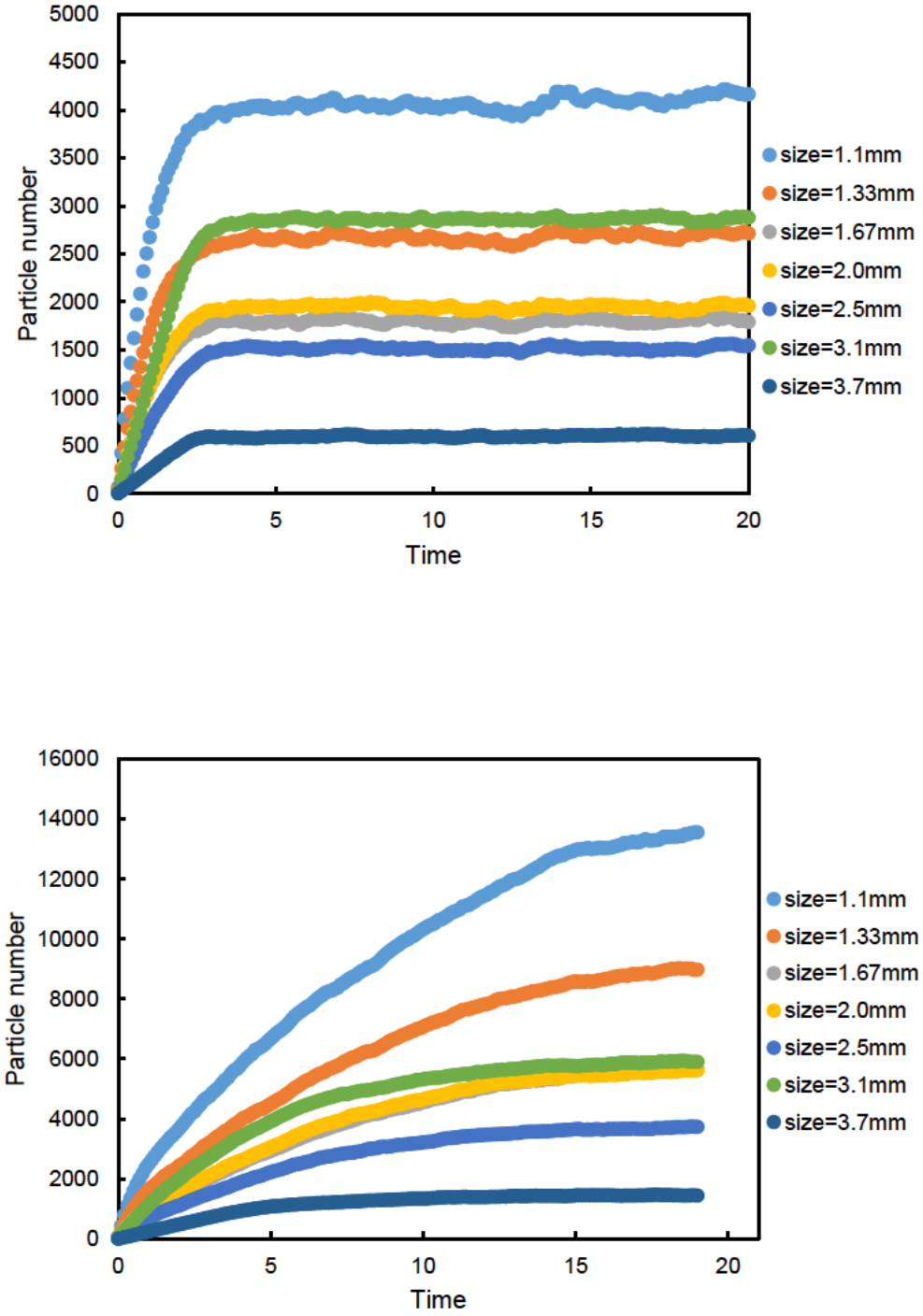

Figure 6-14 Overflow of particles of non-choking and choking cases for validation with DEM simulation and ML feed threshold (C_T) of choking; (a) for C= 89134.04 mm^3/sec, and (b) for C= 91621.5 mm^3/sec (θ=11°) for, A = 2.8mm, f = 30Hz and θ =11°.

6.4.5 Choking judgement for multi-deck screen

Although the database for training is from the simulations of the simple incline screen, the logical choking model should be able to be used for screens with different vibration conditions and inclination angles at different segments, which are similar to multi-deck screens and variable vibration amplitude/frequency screens. In the following, we will apply the logical model to these kinds of screens. For multi-deck screen, the judgement of choking model in the flow chart is illustrated in Figure 6-15. The judgement of choking of two-deck screens with different inclination angles are considered. At the initial stage, the input $(\{d_i, I_i\}^1, A, f, \theta_1)$ for deck-1 is considered. If the screening is choking by using the logical function $\delta_1(\{d_i, I_i\}^1, A, f, \theta_1)$, the judgement is choking for the deck-1. But, if the screening is not choking, the process model (Arifuzzaman, S. M., Dong, Kejun & Yu, Aibing 2022) will predict the inlet for the deck 2 or segment -3. This processs will apply again for the deck 2. The input $(\{d_i, I_i\}^3, A, f, \theta_2)$ for deck-2 is considered. If the screening is choking for deck-2 by using the logical function $\delta_2(\{d_i, I_i\}^3, A, f, \theta_2)$, the judgement is choking for the deck-2 and stop the screeing. But, if the screening is not choking, the logical model will predict the non-choking judgement.

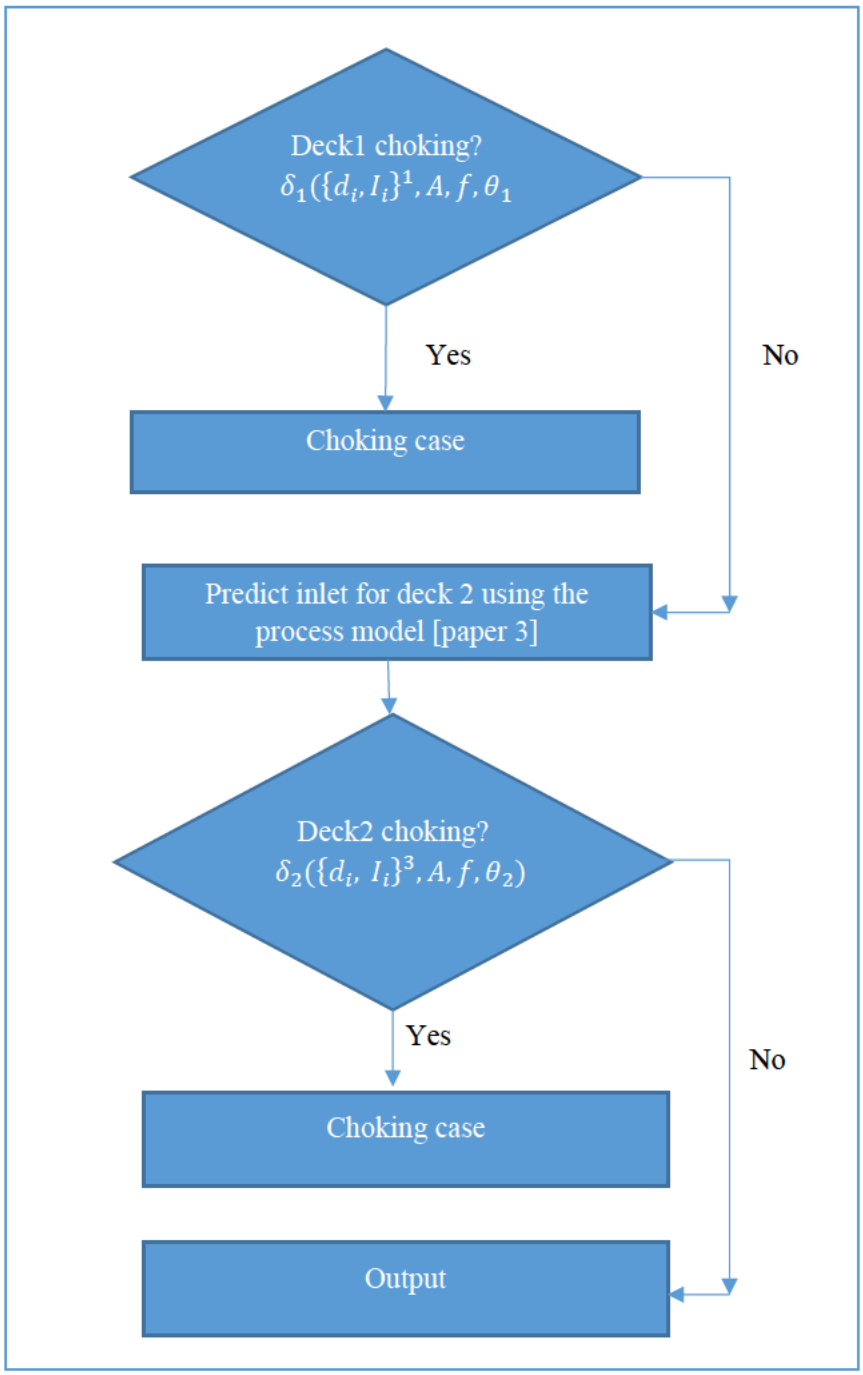

Figure 6-15 Logical choking judgement model flow chart for multi-deck screen.

Figure 6-16 shows the choking judgement phase diagram of multi-deck screen with the change of inclination angle (θ_1 and θ_2) of decks. In Figure 6-16, the choking of screen occurs both decks for the lower value of θ_1=θ_2=6° and non-choking screening shows for the higher value of inclination angle. For the non-choking screening of deck 1, the particles flow to the deck 2 as discussed in Figure 6-15. The logical choking model function δ_2 applies for the deck 2 to

predict the judgement of choking. The particles stuck on the upper part of deck 2 for $\theta_1 < \theta_2$ in Figure 6-16 and choking occurs. For deck 1, the choking occurs for $\theta_1 = 9°$ and 17° for the larger value of θ_2. In summary, the large number of particles stuck on the screen for the lower inclination angle of deck and for $\theta_1 < \theta_2$.

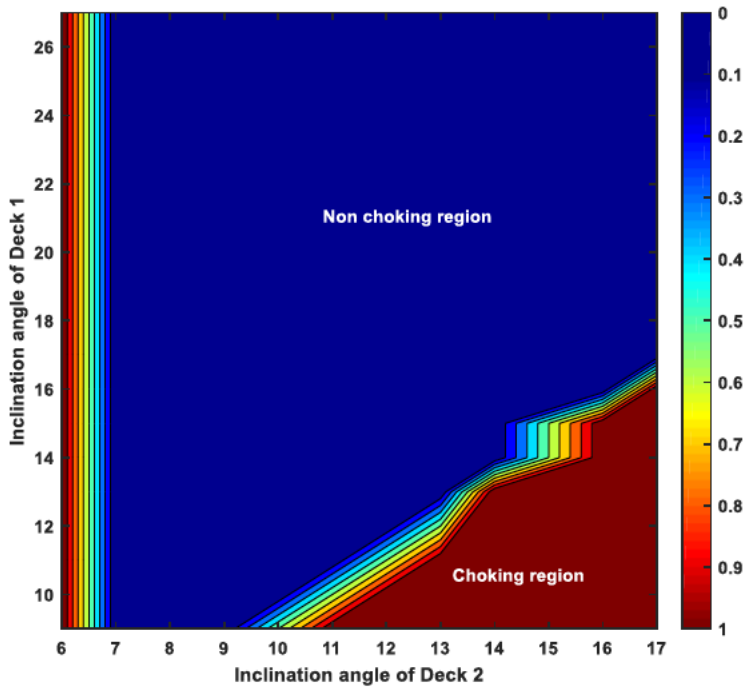

Figure 6-16 Choking judgement phase diagram of multi-deck screen for inclination changes of decks. Where, A =2.0mm, f =20Hz and Feed-1.

Figure 6-17 (a) shows the choking judgement of multi-deck screen with the change of vibration frequency (f_1 and f_2). The decks chokes for a lower value of vibration frequency. For the lower values f_1 <11Hz the screen chokes for deck 1 and deck 2 chokes for f_2 < 9Hz. The particles flow from the upper deck to lower deck slowly and particles stuck on the upper deck for lower value of f_1 and f_2. For higher values of vibration frequencies (f_1 and f_2), the logical choking model shows non-choking of screening and particles overflow using process model (Arifuzzaman, S. M., Dong, Kejun & Yu, Aibing 2022) to deck 2. Figure 6-17 (b) shows the choking judgement of multi-deck screen with the change of vibration amplitude (A_1 and A_2). The logical model judgement shows choking for both decks with a lower value of A_1 and A_2. For lower vibration amplitude, stuck on the screen and particles hardly able to flow. The particles overflow from the upper deck (with non-choking judgement for higher values of A_1 and A_2) to deck 2 and logical model predicts the judgement of choking for deck 2. Too lower

vibration condition is not effective for sieving. A balance of vibration condition is required for a better sieving for the both decks of multi-deck screen to avoid choking.

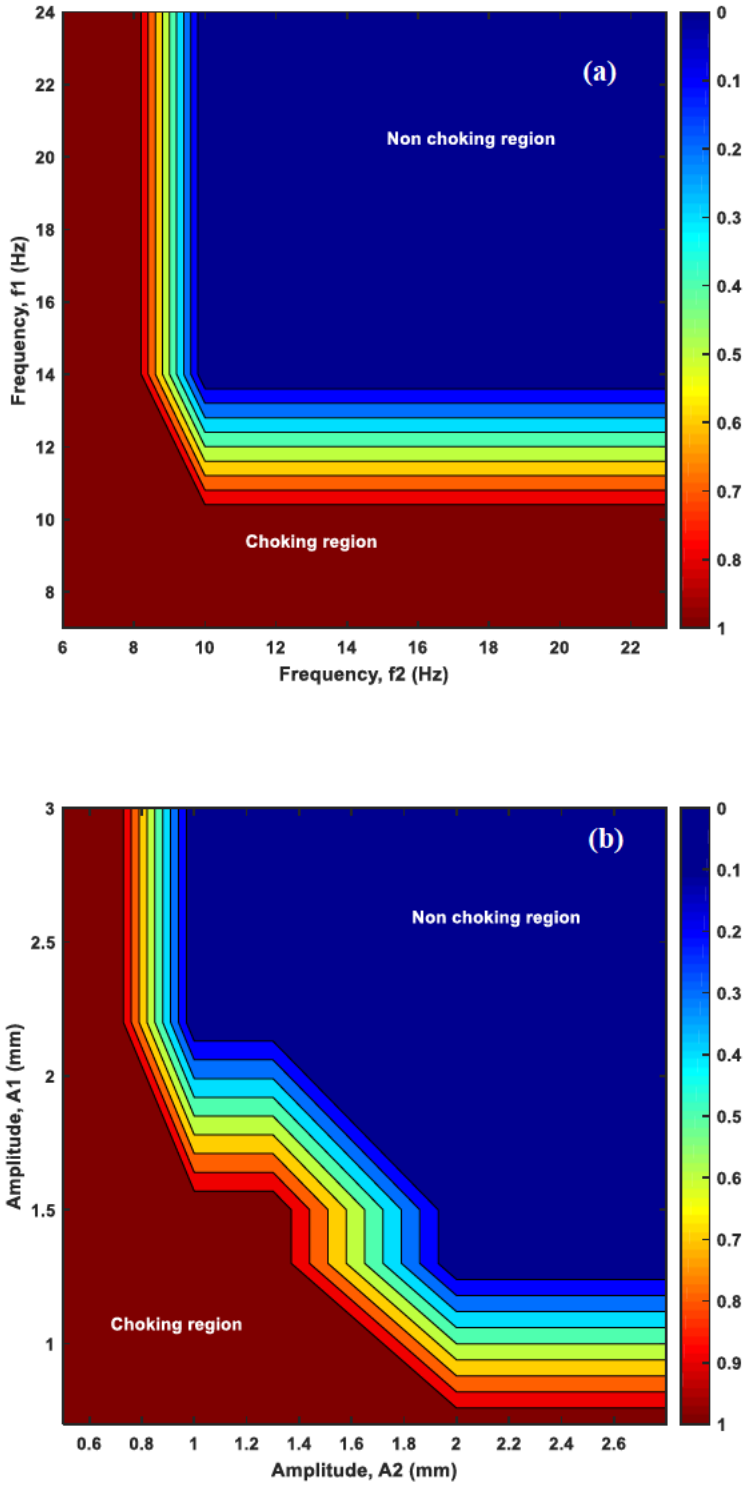

Figure 6-17 Choking judgement of multi-deck screen for; (a) vibration frequency (A_1=A_2 =2.0mm and θ=11°); and (b) vibration amplitude for f_1=f_2 =25Hz with Feed-1.

6.5 Conclusions

In this study, a logical judgement model for choking analysis an inclined vibrating screen is proposed by combining the DEM and machine learning. Operational parameters of screening such as particles size, inlet, and inclination angle are considered comprehensively to construct the logical function for choking prediction.

The logical machine-learning model can directly predict the choking judgement of screen under different operational conditions, and the predicted results are in good agreement with DEM results. However, the model can predict the threshold of controlling variables and feed of different sized particles for choking or non choking of screen. The logical ML model will help to ensure the perfect decision before any screening.

In addition, the logical model also provides few vital observations for choking of the screen. The screening chokes for the lower values of vibration conditions and this choking problem can be removed by increasing the vibration frequency and amplitude. The logical ML model functioned correctly to predict the choking judgement of the multi-deck screen. A low value of inclination angle is not effective for the decks of the multi-deck screen. The stratification of particles jam, and choking occurs. Similarly, the multi-deck screen chokes with lower values of the vibration condition.

Use of the machine learning and DEM combination logical model is a smart way make decisions about screen choking. The logical ML model will be helpful to optimise screening cases before any experiment or simulation work is conducted. The model can be applied to other granular processing industries for decision-making purposes.

Nomenclature

A	vibration amplitude
d_i	particles size (mm)
D_i	screen deck
E_p	probable error
f	vibration frequency
$\boldsymbol{F}_{ij}^{n}$	normal contact force
$\boldsymbol{F}_{ij}^{t}$	tangential contact force

$\boldsymbol{g}$	gravitational acceleration
$\boldsymbol{I}$	moment of inertia of the particle
I_i	Feed particles rate from a segment
m	mass of particle
n_i	number of feed particles rate
O_i	overflow rate from a segment or feed to the downstream segment
R_i	radius of particle *i*
R_j	radius of particle *j*
t	time
Tc	feed threshold
Y	Young's modulus

Greek letters

δ	logical function for choking or not
δ_1	logical function for choking or not for deck 1
δ_2	logical function for choking or not for deck 2
γ_n	normal damping coefficient
ξ_n	relative normal displacement
ξ_s	total tangential displacement
θ	inclination angle of the screen
θ_1	inclination angle of deck 1
θ_2	inclination angle of deck 2
ρ	density (kg/m^3)
$\tilde{\sigma}$	Poisson ratio
μ_r	rolling friction coefficient
μ_s	sliding friction coefficient
ω	particle angular velocity (s^{-1})

Subscripts

i	particle *i*
j	particle *j*
i j	between particles *i* and *j*

Abbreviations

ANN	artificial neural network
DEM	discrete element method
GPR	Gaussian process regression
ML	machine learning
RMSE	root mean square error
SVM	support vector machine

CHAPTER VII: Explicit contact force model for superellipses by Fourier transform and application to superellipse packing

7.1 Introduction

Particulate materials are ubiquitous in nature and are also commonly handled in many industries, such as civil engineering, metallurgy, mining, chemical and pharmaceutical sectors (Basinskas & Sakai 2016; Chu, Chen & Yu 2016; Cundall & Strack 1979; Govender et al. 2019; Kureck et al. 2019; Sakai et al. 2015; Zhong et al. 2016; Zhu et al. 2008). Owing to their discrete nature, continuous modelling of collectives of particles is still in development (Hou et al. 2019; Zheng & Yu 2014), while DEM (Cundall & Strack 1979; Lu, Third & Muller 2015; Zhu, HP et al. 2007; Zhu et al. 2008) is a cost-effective method of numerically studying this type of material with individual particles considered. The DEM uses first principles to model the motion of each particle, and if the interactions between particles can be accurately modelled the simulated results can be reliable. The most general interaction force between particles is contact force. However, calculation of contact force for non-spherical particles has not yet been fully solved (Lu, Third & Muller 2015; Zhong et al. 2016).

In the DEM, contact force is calculated based on contact mechanics (Johnson 1985; Zhu, HP et al. 2007). There are theoretical equations to describe contact force between non-spherical particles; however, to implement these equations in DEM they need to be adapted. Normally, although contacting particles are considered deformed in contact mechanics, in the most commonly used soft-particle DEM models, particles are assumed to be non-deformable, but overlap is allowed. The overlap is then linked to the parameters of contact mechanics to calculate the contact force that makes the particles resist overlap. The relationship between geometrical overlap and contact force involves contact mechanics, which is not discussed here in depth. The other aspect, geometrical overlap calculation, is also non-trivial (Feng, YT, Han & Owen 2012, 2017). Different methods have been proposed to find the geometrical overlap between non-spherical particles, which can be linked to different representations of particle shape (Dong, KJ, Wang, CC & Yu, AB 2015; Lu, Third & Muller 2015). Some methods approximate a particle with multiple elements and calculate the overlap based on the sum of that between the sub-elements (Favier et al. 1999; Vu-Quoc, Zhang & Walton 2000). For polyhedral, polygon and cylindrical particles, the overlap can be obtained by considering contact between different elements including edges, face and vertexes (Feng, YT, Han & Owen 2017; Govender et al. 2019; Kodam et al. 2010). Recently, the common plane method was proposed to simplify such procedures (Nezami et al. 2004; Vorobiev 2012). Similarly, methods have been proposed that adapt the problem to find the shortest distance between two bodies

(Wachs et al. 2012). For smooth surface particles or angular particles tailored with pseudo-potential, the overlap is normally found based on the surface equations of the particles by the geometric potential (GP) method (Boon, Houlsby & Utili 2013; Houlsby 2009; Lin, X & Ng, T-T 1995; Podlozhnyuk, Pirker & Kloss 2017; Zhou, Z-Y et al. 2011) or the common normal (CN) method (Cleary, PW, Stokes & Hurley 1997; Kildashti, Dong & Samali 2018; Lin, X & Ng, T-T 1995; Wellmann, Lillie & Wriggers 2008).

Except for the multi-sphere method, in most methods the overlap needs to be solved by numerical iteration during every time step in the DEM. This increases the computational effort; however, numerical divergence and diffusion may also need to be considered. Therefore, an explicit solution to overlap may overcome these difficulties and help determine the contact mechanics between non-spherical elements. Theoretical analysis of granular systems may also be adopted where explicit equations are required, such as analysis of collective or higher-order dynamics (Jiang, XC et al. 2011; Wu & Fuxreiter 2016).

Non-spherical particles contact model is still an open problem. Fast Fourier Transform (FFT)-based methods are approaches to converting surface displacements and tractions into the spatial frequency domain, where the contact problems such as to solve both the normal and tangential contact problems (Chen, WW 2013). Theoretically, the Fourier transform can be used for infinite-domain and the Fourier series for periodic problems, but most contact problems do not satisfy these conditions. For example, a point-contact problem has its pressure only on a small region of contacting surfaces. If the FFT is directly used to solve such a problem, the results near the borders have notable errors. In order to reduce the periodicity error, (Ju & Farris 1996) substantially extended the domain, (Ai & Sawamiphakdi 1999) decomposed the total pressure into a smooth portion and a zero-mean fluctuating portion.

In a previous study (Kildashti, Dong & Samali 2019), the overlap and contact force between non-spherical particles with respect to orientation angles were observed to be like intersecting waves. Based on this finding, Fourier series has been used to establish explicit force models by fitting the comprehensive force database. This idea has been applied to elliptical particles and showed its applicability. Interestingly, Fourier transform has been used to characterise complex shapes (Shen, Farid & McPeek 2009), but has never been used to model the interaction between non-spherical particles before. However, fitting a Fourier series with a large number of terms may be difficult. Conversely, Fourier transform can be a more general technique to establish

such Fourier series. In the present study, a method was proposed to establish an explicit force model by Fourier transform instead of direct fitting. The packing of non-spherical particles has received increasing attention (Delaney, Gary W & Cleary 2010; Delaney, Gary W., Hilton & Cleary 2011; Donev, Cisse, et al. 2004; Meng, Jiao & Li 2016; Wang, C, Dong & Yu 2015; Zhao, J et al. 2012; Zhou, Z-Y et al. 2011); however, there are few studies on the packing of superellipses. Therefore, the methodology is used to establish an explicit force model of superellipses and simulation of particle packing of such particles.

The remainder of the chapter is organised as follows. Section 7.2 elaborates on the general methodology and how it is applied to superellipses. Section 7.3 evaluates the accuracy of the established explicit force model and the simulation of the packing of superellipses with the model. The results demonstrate that the explicit force model for a given shape can be effectively established and used in the DEM by the proposed methodology. Further, the packing of superellipses shows similar features to that of ellipses and ellipsoids or polygons and cylinders with different shape parameters. The correlations between the packing fraction, coordination number and circularity were also examined. These results demonstrate the capability of using Fourier transform to establish explicit force models for non-spherical particles, and also provide new understanding of non-spherical particle packing.

7.2 Methodology

7.2.1 Definition of superellipse

In mathematics, the superquadrics are a family of geometric shapes defined by formulas that resemble those of ellipsoids and other quadrics, except that the squaring operations are replaced by arbitrary powers. They can be seen as the three-dimensional relatives of the superellipses. The term may refer to the solid object or to its surface, depending on the context. Superellipses are similar to superqudric shapes but not a subset of super quadrics. A superellipse can be defined as:

$$\left|\frac{x}{a}\right|^{\eta} + \left|\frac{y}{b}\right|^{\eta} = 1 \qquad \text{(Eq. 7.1)}$$

where η is 'squareness', as the increase of η makes the shape closer to square; a and b are the semi-axes along the x-axis and y-axis respectively. Regarding symmetry, a superellipse with a and b is a rotation of one with b and a. Thus, here only $a \geq b$ is considered. Consequently, the aspect ratio, defined as $\alpha = a / b$, is always equal to or greater than 1. Also only superellipses with $\eta > 1$, that is, convex particles without multiple contact points between two particles, were considered. Figure 7-1 shows all superellipse shapes considered here with changes of η and α covering a wide range of shapes from circle to nearly square. Therefore, the application of the proposed method on this series may be representative for a wide range of shapes.

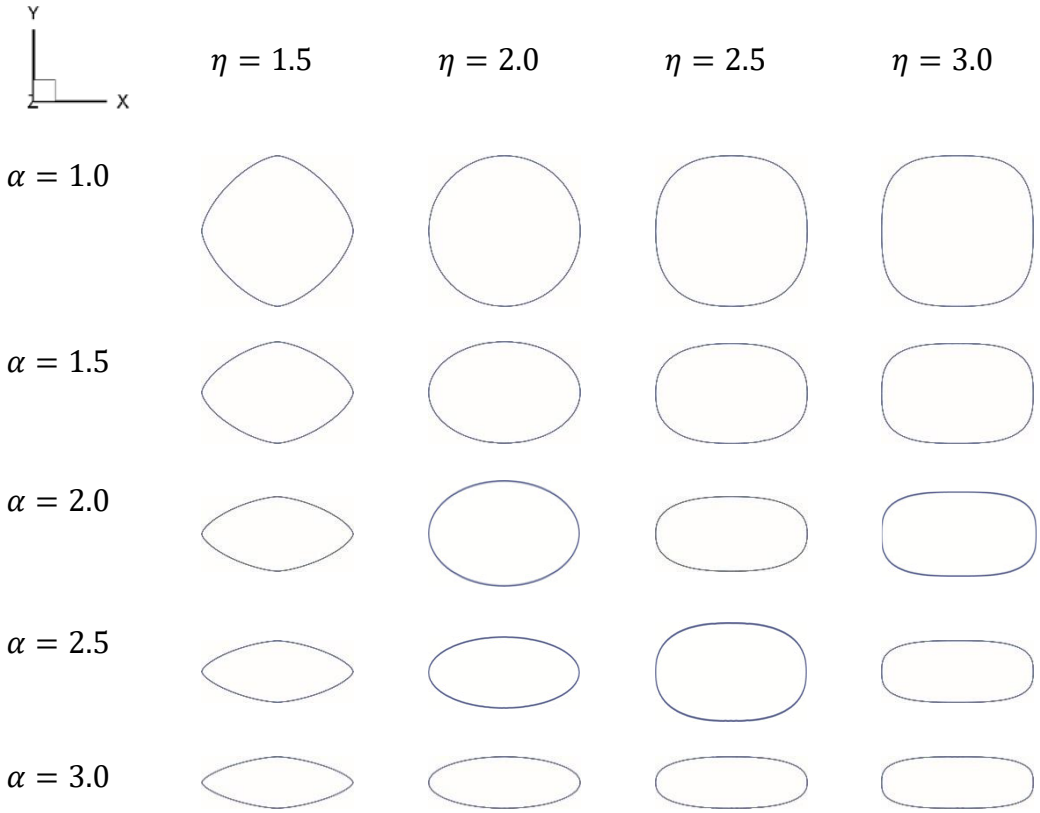

Figure 7-1 Superellipse shapes characterized by the aspect ratio and the squareness.

Normally for a particle the geometrical parameters that need to be considered in DEM include area (or volume in 3D), A, and the moment of inertia, I. For a superellipse, these can be determined by:

$$A = 4ab\frac{\left(\Gamma(1+{}^{1}/_{\eta})\right)^{2}}{\Gamma(1+{}^{2}/_{\eta})} \quad \text{(Eq. 7.2)}$$

$$I_{zz} = ab(a^2+b^2)\eta B\left(\frac{3\eta}{2},\frac{\eta}{2}\right) \quad \text{(Eq. 7.3)}$$

where Γ and *B* are the Gamma Function and the Beta Function respectively.

For a point (*x*,*y*) on the surface of the superellipse, the normal vector of the tangent plane **n** that cross this point can be given by its gradient:

$$\mathbf{n} = \frac{\nabla f(x,y)}{|\nabla f(x,y)|} \quad \text{(Eq. 7.4)}$$

where $f(x,y) = \left|\frac{x}{a}\right|^{\eta} + \left|\frac{y}{b}\right|^{\eta} - 1$.

Alternatively, the superellipse equation can be determined using an intermediate value φ:

$$\begin{aligned} x(\varphi) &= |\cos\varphi|^{\frac{2}{\eta}} \cdot a\ \mathrm{sgn}(\cos\varphi) \\ y(\varphi) &= |\sin\varphi|^{\frac{2}{\eta}} \cdot b\ \mathrm{sgn}(\sin\varphi) \\ 0 &\le \varphi < 2\pi \end{aligned} \quad \text{(Eq. 7.5)}$$

By combining (Eq. 7.4) and (Eq. 7.5), the tangential plane with the normal vector **n** (n_x, n_y) at a point related to φ can be determined by:

$$\begin{aligned} n_x &= \frac{\partial f}{\partial x}/K = \frac{\eta}{a}|\cos\varphi|^{\frac{2(\eta-1)}{\eta}}\mathrm{sgn}(\cos\varphi)/K \\ n_y &= \frac{\partial f}{\partial y}/K = \frac{\eta}{b}|\sin\varphi|^{\frac{2(\eta-1)}{\eta}}\mathrm{sgn}(\sin\varphi)/K \end{aligned} \quad \text{(Eq. 7.6)}$$

where *K* is a normalised parameter that makes $\|\mathbf{n}\| = 1$, and $\|\ \ \|$ is the normal operator.

Thus, for a tangent plane with normal vector **n**, its intersection point with the superellipse surface can be found by solving φ first using the following equation:

$$\varphi = \text{atan2}[\left|\frac{n_y b}{\eta}\right|^{\frac{\eta}{2(\eta-1)}} \text{sgn}(n_y), \left|\frac{n_x a}{\eta}\right|^{\frac{\eta}{2(\eta-1)}} \text{sgn}(n_x)] \quad \text{(Eq. 7.7)}$$

Then *x* and *y* can be obtained by (Eq. 7.5). This will be used in the CN method discussed in the following section.

7.2.2 Contact force for superellipses

There are different ways to calculate the contact force between two non-spherical particles. Here, particles whose surfaces can be described by a continuous function representation (CFR) are considered. For these particles, according to Hertz contact theory (Johnson 1985), the contact force between two particles can be determined by:

$$F_{nij}\hat{\mathbf{n}} = -\frac{4}{3}E_c\sqrt{R_m}(d_n)^{3/2}\,\hat{\mathbf{n}} \quad \text{(Eq. 7.8)}$$

where $E_c = \left(\frac{1-\nu_i^2}{E_i} + \frac{1-\nu_j^2}{E_j}\right)^{-1}$ and $\frac{1}{R_m} = \frac{1}{R_i} + \frac{1}{R_j}$, R_i and R_j are the principal relative radii of curvature, d_n is the penetration depth and $\hat{\mathbf{n}}$ is the normal vector of the contact plane. Note that for 2D shapes, (Eq. 7.8) may be slightly different for different shapes (Kildashti, Dong & Samali 2019), which has not yet been established for superellipses in the literature. Here, (Eq. 7.8) is ad-hoc extended to superellipses by accurately considering d_n and $\hat{\mathbf{n}}$, but approximating R_i and R_j by the radii of the circumscribed circles of the two particles. The theoretical form of (Eq. 7.8) for superellipses needs further study; however, the methodology introduced here can be general for different force models (Kildashti, Dong & Samali 2019).

The overlap parameters d_n and $\hat{\mathbf{n}}$ are normally linked with penetration points on the surface of two particles respectively. There are different methods to find the penetration points according to different concepts, the most commonly used being the GP and CN methods. In previous studies, the CN method was found to provide good agreement with sub-particle FEM modelling of these parameters (Kildashti, Dong & Samali 2018; Kildashti et al. 2018). Therefore, here CN is adopted, which is briefly introduced below.

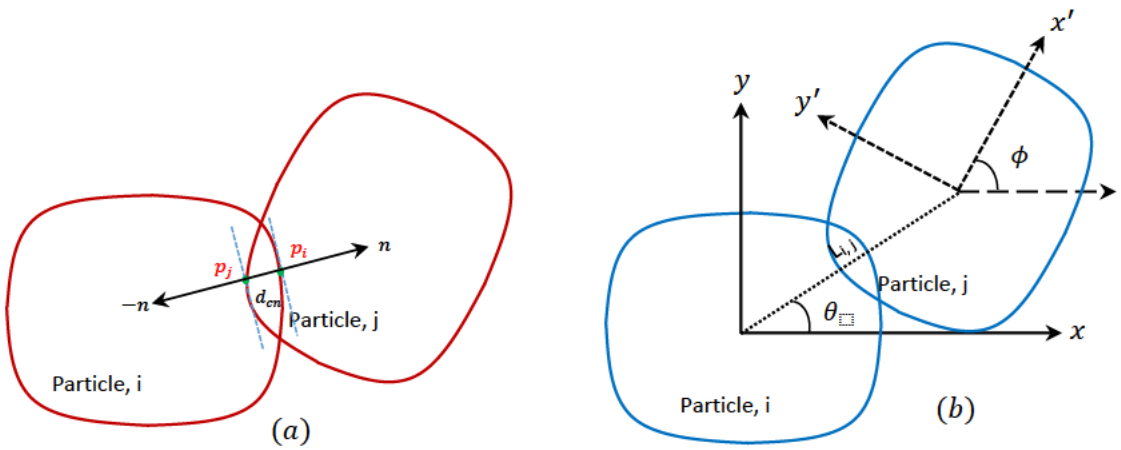

Figure 7-2 Schematics of (a) the common normal method for two superellipses in contact and (b) the dependencies of the overlap on orientation angles and penetration

The CN method was used to find two points $\mathbf{P_i}$ and $\mathbf{P_j}$ at the surfaces of two contacting particles respectively so that their tangent planes align to each other and also to their middle-perpendicular plane, as schematically shown in Figure 7-2 (a). Therefore they These can be obtained by solving the following equations (Kildashti, Dong & Samali 2018; Lin, X & Ng, T-T 1995; Wellmann, Lillie & Wriggers 2008):

$$\begin{gathered} f_i(\mathbf{P_i}) = 0 \\ f_j(\mathbf{P_j}) = 0 \\ \frac{\boldsymbol{\nabla} f_i(\mathbf{P_i})}{\|\boldsymbol{\nabla} f_i(\mathbf{P_i})\|} + \frac{\boldsymbol{\nabla} f_j(\mathbf{P_j})}{\|\boldsymbol{\nabla} f(\mathbf{P_j})\|} = 0 \\ (\mathbf{P_i} - \mathbf{P_j}) \times \boldsymbol{\nabla} \Gamma_i(\mathbf{P_i}) = 0 \end{gathered} \qquad \text{(Eq. 7.9)}$$

where $f_i = 0$ and $f_j = 0$ describe the surfaces of particle i and j respectively. The stable solution procedures to solve the equation set have been discussed in a previous study (Kildashti, Dong & Samali 2018). With $\mathbf{P_i}$ and $\mathbf{P_j}$, $d_n = \|\mathbf{P_i} - \mathbf{P_j}\|$, $\hat{\mathbf{n}} = \frac{(\mathbf{P_i} - \mathbf{P_j})}{\|\mathbf{P_i} - \mathbf{P_j}\|}$, and the contact point is given by $(\mathbf{P_i} + \mathbf{P_j})/2$.

7.2.3 DFT of ODDS database and explicit model by IDFT

Normally in a DEM model, numerical iteration must be used to find $\mathbf{P_i}$ and $\mathbf{P_j}$ in every time step and there is no explicit solution. To overcome this difficulty, the ODDS method (Dong, KJ, Wang, CC & Yu, AB 2015) was proposed to generate a comprehensive force database,

which will be transformed by discrete Fourier transform later. The concept of ODDS is briefly introduced here.

Contact between two superellipses (*i, j*) was considered in the body-fixed coordinate system of particle *i*, as schematically shown in Figure 7-2b. For equal shaped particles, d_n and $\hat{\mathbf{n}}$ should be dependent on $(L_{ij}, \theta\ , \phi)$, where $\boldsymbol{L_{ij}}$ pointing from the centre of particle *i* to the centre of particle *j*. L_{ij} is the length and θ is the direction angle of L_{ij} as shown in Figure 7-2b. ϕ denotes the rotation of particle *j*. Without loss of generality, L_{ij} is replaced with a dimensionless parameter defined as the overlap ratio: $\delta_h = \frac{h_{max} - L_{ij}}{h_{max}}$, where h_{max} denotes the maximum distance between particles *i* and *j* at the onset of contact. To establish d_n and $\hat{\mathbf{n}}$ as functions of $(\delta_h, \theta\ , \phi)$, all possible conditions were considered, that is, the full range of angles as a series of discrete values (i.e., 0°, 1°, … , 359°). Further, for δ_h, at each orientation $(\theta\ , \phi)$, overlap parameters at different pre-set δ_h were calculated and correlated by a Taylor series of δ_h up to order 2 to 3, considering that δ_h is small in DEM. With such a database, calculation of the overlap at arbitrary orientation $(\theta\ , \phi)$ and centre distance (L_{ij}) can be just an interpolation of the stored solution without solving any higher-order equations. This method has been realised (Dong, KJ, Wang, CC & Yu, AB 2015) and used in previous studies (Dong, K, Wang & Yu 2016; Wang, C, Dong & Yu 2015). Here, the database was used to build an explicit equation that could be used without the database.

Actually, for an ellipse, which is similar to a superellipse, it is found that $\hat{\mathbf{n}}$ is complicatedly dependent on $(\theta\ , \phi)$ but changes slightly with δ_h (Kildashti, Dong & Samali 2019). Then by knowing $\hat{\mathbf{n}}_1$ at δ_h = 5% and $\hat{\mathbf{n}}_0$ at δ_h = 0%, $\hat{\mathbf{n}}$ at other δ_h can be linearly interpolated, while in extreme cases in which δ_h > 5%, $\hat{\mathbf{n}}_1$ can be used as $\hat{\mathbf{n}}$. After obtaining $\hat{\mathbf{n}}$, P_i and P_j can be easily found according to (Eq. 7.7). Therefore, the calculation of the overlap was changed to and $\hat{\mathbf{n}}_0$ according to θ, ϕ and δ_h, where δ_h is dependent on $h_{max}(\theta, \phi)$.

Figure 7-3 shows the dependency of h_{max} on orientation angle. In a previous study, a 2D Fourier series was used to fit such relationships (Kildashti, Dong & Samali 2019). The Fourier series is determined by:

$$F(\theta_L,\phi)=\sum_{m=0}^{M}\sum_{n=0}^{N}\left[A_{mn}\cos\frac{\pi m\theta}{\theta_m}\cos\frac{\pi n\phi}{\phi_m}+B_{mn}\sin\frac{\pi m\theta}{\theta_m}\cos\frac{\pi n\phi}{\phi_m}+C_{mn}\cos\frac{\pi m\theta}{\theta_m}\sin\frac{\pi n\phi}{\phi_m}+D_{mn}\sin\frac{\pi m\theta}{\theta_m}\sin\frac{\pi n\phi}{\phi_m}\right] \quad \text{(Eq. 7.10)}$$

where F is the interpolated function of contact information parameters, θ_m and ϕ_m define the boundary of the domain, and M and N are the number of terms used to generate the Fourier series.

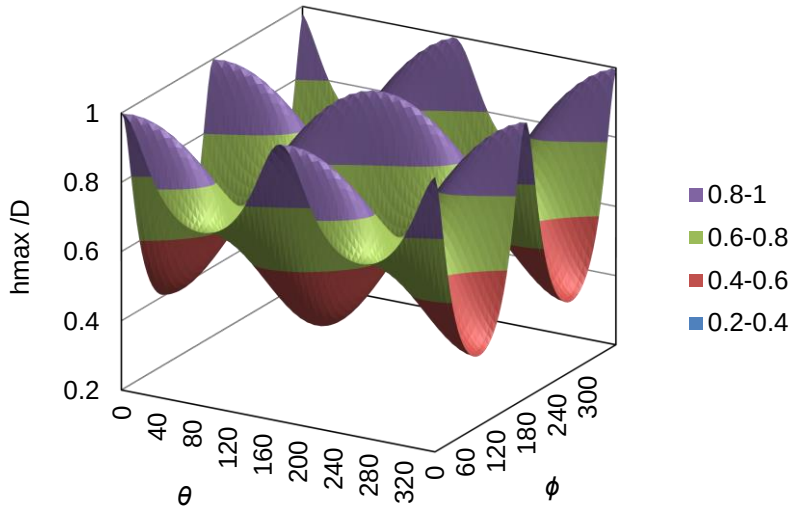

Figure 7-3 h_{max} as a function of θ and ϕ with η=2.5 and α = 2.

To fit (Eq. 7.10), a nonlinear regression program has been used previously (Kildashti, Dong & Samali 2019). Such regression can be time-consuming and difficult if M and N are large. Here, a methodology using Fourier transform to establish such series without regression was proposed. As is known, discrete Fourier transform coverts finite equally spaced data of function into the same length sequence as discrete samples. An inverse discrete Fourier transform can establish the full Fourier series using the transformed terms to calculate the original data. Generally discrete Fourier transform is determined by:

$$x_{p,q} = \sum_{j=0}^{m-1} \sum_{k=0}^{n-1} X_{j,k}\, e^{-2\pi i p j/m} e^{-2\pi i q k/n} \qquad \text{(Eq. 7.11)}$$

And the corresponding inverse discrete Fourier transform can be determined by:

$$X_{j,k} = \frac{1}{nm} \sum_{p=0}^{m-1} \sum_{q=0}^{n-1} x_{p,q}\, e^{2\pi i p j/m} e^{2\pi i q k/n} \qquad \text{(Eq. 7.12)}$$

Here, discrete Fourier transform was conducted on the database of h_{max} as a function of $(\theta\ ,\phi)$, where θ = 0,1,2, ...,359, and ϕ =0,1,2,...,359. Let $X_{j,k} = h_{max}$, $j = \theta$ and $k = \phi$; correspondingly, $m = n$ = 360. By applying (Eq. 7.11), $\{x_{p,q}\}$ can be obtained where p and q are also both running from 0 to 359. Note that $x_{p,q}$ are complex numbers. After $\{x_{p,q}\}$ are obtained, the original data h_{max} can be obtained by using inverse discrete Fourier transform with (Eq. 7.12).

Table 7-1 lists the sorted $x_{p,q}$ for $X_{ij} = h_{max}(\theta, \phi)$ with η = 2.5 and α = 2.5 in descending order of $|x_{p,q}|$ with the first 20 terms. Figure 7-4 further shows the first 100 $|x_{p,q}|$ terms. It can be seen that there are few high peaks and others are rather low. Therefore, in (Eq. 7.12), only using $x_{p,q}$ terms with high magnitudes, a simplified series with limited terms can be used to approximate $X_{j,k}$. Here, the approximate series of (Eq. 7.12), was constructed by using terms with $|x_{p,q}|$ higher than threshold $\lambda x_{\max}$, where x_{max} is the maximum $|x_{p,q}|$ or the second maximum if the maximum is $p = q = 0$, which gives the mean value of $X_{j,k}$; and $0 < \lambda < 1$. Thus, the inverse discrete Fourier transform series was approximated by:

$$\bar{X}_{j,k} = \frac{1}{nm} \sum_{p=0}^{m-1} \sum_{q=0}^{n-1} \delta_{p,q} x_{p,q}\, e^{2\pi i p j/m} e^{2\pi i q k/n} \qquad \text{(Eq. 7.13)}$$

where $\delta_{p,q} = 1$ if $|x_{p,q}| > \lambda x_{max}$, or $\delta_{p,q} = 0$ if $|x_{p,q}| \leq \lambda x_{max}$.

Table 7-1 Presentation of $x_{p,q}$ in descending order of $|x_{p,q}|$ for h_{max}, η = 2.5 and α = 2.5.

No.	p	q	Real	Image	$\lvert x_{p,q}\rvert$
1	2	0	7.58E+03	-1.83E-04	7582.063
2	2	358	7.58E+03	-1.83E-04	7582.063
3	358	0	7.58E+03	1.83E-04	7582.063
4	358	2	7.58E+03	1.83E-04	7582.063
5	4	358	2.72E+03	2.38E-04	2722.682

6	356	2	2.72E+03	-2.38E-04	2722.682
7	2	2	4.54E+02	-1.72E-05	454.0343
8	2	356	4.54E+02	-1.72E-05	454.0343
9	358	4	4.54E+02	1.72E-05	454.0343
10	358	358	4.54E+02	1.72E-05	454.0343
11	6	356	1.58E+02	6.96E-05	158.151
12	6	358	1.58E+02	6.96E-05	158.151
13	354	2	1.58E+02	-6.96E-05	158.151
14	354	4	1.58E+02	-6.96E-05	158.151
15	4	0	1.21E+02	4.32E-05	120.9552
16	4	356	1.21E+02	4.32E-05	120.9552
17	356	0	1.21E+02	-4.32E-05	120.9552
18	356	4	1.21E+02	-4.32E-05	120.9552
19	2	4	6.30E+01	2.87E-04	62.99274

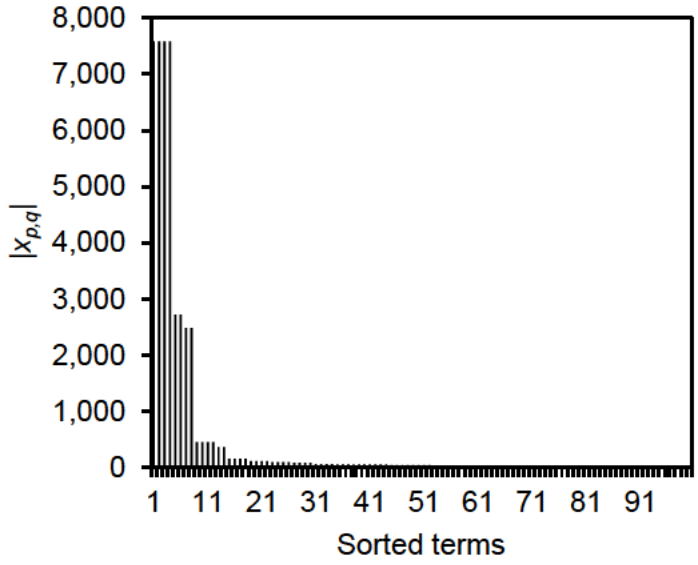

Figure 7-4 Sorted $|x_{p,q}|$ transformed from $h_{\max}$, $\eta = 2.5$ and $\alpha = 2.5$.

As here j and k are integral values with the unit degree, if θ and ϕ are between (j, j + 1) and (k, $k+1$) respectively, $\bar{X}(\theta, \phi)$ can be calculated by linear interpolation by:

$$\bar{X}(\theta,\phi) = [\,1-\Delta\theta \quad \Delta\theta\,]\begin{bmatrix}\bar{X}_{j,k} & \bar{X}_{j,k+1}\\ \bar{X}_{j+1,k} & \bar{X}_{j+1,k+1}\end{bmatrix}\begin{bmatrix}1-\Delta\phi\\ \Delta\phi\end{bmatrix} \qquad \text{(Eq. 7.14)}$$

where $j \le \theta < j+1$ and $\Delta\theta = \theta - j$; $k \le \phi < k+1$ and $\Delta\phi = \phi - k$.

If λ is smaller, the series will be more accurate, but there will be more included terms. Different λ will be tested and errors evaluated later. Further, the described procedures can also be applied to the x and y components of $\hat{\mathbf{n}}_1$ and $\hat{\mathbf{n}}_0$ respectively, which are denoted as n_{x1}, n_{y1}, n_{x0} and n_{y0} respectively.

7.2.4 Implementation of explicit force model in DEM for simulating superellipse packing

In the DEM, two types of motion, translational and rotational, are considered for each particle. These are governed by Newton's second law of motion, as stated by (Cundall & Strack 1979):

$$m_i \frac{d\mathbf{v}_i}{dt} = \sum_j \left(\mathbf{F}_{ij}^n + \mathbf{F}_{ij}^t\right) + m_i\mathbf{g} \qquad \text{(Eq. 7.15)}$$

and

$$\mathbf{I}_i \frac{d\boldsymbol{\omega}_i}{dt} = \sum_j \left(\mathbf{T}_{ij} + \mathbf{T}_{r,ij}\right) \qquad \text{(Eq. 7.16)}$$

where m_i, $\mathbf{v}_i$ and $\boldsymbol{\omega}_i$ are the mass and translational and angular velocities of particle i respectively, $\mathbf{F}_{ij}^n$ and $\mathbf{F}_{ij}^t$ are the normal and tangential components of the contact force exerted on particle i by particle j respectively, $\boldsymbol{g}$ is the gravitational acceleration, $\mathbf{I}_i$ is the moment of inertia of particle i, which is a tensor but can be simplified by using a body-fixed coordinate system (Džiugys & Peters 2001). Here, in 2D only $\mathbf{I}_{zz}$ is considered for superellipses, $\mathbf{T}_{ij}$ and $\mathbf{T}_{r,ij}$ are the torque on particle i from particle j, resulting from the total contact force (i.e., the sum of the normal and tangential forces) and rolling friction respectively. The equations for calculating these forces and torques are listed in Table 7-2. These equations are extended from those for spherical particles (Dong, KJ, Wang, CC & Yu, AB 2015), and are similar to those adopted in various studies on non-spherical particles (Dong, KJ, Wang, CC & Yu, AB 2015;

Zhou, Z-Y et al. 2011). Compared with previous studies, here d_{cn} and $\hat{\mathbf{n}}$ will be directly calculated from the explicit solution without solving any equations at each time step.

Table 7-2 List of equations for force calculation in DEM.

Force or torque	Equation
Normal elastic force, $\boldsymbol{F}_{ij}^{cn}$	$-\frac{4}{3}E_c\sqrt{R_m}(d_n)^{3/2}\,\hat{\mathbf{n}}$
Normal damping force, $\boldsymbol{F}_{ij}^{dn}$	$-\gamma_n\left(8E_c\sqrt{R_m d_n}m_{ij}\right)^{1/2}(\boldsymbol{v}_{ij}\cdot\hat{\mathbf{n}})\hat{\mathbf{n}}$
Tangential damping force, $\boldsymbol{F}_{ij}^{dt}$	$-\gamma_t\left(6\mu m_{ij}\lvert\boldsymbol{F}_{ij}^{cn}\rvert\left(1-min(\xi_t,\xi_{t,max})_t\right)^{1/2}/\xi_{t,max}\right)^{1/2}(\boldsymbol{v}_{ij}\cdot\hat{\mathbf{t}})\hat{\mathbf{t}}$
Tangential elastic force, $\boldsymbol{F}_{ij}^{ct}$	$-\mu\lvert\boldsymbol{F}_{ij}^{cn}\rvert\left[1-\left(1-(min(\xi_t,\xi_{t,max})/\xi_{t,max})\right)^{3/2}\right]\hat{\mathbf{t}}$
Torque by contact forces, $\boldsymbol{T}_{ij}$	$\boldsymbol{r}_{ij}\times(\boldsymbol{F}_{ij}^{n}+\boldsymbol{F}_{ij}^{t})$
Torque by rolling friction, $\boldsymbol{T}_{r,ij}$	$-\mu_r r_{ij}\lvert\boldsymbol{F}_{ij}^{cn}\rvert\widehat{\boldsymbol{\omega}_i}$

$Note.$ E_c is the composite Young's modulus; R_i and R_j are radii of the circumscribed circles for particles i and j respectively; $\boldsymbol{r}_{ii}$ is the vector pointing from the centre of particle i to the contact point with particle j; γ_n and γ_t are the normal and tangential damping coefficients respectively; μ and μ_r are the sliding and rolling friction coefficients respectively; d_n is the penetration depth; ξ_t is the total tangential displacement, at each time step it is added to $v_{t,ij}\cdot\Delta t$ and $\xi_{t,max}=\mu_s[(2-\tilde{\sigma})/2(1-\tilde{\sigma})]\xi_n$; $\hat{\mathbf{n}}$ and $\hat{\mathbf{t}}$ are the normal vector of the contact plane and the unit vector along the tangential direction respectively; and $\boldsymbol{v}_{ij}=\boldsymbol{v}_j-\boldsymbol{v}_i+\boldsymbol{\omega}_j\times\boldsymbol{r}_i-\boldsymbol{\omega}_j\times\boldsymbol{r}_{ji}$, $\boldsymbol{v}_{t,ij}=(\boldsymbol{v}_{ij}\times\hat{\boldsymbol{n}})\times\hat{\boldsymbol{n}}$, $\widehat{\boldsymbol{\omega}_i}=\boldsymbol{\omega}_i/|\boldsymbol{\omega}_i|$.

To use the approximate series, the included terms in the series are first loaded to the program. The rotation of each particle was traced as common practice in DEM simulations of non-spherical particles. Therefore, when considering two particles in contact, θ and ϕ can be readily calculated. Then the corresponding series are used to calculate the overlap parameters. The program also caches the results in the last step, so if the variations of θ and ϕ are small the grid terms in (Eq. 7.14) may not need to be updated.

The established DEM was used to simulate the packing of superellipses as listed in Figure 7-1. The parameters adopted in the DEM simulations are listed in Table 7-3. The material properties are the same as those used in previous studies of particle packing (Dong, K, Wang & Yu 2016; Dong, KJ, Wang, CC & Yu, AB 2015; Wang, C, Dong & Yu 2015). Packing was formed by randomly generating a given number of identical superellipses in a rectangular box of height 150D and width 30D without any overlap and then settling the particles under gravity. The total area of each particle was the same for different superellipse shapes, but the number of

particles differed as the areas of these particles were different. The final packing heights were all about 45*D*.

Table 7-3 List of parameters used in DEM simulation.

Parameter	Value
Particle size (diameter of the circumscribed circle) D	5 mm
Particle density, ρ_P	$2.5 \times 10^3 \mathrm{kg/m^3}$
Particle number	1500–5000
Young's modulus, Y	10^7 Pa
Poisson's ratio	0.29
Superellipse aspect ratio, α	1.0, 1.5, 2.0, 2.5, 3.0
Superellipse squareness, η	1.5, 2.0, 2.5, 3.0
Normal damping coefficient, γ^n	0.3
Tangential damping coefficient, γ^t	0.3
Sliding friction coefficient, μ	0.05, 0.3, 0.5
Rolling friction coefficient, μ_r	0.005
Time step, Δt	$1.0 \times 10^{-5} s$

7.3 Results and discussion

7.3.1 DFT results

Figure 7-5 shows the transformed terms for n_{x0} and n_{y1} for the same shape in Figure 7-4 in the descending order of $|x_{pq}|$. It can be further seen that for all parameters, there are few distinguishing peaks, which reveals that it is applicable to filter low peak terms.

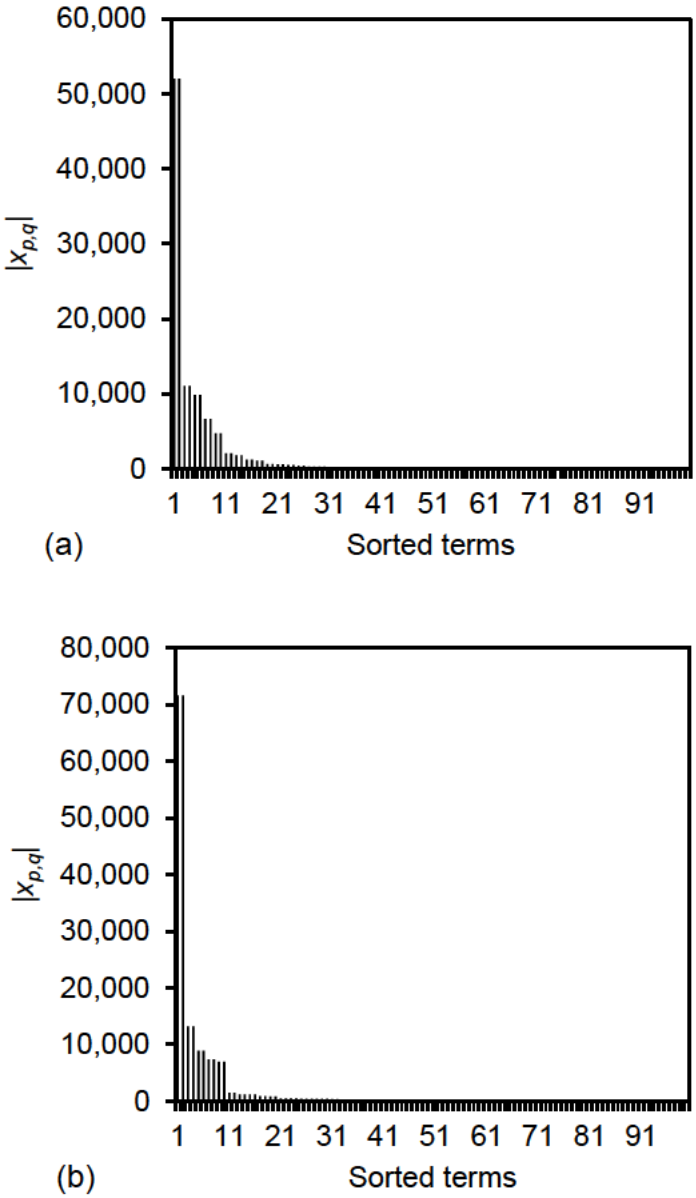

Figure 7-5 Sorted $|x_{p,q}|$ for n_{x0} and n_{y1} for $\eta = 2.5$ and $\alpha = 2.5$.

More specifically, Figure 7-6 shows the number of terms included in the approximate series. From Figure 7-6a it can be seen that the number of included terms increased with the decrease of λ. When using $\lambda = 0.02$, there were about 40 included terms, which was similar to the number of terms used in the previous fitting series of Eq. 3.10 with $M = 6$ and $N = 6$. Conversely, Figure 7-6b shows that the number of terms in the series decreased with the decrease of the aspect ratio and the difference of η to 2. For ellipses ($\eta = 2$), the number of terms was generally lower than 20 when $\alpha < 3$. This demonstrates that using the current method, the terms of the

approximate Fourier series are relatively few and more flexible than using the fixed number of terms in (Eq. 7.10).

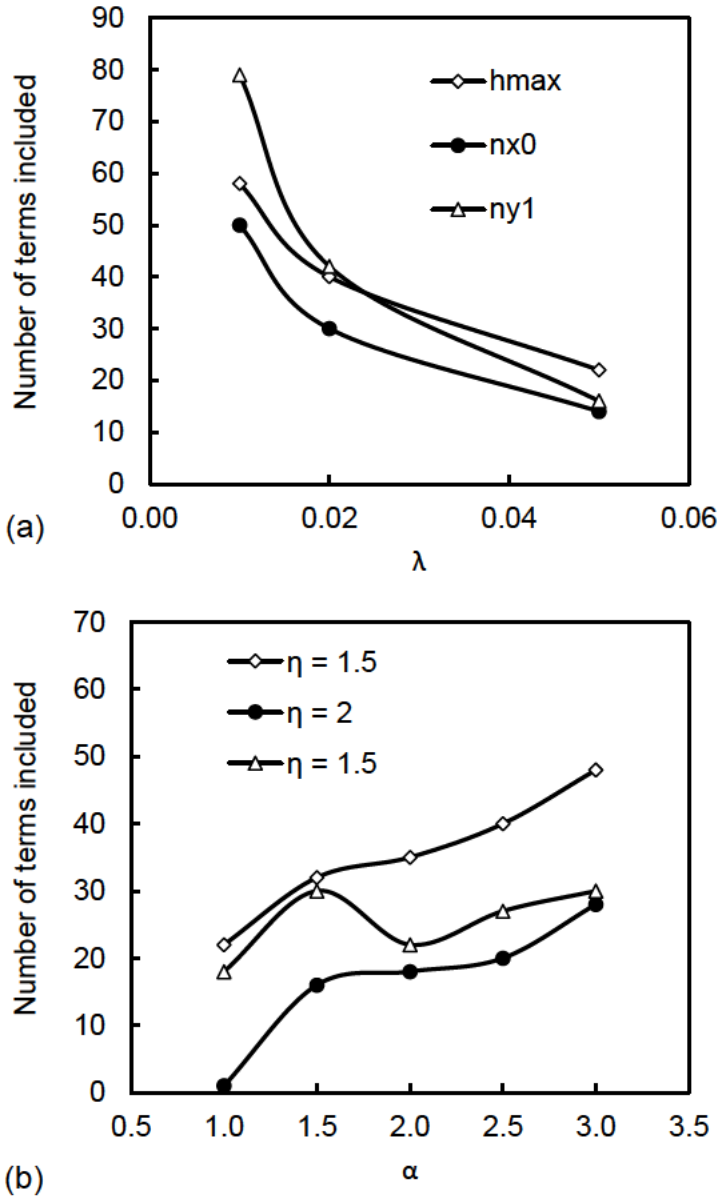

Figure 7-6 Number of terms included in the approximate Fourier series: (a), as a function of λ (η = 1.5, α = 2.5), for the series of h_{max}, n_{x0} and n_{y1}; and (b), as a function of α for the series of h_{max} when λ=0.02.

Figure 7-7 compares the calculated h_{max} and n_{x0} by the approximate series with the original data. It can be seen that the approximate series predicted very comparable results in the full range, though there were small differences. To quantify the differences, Figure 7-8 shows the average errors between the calculated results and the original data. For h_{max}, the errors are

presented as absolute difference, while for $\hat{\mathbf{n}}_1$ and $\hat{\mathbf{n}}_0$ the errors are presented as absolute angle difference. Different λ was used in the figure. It can be seen that with λ = 0.02, the average error for the h_{max} prediction was below 0.006D and that for $\mathbf{n}_1$ was below 2 degrees, which are rather small and thus indicated that the approximations are accurate. It can also be seen that the error generally increased with an increase of α and deviation of η from 2.

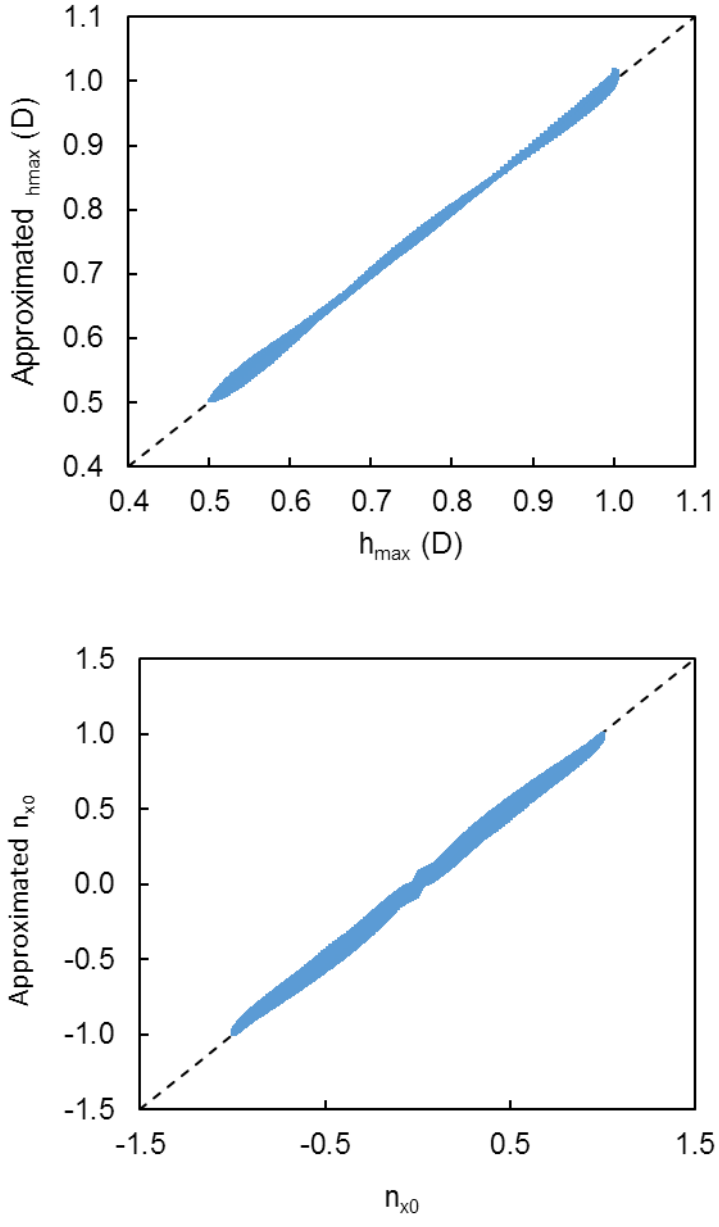

Figure 7-7 Comparison of h_{max} and n_{x0} calculated by the approximate series and the original data. Dashed line represents y = x.

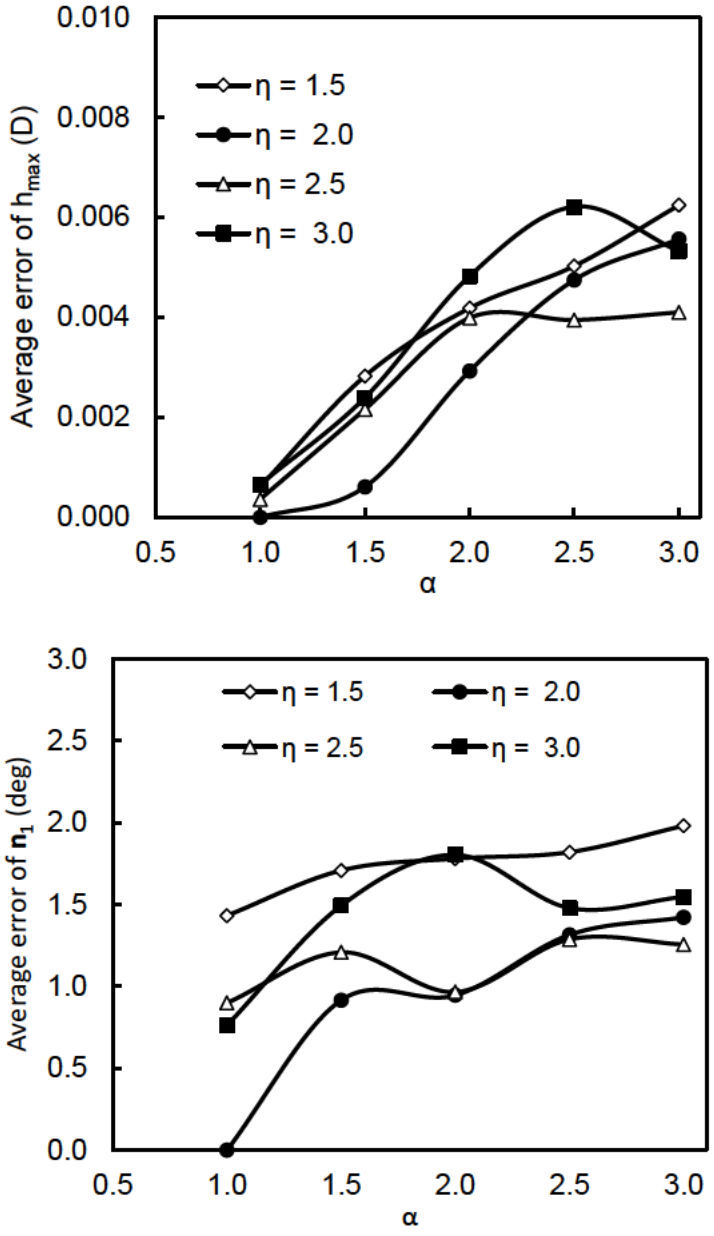

Figure 7-8 Average errors of h_{max} and $\hat{\mathbf{n}}_1$ with λ=0.02.

7.3.2 Packing of superellipses

Using the explicit force model, the packing of superellipses was simulated. Figure 7-9 shows snapshots of the simulated packing of different superellipses. It can be seen that the explicit force model effectively simulated the contact of superellipses with different orientations. The local structures were rather compact without rattling or dangling particles. In addition, using the explicit force model, the maximum transitional velocity and rational velocity both reached

nearly zero in the simulations. These results show that the explicit force model can present stable results without numerical divergence or diffusion.

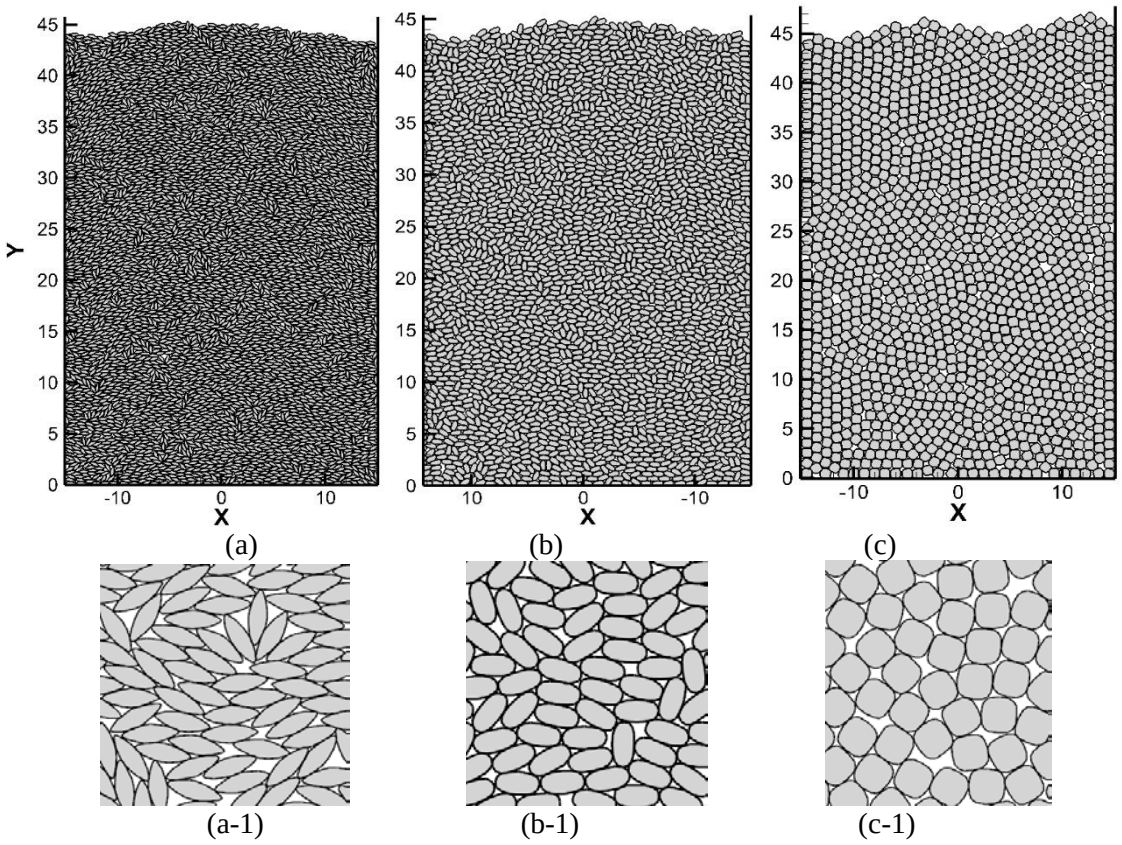

Figure 7-9 Simulated packing of superellipses: (a) η=*1.5*, α = 3.0; (b) η = 2.5 and α = 2.0; and (c) η =3.0, α = 1.0; a-1, b-1 and c-1 are the magnified centre regions of a, b and c respectively.

The packing fraction, ρ, is calculated by the total volume of the particles divided by the total space they occupy. The total space is the product of packing height and container width. To mitigate the effect of boundaries, the top and bottom layers of 3D in a packing were discarded in the analysis. Figure 7-10a shows the packing fraction obtained by using different λ in the approximate series for different ellipses. Using $\lambda = 0.01$ and $\lambda = 0.02$, the results were very close, while using $\lambda = 0.05$, the results were more different than the other two series. Considering this and also the previous error analysis, $\lambda = 0.02$ was used in subsequent simulations. In addition, the packing fractions of ellipses were also compared with the previous data obtained from the FEM simulations (Guises et al. 2009). The simulation conditions were set as the same as in the reference, determined by: Young's modulus 25.8 GPa; Poisson ratio 0.17; particle density 2650 kg/m^3; equivalent area sizes of particles 20 cm; and container width 6 m. Figure 7-10b shows that using the approximate series with $\lambda = 0.02$, the simulated packing

fractions are in good agreement with the data in the reference, which also testifies the validity of the explicit force model. The relatively large discrepancies at α =1 are mainly because when α = 1, the particles are circles and the packing fraction may have large fluctuations as circles can easily form ordered packings locally and hence the packing is very non-uniform (Wang, C, Dong & Yu 2015).

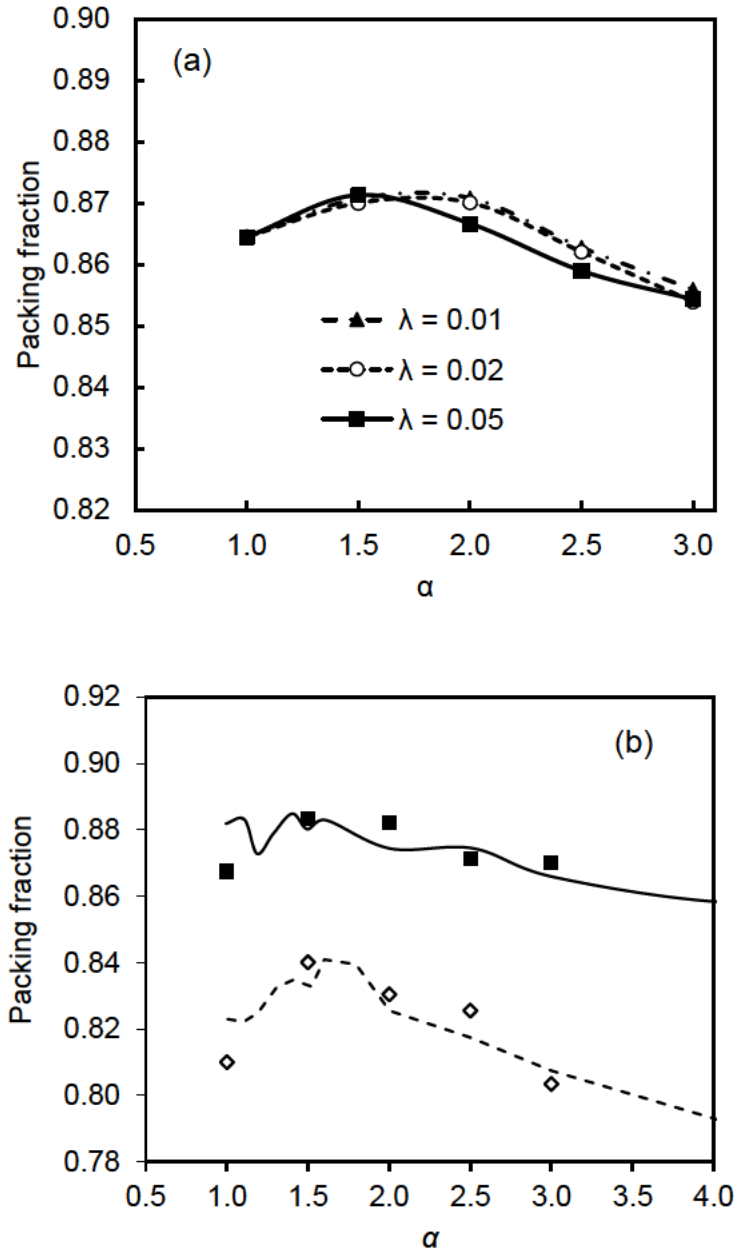

Figure 7-10 Simulated packing fractions of ellipses as a function of aspect ratio: (a), with different λ using the default simulation conditions, μ = 0.3; and (b), comparison to the reference (Jaklič, Leonardis & Solina 2000) using the same conditions as in the reference, where symbols are simulated results with the explicit force model (λ=0.02): ■, μ = 0; and ◇, μ = 0.5; and lines are from the reference: solid line, μ = 0; and dashed line, μ = 0.5.

Although there are few studies of the packing of superellipses in the literature, there are more for similar shapes such as ellipsoids (Donev, Cisse, et al. 2004; Zhou, Z-Y et al. 2011) and superellipsoids (Delaney, Gary W & Cleary 2010). Figure 7-11a shows simulated packing fraction as a function of aspect ratio with different squareness. Interestingly, for $\eta = 2.0$ and 2.5, the highest ρ was not found at $\alpha = 1.0$ but at $\alpha \approx 1.75$. This is similar to the packing of oblates, prolates and ellipses, which can be due to the increase of the degrees of freedom for non-spherical particles (Donev, Cisse, et al. 2004) and the congruent dense packing structures with proper stacking of particles with different orientations (Donev, Stillinger, et al. 2004). When $\eta = 3.0$ and 1.5, the shapes of the superellipses are closer to square, and ρ simply decreased with the increase of α, which is similar to the packing of cylinders (Dong, KJ, Wang, CC & Yu, AB 2015; Zou & Yu 1996). Figure 7-11b shows the change of ρ as a function of η with different α. It can be seen that the series with $\alpha = 1.5$ generated the highest ρ in general. For each α, $\eta = 2.5$ normally generated the highest ρ, yet at $\alpha = 1.0$ it gave the lowest ρ. This indicates that the interplay of η and α may be very complicated when α is close to 1.0, which deserves further studies.

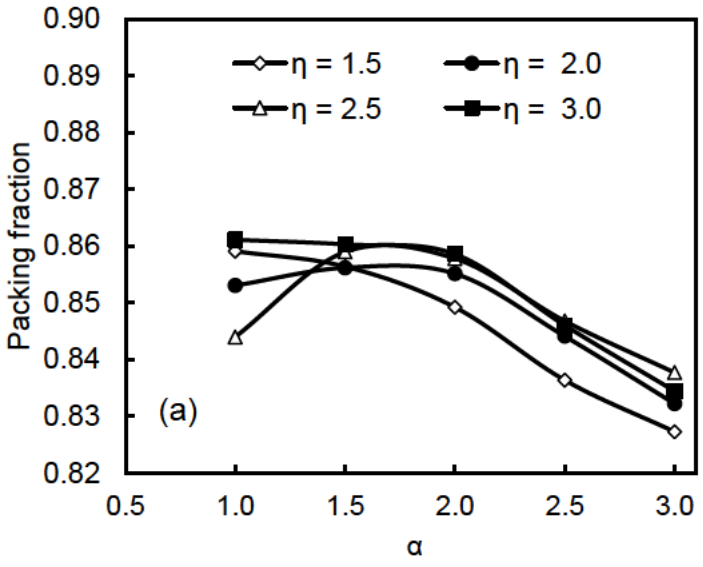

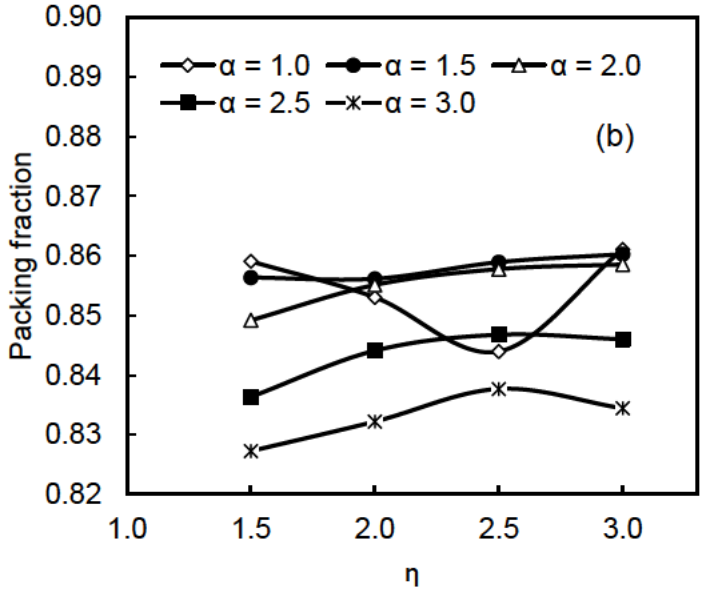

Figure 7-11 Packing fraction: (a), as a function of aspect ratio with different squareness; and (b), as a function squareness with different aspect ratio.

For ellipses ($\eta = 2.0$) and superellipses with $\eta = 2.5$, the peaks at $\alpha \approx 1.75$ gradually diminished with a decrease of sliding friction coefficient (Figure 7-12). This is probably because with a decrease of μ, the particles closer to circular ($\alpha \approx 1$ and $\eta \approx 2$) can more easily form ordered hexagonal packing (Wang, C, Dong & Yu 2015), which leads to increased ρ at the left side of the figure.

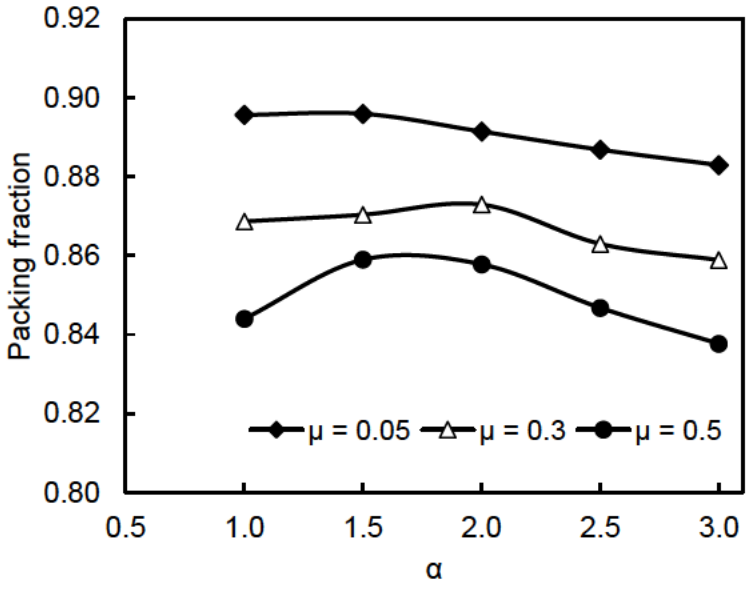

Figure 7-12 Packing fraction as a function of aspect ratio with different sliding friction coefficients, and $\eta = 2.5$.

To model the effect of shape, sphericity or circularity is often used as a common parameter. The circularity of a 2D particle is defined by:

$$\psi = \frac{4\pi A}{P^2} \qquad \text{(Eq. 7.17)}$$

where P is perimeter.

Figure 7-13 plots packing fraction as a function of circularity. With the same sliding friction coefficient, the data points generally collapsed. However, they were more scattered when ψ was close to 1, where the shapes were close to circular. In particular, the highest packing fraction value was close to but not exactly 1. This is due to the complicated changes of ρ between $\alpha = 1$ to $\alpha = 2$ when η is different, particularly for the highest ρ at $\alpha \approx 1.75$ for $\eta = 2$ and $\eta = 2.5$. When $\psi < 0.85$, ρ decreased almost linearly with a decrease of ψ, while the decrease was faster with a higher friction coefficient, which is similar to the packing of cylinders (Zou & Yu 1996) and polygons (Wang, C, Dong & Yu 2015).

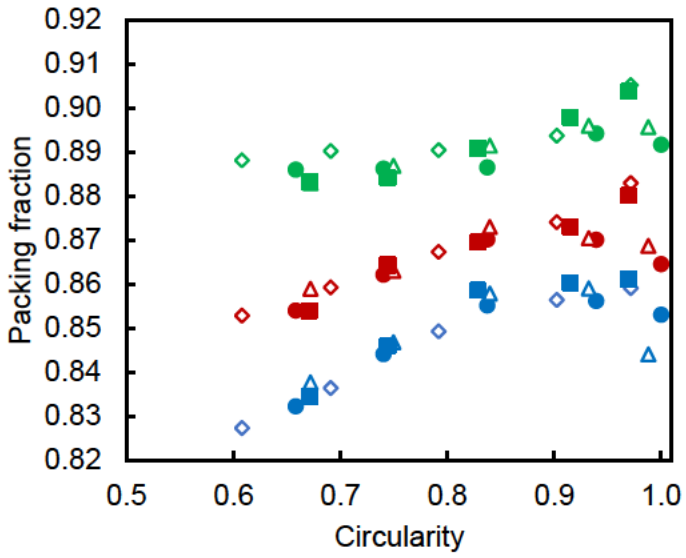

Figure 7-13 Packing fraction as a function of circularity for all the studied superellipses. Symbol shapes: △, $\eta = 1.5$; ●, $\eta = 2.0$;◇, $\eta = 1.5$, and ■, $\eta = 3.0$. Symbol colors: green, μ=0.05; red, μ=0.3; and blue, μ=0.5.

The packing structures were further analysed by coordination number (CN), which is the number of particles contacting each particle. Here, the contacting particles were counted when they generate contact force to the particle (i.e., the cut-off gap for contacting particles was set at zero). Figure 7-14 shows the mean coordination number (denoted as $\bar{C}$) for different superellipses with different sliding friction coefficients. As seen, $\bar{C}$ is mainly dependent on μ, particularly when μ increased from 0.05 to 0.5, $\bar{C}$ generally increased from about 4 to 5.5. Squareness showed little effect on $\bar{C}$ when μ was high and α was not close to 1. Aspect ratio had a more complicated effect on $\bar{C}$. Generally, $\bar{C}$ increased with α rising from 1 to 2, and then decreased with the further increase of α, which is similar to those in the packing of other non-spherical particles (Donev, Cisse, et al. 2004; Zhou, Z-Y et al. 2011). However, between α =1 and α = 2, $\bar{C}$ fluctuated. Further, when μ was low, the effect of α became less significant. This indicates that coordination number is largely controlled by the sliding friction coefficient, then the aspect ratio, but little by the squareness. When friction was low, the packing of different superelliptical particles had similar coordination numbers, suggesting similar local structures. However, when particle shape was close to circular, the packing behaviour was more complicated.

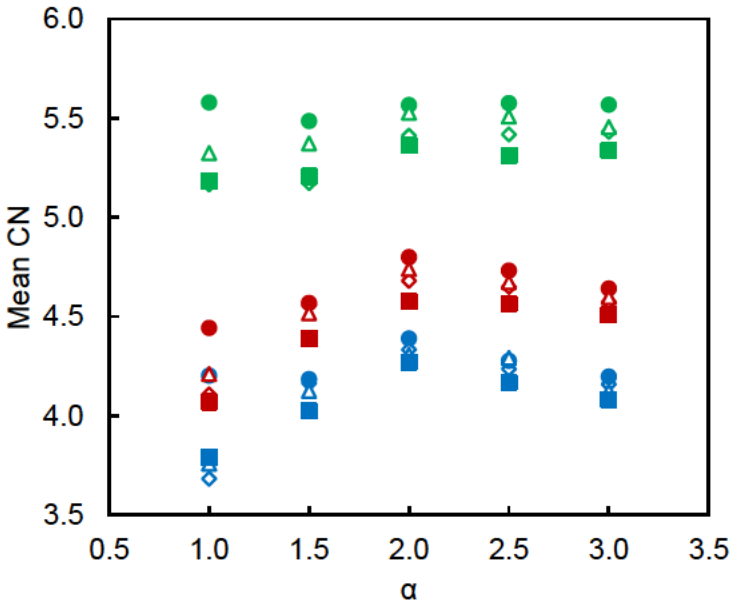

Figure 7-14 Mean coordination number as a function of aspect ratio. Symbol shapes: △, η = 1.5; ●, η = 2.0;◇, η = 1.5, and ■, η = 3.0. Symbol colors: green, μ=0.05; red, μ=0.3; and blue, μ=0.5.

7.3.3 Discussion of the extension of the method

Thus far, the proposed method has been applied to particles of the same shape and size. Theoretically, it can also be applied to particles of different shapes and sizes. For interactions between two types of particles, a database to store the overlap parameters with discretised orientation angles can be built, as was shown in a previous study (Dong, K, Wang, C & Yu, A 2015). Then discrete Fourier transform can be applied to each database and simplified Fourier series can be obtained for different binary interactions. Figure 7-15 demonstrates simulation of the packing of a mixture of two types of superellipses: shape I with η = 3.0 and α = 1.0, and shape II with η = 1.5 and α = 3.0. Here, a new force database and related simplified Fourier series were developed for the interaction between shape I and shape II. Together with the previously obtained explicit force models for interactions between two shape I superellipses and between two shape II superellipses, the packing of the mixture was simulated. This simulation would be time-consuming if there were many different types of particles, either in size or shape. This problem may be tackled in future by combining the model with other methods, such as establishment of the relationship between overlap parameters and particle size ratio. Conversely, the method used here is much faster than using the CN method directly in the program (i.e., to solve (Eq. 7.9) when calculating each pair of particles for each time step). In the simulations undertaken in the present study, the method was generally 6–8 times faster.

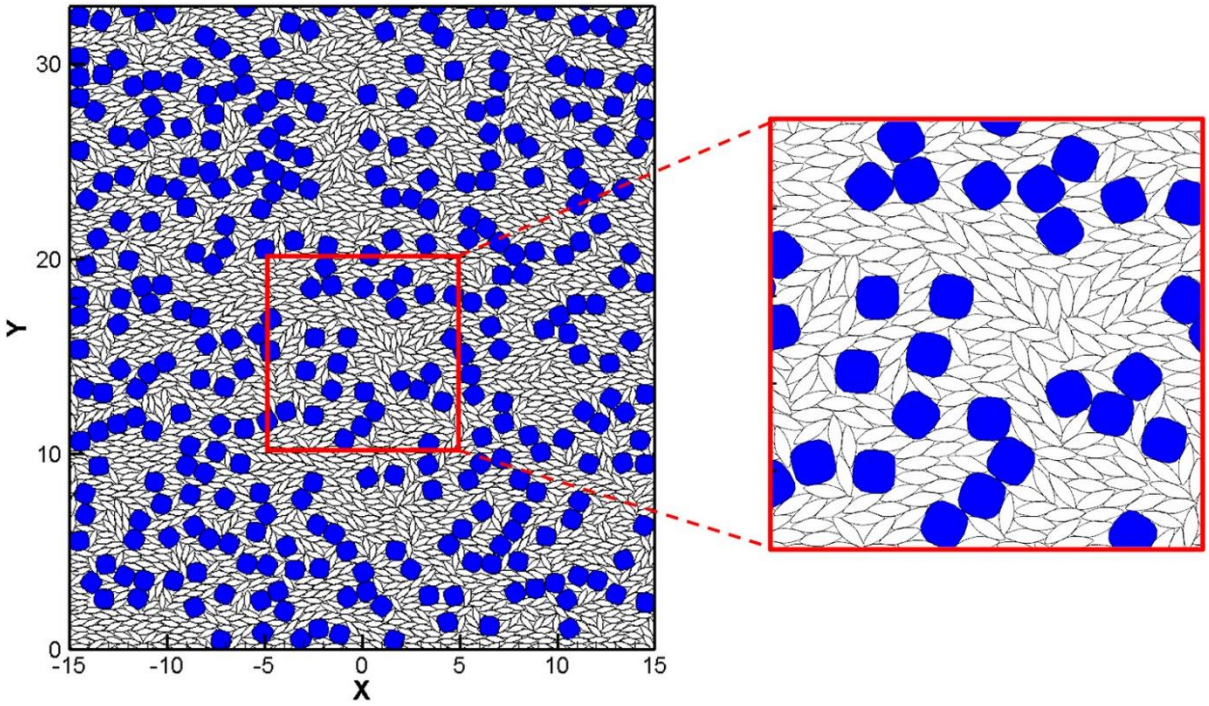

Figure 7-15 Simulated packing of a binary mixture of superellipses: blue particles, η = 3.0, α = 1.0; white particles, η = 1.5, α = 3.0.

7.4 Conclusions

In the present study, a novel method was developed to establish explicit contact force models for superellipses. The method is based on discrete Fourier transform of the key overlap parameters as a function of orientation, and then transformed terms with magnitudes lower than a threshold were filtered in a corresponding inversed Fourier transform. The filtered inverse Fourier series was used to approximate the original data.

The method was applied to a wide range of superellipse shapes. The approximate series were evaluated with different filtering thresholds. It was found that the series was quite accurate when fewer than 40 terms included. The proposed method, although applied to 2D particles here, can be extended to 3D shapes by using higher-order Fourier transform, which could be computational demand but such calculation is always an offline one-off calculation. In addition, Fourier series is demonstrated to be a good candidate for the general form of interparticle forces for non-spherical particles by naturally considering the effect of orientation. Therefore, the methodology can also be useful for other interaction problems for non-spherical

bodies, such as in biology where, in which Fourier series have been used to represent complex shapes (Shen, Farid & McPeek 2009).

Here, the explicit force model has been implemented in DEM and used to simulate the packing of superellipses. It is shown that using the explicit force model the packing of the non-spherical particles can be stably simulated. The simulated packing fractions of the ellipses are in good agreement with the previous FEM simulations. The packing behaviors of superellipses are complicatedly dependent on the squareness, aspect ratio and friction of the particles. Generally when the squareness is close to 2, the effect of the aspect ratio on the packing of superellipses can be similar to that of ellipses or ellipsoids. However, with the squareness deviating more from 2.0, the packing features can be more similar to those of cylinders and polygons. The difference caused by the squareness can be more significant when the sliding friction coefficient increases. The results can improve our understanding on the packing of non-spherical particles.

CHAPTER VIII: Conclusions and future work

8.1 Conclusions

The present study aimed to increase the understanding of the industrial screening process by using DEM simulation and machine learning modelling. Thus, the study focused on understanding the fundamentals of the complicated screening processes by investigating the process model with different controlling factors through particle-scale analysis. The particle-scale analysis was also linked to several macroscopic models and screening processes such as percolation of particles under vibration, the local passing of particles from the screen, choking of screening, non-spherical shaped particles contact detection and packing and machine learning modelling. The computational and theoretical analyses as well as machine leaning helped to clarify the use of particle-scale analysis and screening processes in several areas. Conclusions from the study are as follows:

- The percolation of small particles through a packed bed of large particles under vibration along the vertical direction was investigated by combining simulation and machine learning. For size ratios slightly larger than 0.154, vertical vibration enabled percolation that did not occur spontaneously. For size ratios smaller than the spontaneous threshold of 0.154, vertical vibration had an adverse effect on percolation. The percolation velocity decreased for the higher vibration amplitude and frequency. The radial movement of percolating particles in the vibrated bed also followed the radial dispersion model established for spontaneous percolation. Considering the effects of vibration conditions on percolation velocity, radial dispersion increased by vertical vibration when amplitude and frequency were small. There was a positive correlation between the radial dispersion coefficient and percolation velocity when percolation velocity was relatively high. These findings may help optimise the design of screening processes in various industries. Machine learning was also applied to the DEM simulated results to predict the percolation velocity and size ratio threshold. These results extended the previous spontaneous percolation theory to vibrated beds including the effects of vibration amplitude and frequency on percolation velocity under different size ratios. The relationship between the vertical motion and the horizontal motion of percolating particles in a vibrated bed can be used to guide and model related processes such as screening and sieving. Machine learning was also shown to be effective in the modelling of parameters proposed in current theories of particle segregation (sieving and mixing).

- A physics-informed machine learning process model was developed for an inclined vibrating screen and then applied to screens with different inclination angles, vibration conditions and different segments of the screen. Machine learning was used to construct a local passing function based on the particle size distribution of the inlet flow, vibration conditions and inclination angle of the segment. The data used for machine learning were obtained from numerical simulation. Considering the data model of the local passing function and the mass continuity between segments, a process model was developed. The process model was able to predict the overflow partition curve, which was in good agreement with the original simulated screen under different operational conditions. However, the model assessed the effects of the controlling variables on the sieving performance parameters more efficiently than DEM. If on-site training data were obtained, the model could be used for real applications. In addition, the model was found to be very flexible when handling different operational conditions in different parts of a screen. Therefore, it could be used to model complex multi-deck screens with different vibration conditions and/or different slopes at different decks. In constructing these different screens, the machine learning-based local passing function was found to be the same as that obtained from the original screen. The combination of DEM simulation, data modelling and process modelling could guide smart design and provide superior control of industrial screens.

- A process model for the complicated multi-deck screen was proposed by combining the DEM and machine learning to provide detailed quantitative predictions for particles passing through the overall screen, each layer of the multi-deck screen and each segment of the screen layer. The machine learning and process model were able to optimise the inclined double-layer vibrating screen with various feeding scenarios, vibration conditions for both layers, changes of aperture shape and feeding of the bottom layer from the top layer and upper stream flow. The inlet for the bottom layer is the passing particles from the top layer as the upper stream particles flow to the lower decks. The proposed process model was further developed for double-layer screens to predict the local passing rate of particles. Machine learning modelling optimises the time-consuming simulation process by predicting results rapidly and accurately while considering the local passing of a double layer screen. The current machine learning model may help to predict the results without choking within the range of the training

dataset. The screen performance of the top layer decreased with the increase in vibration amplitude/frequency. Similarly, the bottom-layer screen performance increased with the increase in vibration frequency but decreased at higher values. Varied size particles and amounts affected the performance of the screening process and the process model worked well for result prediction. For the bottom layer, aperture size was smaller than the top layer and the performance of the screen was not effective when the feed contained mostly small undersize particles. Screen performance increased for mostly large or near-mesh-sized particles with the increase in vibrational frequency and amplitude. The data model showed the smart solution for complicated multi-deck screening. The process can be applicable to the other screens and granular processing.

- A logical modelling of choking judgement of an inclined vibrating screen was proposed by combining the DEM and machine learning. Operational parameters of screening processes such as particle size, inlet and inclination angle were considered comprehensively to construct the logical function for choking judgement. The logical machine learning model can directly predict the choking judgement of screen under different operational conditions. The predicted results were in good agreement with DEM. However, the logical model can predict the threshold of controlling variables such as vibration conditions and feed ratio of different-sized particles for choking or non-choking of the screen. The logical machine learning model will help to minimise the computational duration and cost of screening process by predicting the decision before any screening. In addition, the logical model also shows a few vital observations for the choking of the screen. The screening process choked for the lower values of vibration conditions and the choking condition can be removed by increasing the vibration frequency and amplitude. Lower value of the inclination angle was not effective for the decks of the multi-deck screen. The combination of machine learning logical model and DEM is a smart way to find out the choking of the screening. A similar model can be applied to other granular processing industries for decision-making purposes.

- A novel contact force model was developed while considering the overlap and contact force between non-spherical particles. A Fourier series was proposed to establish explicit force models by fitting a comprehensive force database. The method was developed to establish an explicit contact force model for superellipses. The method

was based on discrete Fourier transform of the key overlap parameters as a function of orientation, and then filtering the transformed terms with magnitudes lower than a threshold in corresponding inversed Fourier transform. The method was applied to a wide range of superellipse shapes. In addition, the Fourier series was demonstrated to be a good candidate for considering inter-particle forces between non-spherical particles by naturally accounting for the effect of particle orientation. The explicit force model was also implemented in the DEM and used to simulate the packing of superellipses. Using the explicit force model, simulation of non-spherical particle packing was demonstrated to be stable. These results improved our understanding of the packing of non-spherical particles and future screening process works.

The current research demonstrates the particle scale analysis to understand the percolation of particle under vibration, process modelling of screening under various settings, logical doled of choking prediction of the screen, and contact force model of non-spherical particles. Moreover, numerical studies are also linked with machine learning to develop a smart way for results prediction. Such knowledge is critical for improving the design and control of many types of industrial sieving operations.

8.2 Recommendations for future work

In the present study, a comprehensive numerical and machine learning investigation was undertaken to enhance the understanding of the industrial screening process for granular materials. In this thesis, the machine learning models were applied to particle percolation processes (Chapter 3, paper published) and screening processes (Chapter 4 (paper published) and 5) and choking judgement modelling in Chapter 6. As a new method to combine machine learning and DEM simulation, the method can be extended to other similar processes. Based on this work, further studies are proposed:

i. A process model of an inclined vibrating screen can be extended based on DEM and machine learning for non-spherical-shaped granular materials. Differently shaped particles will be considered as the feed. The passing of differently shaped particles along the screen will be analysed for local parts while considering the effects of vibration conditions, inclination angle and feeding variation.

ii. The concept from Chapter 5 can be applied to develop a process model of the multi-deck screen for non-spherical shaped granular materials sieving while combining the DEM and machine learning. Differently shaped particles flowing along the screen layers will be considered as the feed. The sieving for differently shaped particles will be analysed under different vibration conditions, inclination angle and the threshold of passing along the screen.

iii. Logical choking modelling for inclined double-layer vibrating screens can be applied based on DEM and machine learning. The particle shape and the cohesive force between wet fine particles will be considered. With the help of decision-making choking modelling, the choking judgement of a double-layer screen condition may be rapidly identified. This may enable the controlling variables to be fixed before simulation or empirical study.

iv. Percolation of non-spherical shaped particles under vibration can be extended to understand stratification phenomena of screening with different shaped materials. Specifically, the percolation velocity, dispersion of particles, particle cohesion, vibration motion and aspect ratio threshold of non-spherical shaped particles for spontaneous and vibration percolation could be investigated with the help of DEM and machine learning.

v. The findings of the present thesis can be used further in solving cohesive particles percolation under vibration conditions. The percolation velocity, dispersion of particles and size ratio threshold for spontaneous and vibration percolation could be investigated with the help of DEM and machine learning.

vi. The screening process can be extended for coal preparation with the presence of clay. CFD-DEM coupling will be performed to investigate the particles passing under various controlling variables. Artificial intelligence modelling will be applied to predict the passing of particles and develop a smart design for the screening process.

vii. Granular materials packing (black and red seed) analysis will be performed to find the loose and dense packing while combining DEM and artificial intelligence modelling.

Different parameters including particle size ratio and other particle shapes can be considered to generalize the technique.

viii. The algorithm introduced in Chapter 7 (explicit contact force model) can be extended for ellipsoid particle packing by Fourier. Higher-order Fourier transform of 3D could be computationally demanding. However, such calculations are always important to understand the non-spherical shaped particle screening. The contact model can be applied to the particle percolation and screening process.

References

Ai, X & Sawamiphakdi, K 1999, 'Solving elastic contact between rough surfaces as an unconstrained strain energy minimization by using CGM and FFT techniques'.

Amirifar, R, Dong, K, Zeng, Q & An, X 2018, 'Self-assembly of granular spheres under one-dimensional vibration', *Soft Matter*, vol. 14, no. 48, pp. 9856-69.

Amirifar, R, Dong, K, Zeng, Q & An, X 2019, 'Bimodal self-assembly of granular spheres under vertical vibration', *Soft Matter*, vol. 15, no. 29, pp. 5933-44.

An, XZ, Dong, KJ, Yang, RY, Zou, RP, Wang, CC & Yu, AB 2016, 'Quasi-universality in the packing of uniform spheres under gravity', *Granular Matter*, vol. 18, no. 1, p. 6.

An, XZ, Dong, KJ, Yang, RY, Zou, RP & Yu, AB 2021, 'On the relationships between structural properties and packing density of uniform spheres', *Powder Technology*, vol. 388, pp. 139-48.

Ardi, EG, Dong, K, Yu, A & Yang, R 2017, 'A combined experimental and DEM approach to determine the breakage of particles in an impact mill', *Powder Technology*, vol. 318, pp. 543-8.

Arifuzzaman, SM, Dong, K, Hou, Q, Zhu, H & Zeng, Q 2020, 'Explicit contact force model for superellipses by Fourier transform and application to superellipse packing', *Powder Technology*, vol. 361, pp. 112-23.

Arifuzzaman, SM, Dong, K & Yu, A 2022, 'Process model of inclined double layer vibrating screen based on DEM and machine learning', *Powder Technology (to be submitted)*.

Arifuzzaman, SM, Dong, K & Yu, A 2022, 'Process model of vibrating screen based on DEM and physics-informed machine learning', *Powder Technology*, p. 117869.

Arifuzzaman, SM, Dong, K, Zhu, H & Zeng, Q 2022, 'DEM study and machine learning model of particle percolation under vibration', *Advanced Powder Technology*, vol. 33, no. 5, p. 103551.

Asbjörnsson, G, Bengtsson, M, Hulthén, E & Evertsson, M 2016, 'Model of banana screen for robust performance', *Minerals Engineering*, vol. 91, pp. 66-73.

Asmar, B, Langston, P, Matchett, A & Walters, J 2002, 'Validation tests on a distinct element model of vibrating cohesive particle systems', *Computers & chemical engineering*, vol. 26, no. 6, pp. 785-802.

AstecMobileScreens 2008, 'Astec Mobile Screens, Duo-Vibe high frequency screen, 6' x 12' series, Specification Sheet', *Astec Industries Inc*.

Baldassarri, A, Barrat, A, D'Anna, G, Loreto, V, Mayor, P & Puglisi, A 2005, 'What is the temperature of a granular medium?', *Journal of Physics: Condensed Matter*, vol. 17, no. 24, p. S2405.

Bandemer, H & Espig, D 1978, 'A mathematical model of the batch sieving procedure', *Powder Technology*, vol. 20, no. 2, pp. 227-31.

Barrasso, D, Tamrakar, A & Ramachandran, R 2014, 'A reduced order PBM–ANN model of a multi-scale PBM–DEM description of a wet granulation process', *Chemical Engineering Science*, vol. 119, pp. 319-29.

Basinskas, G & Sakai, M 2016, 'Numerical study of the mixing efficiency of a batch mixer using the discrete element method', *Powder Technology*, vol. 301, pp. 815-29.

Boon, CW, Houlsby, GT & Utili, S 2013, 'A new contact detection algorithm for three-dimensional non-spherical particles', *Powder Technology*, vol. 248, pp. 94-102.

Breu, APJ, Ensner, HM, Kruelle, CA & Rehberg, I 2003, 'Reversing the Brazil-nut effect: Competition between percolation and condensation', *Physical review letters*, vol. 90, no. 1, p. 014302.

Bridgwater, J, Cooke, M & Scott, A 1978, 'Interparticle percolation: equipment development and mean percolation velocities', *Trans. I Chem. E*, vol. 56, p. 157.

Bridgwater, J & Ingram, N 1971, 'Rate of spontaneous inter-particle percolation', *Transactions of the Institution of Chemical Engineers*, vol. 49, no. 3, pp. 163-9.

Bridgwater, J, Sharpe, NW & Stocker, DC 1969, 'Particles mixing by percolation', *Transactions of Institution of Chemical Engineers*, vol. 47, pp. 14-9.

Brilliantov, NV, Spahn, F, Hertzsch, J-M & Pöschel, T 1996, 'Model for collisions in granular gases', *Physical Review E*, vol. 53, no. 5, p. 5382.

Brito, C, Ikeda, H, Urbani, P, Wyart, M & Zamponi, F 2018, 'Universality of jamming of nonspherical particles', *Proceedings of the National Academy of Sciences*, vol. 115, no. 46, pp. 11736-41.

Broadbent, SR & Hammersley, JM 1957, 'Percolation processes: I. Crystals and mazes', *Mathematical Proceedings of the Cambridge Philosophical Society*, vol. 53, no. 3, pp. 629-41.

Bui, VH, Bui, MD & Rutschmann, P 2019, 'Combination of discrete element method and artificial neural network for predicting porosity of gravel-bed river', *Water*, vol. 11, no. 7.

Bzdok, D, Altman, N & Krzywinski, M 2018, 'Statistics versus machine learning', *Nature Methods*, vol. 15, no. 4, pp. 233-4.

Calanog, EM & Geiger, GH 1973, 'A note on screening probability', *Industrial & Engineering Chemistry Process Design and Development*, vol. 12, no. 3, pp. 395-6.

Campbell, CS 1990, 'Rapid granular flows', *Annual Review of Fluid Mechanics*, vol. 22, no. 1, pp. 57-90.

Chen, F, Jelagin, D & Partl, MN 2020, 'Vibration-induced aggregate segregation in asphalt mixtures', *Materials and Structures*, vol. 53, no. 2, p. 27.

Chen, G 1997, 'Stochastic modeling of rock fragment flow under gravity', *International Journal of Rock Mechanics and Mining Sciences*, vol. 34, no. 2, pp. 323-31.

Chen, S, Baumes, LA, Gel, A, Adepu, M, Emady, H & Jiao, Y 2018, 'Classification of particle height in a hopper bin from limited discharge data using convolutional neural network models', *Powder Technology*, vol. 339, pp. 615-24.

Chen, WW 2013, 'FFT-Based Methods for Contact Mechanics', in QJ Wang & Y-W Chung (eds), *Encyclopedia of Tribology*, Springer US, Boston, MA, pp. 1076-80.

Chen, Z, Li, Z, Xia, H & Tong, X 2021, 'Performance optimization of the elliptically vibrating screen with a hybrid MACO-GBDT algorithm', *Particuology*, vol. 56, pp. 193-206.

Chu, K, Chen, J & Yu, A 2016, 'Applicability of a coarse-grained CFD–DEM model on dense medium cyclone', *Minerals Engineering*, vol. 90, pp. 43-54.

Cleary, P, Fernandez, J, Sinnott, M & Morrison, R 2010, 'Using DEM and SPH to model wet Industrial Banana Screens', *Comminution 2010, proceedings*, vol. In: Comminution 2010;

April 13-16, 2010; Vineyard Hotel, Cape Town, South Africa. Minerals Engineering Elsevier, pp. 1-21.

Cleary, PW 2000, 'DEM simulation of industrial particle flows: case studies of dragline excavators, mixing in tumblers and centrifugal mills', *Powder Technology*, vol. 109, no. 1, pp. 83-104.

Cleary, PW 2009, 'Industrial particle flow modelling using discrete element method', *Engineering Computations*, vol. 26, no. 6, pp. 698-743.

Cleary, PW, Sinnott, MD & Morrison, RD 2009, 'Separation performance of double deck banana screens–Part 1: Flow and separation for different accelerations', *Minerals Engineering*, vol. 22, no. 14, pp. 1218-29.

Cleary, PW, Sinnott, MD & Morrison, RD 2009, 'Separation performance of double deck banana screens – Part 2: Quantitative predictions', *Minerals Engineering*, vol. 22, no. 14, pp. 1230-44.

Cleary, PW, Stokes, N & Hurley, J 1997, 'Efficient collision detection for three dimensional super-ellipsoidal particles'.

Cleary, PW, Wilson, P & Sinnott, MD 2018, 'Effect of particle cohesion on flow and separation in industrial vibrating screens', *Minerals Engineering*, vol. 119, pp. 191-204.

Cundall, PA & Strack, OD 1979, 'A discrete numerical model for granular assemblies', *Géotechnique*, vol. 29, no. 1, pp. 47-65.

Dai, B-B, Yuan, W-H, Liu, J-K, Liu, F-T & Chang, D 2021, 'Estimating the segregation of a granular bed subjected to vibration in various modes', *Advanced Powder Technology*, vol. 32, no. 5, pp. 1450-62.

Dai, W, Liu, Q & Chai, T 2015, 'Particle size estimate of grinding processes using random vector functional link networks with improved robustness', *Neurocomputing*, vol. 169, pp. 361-72.

Davoodi, A, Asbjörnsson, G, Hulthén, E & Evertsson, M 2019, 'Application of the discrete element method to study the effects of stream characteristics on screening performance', *Minerals*, vol. 9, no. 12, p. 788.

Davoodi, A, Bengtsson, M, Hulthén, E & Evertsson, CM 2019, 'Effects of screen decks' aperture shapes and materials on screening efficiency', *Minerals Engineering*, vol. 139, p. 105699.

Delaney, GW & Cleary, PW 2010, 'The packing properties of superellipsoids', *EPL (Europhysics Letters)*, vol. 89, no. 3, p. 34002.

Delaney, GW, Cleary, PW, Hilden, M & Morrison, RD 2012, 'Testing the validity of the spherical DEM model in simulating real granular screening processes', *Chemical Engineering Science*, vol. 68, no. 1, pp. 215-26.

Delaney, GW, Hilton, JE & Cleary, PW 2011, 'Defining random loose packing for nonspherical grains', *Physical Review E*, vol. 83, no. 5, p. 051305.

Djoković, JM, Tanikić, DI, Nikolić, RR & Kalinović, SM 2017, 'Screening efficiency analysis of vibrosieves with the circular vibrations', *Civil and Environmental Engineering*, vol. 13, no. 1, pp. 77-83.

Donev, A, Cisse, I, Sachs, D, Variano, EA, Stillinger, FH, Connelly, R et al. 2004, 'Improving the density of jammed disordered packings using ellipsoids', *Science*, vol. 303, no. 5660, pp. 990-3.

Donev, A, Stillinger, FH, Chaikin, P & Torquato, S 2004, 'Unusually dense crystal packings of ellipsoids', *Physical Review Letters*, vol. 92, no. 25, p. 255506.

Dong, HL, Liu, CS, Zhao, YM & Zhao, LL 2012, 'Banana Screening Method and Simulation of Banana Screening Process Using Discrete Element Method', *Trans Tech Publ*, vol. 524, pp. 949-52.

Dong, K, Esfandiary, AH & Yu, A 2017, 'Discrete particle simulation of particle flow and separation on a vibrating screen: Effect of aperture shape', *Powder Technology*, vol. 314, pp. 195-202.

Dong, K, Kuang, S, Vince, A, Hughes, T & Yu, A 2010, 'Numerical simulation of the in-line pressure jig unit in coal preparation', *Minerals Engineering*, vol. 23, no. 4, pp. 301-12.

Dong, K, Wang, B & Yu, A 2013, 'Modeling of particle flow and sieving behavior on a vibrating screen: from discrete particle simulation to process performance prediction', *Industrial & Engineering Chemistry Research*, vol. 52, no. 33, pp. 11333-43.

Dong, K, Wang, C & Yu, A 2015, 'A novel method based on orientation discretization for discrete element modeling of non-spherical particles', *Chemical Engineering Science*, vol. 126, pp. 500-16.

Dong, K, Wang, C & Yu, A 2016, 'Voronoi analysis of the packings of non-spherical particles', *Chemical Engineering Science*, vol. 153, pp. 330-43.

Dong, K & Yu, A 2012, 'Numerical simulation of the particle flow and sieving behaviour on sieve bend/low head screen combination', *Minerals Engineering*, vol. 31, pp. 2-9.

Dong, K, Yu, A & Brake, I 2009, 'DEM simulation of particle flow on a multi-deck banana screen', *Minerals Engineering*, vol. 22, no. 11, pp. 910-20.

Dong, KJ, Wang, CC & Yu, AB 2015, 'A novel method based on orientation discretization for discrete element modeling of non-spherical particles', *Chemical Engineering Science*, vol. 126, no. 0, pp. 500-16.

Džiugys, A & Peters, B 2001, 'An approach to simulate the motion of spherical and non-spherical fuel particles in combustion chambers', *Granular Matter*, vol. 3, no. 4, pp. 231-66.

Efron, B & Tibshirani, R 1997, 'Improvements on cross-validation: The 632+ bootstrap method', *Journal of the American Statistical Association*, vol. 92, no. 438, pp. 548-60.

Elskamp, F, Kruggel-Emden, H, Hennig, M & Teipel, U 2016, 'Discrete element investigation of process models for batch screening under altered operational conditions', *Powder Technology*, vol. 301, pp. 78-95.

Elskamp, F, Kruggel-Emden, H, Hennig, M & Teipel, U 2017, 'A strategy to determine DEM parameters for spherical and non-spherical particles', *Granular Matter*, vol. 19, no. 3, p. 46.

Esfandiary, AH 2014, *Simulation and modelling of screening processes*, The University of New South Wales.

Fan L. and Zhu, C 1998, 'Size and Properties of Particles', in C Zhu & L-S Fan (eds), *Principles of Gas-Solid Flows*, Cambridge University Press, Cambridge, pp. 3-45.

Favier, J, Abbaspour-Fard, M, Kremmer, M & Raji, A 1999, 'Shape representation of axi-symmetrical, non-spherical particles in discrete element simulation using multi-element model particles', *Engineering Computations*, vol. 16, no. 4, pp. 467-80.

Feng, YQ & Yu, AB 2007, 'Microdynamic modelling and analysis of the mixing and segregation of binary mixtures of particles in gas fluidization', *Chemical Engineering Science*, vol. 62, no. 1, pp. 256-68.

Feng, YQ & Yu, AB 2010, 'Effect of bed thickness on the segregation behavior of barticle mixtures in a gas fluidized bed', *Industrial & Engineering Chemistry Research*, vol. 49, no. 7, pp. 3459-68.

Feng, YT, Han, K & Owen, DRJ 2012, 'Energy-conserving contact interaction models for arbitrarily shaped discrete elements', *Computer Methods in Applied Mechanics and Engineering*, vol. 205-208, no. Supplement C, pp. 169-77.

Feng, YT, Han, K & Owen, DRJ 2017, 'A generic contact detection framework for cylindrical particles in discrete element modelling', *Computer Methods in Applied Mechanics and Engineering*, vol. 315, pp. 632-51.

Fernandez, J, Cleary, P, Sinnott, M & Morrison, R 2011, 'Using SPH one-way coupled to DEM to model wet industrial banana screens', *Minerals Engineering*, vol. 24, no. 8, pp. 741-53.

Ferrara, G, Preti, U & Schena, G 1987, 'Computer-aided use of a screening process model', pp. 153-66.

Gangfeng, Z, Jinbo, Z, Wandong, X & Shili, L 2016, 'Banana flip-flow screen benefits coal preparation', *Filtration + Separation*, vol. 53, no. 4, pp. 38-41.

Govender, N, Wilke, DN, Wu, C-Y, Tuzun, U & Kureck, H 2019, 'A numerical investigation into the effect of angular particle shape on blast furnace burden topography and percolation using a GPU solved discrete element model', *Chemical Engineering Science*, vol. 204, pp. 9-26.

Guises, R, Xiang, J, Latham, J-P & Munjiza, A 2009, 'Granular packing: numerical simulation and the characterisation of the effect of particle shape', *Granular Matter*, vol. 11, no. 5, pp. 281-92.

Gupta, VS, Fuerstenau, DW & Mika, TS 1975, 'An investigation of sieving in the presence of attrition', *Powder Technology*, vol. 11, no. 3, pp. 257-71.

Halidan, M, Chandratilleke, GR, Dong, KJ & Yu, AB 2018, 'Mixing performance of ribbon mixers: Effects of operational parameters', *Powder Technology*, vol. 325, pp. 92-106.

Harzanagh, AA, Orhan, EC & Ergun, SL 2018, 'Discrete element modelling of vibrating screens', *Minerals Engineering*, vol. 121, pp. 107-21.

Hausner, H 1972, *Effect of quench sintering on the grain structure of sintered metals*, Polytechnic Inst., Brooklyn, vol. 8, no. 3, pp. 159-61.

He, L & Tafti, DK 2019, 'A supervised machine learning approach for predicting variable drag forces on spherical particles in suspension', *Powder Technology*, vol. 345, pp. 379-89.

Hertz, H 1882, 'Ueber die Berührung fester elastischer Körper', *Journal fur die Reine und Angewandte Mathematik*, vol. 1882, no. 92, pp. 156-71.

Hoomans, BPB, Kuipers, JAM & van Swaaij, WPM 2000, 'Granular dynamics simulation of segregation phenomena in bubbling gas-fluidised beds', *Powder Technology*, vol. 109, no. 1, pp. 41-8.

Hou, Q, Zhou, Z, Curtis, JS & Yu, A 2019, 'How to generate valid local quantities of particle–fluid flows for establishing constitutive relations', *AIChE Journal*, vol. 65, no. 10, p. e16690.

Houlsby, G 2009, 'Potential particles: a method for modelling non-circular particles in DEM', *Computers and Geotechnics*, vol. 36, no. 6, pp. 953-9.

Hudson, RB, Jansen, ML & Linkson, PB 1969, 'Batch sieving of deep particulate beds on a vibratory sieve', *Powder Technology*, vol. 2, no. 4, pp. 229-40.

Hutter, K & Rajagopal, K 1994, 'On flows of granular materials', *Continuum Mechanics and Thermodynamics*, vol. 6, no. 2, pp. 81-139.

Iwashita, K & Oda, M 1998, 'Rolling resistance at contacts in simulation of shear band development by DEM', *Journal of engineering mechanics*, vol. 124, no. 3, pp. 285-92.

Iwashita, K & Oda, M 2000, 'Micro-deformation mechanism of shear banding process based on modified distinct element method', *Powder Technology*, vol. 109, no. 1, pp. 192-205.

Jaeger, HM, Nagel, SR & Behringer, RP 1996, 'Granular solids, liquids, and gases', *Reviews of modern physics*, vol. 68, no. 4, p. 1259.

Jahani, M, Farzanegan, A & Noaparast, M 2015, 'Investigation of screening performance of banana screens using LIGGGHTS DEM solver', *Powder Technology*, vol. 283, pp. 32-47.

Jaklič, A, Leonardis, A & Solina, F 2000, 'Superquadrics and their geometric properties', in *Segmentation and recovery of superquadrics*, Springer, pp. 13-39.

Jansen, ML & Glastonbury, JR 1968, 'The size separation of particles by screening', *Powder Technology*, vol. 1, no. 6, pp. 334-43.

Jiang, H, Zhao, Y, Duan, C, Liu, C, Wu, J, Diao, H et al. 2017, 'Dynamic characteristics of an equal-thickness screen with a variable amplitude and screening analysis', *Powder Technology*, vol. 311, pp. 239-46.

Jiang, H, Zhao, Y, Duan, C, Yang, X, Liu, C, Wu, J et al. 2017, 'Kinematics of variable-amplitude screen and analysis of particle behavior during the process of coal screening', *Powder Technology*, vol. 306, pp. 88-95.

Jiang, H, Zhao, Y, Qiao, J, Duan, C, Chen, Z, Zhou, E et al. 2017, 'Process analysis and operational parameter optimization of a variable amplitude screen for coal classification', *Fuel*, vol. 194, pp. 329-38.

Jiang, XC, Zeng, QH, Chen, CY & Yu, AB 2011, 'Self-assembly of particles: some thoughts and comments', *Journal of Materials Chemistry*, vol. 21, no. 42, pp. 16797-805.

Johnson, KL 1985, *Contact mechanics*, Cambridge University Press, The Edinburgh Building, Cambridge CB2 2RU, UK.

Jordan, MI & Mitchell, TM 2015, 'Machine learning: Trends, perspectives, and prospects', *Science*, vol. 349, no. 6245, pp. 255-60.

Ju, Y & Farris, T 1996, 'Spectral analysis of two-dimensional contact problems'.

Just, G & Free, G 1971, 'The gravity flow of material in the sublevel caving mining system', pp. 88-97.

Kapur, PC, Ball, B & Fuerstenau, DW 1977, 'A stochastic approach to sieving kinetics', *International Journal of Mineral Processing*, vol. 4, no. 2, pp. 131-47.

Karniadakis, GE, Kevrekidis, IG, Lu, L, Perdikaris, P, Wang, S & Yang, L 2021, 'Physics-informed machine learning', *Nature Reviews Physics*, vol. 3, no. 6, pp. 422-40.

Kildashti, K, Dong, K & Samali, B 2018, 'A revisit of common normal method for discrete modelling of non-spherical particles', *Powder Technology*, vol. 326, pp. 1-6.

Kildashti, K, Dong, K & Samali, B 2019, 'Explicit force model for discrete modelling of elliptical particles', *Computers and Geotechnics*, vol. 110, pp. 122-31.

Kildashti, K, Dong, K, Samali, B, Zheng, Q & Yu, A 2018, 'Evaluation of contact force models for discrete modelling of ellipsoidal particles', *Chemical Engineering Science*, vol. 177, pp. 1-17.

Kodam, M, Bharadwaj, R, Curtis, J, Hancock, B & Wassgren, C 2010, 'Cylindrical object contact detection for use in discrete element method simulations. Part I – Contact detection algorithms', *Chemical Engineering Science*, vol. 65, no. 22, pp. 5852-62.

Kou, M, Zhou, H, Wu, S & Shen, Y 2020, 'DEM simulation of cubical particle percolation in a packed bed', *Powder Technology*, vol. 361, pp. 306-14.

Kudrolli, A 2004, 'Size separation in vibrated granular matter', *Reports on progress in physics*, vol. 67, no. 3, p. 209.

Kureck, H, Govender, N, Siegmann, E, Boehling, P, Radeke, C & Khinast, JG 2019, 'Industrial scale simulations of tablet coating using GPU based DEM: A validation study', *Chemical Engineering Science*, vol. 202, pp. 462-80.

Laguitton, D & Leung, J 1989, 'Advances in expert system applications in mineral processing', in GS Dobby & SR Rao (eds), *Processing of Complex Ores*, Pergamon, Amsterdam, pp. 565-74.

Langston, PA, Tüzün, U & Heyes, DM 1994, 'Continuous potential discrete particle simulations of stress and velocity fields in hoppers: transition from fluid to granular flow', *Chemical Engineering Science*, vol. 49, no. 8, pp. 1259-75.

Langston, PA, Tüzün, U & Heyes, DM 1995, 'Discrete element simulation of granular flow in 2D and 3D hoppers: Dependence of discharge rate and wall stress on particle interactions', *Chemical Engineering Science*, vol. 50, no. 6, pp. 967-87.

Li, J, Webb, C, Pandiella, SS & Campbell, GM 2003, 'Discrete particle motion on sieves—a numerical study using the DEM simulation', *Powder Technology*, vol. 133, no. 1, pp. 190-202.

Li, J, Yu, AB, Bridgwater, J & Rough, SL 2010, 'Spontaneous inter-particle percolation: A kinematic simulation study', *Powder Technology*, vol. 203, no. 2, pp. 397-403.

Li, L & Iskander, M 2022, 'Use of machine learning for classification of sand particles', *Acta Geotechnica*.

Li, X, Hou, Q, Dong, K, Zou, R & Yu, A 2020, 'Promote cohesive solid flow in a screw feeder with new screw designs', *Powder Technology*, vol. 361, pp. 248-57.

Li, Y-W, Zhao, L-L, Hu, E-Y, Yang, K-K, He, J-F, Jiang, H-S et al. 2019, 'Laboratory-scale validation of a DEM model of a toothed double-roll crusher and numerical studies', *Powder Technology*, vol. 356, pp. 60-72.

Li, Y, Bao, J, Yu, A & Yang, R 2020, 'A combined data-driven and discrete modelling approach to predict particle flow in rotating drums', *Chemical Engineering Science*, p. 116251.

Li, Y, Bao, J, Yu, A & Yang, R 2021, 'ANN prediction of particle flow characteristics in a drum based on synthetic acoustic signals from DEM simulations', *Chemical Engineering Science*, p. 117012.

Li, Z, Li, K, Ge, X & Tong, X 2019, 'Performance optimization of banana vibrating screens based on PSO-SVR under DEM simulations', *Journal of Vibroengineering*, vol. 21, no. 1, pp. 28-39.

Li, Z & Tong, X 2017, 'Applications of the discrete element method and Fibonacci sequence on a banana screen', *Journal of Engineering, Design and Technology*, vol. 15, no. 1, pp. 2-12.

Li, Z, Tong, X, Zhou, B & Wang, X 2015, 'Modeling and parameter optimization for the design of vibrating screens', *Minerals Engineering*, vol. 83, pp. 149-55.

Liao, Z, Yang, Y, Sun, C, Wu, R, Duan, Z, Wang, Y et al. 2021, 'Image-based prediction of granular flow behaviors in a wedge-shaped hopper by combing DEM and deep learning methods', *Powder Technology*, vol. 383, pp. 159-66.

Lin, X & Ng, T-T 1995, 'Contact detection algorithms for three-dimensional ellipsoids in discrete element modelling', *International Journal for Numerical and Analytical Methods in Geomechanics*, vol. 19, no. 9, pp. 653-9.

Lin, X & Ng, T-T 1997, 'A three-dimensional discrete element model using arrays of ellipsoids', *Géotechnique*, vol. 47, no. 2, pp. 319-29.

Lin, X & Ng, TT 1995, 'Contact detection algorithms for three-dimensional ellipsoids in discrete element modelling', *International Journal for Numerical and Analytical Methods in Geomechanics*, vol. 19, no. 9, pp. 653-9.

Liu, C, Wang, H, Zhao, Y, Zhao, L & Dong, H 2013, 'DEM simulation of particle flow on a single deck banana screen', *International Journal of Mining Science and Technology*, vol. 23, no. 2, pp. 273-7.

Liu, S, Zhou, Z, Dong, K, Yu, A, Pinson, D & Tsalapatis, J 2015, 'Numerical investigation of Burden distribution in a blast furnace', *steel research international*, vol. 86, no. 6, pp. 651-61.

Lominé, F & Oger, L 2009, 'Dispersion of particles by spontaneous interparticle percolation through unconsolidated porous media', *Physical Review E*, vol. 79, no. 5, p. 051307.

Lominé, F & Oger, L 2010, 'Transit time during the interparticle percolation process', *Physical Review E*, vol. 82, no. 4, p. 041301.

Lu, G, Third, J & Müller, C 2015, 'Discrete element models for non-spherical particle systems: from theoretical developments to applications', *Chemical Engineering Science*, vol. 127, pp. 425-65.

Lu, G, Third, JR & Muller, CR 2015, 'Discrete element models for non-spherical particle systems: From theoretical developments to applications', *Chemical Engineering Science*, vol. 127, pp. 425-65.

Lu, G, Third, JR & Müller, CR 2015, 'Discrete element models for non-spherical particle systems: From theoretical developments to applications', *Chemical Engineering Science*, vol. 127, pp. 425-65.

Mahdi, FM & Holdich, RG 2017, 'Using statistical and artificial neural networks to predict the permeability of loosely packed granular materials', *Separation Science and Technology*, vol. 52, no. 1, pp. 1-12.

Mailman, M, Schreck, CF, O'Hern, CS & Chakraborty, B 2009, 'Jamming in Systems Composed of Frictionless Ellipse-Shaped Particles', *Physical review letters*, vol. 102, no. 25, p. 255501.

Makinde, OA, Ramatsetse, BI & Mpofu, K 2015, 'Review of vibrating screen development trends: Linking the past and the future in mining machinery industries', *International Journal of Mineral Processing*, vol. 145, pp. 17-22.

MATLAB 2021a, 'Exact GPR Method', *https://au.mathworks.com/help/stats/exact-gpr-method.html*, vol. Accessed 14th March 2021.

MATLAB 2021b, 'Understanding Support Vector Machine Regression', *https://au.mathworks.com/help/stats/understanding-support-vector-machine-regression.html#buyrzay*, p. Accessed 26th October 2021.

MATLAB 2022, 'Classification Learner', *https://au.mathworks.com/help/stats/classificationlearner-app.html*, vol. Accessed 6th May.

Meng, L, Jiao, Y & Li, S 2016, 'Maximally dense random packings of spherocylinders', *Powder Technology*, vol. 292, pp. 176-85.

Meyers, A & Mylec, A 2000, 'Performance of Banana Screens in D&R Applications', *ACARP Report C*, vol. 7048.

Mikami, T, Kamiya, H & Horio, M 1998, 'Numerical simulation of cohesive powder behavior in a fluidized bed', *Chemical Engineering Science*, vol. 53, no. 10, pp. 1927-40.

Mindlin, RD 1953, 'Elastic spheres in contact under varying oblique forces', *J. Applied Mech.*, vol. 20, pp. 327-44.

Mishra, AK 2021, 'AI4R2R (AI for Rock to Revenue): A Review of the Applications of AI in Mineral Processing', *Minerals*, vol. 11, no. 10, p. 1118.

Muguruma, Y, Tanaka, T & Tsuji, Y 2000, 'Numerical simulation of particulate flow with liquid bridge between particles (simulation of centrifugal tumbling granulator)', *Powder Technology*, vol. 109, no. 1, pp. 49-57.

Napier-Munn, T & Wills, B 2006, 'An introduction to the practical aspects of ore treatment and mineral recovery', *Mineral Processing Technology. Oxford: Elsevier*.

Nezami, EG, Hashash, YMA, Zhao, D & Ghaboussi, J 2004, 'A fast contact detection algorithm for 3-D discrete element method', *Computers and Geotechnics*, vol. 31, no. 7, pp. 575-87.

Nguyen, QH, Ly, H-B, Ho, LS, Al-Ansari, N, Le, HV, Tran, VQ et al. 2021, 'Influence of data splitting on performance of machine learning models in prediction of shear strength of soil', *Mathematical Problems in Engineering*, vol. 2021, p. 4832864.

Ogunmodimu, O, Govender, I, Mainza, AN & Franzidis, J-P 2021, 'Development of a mechanistic model of granular flow on vibrating screens', *Minerals Engineering*, vol. 163, p. 106771.

Pani, AK & Mohanta, HK 2014, 'Soft sensing of particle size in a grinding process: Application of support vector regression, fuzzy inference and adaptive neuro fuzzy inference techniques for online monitoring of cement fineness', *Powder Technology*, vol. 264, pp. 484-97.

Pani, AK & Mohanta, HK 2015, 'Online monitoring and control of particle size in the grinding process using least square support vector regression and resilient back propagation neural network', *ISA Transactions*, vol. 56, pp. 206-21.

Peng, L, Feng, H, Wang, Z, Wang, H, Yang, H & Huang, H 2019, 'Screening mechanism and properties of a cantilevered vibrating sieve for particles processing', *Applied Sciences*, vol. 9, no. 22, p. 4911.

Peng, L, Jiang, H, Chen, X, Liu, D, Feng, H, Zhang, L et al. 2019, 'A review on the advanced design techniques and methods of vibrating screen for coal preparation', *Powder Technology*, vol. 347, pp. 136-47.

Peng, L, Wang, Z, Ma, W, Chen, X, Zhao, Y & Liu, C 2018, 'Dynamic influence of screening coals on a vibrating screen', *Fuel*, vol. 216, pp. 484-93.

Podlozhnyuk, A, Pirker, S & Kloss, C 2017, 'Efficient implementation of superquadric particles in Discrete Element Method within an open-source framework', *Computational Particle Mechanics*, vol. 4, no. 1, pp. 101-18.

Qiao, J, Dong, K & Duan, C 2021, 'DEM study on the segregation of a non-spherical intruder in a vibrated granular bed', *Processes*, vol. 9, no. 3.

Qiao, J, Duan, C, Dong, K, Wang, W, Jiang, H, Zhu, H et al. 2021, 'DEM study of segregation degree and velocity of binary granular mixtures subject to vibration', *Powder Technology*, vol. 382, pp. 107-17.

Qiao, J, Duan, C, Jiang, H, Zhao, Y, Chen, J, Huang, L et al. 2018, 'Research on screening mechanism and parameters optimization of equal thickness screen with variable amplitude based on DEM simulation', *Powder Technology*, vol. 331, pp. 296-309.

Rahman, M, Zhu, H, Yu, A & Bridgwater, J 2008, 'DEM simulation of particle percolation in a packed bed', *Particuology*, vol. 6, no. 6, pp. 475-82.

Raissi, M & Karniadakis, GE 2018, 'Hidden physics models: Machine learning of nonlinear partial differential equations', *Journal of Computational Physics*, vol. 357, pp. 125-41.

Rasmussen, CE & Williams, C 2006, 'Gaussian processes for machine learning.,(MIT Press: Cambridge, MA)'.

Rustan, A 2000, 'Gravity flow of broken rock: What is known and unknown', *The Australasian Institute of Mining and Metallurgy*, pp. 557-68.

Sahini, M & Sahimi, M 1994, *Applications of percolation theory*, CRC Press.

Sakai, M, Shigeto, Y, Basinskas, G, Hosokawa, A & Fuji, M 2015, 'Discrete element simulation for the evaluation of solid mixing in an industrial blender', *Chemical Engineering Journal*, vol. 279, pp. 821-39.

Sanders, GJ 1978, *Partition curves as a basis for process selection*, University of New South Wales.

Sarker, IH 2021, 'Machine learning: Algorithms, real-world applications and research directions', *SN Computer Science*, vol. 2, no. 3, pp. 1-21.

Scott, AM & Bridgwater, J 1975, 'Interparticle percolation: A fundamental solids mixing mechanism', *Industrial & Engineering Chemistry Fundamentals*, vol. 14, no. 1, pp. 22-7.

Shanmugam, BK, Vardhan, H, Raj, MG, Kaza, M, Sah, R & Hanumanthappa, H 2021, 'Artificial neural network modeling for predicting the screening efficiency of coal with varying moisture content in the vibrating screen', *International Journal of Coal Preparation and Utilization*, pp. 1-19.

Shen, L, Farid, H & McPeek, MA 2009, 'Modeling three-dimensional morphological structures using spherical harmonics', *Evolution: international journal of organic evolution*, vol. 63, no. 4, pp. 1003-16.

Silva, BBe, Cunha, ERd, Carvalho, RMd & Tavares, LM 2018, 'Modeling and simulation of green iron ore pellet classification in a single deck roller screen using the discrete element method', *Powder Technology*, vol. 332, pp. 359-70.

Sinnott, MD, Cleary, PW & Morrison, RD 2017, 'Combined DEM and SPH simulation of overflow ball mill discharge and trommel flow', *Minerals Engineering*, vol. 108, pp. 93-108.

Soldinger, M 1999, 'Interrelation of stratification and passage in the screening process', *Minerals Engineering*, vol. 12, no. 5, pp. 497-516.

Soldinger, M 2000, 'Influence of particle size and bed thickness on the screening process', *Minerals Engineering*, vol. 13, no. 3, pp. 297-312.

Soldinger Stafhammar, M 2002, *Screening of crushed rock material*, Chalmers University of Technology.

Standish, N 1985, 'The kinetics of batch sieving', *Powder Technology*, vol. 41, no. 1, pp. 57-67.

Standish, N, Bharadwaj, AK & Hariri-Akbari, G 1986, 'A study of the effect of operating variables on the efficiency of a vibrating screen', *Powder Technology*, vol. 48, no. 2, pp. 161-72.

Standish, N & Meta, IA 1985, 'Some kinetic aspects of continuous screening', *Powder Technology*, vol. 41, no. 2, pp. 165-71.

Stesscl, RI & Cole, K 1996, 'Laboratory investigation of a new trommel model', *Journal of the Air & Waste Management Association*, vol. 46, no. 6, pp. 558-68.

Subasinghe, Schaap, W & Kelly, EG 1989, 'Modelling the screening process — an empirical approach', *Minerals Engineering*, vol. 2, no. 2, pp. 235-44.

Subasinghe, G, Schaap, W & Kelly, E 1989, 'Modelling the screening process: A probabilistic approach', *Powder Technology*, vol. 59, no. 1, pp. 37-44.

Taggart, A 1945, 'Handbook of mineral dressing, John Wileyand Sons', *Inc., NY*, pp. 19-105.

Tai, CH & Hsiau, SS 2004, 'Dynamic behaviors of powders in a vibrating bed', *Powder Technology*, vol. 139, no. 3, pp. 221-32.

Takabatake, K, Mori, Y, Khinast, JG & Sakai, M 2018, 'Numerical investigation of a coarse-grain discrete element method in solid mixing in a spouted bed', *Chemical Engineering Journal*, vol. 346, pp. 416-26.

Tang, J, Zhao, L, Yu, W, Yue, H & Chai, T 2010, 'Soft sensor modeling of ball mill load via principal component analysis and support vector machines', in Z Zeng & J Wang (eds), *Advances in Neural Network Research and Applications*, Springer Berlin Heidelberg, Berlin, Heidelberg, pp. 803-10.

Tang, P & Puri, VM 2005, 'An innovative device for quantification of percolation and sieving segregation patterns–single component and multiple size fractions', *Particulate Science and Technology*, vol. 23, no. 4, pp. 335-50.

Thornton, C & Yin, KK 1991, 'Impact of elastic spheres with and without adhesion', *Powder Technology*, vol. 65, no. 1, pp. 153-66.

Tian, ZA, Dong, KJ & Yu, AB 2014, 'Structural evolution in the packing of uniform spheres', *Physical Review E*, vol. 89, no. 3, p. 032202.

Toleva, B 2021, 'The proportion for splitting data into training and test set for the bootstrap in classification problems', *Business Systems Research Journal*, vol. 12, pp. 228-42.

Trumic, M & Magdalinovic, N 2011, 'New model of screening kinetics', *Minerals Engineering*, vol. 24, no. 1, pp. 42-9.

Tsugeno, Y, Sakai, M, Yamazaki, S & Nishinomiya, T 2021, 'DEM simulation for optimal design of powder mixing in a ribbon mixer', *Advanced Powder Technology*, vol. 32, no. 5, pp. 1735-49.

Vapnik, V 1995, *The nature of statistical learning theory*, New York vols, Springer,New York.

Vorobiev, O 2012, 'Simple Common Plane contact algorithm', *International Journal for Numerical Methods in Engineering*, vol. 90, no. 2, pp. 243-68.

Vu-Quoc, L, Zhang, X & Walton, OR 2000, 'A 3-D discrete-element method for dry granular flows of ellipsoidal particles', *Computer Methods in Applied Mechanics and Engineering*, vol. 187, no. 3-4, pp. 483-528.

Wachs, A, Girolami, L, Vinay, G & Ferrer, G 2012, 'Grains3D, a flexible DEM approach for particles of arbitrary convex shape — Part I: Numerical model and validations', *Powder Technology*, vol. 224, no. 0, pp. 374-89.

Walton, OR 1993, 'Numerical simulation of inclined chute flows of monodisperse, inelastic, frictional spheres', *Mechanics of materials*, vol. 16, no. 1-2, pp. 239-47.

Wang, C, Dong, K & Yu, A 2015, 'Structural characterization of the packings of granular regular polygons', *Physical Review E*, vol. 92, no. 6, p. 062203.

Wang, G & Tong, X 2011, 'Screening efficiency and screen length of a linear vibrating screen using DEM 3D simulation', *Mining Science and Technology (China), vol. 21, no. 3, pp. 451-55*.

Wang, X, Li, Z, Tong, X & Ge, X 2018, 'The influence of particle shape on screening: case studies regarding DEM simulations', *Engineering Computations*, vol. 35, no. 3, pp. 1512-27.

Wellmann, C, Lillie, C & Wriggers, P 2008, 'A contact detection algorithm for superellipsoids based on the common-normal concept', *Engineering Computations*, vol. 25, no. 5, pp. 432-42.

wikipedia 'Granular material (particulate),https://en.wikipedia.org/wiki/Granular_material, Accessed 08 August 2021.', in.

Wilkinson, D & Edwards, SF 1982, 'Spontaneous interparticle percolation', *Proc. R. Soc. Lond. A*, vol. 381, no. 1780, pp. 33-51.

Williams, JC & Shields, G 1967, 'The segregation of granules in a vibrated bed', *Powder Technology*, vol. 1, no. 3, pp. 134-42.

Wills, BA & Finch, JA 2016, 'Chapter 8 - Industrial Screening', in BA Wills & JA Finch (eds), *Wills' Mineral Processing Technology (Eighth Edition)*, Butterworth-Heinemann, Boston, pp. 181-97.

Windows-Yule, C 2016, 'Convection and segregation in fluidised granular systems exposed to two-dimensional vibration', *New Journal of Physics*, vol. 18, no. 3, p. 033005.

Wolff, ER 1954, 'Screening principles and applications', *Industrial & Engineering Chemistry*, vol. 46, no. 9, pp. 1778-84.

WovenWireScreens 'Gaptechnology, http://www.gaptechnology.co.uk/woven-wire-screens/, Accessed 16th Jun (2022).'.

Wu, H & Fuxreiter, M 2016, 'The structure and dynamics of higher-order assemblies: Amyloids, signalosomes, and granules', *Cell*, vol. 165, no. 5, pp. 1055-66.

Xiong, X, Niu, L, Gu, C & Wang, Y 2017, 'Vibration characteristics of an inclined flip-flow screen panel in banana flip-flow screens', *Journal of Sound and Vibration*, vol. 411, pp. 108-28.

Yan, H, Li, Y, Yuan, F, Peng, F, Yang, X & Hou, X 2020, 'Analysis of the screening accuracy of a linear vibrating screen with a multi-layer screen mesh', *Strojniški vestnik - Journal of Mechanical Engineering*, vol. 66, no. 5, pp. 289-99.

Yan, Z, Wilkinson, SK, Stitt, EH & Marigo, M 2015, 'Discrete element modelling (DEM) input parameters: understanding their impact on model predictions using statistical analysis', *Computational Particle Mechanics*, vol. 2, no. 3, pp. 283-99.

Yang, RY, Zou, RP & Yu, AB 2003, 'Numerical study of the packing of wet coarse uniform spheres', *AIChE Journal*, vol. 49, no. 7, pp. 1656-66.

Yi, LY, Dong, KJ, Zou, RP & Yu, AB 2011, 'Coordination number of the packing of ternary mixtures of spheres: DEM simulations versus measurements', *Industrial & Engineering Chemistry Research*, vol. 50, no. 14, pp. 8773-85.

Yin, Z, Zhang, H & Han, T 2016, 'Simulation of particle flow on an elliptical vibrating screen using the discrete element method', *Powder Technology*, vol. 302, pp. 443-54.

Yu, AB & Hall, JS 1994, 'Packing of fine powders subjected to tapping', *Powder Technology*, vol. 78, no. 3, pp. 247-56.

Yu, C, Lin, D, Xu, N, Wang, X, Pu, K, Wang, Z et al. 2023, 'DEM simulation of particle flow and separation in a vibrating flip-flow screen', *Particuology*, vol. 73, pp. 113-27.

Zhang, B, Gong, J, Yuan, W, Fu, J & Huang, Y 2016, 'Intelligent prediction of sieving efficiency in vibrating screens', *Shock and Vibration*, vol. 2016, p. 9175417.

Zhang, S-l, Wu, G-j, Yang, X-g, Jiang, W-h & Zhou, J-w 2018, 'Digital image-based identification method for the determination of the particle size distribution of dam granular material', *KSCE Journal of Civil Engineering*, vol. 22, no. 8, pp. 2820-33.

Zhang, Y & Ling, C 2018, 'A strategy to apply machine learning to small datasets in materials science', *npj Computational Materials*, vol. 4, no. 1, p. 25.

Zhao, J, Li, S, Zou, R & Yu, A 2012, 'Dense random packings of spherocylinders', *Soft Matter*, vol. 8, no. 4, pp. 1003-9.

Zhao, L-L, Li, Y-W, Yang, X-D, Jiao, Y & Hou, Q-F 2019, 'DEM study of size segregation of wet particles under vertical vibration', *Advanced Powder Technology*, vol. 30, no. 7, pp. 1386-99.

Zhao, L, Zhao, Y, Bao, C, Hou, Q & Yu, A 2016, 'Laboratory-scale validation of a DEM model of screening processes with circular vibration', *Powder Technology*, vol. 303, pp. 269-77.

Zhao, L, Zhao, Y, Bao, C, Hou, Q & Yu, A 2017, 'Optimisation of a circularly vibrating screen based on DEM simulation and Taguchi orthogonal experimental design', *Powder Technology*, vol. 310, pp. 307-17.

Zhao, L, Zhao, Y, Liu, C, Li, J & Dong, H 2011, 'Simulation of the screening process on a circularly vibrating screen using 3D-DEM', *Mining Science and Technology (China)*, vol. 21, no. 5, pp. 677-80.

Zhao, Z, Jin, M, Qin, F & Yang, SX 2021, 'A novel neural network approach to modeling particles distribution on vibrating screen', *Powder Technology*, vol. 382, pp. 254-61.

Zheng, Q & Yu, A 2014, 'Why have continuum theories previously failed to describe sandpile formation?', *Physical Review Letters*, vol. 113, no. 6, p. 068001.

Zhong, W, Yu, A, Liu, X, Tong, Z & Zhang, H 2016, 'DEM/CFD-DEM modelling of non-spherical particulate systems: theoretical developments and applications', *Powder Technology*, vol. 302, pp. 108-52.

Zhou, H, Luo, Z, Zhang, T, You, Y, Li, H & Zou, Z 2016, 'Influence of rolling friction coefficient on inter-particle percolation in a packed bed by discrete element method', *Archives of Metallurgy and Materials*, vol. 61, no. 4, pp. 1795-804.

Zhou, H, Wu, S, Kou, M, Luo, Z-g, Zou, Z-s & Shen, Y 2018, 'Analysis of cohesive particle percolation in a packed bed using discrete element method', *ISIJ international*, vol. 58, no. 1, pp. 43-51.

Zhou, YC, Wright, BD, Yang, RY, Xu, BH & Yu, AB 1999, 'Rolling friction in the dynamic simulation of sandpile formation', *Physica A: Statistical Mechanics and its Applications*, vol. 269, no. 2, pp. 536-53.

Zhou, Z-Y, Zou, R-P, Pinson, D & Yu, A-B 2011, 'Dynamic simulation of the packing of ellipsoidal particles', *Industrial & Engineering Chemistry Research*, vol. 50, no. 16, pp. 9787-98.

Zhu, H, Zhou, Z, Yang, R & Yu, A 2007, 'Discrete particle simulation of particulate systems: theoretical developments', *Chemical Engineering Science*, vol. 62, no. 13, pp. 3378-96.

Zhu, HP, Rahman, M, Yu, AB, Bridgwater, J & Zulli, P 2009, 'Effect of particle properties on particle percolation behaviour in a packed bed', *Minerals Engineering*, vol. 22, no. 11, pp. 961-9.

Zhu, HP & Yu, AB 2006, 'A theoretical analysis of the force models in discrete element method', *Powder Technology*, vol. 161, no. 2, pp. 122-9.

Zhu, HP, Zhou, ZY, Yang, RY & Yu, AB 2007, 'Discrete particle simulation of particulate systems: Theoretical developments', *Chemical Engineering Science*, vol. 62, no. 13, pp. 3378-96.

Zhu, HP, Zhou, ZY, Yang, RY & Yu, AB 2008, 'Discrete particle simulation of particulate systems: A review of major applications and findings', *Chemical Engineering Science*, vol. 63, no. 23, pp. 5728-70.

Zou, RP & Yu, AB 1996, 'Evaluation of the packing characteristics of mono-sized non-spherical particles', *Powder Technology*, vol. 88, no. 1, pp. 71-9.